AN EXPERIMENTAL INVESTIGATION ON THE MICROMECHANICS OF NON-ACTIVE CLAYS IN SATURATED AND PARTIALLY SATURATED STATES

Matteo Pedrotti

Thesis submitted to the Department of Civil and Environmental Engineering, University of Strathclyde, Glasgow, in fulfilment of the requirements for the degree of

Doctor of Philosophy

in

Civil and Environmental Engineering

February 2016,

Glasgow, UK

Declaration of authenticity and author's right

This thesis is the result of the author's original research. It has been composed by the author and has not been previously submitted for examination which has led to the award of a degree.

The copyright of this thesis belongs to the author under the terms of the United Kingdom Copyright Acts as qualified by Univerity of Strathclyde Regulation 3.50. Due acknowledgement must always be made of the use of any material contained in, or derived from, this thesis.

Signed:

Date: 18 February 2016

Abstract

This thesis presents an experimental investigation of the micromechanical behaviour of non-active clay, both in saturated and unsaturated states.

For the case of saturated clays, 1-D compression tests on kaolin saturated with fluids having different dielectric permittivity (air, acetone, and water) and pH (acid and basic aqueous solutions) were performed. Based on the Pore-Size Distribution (PSD) of samples taken on both the virgin and the unloading curves, the electrochemical and mechanical forces controlling inter-particle interaction and the particle configuration along reversible and non-reversible compression paths were inferred. Ultimately, a conceptual micromechanical model was formulated and designed in such a way that it could be potentially implemented in a Discrete Element Model (DEM) for clay geomaterials. To show the capability of the conceptual micromechanical model, an 'embryonic' 1-D DEM model was developed. It was shown to be capable of capturing, at a qualitative level, the 1-D response of clay saturated with fluids of different dielectric permittivity.

Moving to the unsaturated state, an observation was initially made that the mono-modal PSDs of kaolin in reconstituted and dry states fit quite well the pore-size distribution of the micro-pores and the macro-pores respectively in compacted samples. Based on this observation, an assumption was put forward that macro-pores are filled with air ('air-saturated') and micro-pores are filled with water ('water-saturated'). The comparison of the PSD of samples compacted with water and acetone and the comparison of the PSDs of samples freeze-dried and oven-dried appeared to corroborate such an assumption.

A particle-based microstructural conceptual model for unsaturated soils was then formulated. Such a model can explain the evolution of PSD observed at various compaction water contents. Besides, this microstructural conceptual model was proven to be as effective as the traditional aggregate-based microstructural model in interpreting some of the classical responses of

unsaturated soils including volumetric collapse upon wetting. A particle-based microstructural model provides an alternative approach to the aggregate-based microstructural model that has (potentially) the advantage of facilitating the formulation of DEM models for unsaturated clays. Another advantage is that the conceptual microstructural model and, hence, any DEM models would remain essentially the same for saturated and unsaturated states.

Following the idea that macro-pores are filled with air and micro-pores are filled with water, it was assumed that the response of unsaturated soils can be modelled by considering separately the response of the dry part (air-saturated) and wet part (water-saturated). To model 1-D compression, the void ratio of the dry part was read from the 1-D compression of dry kaolin and the void ratio of the wet part was read from the 1-D compression of the saturated reconstituted kaolin. This approach allowed modelling the water-undrained compression tests in Tarantino & De Col (2008) with excellent accuracy.

Ai miei genitori,

Antonella e Corrado.

Acknowledgments

Table of Contents

Table of Figures

List of Tables

Introduction

The thesis focuses on the micro-mechanical response of non-active clay under both saturated and partially saturated conditions. The main motivation behind this research was to formulate a particle-based micro-mechanical conceptual model serve as a basis for the implementation of DEM for clays. Over the last 10 years, the number of publications related to discrete element model (DEM) in geomechanics has more than quintupled. DEM has proven to be a powerful tool for understanding particle-scale interaction and fundamental concepts in granular materials but little has been done for clays so far, mainly because of the huge computational effort required.

Under saturated conditions, micro-mechanisms controlling the response of clays have been poorly elucidated. For example, no particular attention has been paid to the micro-mechanisms controlling reversible and non-reversible volume changes.

When discussing inter-particle forces in clay geomaterials, electrochemical interactions are generally invoked, very often in terms of diffuse double layer interaction. Such an interaction is associated with a non-contact configuration since the electrostatic repulsion prevents particles coming into contact. The inter-particle interaction resulting from the overlapping of the diffuse double layer has led to the view that clay particles behave fundamentally differently from sand particles. Clay particle interaction is controlled by electrochemical forces in contrast to sand particle interaction that is indeed mechanical in nature. Clay particles are 'floating' in an electrical field whereas sand particles are brought into contact when loaded.

This view however, conflicts with another view of micro-mechanical interactions in clays that underlies the "progenitor" of elasto-plastic models for clays, the original Cam Clay model. This model was indeed formulated on the

assumption that the energy input to the system is entirely dissipated in frictional work, i.e. clay particle interactions are mechanical in nature.

Yet the question remains open about the role of electrochemical and mechanical interaction in clays and the micro-mechanisms controlling plastic and elastic behaviour. A better understanding of such micro-mechanisms will help inform macroscopic constitutive models and lay the basis for models for clays based on the Discrete Element Method (DEM).

For the case of partially saturated clays, much more emphasis has been given to clay microstructure to interpret and model hydro-mechanical response at the macroscopic level. It is generally assumed that aggregates form in partially saturated clays, especially when they are in a compacted state. Aggregates are viewed as the elementary units controlling the macroscopic behaviour and microstructural variables reflecting the nature and/or size of the aggregates are often incorporated into macroscopic models.

Despite the fact that the aggregated nature of compacted partially saturated soils is generally accepted, a number of aspects still deserves to be further investigated. For example, the mechanism leading to the formation of aggregates during compaction has not been fully understood. Whether or not the aggregates form an indivisible unit also remains an open question.

The presence of aggregates is in general associated with double porosity. The family of macro-pores has often been observed to evolve upon hydro-mechanical paths. This has been attributed to a rearrangement of the aggregates but can also be associated with a breakage of the aggregates.

Another intriguing observation is that compacted kaolinite clay shows two distinct modal pore sizes that remain essentially stable over a very wide range of compaction water content. When the compaction water content decreases from the optimum water content, the frequency of the two families of pores changes but not their modal size. This aspect, for example, is difficult to interpret based on the aggregate microstructural conceptual model.

Microstructure has been always invoked to explain differences between the response of reconstituted and compacted clays, as if the mechanism of soil formation is indelibly imprinted on the soil. It is commonly assumed that reconstituted and compacted soils exhibit a fundamentally different behaviour due to different microstructures. However, if one looks at the variety of pore size distributions in both compacted and reconstituted soils, the boundary between these states is perhaps much more blurred. It may therefore be worth comparing the microstructure as well as the macroscopic behaviour of soils in reconstituted and compacted states to identify similarities and differences. It may be interesting to investigate the aspects of compacted soil behaviour that can be extrapolated to reconstituted soils and vice versa.

To address these points, the dissertation has been developed along five chapters. The first chapter, presents a literature review and the motivations behind this study on the microstructure of non-active clays. Current state-of-the-art on the micro-mechanisms in saturated and partially saturated clays has been critically reviewed.

Fundamentals of clay mineralogy including inter-particle interactions based on diffuse double layer and Van der Waals forces are presented. Studies investigating the effects of such forces on the response at macroscopic level have been discussed. These include the rheology of suspensions and the study of the mechanical response of saturated clays. Particle configuration, on the other hand, has been mainly investigated relying on the study of existing conceptual models for partially saturated clays, where more attention has been historically paid.

In the second chapter, the Mercury Intrusion Porosimetry (MIP) technique is presented. The MIP has been proven to be a powerful tool to investigate microstructure as it provides quantitative information about the distribution of pores and, indirectly, the arrangement of particles. Accordingly, MIP has been used in this work as a major tool to investigate clay microstructure and its evolution upon hydro-mechanical paths. A brief literature review on the technique and the way of analysing the data is presented. Subsequently a

study of the magnitude of the error of the measure of the pore size due to the sample preparation and the intrusion/extrusion of the mercury is presented. Finally, a conceptual model of the mercury intrusion/extrusion in a porous material is proposed.

In the third chapter, a conceptual micromechanical model for non-active clays is developed. This has been formulated with the view to lay the basis for discrete element modelling of clays. Micro-mechanisms controlling reversible and non-reversible behaviour have been proposed based on the role played by the edge-to-face interaction. To demonstrate the potential of the conceptual model to serve as a basis for DEM formulations, an 'embryonic' DEM model has been developed. This was aimed at checking the capability of the DEM formulation to reproduce, at a qualitative level, major features of the response of clays in 1-D compression.

In the fourth chapter, partially saturated clays have been investigated. Following the idea that macro-pores are filled with air and micro-pores are filled with water, the assumption has been made that the response of unsaturated soils can be modelled by considering separately the response of the dry part (air-saturated) and wet part (water-saturated).

The conceptual model proposed in chapter 3 for the saturated clays was therefore extended to partially saturated states. To model 1-D compression at constant water content, the void ratio of the dry part was assumed to be read from the 1-D compression of dry kaolin and the void ratio of the wet part to be read from the 1-D compression of the saturated (reconstituted) kaolin. Although the approach seems apparently very simplistic, it allowed modelling of macroscopic experiments with astonishing accuracy.

Finally, chapter five incorporates a series of preliminary experiments on particle interaction and configuration at different pH and electrolyte concentration of the pore-water. For such experiments, a clear interpretation

was not always possible. Nevertheless, it is believed that such experimental campaign may lay the basis for future research works and thus still worth being presented.

Chapter 1.   Literature review

1.1 Overview of the chapter

The following chapter is organised in three main sections:

- Discrete element modelling of soil mechanical behaviour
- Microstructure of clays in suspension and consolidated state
- Microstructure of non-active clays under partially saturated conditions

In the first part a brief review of the discrete element modelling in soil mechanics is given. Particular focus has been paid to the importance of developing a DEM for clays. This review highlighted that the relationship between the particle-scale interaction and the overall macroscopic material response in clay might not be fully understood yet.

In the second part of the chapter the main conclusions on the existing knowledge regarding the microstructure of clays under saturated conditions are presented. When possible, microstructure has been separately analysed in terms of particle interaction and particle configuration.

In this section, microstructure is presented relying on the state of the art of clay science rather than in soil mechanics, since topics as clay mineralogy, particle electrical charge and particle interactions, including double layer and Van der Waals are presented. Such topics, although not always covered in the geotechnics background, are believed to be fundamental if the microstructure of clays is to be fully investigated.

The effect of the different particle interactions has been considered at macroscopic level both by means of the study of the rheology of suspensions and the study of the mechanical response of consolidated clays exposed to pore-water having different chemistry.

In the third part of the chapter the microstructure of non-active clays under partially saturated conditions is presented. The literature review has been

discussed with the goal of highlighting existing contradictions in terms of microstructural conceptual model.

1.2 Discrete element modelling of soil mechanical behaviour

The mechanical response of geo-materials has been traditionally analysed and modelled within the context of continuum mechanics. Although in the past 50 years significant progress has been made in advancing the understanding and modelling of soil mechanical response at macroscopic level (e.g. development of critical state mechanics framework), the relationship between the particle-scale interaction and the overall macroscopic material response is not completely understood.

In this respect, the Discrete Element Modelling (DEM) has proven to be an incredibly powerful tool because it allows capturing the interplay between particle-scale interactions and the overall observed granular material response. The DEM has rapidly gained acceptance as a major tool for investigating the behaviour of soils, and key aspects of soil response have been demonstrated to "emerge" from DEM models. Particle-scale interaction cannot be measured in laboratory tests, but it can easily be monitored in "virtual" tests. The DEM has been used as a "computer laboratory" to simulate direct shear test or triaxial tests and to investigate soil liquefaction, and it could have other important applications in more fundamental work (Thornton & Liu, 2000, Thornton, 2007, Cui & O'sullivan, 2006). It has been applied to investigate the effect of interparticle friction, rolling, and dilation on the macroscopic angle of shearing resistance and to explore the role of particle crushing in controlling the compression behaviour of soils. By using DEM, the degree of inherent anisotropy in the material can be quantified, and the mechanisms controlling the evolution of anisotropy (induced anisotropy) during loading can be monitored. The essence of the DEM is to recognise the particulate nature of soils, in contrast to the basic assumptions of continuum mechanics (Simpson & Tatsuoka, 2008, O'Sullivan, 2011).

Given these factors, the discrete element modelling is being used more and more within the geotechnical research community. In the last 10, years the

number of publications related with DEM in geomechanics has more than quintupled. (Zhu et al., 2007).

While the major contribution of DEM in geomechanics is mainly related to understanding the fundamental nature of soil behaviour, attempts have been made to apply DEM directly to solve larger-scale engineering problems. (Butlanska et al., 2013), although scale dependency problems may arise. For example, DEM can overcome limitations of conventional continuum mechanics-based approaches in which the development of finite displacements or localizations within the material require re-meshing and pose convergence challenges (O'Sullivan, 2011, Simpson & Tatsuoka, 2008).

The principal challenge in the use of DEM to simulate large deformation problems of industrial relevance, however, is the number of particles that are included in the DEM models. Although Cundall (2001) predicted that by 2011 a DEM simulation involving 10 million particles would constitute an easy problem, it is clear that the within geotechnical community the largest simulations remain at least one order of magnitude smaller than this aspiration. Nevertheless, DEM simulations can provide insight into the mechanisms involved in field-scale applications. So far, problems of greatest interest within the geomechanics community are probably pile installation and cone penetration test (CPT) simulations (O'Sullivan, 2011).

1.2.1 DEM for granular materials

Two approaches to DEM have been developed: soft-particle and hard-particle. The soft-particle method, originally developed by Cundall & Strack (1979), was the first granular dynamics simulation technique published in the literature. In this approach, particles are permitted to suffer minute deformations, and these deformations are used to calculate elastic, plastic and frictional forces between particles. The motion of particles is described by the well-established Newton's laws of motion. A characteristic feature of the soft-sphere models is that they are capable of handling multiple particle contacts, which is of importance when modelling quasi-static systems. By contrast, a sequence of collisions is processed in a hard-particle simulation. One instantaneous collision is

considered and forces between the particles are often not explicitly considered. As a result, the hard-particle method is most useful in rapid granular flows (Zhu et al., 2007).

According to Cundall & Strack (1979), who first introduced the DEM simulation in geotechnical problems, the calculation performed in the distinct element method (for soft-spheres) alternate between the application of Newton's second law to the disk and a force-displacement law at contact. Newton's second law gives the motions of a particle resulting from the forces acting on it.

i) The force-displacement law is used to find contact forces from displacements

ii) The deformations of the individual particles are small in comparison with the deformations of the system

iii) The system's deformations are mainly due to the movements of particles as rigid bodies, therefore precisely modelling the particle deformations are not necessary to obtain a good approximation of the mechanical behaviour.

1.2.2 DEM for clays

DEM analyses in geotechnics have been mainly implemented to simulate the response of granular materials, which are defined as geomaterials exceeding 100 μm in particle size (O'Sullivan, 2011). Such a particle dimensions is generally sufficient to guarantee that surface attraction and non-contact forces are negligible with respect to the particle inertia (non-cohesive material). Under these circumstances, particle interaction forces are assumed to be mechanical in nature. The force-displacement constitutive relationships at the contact, although difficult to measure experimentally, are generally assumed to be elastic and/or plastic and/or viscous according to classical mechanical responses of solid materials. In addition, the elementary unit is generally assumed to be a sphere as grains have typically a high degree of sphericity.

On the other hand, the role of the microstructure (particle configuration and electrochemical and mechanical particle interaction) is dominant in clays. The initial particle configuration has to be hypothesized (parallel and/or non-parallel particles, aggregated or non-aggregated particles) and particle dimension might not be assumed to be constant as is the case in active-clays. In addition, particle interactions are much more complex (being a combination of electro-chemical forces of various nature and mechanical forces) and in principle difficult to infer from microstructural investigation, essentially based on non-optical microscopy (Scanning Electron Microscope) and Mercury Intrusion Porosimetry.

As stated by Anderson & Lu (2001), while the microscopic and discrete methodology enjoys great success in granular soils (among many others Oda & Konishi (1974), Ng & Dobry (1994), Chang et al. (1992), Ng (1994) and Cundall & Strack (2013)), several fundamental challenges are faced when dealing with clays:

i) Clay particles are usually extremely small in size, typically on the order of micron or sub-micron scale which can give rise to numerical oscillation problems if the elementary unit in the DEM is designed with realistic dimensions;

ii) Particle geometry is irregular and complicated, varying from a thin sheet for kaolinite to needle shaped rods for hallosite;

iii) Clay particles are minerals and their chemical composition and electro-chemical interactions can vary greatly depending on the soil's geological and environmental history;

iv) Particle size may vary depending on the nature of the clay ("active" or "non-active").

Due to the above fundamental differences between clays and granular materials, forces governing the physical and mechanical interactions between individual particles are complex. In addition to the mechanical and hydraulic forces commonly dominating particle interactions in granular soils, electro-

chemical interparticle forces have been recognised to be play a fundamental role in clays and these are affected by particle size, pore-water chemistry, and clay mineralogy.

Due to the uncertainty about the interparticle forces to be modelled in DEM and the difficulty of formulating distinct element models with plate-like particles, there have been limited contributions to the discrete modelling of clayey soils. These include sedimentation of clay particles (Anderson & Lu, 2001, Lu et al., 2008, Anandarajah & Chen, 1997, Anandarajah, 1997), consolidation of non-swelling clays (2D Anandarajah 2000 and 3D Yao & Anandaraja 2003)), volumetric behaviour of swelling (active) clays (Anderson & Lu, 2001, Katti et al., 2009, Anandarajah & Amarasinghe, 2012), and the effect of soil suction on hydraulic and mechanical response (Péron et al., 2009, Liu & Sun, 2002, Anandarajah & Amarasinghe, 2011).

Although all the proposed models succeeded in simulating some of the modelled behaviours from a qualitative point of view, they cannot be considered exhaustive, but just at an early development stage.

Simulations of sedimentation tests have been shown to be capable of capturing the qualitative trend of sedimentation time and floc dimensions upon electrolyte concentration increase. At the same time, they failed in predicting mechanical response from a quantitative point of view including the final volume of the sediments (which depends on the initial microstructure). Consolidation curve obtained from simulation of 1-D compression on non-active clays fitted experimental data, but they were the result of an initial configuration where particles were not in contact and the non-reversible mechanisms were attributed to the creation of new non-reversible bonding between particles rather than frictional dissipation.

Besides modelling issue such as from 2D to 3D scaling problems and geometry of the elementary units (spherical, plat-like, and so on), two issues are considered to be the relevant limitation of the existing models:

i) Neglecting edge-to-face particle attraction, both for modelling problems (complexity in having a discrete element with two different charges on the same particle) and theoretical assumptions (particles are generally assumed to be homogenously charged). Experimental data in the next chapter will show that the activated edge to face attraction plays a crucial role in the mechanical behaviour of non-active clays.

ii) Limited understanding of the interparticle forces involved and difficulty in assessing model parameters.

1.3 Microstructure of clays in suspension and consolidated state

1.3.1 Structure of kaolin

Clay minerals occur in small particle sizes. The structure of common clay minerals is two-dimensional arrays of silicon-oxygen tetrahedra and two-dimensional arrays of aluminium- or magnesium-oxygen-hydroxyl octahedra. Different kinds of clay depend on the stacking arrangements of tetrahedral and octahedral sheets (Van Olphen, 1977, Mitchell & Soga, 2005).

In the silicon-oxygen sheets, the silicon atoms are coordinated with four oxygen atoms. The oxygen atoms are located at the four corners of the tetrahedron with the silicon atom in the centre. The silica tetrahedrons are interconnected in a sheet structure, where each tetrahedron shares three of the four oxygen atoms with the neighbouring tetrahedrons (Figure 1). The oxygen-to-oxygen distance is 2.55 Å (1 Å=0.1 nm), the space available for the silicon ion is 0.55 Å, and the thickness of the sheet in clay mineral structure is 4.63 Å (Grim, 1968, Mitchell & Soga, 2005).

In the aluminium- or magnesium-oxygen-hydroxyl octahedra, the Al or Mg are coordinated with six oxygen atoms or OH groups, which are located around the Al or Mg atom with their centres on the six corners of a regular octahedron. The interconnection between different octahedral sheets is due to the sharing of oxygen atoms with the neighbouring octahedron. The oxygen atoms and hydroxyl groups lie in two parallel planes with Al or Mg atoms between these planes (Van Olphen, 1977) (Figure 1). The oxygen-to-oxygen distance is 2.60 Å and the space available for the octahedrally coordinated cation is 0.61 Å. The thickness of the sheet is 5.05 Å (Grim, 1968, Mitchell & Soga, 2005).

The combination of an octahedral sheet and one or two tetrahedral sheet is called a unit layer. Most clay minerals consist of such unit layers, which are stacked parallel to each other (Van Olphen, 1977).

The clay minerals in the kaolinite group are composed of altering silica and octahedral sheets. The tips of the silica tetrahedral and one of the planes atoms in the octahedral sheet are common (Figure 3).
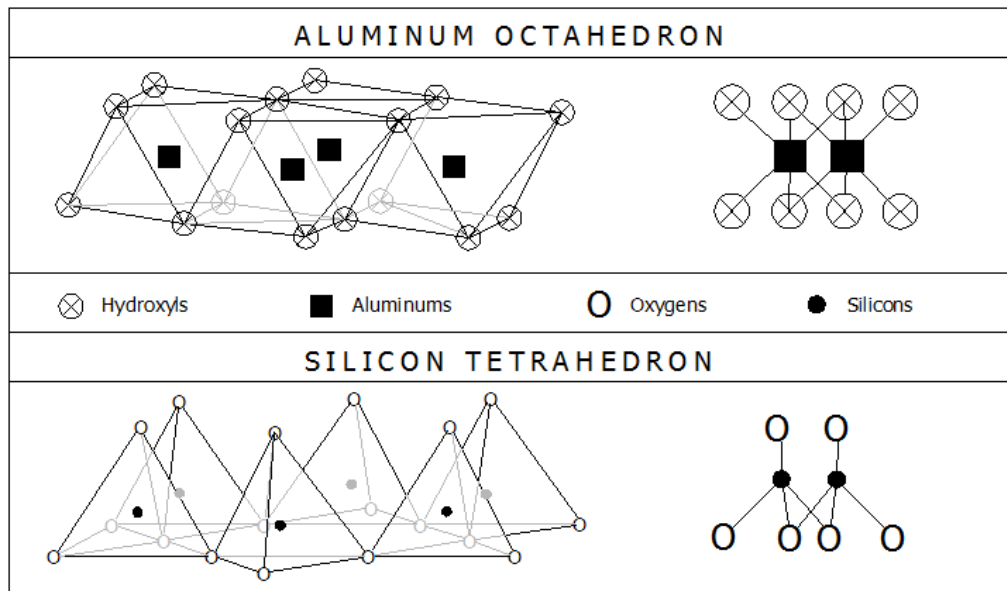
Figure 1. Aluminium octahedron and silicon tetrahedron (Mitchell & Soga, 2005)

The distance between a certain plane in the unit layer and the corresponding plane in the next unit layer (so called *c spacing*), is about 7.1-7.2 Å (Mitchell & Soga, 2005, Van Olphen, 1977). Mineral particles of kaolinite consist of the basic unit layers stacked in the c direction. The bonding between successive layers is by both Van der Waals forces and hydrogen bonds. The bonding is sufficiently strong that there is no interlayer swelling in the presence of water (Mitchell & Soga, 2005). This peculiarity determines the 'non-swelling' clay denomination for clays belonging to the kaolinite group.

For kaolinite, the ratio of edge surfaces is high, about 12%–34% (Ferris and Jepson 1975; Brady et al. 1996; Zbik and Smart 1998), and the face charge due to isomorphic substitution is not severe (Brady & Weil, 1996, Wang & Siu, 2006, Van Olphen, 1977).

Kaolin particles are hexagonal plate-like with an equivalent Stoke's diameter of about 1 μm. Thickness of particles may vary significantly, starting from values of at least 50 nm (Mitchell & Soga, 2005), which corresponds to at least a hundred unit layers stacked together in the c-direction.

1.3.2 Surface charges of kaolin

Charges on the kaolin surface are the result of permanent charges and pH-dependant charges. Charge sources are:

- Isomorphic substitution of cations that are located at surface faces (permanent charges).

- Protonation/deprotonation of hydroxyl groups of broken edges (pH-dependant charges) (Rand & Melton, 1977, Van Olphen, 1977, Mitchell & Soga, 2005).

According to Mitchell & Soga (2005), there are isomorphic substitutions in clay minerals when some of the tetrahedral and octahedral spaces are occupied by cations other than those in the ideal structure. Isomorphic substitutions in kaolin are usually substitutions of Al^{3+} for Si^{4+} in the silica sheet or of a divalent ion for Al^{3+} in the octahedral sheet (Schofield & Samson, 1954, Van Olphen, 1977, Wang & Siu, 2006, Mitchell & Soga, 2005) thus creating a negative net charge of the faces.

Pore fluid pH affects the charge of the surface by protonation or deprotonation of ionisable groups located at the edges or at the basal faces (Table 1). The electro-neutrality of the edges gives rise to the transformation of the oxygens into silanol (>SiOH) or aluminol (>AlOH) groups (Sposito, 1984, Huertas et al., 1998).

Table 1: Protonation and deprotonation reactions in kaolin

PROTONATION	$Al\text{-}OH + H^+$	↔	$Al\text{-}OH_2^+$
DEPROTONATION	$Al\text{-}OH + OH^-$	↔	$Al\text{-}O^-\ H_2O$
	$Si\text{-}OH + OH^-$	↔	$Si\ O^-\ H_2O$

The silanol groups contribute only to the negative charge forming $>SiO^-$ by deprotonation. The aluminol group can create either positive or negative charges depending on the kind of the reaction (protonation or deprotonation). Those reactions result in the formation of surface complexes $>AlOH_2^+$ and AlO^- respectively (Table 1).

The role played by $>Al_2OH$ groups at the basal plane is still not clear though those are less reactive than aluminol groups at the edges. (Huertas et al., 1998, Ganor et al., 1995)

In general the silica tetrahedral face is negatively charged at pH higher than 3 (Wang & Siu, 2006, Gupta et al., 2011, Carty, 1999) and the related point of zero charge (PZC) has been found to be at pH ranging from 2-4. The alumina octahedral face is considered to be positively charged at acidic values of pH and negatively charged at basic values of pH (Carty, 1999, Gupta et al., 2011, Wang & Siu, 2006). Nevertheless, the overall surface charge on the basal planes is generally considered to be negative (Wang & Siu, 2006) because of the isomorphic substitution, with the charge magnitude being dependent on pH.

AUTHORS	pH PZC
Gupta et al. 2011	5.0-6.0
Huertas et al. 1998	5.5
Braggs et al. 1994	5.3
Kretzschmar et al. 1998	5.7
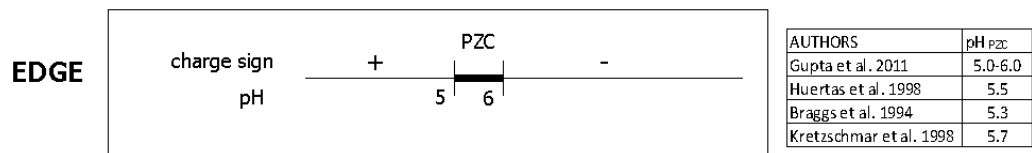
Figure 2. Point of zero charge in kaolin edge

On the other hand, edge charges are more pH dependent than face ones. They are considered to be positively charged for acidic conditions and negatively charged for alkaline conditions (Figure 2).

As shown in Figure 3 protonation and deprotonation reactions will occur if the edge goes into contact with solutions at different pH.
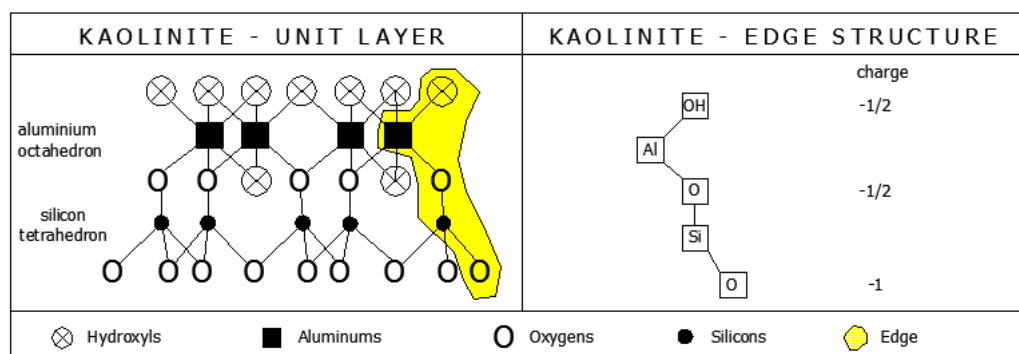
Figure 3: Kaolinite edge surface charges (Modified from Mitchell & Soga 2005)

Starting from the configuration shown in Figure 3, with a negative charge on the edge surface, in the presence of free H^+ (acidic solution), the charge will gradually move toward a zero charge condition (point of zero charge, PZC, of the edge surface) and then to a positive charge condition, because protonation reactions occur. On the other hand, in the presence of free OH^- (basic solution) the edge surface will move towards a more negative charge condition because of the deprotonation reaction.

According to many authors, including Gupta et al. (2011), Huertas et al. (1998), Braggs et al. (1994) and Kretzschmar et al. (1998), the PZC of the surface edges of kaolin particles is placed between pH values of 5 and 6 (Figure 2).

A reasonable layout of charge configuration of the edge surface is reported in Figure 4.

In conclusion, surface charges of kaolinite may be summarized as follow:

- Edge surfaces are charged because of protonation or deprotonation of broken edges, with highly pH-dependent positive or negative charges.
- Faces are negatively charged because of isomorphic substitution with negative charges that are slightly pH dependent.
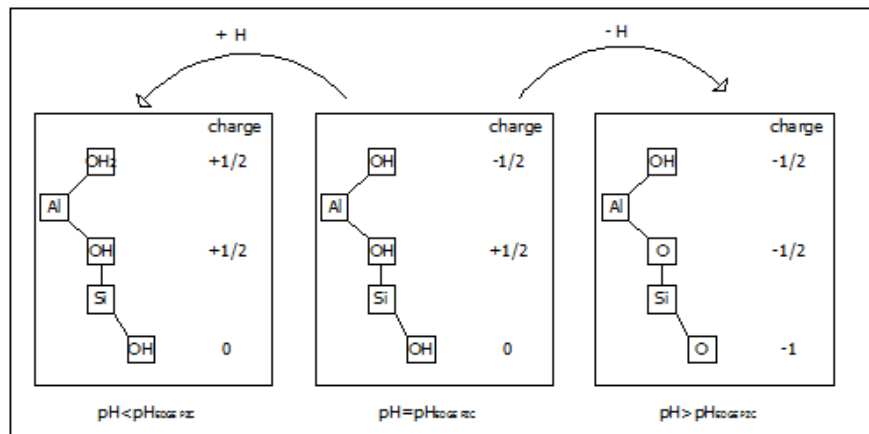
Figure 4: Kaolin edge surface charges at different pH (modified from Wang & Siu 2006)

1.3.3 Dissolution of kaolin

The acid-basic reactions (protonation/deprotonation) at the kaolinite-water interface are responsible for kaolin dissolution. As discussed above, protonation and deprotonation involve three different surface sites:

- Protonation and deprotonation of external hydroxyls in the aluminium basal plane (Al-OH-Al)
- Protonation and deprotonation of aluminol groups at the edges (Al-OH) or internal hydroxyl groups (Al-OH-Si)
- Deprotonation of silanol groups at the edges (Si-OH)

The protonation and deprotonation reactions at these sites occur at different pH ranges and thus each site is responsible for the surface charge under a given pH condition (Huertas et al., 1998).

For acidic conditions the kaolinite surface undergoes two successive protonation that will cause dissolution. The first protonation will take place at the external hydroxyls of the octahedral sheet (pH lower than 3) and the second one either at the inner hydroxyl group or at the edge of aluminol groups. On the other hand, two successive deprotonation may take place for alkaline conditions at about pH=5.5 and pH=9, the former at the silanol groups site and the latter at aluminol sites (Huertas et al., 1998) respectively. For acidic conditions, Ganor et al. (1995) proposed a possible atomic model for

dissolution. The model shows how the progressive weakening and breakdown of the Al-O-Si bonds (Figure 5) leads to successive breakdown of Al-OH-Al and Si-O-Si bonds and a fast releasing of Al^{3+} and H_4SiO_4 into solution (Figure 5).

On the other hand, a clear mechanism for dissolution under alkaline conditions has not been discussed in the literature.
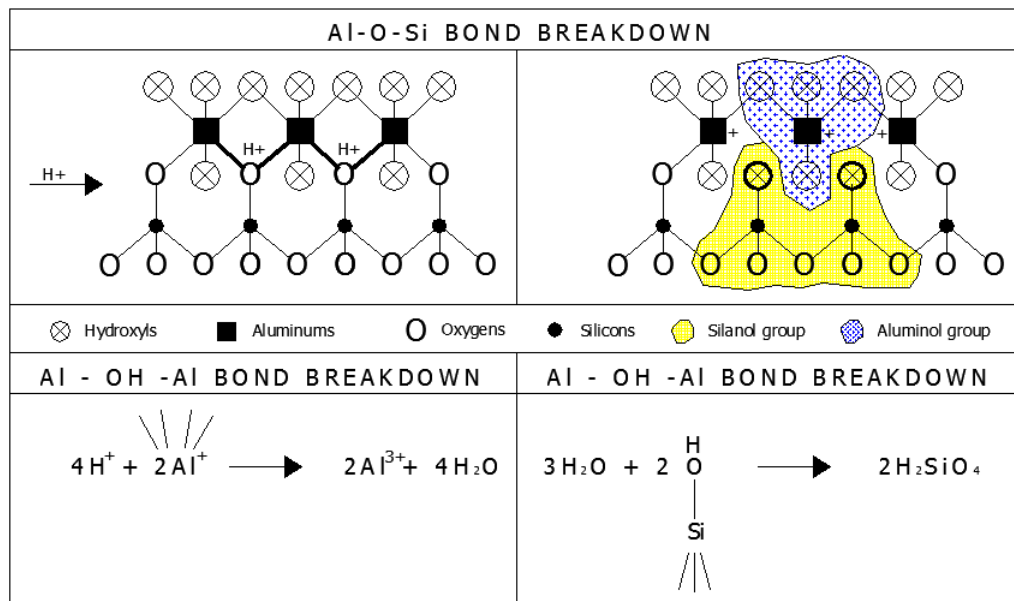
Figure 5: Mechanism of dissolution reaction at acidic conditions in kaolin clay (modified from Ganor et al. 1995)

1.3.4 Elementary unit and relevant interparticle forces for kaolin

Interparticle forces for clay particles have been discussed in the literature when formulating models at nano- and micro-scale to simulate, qualitatively or quantitatively, the response of clays observed at macroscopic level. Most of the existing electro-chemical models presented in the literature refer to swelling clays. As discussed in the previous section, a single particle of clay is comprised of several (hundreds) of unit layers stacked in the c-direction. In swelling clays, the distance between the unit layers is variable and controlled by the pore-fluid chemistry. As a result, electro-chemical models have generally focused on the interaction between the unit layers of swelling clays rather than between particles. Such inter-layer interactions are, as a matter of fact, believed to dominate the macroscopic behaviour, more than the particle-

to-particle interaction itself. In this context, the term "particle" has often been misused because it has been referred to a single unit layer rather than the particle itself.

On the other hand, the unit layer distance in non-active clay is constant and is not affected by changes in the pore-fluid chemistry (no interlayer swelling). Since the dimension of the particle does not vary, the particle itself should be considered as the elementary unit when formulating conceptual or quantitative microscopic models.

Therefore, one may defines swelling and non-swelling (or active and non-active) clays in regards of nature of the single particle. Clay particles are made by unit layers stacked in the c directions. The number of such unit layer and their relative distance controls the particle dimensions. For a given number of layers constituting one clay particle, the interlayer space might be different. When such space is small enough to prevent water (or any other kind of fluid) –intercalation, the dimension of the particle is fixed, and therefore such clay is a non-swelling clay. On the other hand, when the interlayer spacing is not constant but it is fluid-dependent, such particles can swell and compress in thickness, therefore, it is defined as a swelling clay. In non-swelling clay, unit layer interaction is not usually studied, because it is not relevant since particle dimensions are fixed. On contrary, interlayer interaction within one single particle is of great interest for swelling clays. Therefore, in the latter problem, the forces that have to be considered are forces that work on a smaller range of distances. Indeed, interactions as hydration forces, solvation forces, hydrogen bonds and Bjorn repulsion are relevant only at a few nanometres distance. Such forces are relevant in active clays but they can be assumed to be negligible for non-active clays. Indeed, since in active clays the elementary unit is the unit layer, the distances between the elementary units are of the order of few nanometres. On the other hand, in non-active clays, where the elementary unit is the particle, the distances between particles are never less then hundreds of nanometres.

1.3.5 **Van der Waals**

Whether or not a single molecule is charged, it usually has a non-equally distributed charge. Indeed, one side can be more negatively charged than the other one giving rise to a dipole.

Van der Waals interaction is defined as the sum of three different phenomena (Keesom interaction, Debye interaction and London interaction) associated with dipole-dipole interaction:

i)   Keesom interaction is associated with the ability of two freely rotating dipoles to orient with their opposite charges facing each other. This randomly orientated dipole-dipole interaction is attractive (Butt et al., 2003).

ii) Debye interaction is defined as the attractive interaction caused by the orientation of an induced dipole in a polarisable molecule when it is next to a molecule with a static dipole moment (Butt et al., 2003).

iii) London force (or dispersion force) is associated with the attraction between nonpolar molecules. An atom has a positively charged nucleus around which electrons circulate at high frequency. At any instant, the atom is therefore polar with the direction of the polarity changing at high frequency. When two such oscillators approach each other, the electrical fields generated by the temporary dipoles interact. Attractive orientations have higher probabilities than repulsive ones. On average, this leads to attractive forces (Butt et al., 2003).

Although all three phenomena described above are characterised by the same distance dependency, London dispersion forces are the dominant ones in clays (Butt et al., 2003). Assuming that the intermolecular distance d is small enough to consider the propagation of the electric field as instantaneous, the potential energy (Helmholtz free energy) between two molecules decreases with $1/d^6$. The assumption of instantaneous propagation is actually acceptable only at intermolecular distances less than 100 nm. For greater distance the

Helmholtz energy between two molecules decreases more rapidly. This effect is known as retardation (Casimir & Polder, 1948).

In the case of macroscopic solids, Van der Waals interaction may be calculated with two different approaches, microscopic and macroscopic.

The microscopic approach exploits the Hamaker theory (Hamaker, 1937). This approach moves from the interaction between two molecules to the interaction between two macroscopic solids. By assuming that the interaction is pairwise additive, the total interaction energy is calculated by summing up forces between all of the pairs of molecules in the two distinct solids. The interaction force has been shown to be linearly proportional to the Hamaker's constant and inversely proportional to the square value of the surface distance. In the microscopic approach the influence of neighbouring molecules is ignored (Milonni & Lerner, 1992).

This problem is by-passed in the macroscopic approach developed by Lifshitz (1956). The discrete structure of the solids is neglected and the solids are considered as a continuum medium. Applying the macroscopic approach, the distance dependency of the force between two infinite parallel solids has been shown to be the same as the one derived from the microscopic approach, with just the Hamaker's constant being calculated differently (Butt et al., 2003). According to Lifshitz (1956), the Hamaker's constant depends on the contribution of many frequencies (solid and liquid media). Thus, if the material of the two parallel bodies is similar, it is possible to show that the Hamaker's constant is positive, and thus the Van der Waals interaction is always attractive (Butt et al., 2003). In order to calculate the Hamaker's constant, the dielectric properties of the solid materials and the medium need to be known.

Figure 6 shows the effect of the dielectric constant of pore fluid on Hamaker's constant. The Hamaker's constant shows a minimum for a dielectric constant of about 20 and increases monotonically at higher values of the dielectric constant.
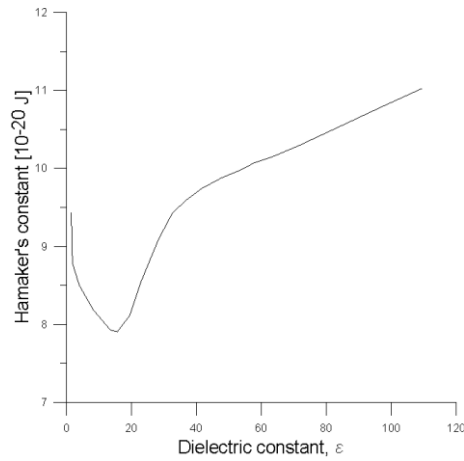
Figure 6: Hamakers's constant trend in clays at different dielectric constants (Chen et al., 2000)

Regarding the values of Hamaker's constant, interesting studies have been performed by Moore & Mitchell (1974). By studying the undrained strength of kaolinite with different dielectric constants they have inferred that the Hamaker's constant values are consistent with Lifshitz theory.

According to Mitchell & Soga (2005), a simplified equation to evaluate the Van der Waals interaction is the Casimir-Polder equation (equation 1), which has been derived by following the microscopic approach. The Casimir-Polder equation (equation 1) for the attraction energy between parallel plates, has been developed by considering the Casimir effect (attraction between two parallel uncharged metallic shells without any external electromagnetic field) as a macroscopic manifestation of the Van der Waals forces between two parallel plates (Casimir & Polder, 1948, Milonni & Shih, 1992):

$$V_A = -\frac{A_H}{48\pi}\left[\frac{1}{d^2} + \frac{1}{(d+\delta)^2} - \frac{2}{(d+\delta/2)^2}\right]$$
[1]

where d is the half distance between plates measured from the plane of the surface layer atoms, δ is the thickness of the plate measured between the same planes, and A_H is the Hamacker constant, which is of the order of 10^{-20} J for soil colloids. The Casimir-Polder equation (equation 1) "is not exact, but it is a good approximation for particle separations less than 100 nm, which

would seem to cover the practical range of interest for geotechnical problems" (Mitchell & Soga, 2005).

1.3.6 Electric field

As described in the mineralogy of kaolin, each particle surface is electrically charged. Such distribution of charges generates an electric field that interacts with the charges on the other particles with forces that are Coulombian in nature.

In order to understand and compute the evolution of the electro-magnetic field generated by the surface charges, two Maxwell's equations have to be considered.

i) The Gauss Law for electricity that relates a distribution of charges to the resulting electric field (equation 2): "*The net electric flux through any closed surface is equal to 1/e times the net electric charge enclosed within that closed surface*"

ii) Faraday's Law of induction that models the electric field generated by a time-variable magnetic field (equation 3): "*when the magnetic flux linking a circuit changes, an electromotive force is induced in the circuit proportional to the rate of change of the flux linkage*".

$$\text{GAUSS LAW: } \nabla \cdot E = \frac{\rho}{\varepsilon} \tag{2}$$

$$\text{FARADAY'S LAW: } \nabla \times E = -\frac{\partial B}{\partial t} = 0 \rightarrow E = -\nabla \varphi \tag{3}$$

In equations 2 and 3, E is the electric field, $\nabla \cdot E$ is the divergence of the electric field, ε is the dielectric constant of the medium, ρ is the total electric charge density (in the medium), $\nabla \times E$ is the curl operator of the electric field, B is the magnetic field, and t is the time. Under the assumption of electrostatic conditions and therefore in absence of a magnetic field, $\frac{\partial B}{\partial t}$ is nil, therefore $E = -\nabla \varphi$ (equation 3) where φ is the electric potential.

By combining equations 2 and 3, the Poisson's equation is obtained (equation 4)

$$\text{POISSON'S EQUATION: } \nabla \cdot E = \nabla(-\nabla\Phi) = -\nabla^2\varphi = \frac{\rho}{\varepsilon} \qquad [4]$$

Poisson's equation gives the spatial evolution of the electric potential, φ, in a dielectric medium, ε, having a distribution of electric charges with density ρ. There are two cases that are worth considering:

i)   Zero electric charge distribution in the media ($\rho = 0$)

ii)   Electric charge distribution that follows a Boltzmann's distribution

If the charge density ρ is zero Poisson's equation becomes Laplace's equation (equation 5).

$$\text{LAPLACE'S EQUATION: } \nabla^2\varphi = 0 \qquad [5]$$

Analytical solutions of Laplace's equation exist for two and three dimensional problems. Such solutions are generally computed by using Green's functions.

For the case of the electric fields of simple geometry, solutions of the Laplace's equation can be derived directly from the definition of the electric potential (equation 6) involving little computational efforts:

$$\varphi(z) = \frac{1}{4\pi\varepsilon} \int \frac{\sigma(x)}{|x - z|} dx \qquad [6]$$

where σ is the charge distribution on the surface, z is the distance from the surface and x is the spatial coordinate on the surface.

1.3.7 Double layer

In order to solve Poisson's equation (equation 4) for the case of a medium having an electric charge distribution ρ (electrolyte solution), it is necessary to assess how the free ions distribute in the proximity of the electrical charged surface.

The double layer theory describes the distribution of ions around particles in suspension (Gouy, 1910, Chapman, 1913, Derjaguin & Landau, 1941,

Verwey et al., 1948, Van Olphen, 1977, Mitchell & Soga, 2005, Stern, 1924). According to this theory, ions around particles in suspension are distributed in two charged layers in order to neutralize the surface charge of the particles (Figure 7).

Assuming that the surface particles are negatively charged, the negative surface charges attract positive ions in a first layer , known as Stern layer (Stern, 1924), causing a high concentration of ions firmly attached to the surface.

In the second layer, known as the diffuse layer, the positive ions are both attracted by the negative charges of the surface and repelled by the positive charges of the Stern layer. The sum of both interaction forces acting on the positive ions is still attractive but it decreases with increasing distance from the surface. Hence the concentration of positive ions decreases moving away from the surface. The ion concentration keeps decreasing until it reaches equilibrium with the concentration of the ions in the free solution, where the repulsion and the attraction of positive ions are balanced.

In the diffuse layer, there are also negative ions that are attracted by the positive charge of the Stern layer and repelled by the negative charges of the surface. Hence the density of negative ions will gradually increase moving away from the Stern layer until it reaches equilibrium with the concentration of negative ions in the suspension. Therefore, the diffuse layer is positively charged but the concentration of positive ions is smaller than that of the Stern layer.
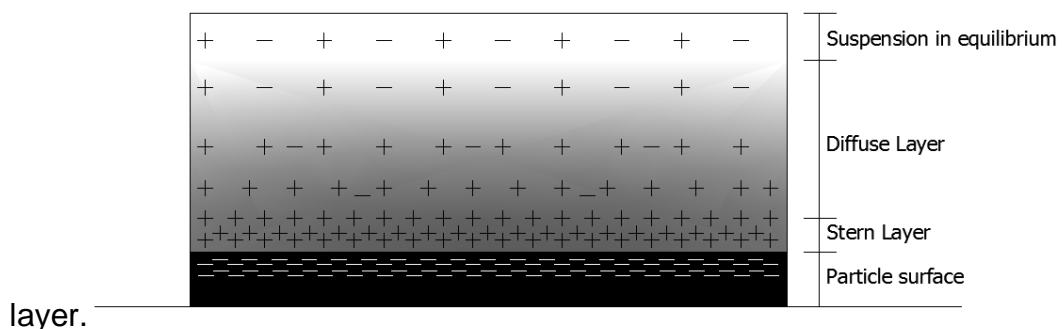
Figure 7: Double layer distribution

According to Mitchell & Soga (2005), a reasonable mathematical description of the diffuse double layer has been developed for the assumption of planar surfaces. The following idealizing assumptions have been made:

- Ions in the double layer are point charges, and there is no mutual interaction between them;

- Charges on the particle surface are uniformly distributed;

- The particle surface is a plate that is very large relative to the thickness of the double layer (one-dimensional condition);

- The permittivity of the medium adjacent to the particle surface is independent of the distance from the particle surface

The electric potential, φ, is plotted in Figure 8 as a function of the distance from the surface according to Gouy-Chapman theory. The potential has a maximum value at the surface and it decreases approximately exponentially with the distance from the surface charge. As a first approximation, no difference is made between the potential at the surface (φ_0), the potential at the limit of the Stern layer, and the ζ potential. These three potential values are not the same from a theoretical point of view since they are computed at different distance from the surface. Nevertheless, ζ potential is often the only potential that in colloidal science is possible to measure. Such an assumption implies to neglect the Stern layer, or to consider it as part of the particle surface (generally so-called "solid water").
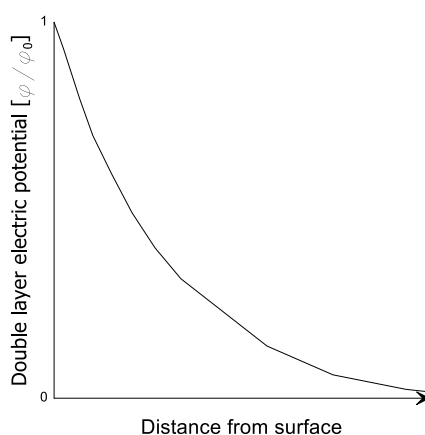
Figure 8: Variation of electrical potential with distance from a charged surface (Mitchell & Soga, 2005)

The concentration of ions (ions/m^3) in a force field at equilibrium with electric potential Φ is assumed to have a Boltzmann distribution (equation 7):

$$n_i = n_{i0} \exp\left(\frac{-v_i e\Phi}{kT}\right) \quad\quad [7]$$

Where n_i is the concentration of the ions with a valence v_i. n_{i0} is the concentration at the equilibrium in the solution, k is the Boltzmann constant (1.38x10^{-23} J K^{-1}), T is the temperature (K) and e is the electronic charge (1.602x10^{-19} C). For the sake of simplicity, Poisson's equation is considered in the one-dimensional case (equation 8), where φ [V] is the electric potential, ρ (C/m^3) charge distribution in the medium, z [m] the distance from the charged surface and ε_m (C^2 J^{-1} m^{-1}) [$\varepsilon_m = \varepsilon_0 \varepsilon$] the static permittivity of the medium (Mitchell & Soga, 2005).

$$\frac{d^2\Phi}{dz} = -\frac{\rho}{\varepsilon_m} \quad\quad [8]$$

For the case of single cation and anion species of equal valence, the Poisson-Boltzmann equation is obtained (equation 9):

$$\frac{d^2\Phi}{dz} = -\frac{2n_{i0}v_i e}{\varepsilon_m} \cdot \sinh\frac{ve\Phi}{kT} \qu\quad [9]$$

A simple solution for a single double layer shows that the centre of gravity of the diffuse charge in the double layer is at distance *1/K*. The centre of gravity *1/K* is defined in equation 10 where ε is the relative permittivity of the medium and ε_0 the vacuum permittivity:

$$\frac{1}{K} = \left(\frac{\varepsilon_0 \varepsilon kT}{2n_{0i}e^2 v_i^2}\right)^{1/2} \quad\quad [10]$$

According to equation 10, the 'size' of the double layer (*1/K*) is inversely proportional to the ion valence, v_i, and the ion concentration, n_{i0}, and directly proportional to the root square of the dielectric constant of the medium, ε.

Equations 9 and 10 are associated with case of single charged surface in a free-electrolyte solution (Laplace's equation). However, a single double layer is not representative of the actual ion distribution. Double layers of adjacent particles will tend to overlap and thus a different charge distribution, ρ, has to be expected.

Figure 9 shows the charge distribution for the case of interacting double layers between two parallel flat plates (both negatively charged) at distance *2d (d=1/K)*. Numerical and mathematical relationships for the solution of the differential equation for the overlapping electric double layers are reported by many authors including Van Olphen (1977) and Mitchell & Soga (2005).

According to Van Olphen (1977), when two particles approach each other in a suspension owing to their Brownian motion, their double layers begin to interact and the ion distribution in the double layers varies. If the particle charges are the same, work must be done to bring the particles to a closer distance and overcome repulsion (double layer repulsion). On the other hand, if the particle charges have opposite sign, there will be attraction between the two double layers (Colombian attraction).
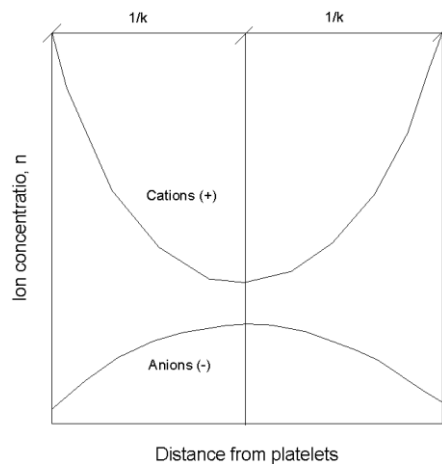
Figure 9. Charge distribution for interacting double layers from parallel flat plates (Mitchell & Soga, 2005)

According to the Gouy-Chapman theory (Gouy, 1910, D. L. Chapman, 1913) a simplified solution for the electrical potential, φ, between two plate surfaces can be expressed as follows:

$$\varphi(z) \sim 2 \left(\frac{4kT\gamma_0}{ve} \right) \exp(-kz)$$ [11]

where *1/K* is defined in equation 10 and γ_0 is defined as follows:

$$\gamma_0 = \frac{\exp\left(\frac{ve\varphi_0}{2kT}\right) - 1}{\exp\left(\frac{ve\varphi_0}{2kT}\right) + 1}$$ [12]

1.3.8 DLVO theory and net potential curve

Derjaguin & Landau (1941) and Verwey et al. (1948) extended the Gouy-Champman theory to explain the stability of aqueous dispersions. This theory is often called DLVO theory. The interaction between particles in suspension is explained by the balance between double layer repulsion (attention must be paid here because double layer interaction might be also attractive) and Van der Waals attraction.

As defined by Van Olphen (1977) the "net potential curve of particle interaction is constructed simply by adding the attractive and the repulsive potential at each particle distance, considering the attractive potential negative and the repulsive potential positive".

Figure 10 shows an example of a net potential curve. At very small distances (few nanometres) DLVO theory predicts that the Van der Waals attraction always dominates (energy trap). At higher distances, the net interaction curve generally shows a maximum in the repulsive section, called energy barrier. The height of the energy barrier indicates the kinetic energy that two approaching particles must have to aggregate. Hence the energy barrier determines the stability of the suspension. In fact, once the energy barrier is cleared the two particles will enter in the attraction field where the Van der Waals forces are dominant.

As explained before, the energy of repulsion is sensitive to changes in electrolyte concentration, cation valence, and dielectric constant. On the other hand, the Van der Waals attractive energy is sensitive only to changes in the dielectric constant and temperature (Mitchell & Soga, 2005) and it is always attractive if the particle materials are similar (Butt et al., 2003). In conclusion, the DLVO theory explains how to control the stability of the suspension by controlling the double layer extension and the amount of associated energy.
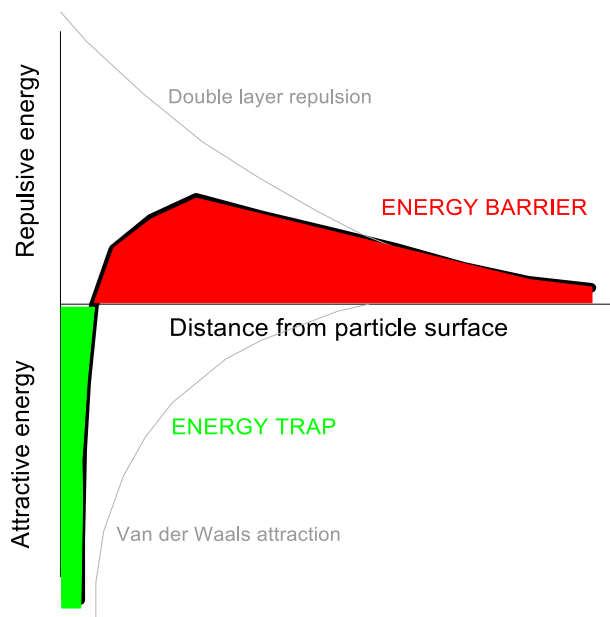
Figure 10: Net potential curve

1.3.9 **Non DLVO theories**

For the sake of completeness, a brief résumé of non-DLVO theories is discussed here. The main theory in colloid science that does not consider the combination of Van der Waals and double layer forces is the hydration theory. In this theory, "the repulsion between particles is attributed to the orientation of water dipoles in the electric field around the charged particles. In such a solvation shell, the degree of orientation of the dipoles would gradually decrease with increasing distance from the charged surface. The diffuse hydration shells begin to interfere when the particles approach each other, the mutual repulsion of the oppositely oriented water dipoles around the colliding particles would account for particle repulsion" (Van Olphen, 1977).

In colloidal suspensions with hydrophilic surfaces that are brought into contact, repulsive forces up to about 1nm range have been measured in aqueous electrolyte on a variety of surfaces. "Because of the correlation with the low (or negative) energy of wetting of these solids with water, the repulsive force has been attributed to the energy required to remove the water of hydration from the surface, or the surface adsorbed species, presumably because of strong charge-dipole, dipole-dipole, or H-bonding interactions" (Butt et al., 2003).

"Clays are *lyophobic* (liquid hating) or *hydrophobic* (water hating) colloids rather than *lyophilic* or *hydrophilic* colloids, even though water wets clays and is adsorbed on particle surfaces. Historically, this designation resulted from the need to distinguish colloids such as clay from colloids already termed hydrophilic, such as gums, which exhibit such an affinity for water that they spontaneously form a colloidal solution" (Van Olphen, 1977).

According to Van Olphen (1977) hydrophobic colloids are liquid dispersions of small, solid particles that are:

- Two-phase systems with a large interfacial surface area.
- Behaviourally dominated by surface forces.
- Able to flocculate in the presence of small amounts of salt.

Clay–water–electrolyte systems satisfy all of these criteria.(Mitchell & Soga, 2005). Between hydrophobic suspensions a totally different interaction is observed. The origin of the hydrophobic force is, however, still under debate (Butt et al., 2003). Many hypotheses have been proposed such as the change in water structure when two surfaces approach each other (Mitchell & Soga, 2005) or the presence of gas bubbles residing on the hydrophobic surfaces that, once they come into contact, fuse and form a meniscus (Steitz et al., 2003).

The argument against the hydration theory to explain clay suspension stability is that the orientation effect can be significant only up to a few

molecules of water from the surface if compared with Van der Waals forces (Van Olphen, 1977).

1.3.10 Particle arrangement in suspensions

By studying the microstructure of natural soils, many different particle arrangements have been observed. Following the pioneering work of Lambe (1958), over the years, there has been a proliferation of terms for the description of the different existing fabrics, such as honeycomb structure, stair-stepped cardhouse, clusters, turbostatic systems and aggregation. Lambe (1958), Sides (1971), Collins and McGown (1974) and Mitchell & Soga (2005) reviewed and clarified many of the terms used in the literature through the years. Soil microstructure was defined by Mitchell & Soga (1976) as the combination of the arrangement of particles and interparticle bonding caused by different environmental conditions on the depositional process or on the post-depositional process. The basis of many of these earlier concepts (among the many Lambe (1958) was that particle arrangements could be associated with certain depositional environments, although other factors have been later recognised to control particle arrangement such as size, shape, mineralogy, and cations involved. Lambe (1958) determined the most widely used modes for particle configurations which are still in use nowadays (Figure 11). On the other hand, Van Olphen (1977) is considered the starting point of many researches concerning the particle interaction and the rheology of clay suspensions.

Despite the fact that more than 40 years have passed since Van Olphen's publication, little has changed in the knowledge of clay suspensions, at least from a qualitative point of view. The fundamental principles of particle associations in clay suspensions have been schematized by Van Olphen (1977). Interaction between particles occurs in three different modes and combinations therefrom (Schofield & Samson, 1954, Van Olphen, 1977):

- Face-to-Face (FF): face and edge have the charge of the same sign, thus the particle interaction is governed by the balance between double layer repulsion and Van der Waals attraction (net energy).

- Edge-to-Face (EF): face and edge have charges of opposite sign. The interaction is due to the attraction between the opposite double layers at the face and the edge respectively (Coulomb attraction).
- Edge-to-Edge (EE): face and edge have the charge of the same sign, thus the particle interaction is governed by the balance between double layer repulsion and Van der Waals attraction (net energy).

The three types of association will not necessarily occur simultaneously or to the same extent (Van Olphen, 1977). By following the pioneering work of Van Olphen (1977) it is possible to define the following configurations of particle associations (Figure 11):

- Dispersed (and deflocculated): particles do not have any kind of association and show a heterogeneous face to face distribution.
- Aggregated: particles are associated in face-to-face mode forming aggregates.
- Flocculated: particles are associated in edge-to-face or edge-to-edge mode forming floccules.

Moving from these definitions, it is possible to define a number of configurations resulting from one or more of these associations (Figure 11). Because of the wide use of these terms in different scientific fields, it is worth recalling the original statements by Van Olphen (1977):

"Although the three types of association are really three modes of flocculation in the colloid chemical sense, only the EE and the EF types of association lead to agglomerates which would deserve the name of flocs. The thicker particles which results from FF association cannot be properly called "flocs"; hence, the suggestion has been made that a different term to be coined for this type of association. The terms "oriented aggregation" or "parallel aggregation" or, briefly, "aggregation" have been proposed (…). At the same time, the proposal has been made that only the dissociation of the edge-to-face and edge-to-edge linked particles be described as "deflocculation", and that the splitting of face-to-face associate "aggregates" into thinner flakes be described as dispersion of the clay (…). The terms "aggregates" should not be

confused with the same term which is commonly used in soil science to describe the macroscopic crumb in a soil."
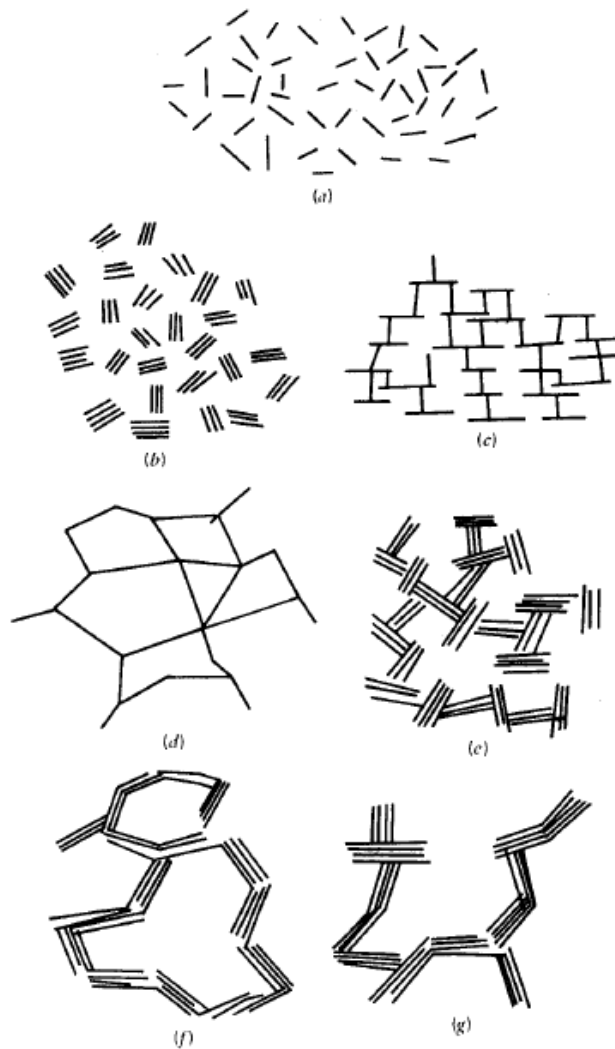
Figure 11. Modes of particle associations in clay suspensions and terminology. a) Dispersed and deflocculated, b) aggregated but deflocculated (face to face association), c) edge-to face flocculated but dispersed, d) edge-to edge flocculated but dispersed, e) edge-to-face flocculated and aggregated, f) edge-to-edge flocculated and aggregated and g) edge-to-face and edge-to-edge flocculated and aggregated. From Mitchell & Soga (2005) modified from Van Olphen (1977)

1.3.11 Rheology of clay suspensions

The study of the rheological behaviour of clay suspension may help understand how particle association occurs. Van Olphen (1977) reported that

the viscosity of dilute clay suspensions increases with the degree of particles flocculation (EF or EE association) and decreases when the FF association increases. Hence Bingham yield stress of colloidal suspension is a measure of the number and the strength of the cross linkages in a card house structure.

Van Olphen (1977) proposed to analyse the particle-association process occurring in a clay suspension at various concentrations of electrolyte from the change in the Bingham yield stress. In an electrolyte-free suspension, it is reasonable to assume that double layers in proximity of both the faces and the edges are well developed. If the face and the edge have the same charge, the resulting repulsion will therefore be greater than Van der Waals attraction. In contrast, if the double layers of the faces and edges have opposite signs, they will attract each other.

Starting from a suspension of kaolin that generated edge to face association (thus high viscosity), the concentration of the electrolyte was increased by van Olphen (1977) and the viscosity of the system was studied. In the presence of a small concentration of electrolyte both double layers are compressed and so are their effective charges. Because of the reduction of the double layers both the face-to-face (or edge-to-edge) repulsion and the edge-to-face attraction due to the signs of the double layers are reduced. "Apparently, as it is possible to see in the experimental data, the effect is that the former attraction between edge-face will be reduced, but the repulsion between face-face and edge-edge is still greater than the Van der Waals attraction" (Van Olphen, 1977). The effect of increasing the salt concentration, eventually, is the disengagement of a part of the card-house structure (less cross links) and consequently a reduction of the Bingham yield stress.

Wang & Siu (2006) carried out a study on the effects of electrolyte concentration on kaolin suspensions at different pH. They showed that, by increasing the electrolyte concentration at pH values less than the pH at the isoelectric point of the edge surface (IEP_{edge}), the Coulombian attraction between double layers with opposite charge is reduced. This, in turn, weakens the formation of edge-to-face flocculated structure and decreases the Bingham

yield stress. Moreover, the face-to-face aggregation is promoted due to the reduction of double layer repulsion between faces.

On the other hand, by increasing the electrolyte concentration at pH greater than IEP_{edge}, the yield stress will increase. This is because the reduction in the double-layer repulsion (negative double layers at all sites) promotes van der Waals attraction. Hence, an aggregated (and flocculated) structure is formed under such conditions.

1.3.12 Sedimentation

The factors that control the sedimentation time and the final volume of the sediment in clay suspension are the electrolyte concentration, the pH, and the dielectric constant of the pore-fluid. Faster sedimentation times are usually related to flocculation of clay particles, and slow sedimentation times are usually associated with a more disperse configuration. In the same way, higher final sedimentation volumes are the consequence of an open edge-to-face network, and lower final volumes of a dispersed or oriented particle configuration.

According to the DLVO theory, an increase in the electrolyte concentration will decrease the electric potential for a given distance between particles. Studies on kaolin suspensions have shown that, by increasing the electrolyte concentration, the sedimentation time increases and the final volume of the sediment decreases (Chen & Anandarajah, 1998, Stawinski et al., 1990). At low electrolyte concentration kaolin sediment presents a 3D network of particles, due to flocs having edge-to-face configuration. The size of the flocs decreases with the increase of electrolyte concentration.

Chen et al. (2000) have studied the change in equilibrium time of a kaolin suspension with pore fluids of different dielectric constant. It has been found that the equilibrium time increases for dielectric constant values up to about 25, it then decreases up to a dielectric constant of 60-80 and it increases again at higher values of dielectric constant. They suggested that double layer cannot develop in nonpolar fluids and that Van der Waals forces are relatively

large. On the other hand, for fluids with dielectric constant about 25 the Van der Waals forces are at their minimum and the double layer is relatively large. Finally, in systems with high dielectric constant values, the double layers are well developed and increase with dielectric constant (Figure 12).
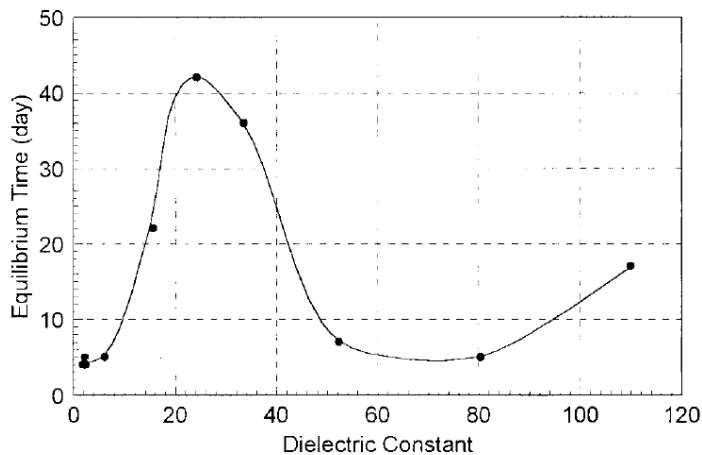
Figure 12. Equilibrium time in sedimentation tests of kaolin mixed with solutions at different dielectric constant (Chen et al., 2000)

When kaolin is suspended in a solution at various pH values, it is observed that the sedimentation time increases and the volume of the final sediment decreases when the pH becomes higher than the pH at the PZC (Wahid et al., 2011a, Wang & Siu, 2006). The final sediment void ratio obtained for acidic solutions appears to be about two times higher than that obtained for alkaline solutions (Figure 13). This suggests that distinct fabrics are formed below and above this transition value of pH (PZC): the fabric changes from a card-house network (edge-to-face interaction) to a closely packed structure (face-to-face interaction).

Studies on illite and montmorillonite clays reported similar qualitative trends. When illite and montmorillonite are flocculated with high salt concentration they show a 3D network similar to kaolin in distilled water or acidic suspensions (O'Brien, 1971, Lambe, 1960, Sloane & Kell, 1966, Sides & Barden, 1971, Keren & Sparks, 1995). In contrast, illite and montmorillonite in distilled water

show an abundance of face-to-face orientated parallel particles (dispersed configuration), similarly to kaolin clay in alkaline suspensions (Wahid et al., 2011a, Wang & Siu, 2006, Keren & Sparks, 1995).
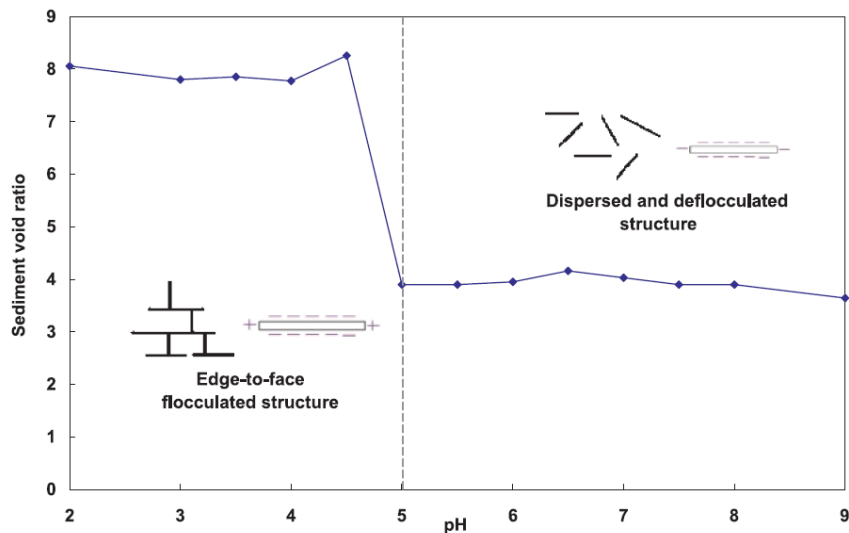
Figure 13. Final sediment void ratio of sedimentation tests on kaolin mixed with solutions with different pH (Wang & Siu, 2006)

1.3.13 Experimental investigation on the effects of the interparticle forces on the mechanical response of non-active clays

Reconstituted clays show a different response (both in compression and shear) depending on the chemistry of the pore fluid. Electrolyte concentration, dielectric constant and pH of the pore fluid have been found to be factors controlling the change in the mechanical behaviour. When discussing the effects of pore-fluid chemistry on soil macro mechanical behaviour two different aspects have to be considered. Effects may be caused by either the initial microstructure in turn induced by the different pore-fluid chemistry, or the different nature of interparticle forces.

Compression behaviour of kaolin samples reconstituted from slurry showed very little sensitivity to electrolyte concentration (Chen et al., 2000, Wahid et al., 2011a). This is in contrast with the response observed from reconstituted samples of bentonite (swelling clay) where the higher the electrolyte

concentration, the stiffer is the sample upon virgin compression (Di Maio, 1996). The same trend was observed upon unloading, where swelling was more pronounced for bentonite samples having lower electrolyte concentrations (Di Maio, 1996).

Wahid et al. (2011b) changed the electrolyte concentration of the pore-fluid during the loading of reconstituted kaolin. No differences in compressibility were recorded before and after the change in the electrolyte concentration. The authors observed that any change in concentration (either an increase or a decrease) always caused a decrease in volume. They explained these phenomena as a change in the microstructure. However, since i) the change in volume upon the change in electrolyte concentration was not followed by a change in compressibility, ii) the fluid took several months in order to be replaced, and iii) the amount of settlement was small when compared with the settlements due to the external loading, recorded settlements are likely to be associated with secondary deformations.

On the other hand, a similar experiment on bentonite (Di Maio 1996) showed that an increase in electrolyte concentration on reconstituted samples caused a "chemical consolidation" and a decrease in electrolyte concentration caused a "chemical swelling". Unlike kaolin, the sample showed a different compressibility upon the subsequent loading steps after the pore-fluid had been changed (Di Maio, 1996). In addition, Di Maio (1996) showed that the residual shear strength of bentonite increased when the salt concentration increased. No data seem to be available for the shear strength of kaolin prepared at different electrolyte concentrations.

Chen et al. (2000) and Olgun & Yildiz (2012) have studied the compressibility of kaolin specimens prepared by sedimentation with the pore fluid having various dielectric constants. The different samples showed similar compressibility once the applied vertical stress becomes higher than about 50 kPa. On the other hand, Sridharan & Venkatappa Rao (1973) performed compressibility tests on samples prepared by mixing dry clay with fluids having different dielectric constant and compacted to the same initial void ratio. This

study showed that compressibility of saturated compacted kaolin increased when the dielectric constant decreased. The same experiment was carried out on montmorillonite samples and showed an opposite behaviour upon loading (compressibility decreased when the dielectric constant decreased). The unloading paths for both kaolin and montmorillonite showed the same behaviour. The higher the dielectric constant, the higher is the swelling of the samples. Sridharan & Venkatappa Rao (1973) also replaced fluid in consolidated kaolin and montmorillonite during the loading process. Tests on kaolin showed that volumetric collapse was recorded when the dielectric constant was increased (from carbon tetrachloride to water) along a virgin compression. In addition, compressibility changed when the fluid was replaced with another one. On the other side, no significant change in volume was recorded when the dielectric constant was decreased (from water to carbon tetrachloride) but the compressibility upon loading changed again. The same test on montmorillonite showed opposite behaviours.

Such behaviour has been explained in terms of effective stress, by defining it as a combination of inter-granular interaction at the contact and electrical repulsion. However, from an electrochemical point of view, what causes the change in behaviour between active and non-active clays, has never been provided. In particular, for the case of non-active clays, the most common conclusion is that such clays do not depend on the chemical interaction. Consequently, a real justification for the change in void ratio when the dielectric constant changes in non-active clays is not considered by any previous theory.

Sridharan & Venkatappa Rao (1973) and Olgun & Yildiz (2012) obtained the same trend when they tested the shear strength of both kaolin and montmorillonite prepared with pore-fluid having different dielectric constants. The shear strength increased when the dielectric constant was decreased.

Sachan & Penumadu (2007) and Wahid et al. (2011b) also proved that the mechanical behaviour of kaolin is strongly pore-fluid pH dependent. Both authors reported that kaolin in basic solutions has a much stiffer behaviour and a closer packing that the one in acidic solutions.

In conclusion, differences have been inferred experimentally in the response of non-active (kaolin) and active clays (bentonite or montmorillonite).

For non-active clays:

i)   no differences in compressibility and shear strength found when the electrolyte concentration was changed

ii)   differences in compressibility and shear strength found when the dielectric constant was changed

For active clays differences in compressibility and shear strength have been found when both the electrolyte concentration and the dielectric constant were changed.

The generally accepted conclusion is the one reported by Sridharan & Venkatappa Rao (1973) who state that non-active clays are controlled by mechanical interactions (despite of the experimental effects of dielectric constant on the void ratio and compressibility), whilst active clays by electro-chemical interactions.

1.4 Microstructure of non-active clays under partially saturated conditions

1.4.1 Traditional conceptual model for compacted clays

Early works on particle orientation in compacted clays (e.g. Lambe (1958), Seed & Chan (1959), Mitchell (1956)) concluded that clays compacted on the dry side of optimum owe their density to the development of a random or cardhouse fabric (flocculated) and that those compacted on the wet side of optimum produce a more oriented arrangement of particles (dispersed). Similar conclusions have been drawn by later works (Sloane & Kell, 1966, Yoshinaka & Kazama, 1973) on compacted kaolin clay. However, they concluded that very little particle fabric was observed (either face-to-face or edge-to-face) and that a flocculated or dispersed structure was concerning more packets or books of particles. In recent years, Cetin et al. (2007) carried out a comprehensive investigation on particle orientation of compacted clayey silt. They showed that particle orientation is nearly random at the very dry side of the compaction curve (edge-to-face and edge-to-edge particle contacts). Moving towards the optimum moisture content, the orientation decreases down to an average angle with the horizontal plane (normal to the compaction force) between 0° and 10°. When the moisture content is above the optimum the average angle starts increasing again, indicating that additional moisture content does not cause additional preferred orientation.

These studies on particles orientation show a significant limitation as they cannot differentiate between global and local orientation of particles. Indeed, orientation might or might not increase within packets of parallel particles, but each packet might still remain misaligned with neighbour ones.

Extensive studies on microstructure of compacted soils by means of Mercury Intrusion Porosimetry (MIP) led to significant changes in the microstructural interpretation. Because of the bi-modal pore size distribution exhibited by clay compacted on the dry side of optimum, it was assumed to form an aggregated structure. A wide experimental evidence based on

Mercury Intrusion Porosimetry and Scanning Electron Microscope images mainly on clayey silt (silt percentage generally higher than the 50%), rather than silty clay (silt percentage less than 50%) has been provided to corroborate this assumption (e.g. Cui & Delage (1996), Romero & Simms (2008), Monroy et al. (2010)).

The conceptual model of aggregation put forward by Alonso et al. (1987), based on the definitions provided by Collins & McGrown (1974), has gained wide acceptance and has remained almost unaltered for almost three decades. It is therefore worthwhile having an insight into the basic concepts developed by Alonso et al. (1987):

"The description of micro-fabric is based on three types of form: elementary particle arrangements, particle assemblages and pore space. Elementary clay arrangements, in a more or less parallel configuration, are dominant in expansive soils, whereas grain arrangements predominate in collapsible soils. Expansion can take place within clay arrangements. The particle assemblages are integrated by arrays of elementary particle configurations and they are described as matrices if a predominantly three-dimensional structure is formed, aggregations if a grain-like configuration results. Purely expansive soils or clayey compacted wet of optimum exhibit predominantly a matrix type of microfabric. On the other hand, clay aggregations and connectors are in common in collapse-prone soils. Therefore, the aggregates interact with each other much like rigid grains interact in a granular material. Unlike sand or silt particles, however, the aggregates may experience volume change."

As reported in Figure 14, the pore size distribution of compacted soils is generally divided into macro-pores and micro-pores (e.g. Alonso et al. (1987), Delage et al. (1996), Romero et al. (1999), Delage et al. (2006), Alonso et al. (2010), Delage (2010), Monroy et al. (2010), Romero et al. (2011), Casini et al. (2012), Alonso et al. (2012)). Macro-pores are related to pores existing in between aggregates (so-called inter-aggregate porosity) and micro-pores are related to pores existing between the clay particles forming the aggregates,

and therefore to the porosity within the aggregates themselves (so-called intra-aggregate porosity).

Such conceptual model gained wide acceptance after the end of the 90s. The most advanced hydro-mechanical frameworks for partially saturated clays have been based on the assumption that clay particles form aggregates and the aggregates represent the elementary unit of the clay microstructure rather than individual particles. Although such a microstructural concept has led to successful macroscopic models, often incorporating microstructural variables or parameters (Gallipoli et al., 2003, Tarantino, 2007, Alonso et al., 2012), a full experimental validation of such microstructural concepts is still missing despite the number of contributions on microstructural aspects of partially saturated soils including Delage & Lefebvre (1984), Delage et al. (1996), Delage et al. (2006), Romero et al. (1999), Romero & Simms (2008), Romero et al. (2011), Tarantino & De Col (2008) and Tarantino (2010).
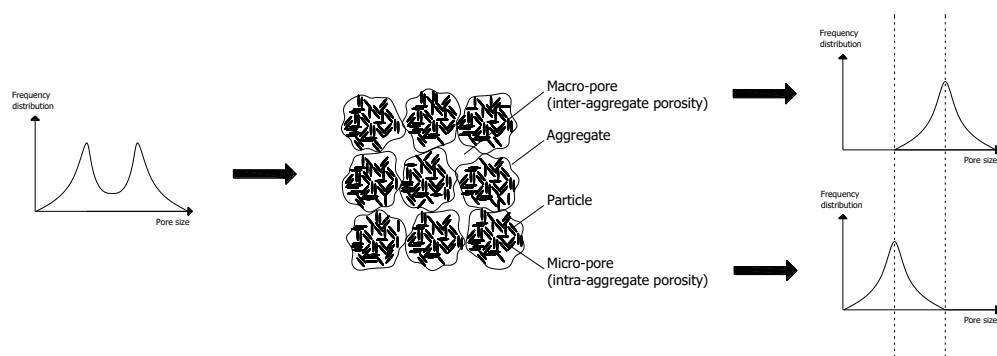
Figure 14. Traditional conceptual model for compacted soils

1.4.2 **Evolution of pore size distribution at different compaction water contents**

Tarantino & De Col (2008) performed mercury intrusion porosimetry tests on 5 samples compacted at the same vertical stress (1200 kPa) and different water contents (Figure 15). Speswhite kaolin with plastic limit $w_P=0.32$ and liquid limit $w_L=0.64$ was chosen for the tests. The grain size distribution showed it to have 0.20 silt fraction and 0.80 clay fraction. Samples were compacted in

steps (150-300-600-1200 kPa). No drainage was allowed during the test and the water content remained constant. After compaction, samples were dehydrated by the freeze-drying technique and then tested in the MIP. Figure 16a shows the pore size distributions of the 5 samples tested.

Similar experiments were carried out by Casini et al. (2012). They presented the pore size distributions of an Aeolian silt compacted at different water contents but this time at the same void ratio. The clay minerals determined by X-ray diffraction were illite, kaolinite and inter-stratified illite-smectite. No significant swelling properties were observed. The samples were prepared by one-dimensional static compaction. Figure 16b shows pore-size distributions of samples compacted at void ratio e=0.5 and different water contents (13%, 15%, 18%, and 18.6%).
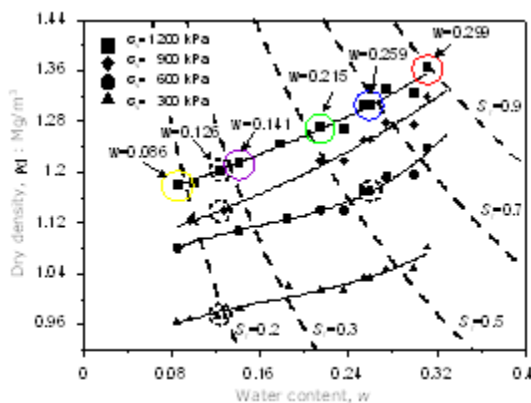
Figure 15. Post-compaction dry density against water content of statically compacted kaolin. Dotted lines indicate contours of equal degree of saturation, S_r; circles indicate samples tested in mercury intrusion porosimeter (Tarantino & De Col, 2008)

In both cases (constant vertical stress or constant final void ratio), the effect of the different compaction water contents on pore-size distribution is the same. Pore-size distribution presents two dominant sizes (two modal values) but pore size of the two classes of pores remains steady throughout the entire range of compaction water contents. For any increase in the water content, the volume associated with the micro-pores (commonly associated with intra-aggregate porosity) increases and the one associated with the macro-pores

(commonly associated with inter-aggregate porosity) decreases. When the compaction water content changes, the volume of voids redistributes from one class of pores to the other. It is worth noting that, although the volume associated with each class of pores changes, the dominant pore sizes do not. For example, a decrease in the compaction water content causes the volume of voids related to the macro-porosity (commonly associated with inter-aggregate porosity) to increase with the pore size of that class of pores remaining steady.
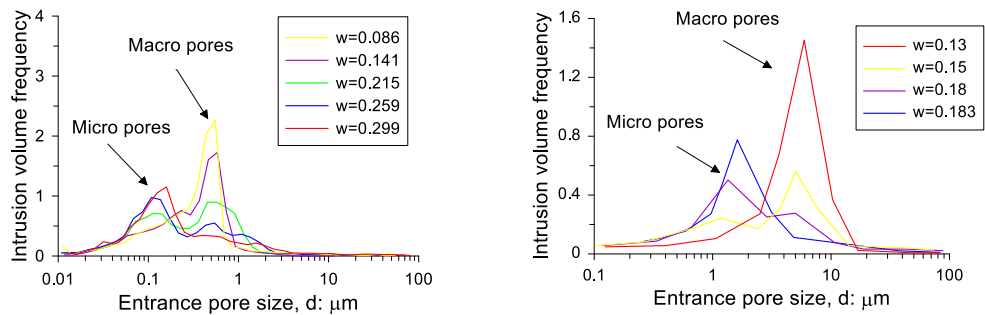
A) *Pore size distibution of kaolin clay compacted at 1200 kpa (Tarantino & De Col, 2008)*

B) *Pore size distribution of aeolian silt compacted at the same void ratio (Casini et al., 2012)*

Figure 16. Pore size distribution of compacted samples at different water contents. a) same vertical stress and b) same final void ratio.

Closer inspection of data in Figure 16 actually reveals that the widely accepted assumption about the 'aggregated' nature of compacted soils (i.e. macro-porosity associated with inter-aggregate porosity and micro-porosity associated with intra-aggregate porosity) is open to debate. The following reasoning leads to a paradox highlighting the limitations of the 'aggregate assumption':

i)   If the volume of voids associated with inter-aggregate pores increases and the modal inter-aggregate pore-size remains unchanged, then the number of inter-aggregate pores has to increase.

ii)   An increased number of inter-aggregate pores would imply an increased number of aggregates.

iii) If it is assumed that all particles are involved in the aggregation, a higher number of aggregates would imply smaller aggregates.

iv) Smaller aggregates should create pores of smaller dimension, which is not the case as the modal size of macro-pores remains stable.

Similar conditions apply in the case of the micro-pores (intra-aggregate porosity).

In conclusion it appears difficult to explain why the volume of voids associated with the pores within and between the aggregates changes significantly without any change observed in the actual size of the pores.

1.4.3 Mono-modal pore size distribution of compacted samples

Figure 17 shows the pore size distributions of samples compacted at very low water content and samples compacted at water content close to the optimum. In both cases, the resulting pore size distributions appear to be mono-modal.

If one attempts to explain such mono-modal pore size distributions by means of the traditional conceptual 'aggregate-based' model, it can be easily observed that another paradox arises. An aggregate structure implies two classes of pores, i.e. pores within the aggregates and between the aggregates respectively, and should be accompanied by a bi-modal pore-size distribution. Accordingly, a mono-modal pore-size distribution should represent a non-aggregated structure.

At high compaction water content, the pore-size distribution is mono-modal and the modal size corresponds to the one that was associated with the intra-aggregate porosity in Figure 16. This would imply that only pores within the aggregates are present and no pores between the aggregates exist. In turn, this would imply that the compacted soil is made by one huge single aggregate!

On the other hand, when the compaction water content is very low, the only class of pores that exists is the one that was associated with the inter-aggregate porosity in Figure 16. According to the 'aggregate-based'

conceptual model, this would imply that no pores exist within the aggregates, i.e. the aggregates are made of single particles!

A) *Pore size distibution of kaolin clay compacted at 1200 kpa (Tarantino & De Col, 2008)*

B) *Pore size distribution of aeolian silt compacted at the same void ratio (Casini et al., 2012)*
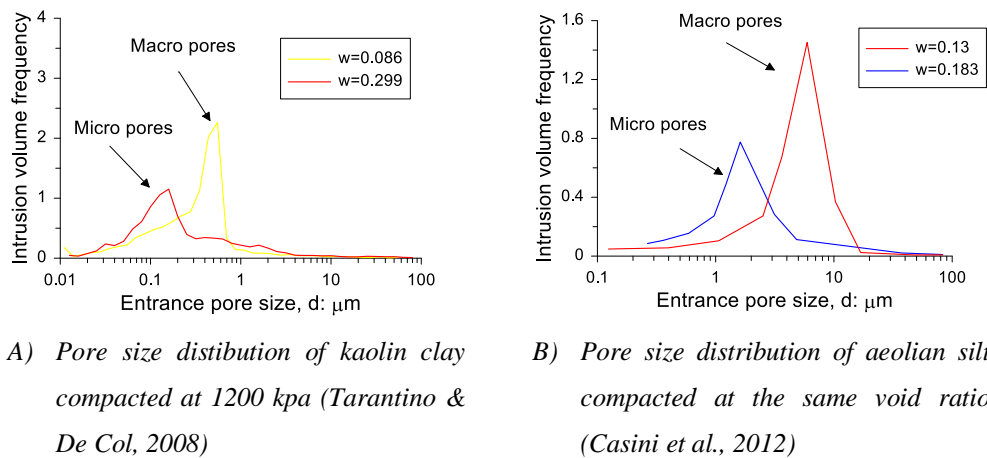
Figure 17. Mono-modal pore size distribution of compacted samples at different water contents. a) same vertical stress and b) same final void ratio.

1.4.4 Reconstituted vs compacted samples

Reconstituted samples are traditionally considered to have a matrix-like microstructure and the pore size distribution is generally mono-modal. Samples compacted on the wet side of optimum are generally assumed to have a microstructure similar to reconstituted soils because of their mono-modal pore size distribution (e.g. Delage et al. (1996)). On the other hand, samples compacted on the dry side of optimum, because of their bi-modal pore-size distribution, are assumed to have an aggregate microstructure (traditional 'aggregate-based' conceptual model).

Figure 18 shows the mono-modal pore-size distributions of samples of kaolin clay reconstituted from slurry and compacted at water content close to optimum respectively and their comparison with the bi-modal pore size distribution of kaolin clay compacted on the dry side of optimum. The modal value of the two mono-modal pore-size distributions (samples reconstituted and compacted close the optimum respectively) are the same and the modal

pore-size coincides with the modal value of the micro-porosity showed by kaolin compacted on the dry-side of optimum.
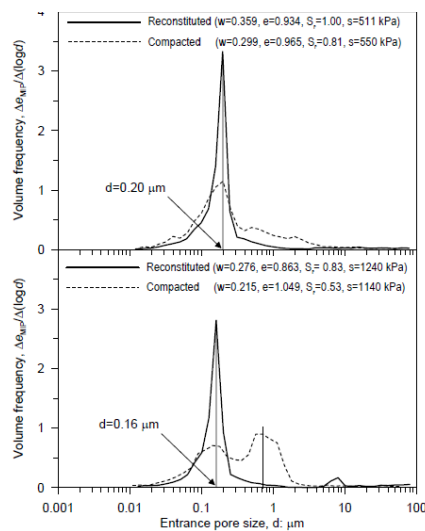
Figure 18. Comparison of pore size distribution of compacted and reconstituted samples of Speswhite kaolin at similar suction (Tarantino, 2010)

When the water content becomes high, the pore size distribution switches from a bi-modal to a mono-modal one, with pores that generally have dimensions of the micro-pores associated with the intra-aggregate porosity in a bi-modal pore-size distribution.

Based on experimental evidence mainly associated with the hydraulic behaviour of compacted soils, Romero et al. (1999), Tarantino (2009), Romero et al. (2011) concluded that aggregates are made by 'reconstituted' soil. Moreover Tarantino (2010) suggested that the mono-modal pore size distribution of samples compacted on the wet of optimum and reconstituted samples is not associated with an aggregate-less microstructure. Indeed, the two classes of pores (micro- and macro-) have size of the same order of magnitude and tend to overlap, thus giving rise to an apparent mono-modal pore-size distribution. In particular, it is the macro-porosity that tends to decrease in size upon wetting and approaching the size of the micro-pores.

Similar conclusions were implicitly drawn by Delage & Lefebvre (1984). By studying reconstituted and natural soils, they concluded that those soils are made by very small aggregate despite an apparent mono-modal pore-size distribution. If reconstituted soils are made by very small aggregates, and aggregates in compacted samples are made up of reconstituted soil, one may conclude that aggregates in compacted soils are made up of very small aggregate. Again, some contradictions will arise by using the traditional 'aggregate' conceptual model:

i)   Particle dimension – For the case of speswhite kaolin clay, when compacted, the inter-aggregate porosity is in the range of 1 μm diameter. On the other hand, inter-aggregate porosity in reconstituted kaolin has been considered to be at about 0.2 μm. Experimentally, no data have ever been provided to show that the inter-aggregate porosity can range from 0.2 to 1 μm, but data exist only at the two extremes.

ii)   Number of particles per aggregate - Figure 16 shows that the higher the water content, the higher is the volume of the micro-pores, traditionally assumed to be associated with the intra-aggregate porosity, although the dimension of the pores does not change. Such an increase cannot be explained by either invoking bigger aggregates or a higher number of aggregates. In both cases the overall number of voids between particles (intra-aggregate porosity) should remain constant regardless the number or the size of the aggregates, since the number of particles forming the aggregates does not change. This could be indeed explained if the number of particles involved in the aggregation (regardless the number or the size of the aggregate) is changing. But, if one assumes that all the particle are in aggregated state, as implicitly assumed in the literature, such an increase of the volume associated to the intra-aggregate porosity cannot be explained.

1.4.5 **Dry side and wet side of optimum**

When the same soil is compacted to the same void ratio on the dry and wet sides of optimum respectively, the pore size distributions appears to be totally

different. Figure 19a shows the Proctor curve of an Aeolian silt and Figure 19b shows the pore size distribution of two samples of Aeolian silt compacted to the same dry density 16 [kN/m³] but at different water contents, one on the dry side of optimum and the other one on the wet side of optimum (the pore-size distribution of a sample compacted at the optimum is also shown in the figure).

A) Aeolian   silt   standard   proctor   B) Compacted   aeolian   silt   pore   size
   compaction curve   distributions
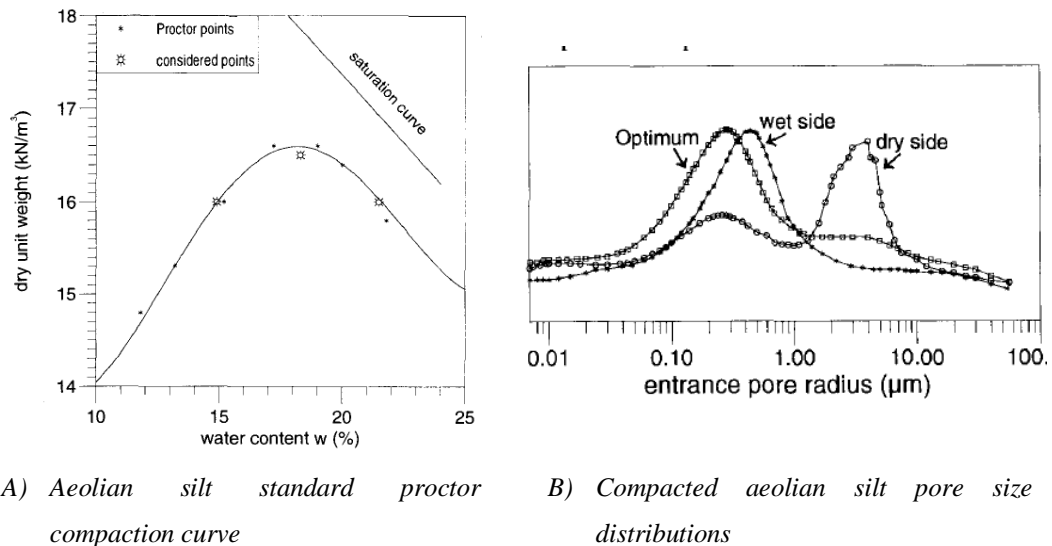
Figure 19. Compaction curve and pore size distribution of Aeolian silt (Delage et al., 1996)

The sample at the dry side of optimum shows a clear bi-modal pore size distribution whereas the one compacted at the wet side of optimum shows a mono-modal pore size distribution. Differences in sample preparation were minimal. Both samples were prepared by spraying water on an initially dry soil powder, they were both compacted, and they were both partially saturated before and after compaction. Nonetheless these two samples showed a microstructure that is radically different. According the traditional 'aggregate' model, the sample compacted on the dry side of optimum is made of aggregates whereas the sample compacted on the wet side of optimum is aggregate-less. The question remains open about the microstructural mechanisms leading to aggregation in the sample compacted on the dry side of optimum in contrast to the sample compacted on the wet side of optimum where aggregation was not promoted.

1.4.6 Evolution of the pore size distribution upon wetting

Monroy (2006) presented the evolution of the pore size distribution of a compacted samples upon wetting under free-swelling conditions. The soil was a weathered London clay with liquid limit $w_L=0.83$ and plastic index $I_P=0.54$. The grain size distribution showed it to have 0.58 clay fraction and fines content of 98% (particles smaller than 0.06 mm). Samples were compacted to a dry density of 1.384 (Mg/m³) and the degree of saturation was about 67% after compaction. Samples were subjected to a wetting and were then dehydrated by means of freeze-drying technique and tested in the MIP. The evolution of the pore size upon wetting is reported in Figure 20.
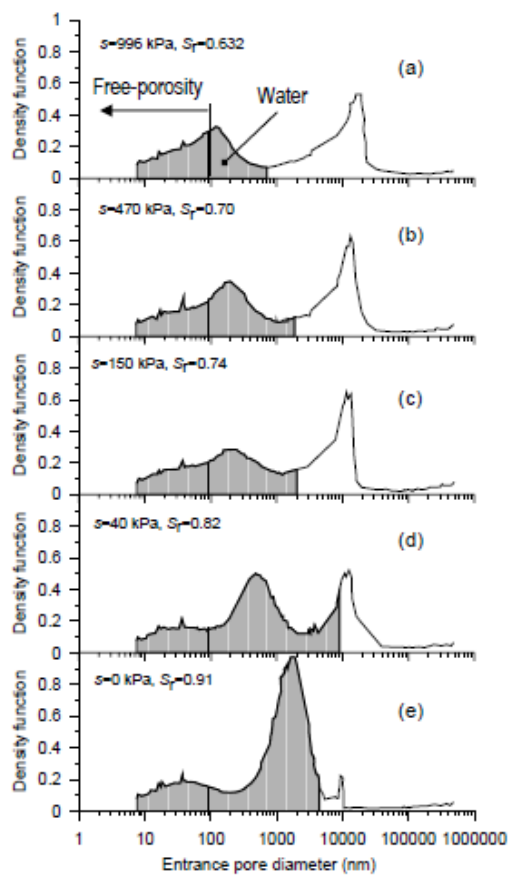
Figure 20. Evolution of pore size distribution of compacted London clay upon wetting (after Monroy (2006)

Experimental data show that the intra-aggregate porosity swells (increase in size and number of pores), whilst the inter-aggregate porosity disappear

(pore size is steady while the associated volume is reducing). According to the traditional conceptual model two feasible explanations may be given for the inter-porosity decreasing:

i)   Aggregate slippage
ii)   Aggregate swelling is invading the inter-porosity.

However, in both cases a shift towards smaller pore size of the macro-pores should have been recorded. Moreover, the case of aggregate swelling it is usually considered when the swelling of the sample is prevented.

As in the previous cases, the volume associated with one pore class rather than the other one redistributed when the water content increases. However, the intra-aggregate porosity changes in size and volume of voids, but the inter-aggregate porosity change only in associated volume of voids, as the pores between the aggregates do not change in size, but simply disappear.

1.5 Conclusions

The understanding of the micro-mechanisms controlling the hydro-mechanical behaviour of clays and the development of a conceptual microstructural model seems to be crucial in order to develop a DEM for clays. Overall, there seems to be a lack of understanding of the mechanical and electro-chemical interaction between clay particles in non-active clays, which will be the focus of this dissertation.

In order to better understand the nature of the forces between clay particles and their dependency to pore-water chemistry, this chapter has reviewed basic concepts about kaolin mineralogy and the different electro-chemical interactions between clay particles. In addition, the most widely accepted conceptual models for particle configurations and their mechanical implication have been discussed for suspensions, slurry states and compacted states.

Conceptual microstructural models developed for suspensions have been presented in the colloidal science literature with focus on electro-chemical interactions. On the other side, conceptual microstructural model for soils (reconstituted and compacted) have generally neglected electro-chemical interactions in non-swelling clays and mainly attributing mechanical interactions between particles. There is therefore a gap to bridge between the colloidal science and soil mechanics approach to microstructural interactions in clays.

In soil mechanics, the link between microscopic and macroscopic behaviour have been investigated differently in saturated and partially saturated soils. In saturated soils, there is a lack of understanding of microstructural mechanisms controlling macroscopic behaviour. Thanks to the effective stress concept, it is possible to model macroscopic behaviour without referring to the microstructure. Indeed, the effective stresses are not microstructure related.

On the other hand, microstructural conceptual models have been developed in the mechanics of partially saturated soils to inform the macroscopic

(continuum) constitutive models. Again, there appears to be a gap to bridge between saturated and unsaturated soil mechanics.

Finally, it has been shown that the traditional micro-mechanical 'aggregate-based' conceptual model developed for partially saturated soils and widely adopted for more than 30 years shows a number of contradictions when data from pore-size distributions are analysed in depth.

As final comment to the chapter it is worth giving some clarification on the definition of aggregate, micro-porosity and macro-porosity which will be used in the rest of the thesis. Since such terms are transversal to different disciplines are often used with different meaning.

The term aggregate is used to identify the particle association that occurs in compacted soils, which in turn gives rise to an aggregated microstructure (such definition is adopted for chapter 4).

On the other hand, particle associations in suspension will be defined either as flocs when particles floccule in an edge-to-face configuration, or as parallel aggregates when particles associate in a parallel mode (such definition is adopted for chapter 5)

As highlighted in the literature review of compacted soils, the terms micro-pores and macro-pores are generally associated with the intra-aggregate porosity and with the inter-aggregate porosity respectively (chapter 4). In this thesis such two terms might assume a different meaning when talking about saturated soils (chapter 3). Saturated soils generally show a mono-modal pore size distribution and no aggregation is considered. Under such conditions, micro-pores are defined as the porosity corresponding to the modal value of the pore size distribution and macro-pores as the porosity corresponding to the tail (on the right side) of the same distribution.

Chapter 2.   Mercury intrusion porosimetry

2.1 Introduction

The research work carried out within this dissertation is focused on the microstructural response of clays including particle configuration (fabric) and mechanical and electro-chemical interactions between clay particles. As a result, tools to investigate microstructure of clays are pivotal to this work.

The most reliable technique for quantitative microstructural investigation currently available is the Mercury Intrusion Porosimetry (MIP). Such a technique allows determining the pore size distribution of a porous material for a range of pores ranging from a few nanometres to tens of microns and indirectly speculating on the particle arrangement. MIP has been used over the last 30 years for microstructural investigation in soil mechanics and has gained wide acceptance within the geotechnical community. Since the pioneering work of Delage and Pellerin (1984), pore size distribution and its evolution upon hydro-mechnical paths have been used to inform hydro-mechanical constitutive models including Romero et al. (1999), Delage et al. (2006), Tarantino (2007), Tarantino & De Col (2008), Monroy et al. (2010), Romero et al. (2011).

MIP does not provide a direct view of microstructure as is the case with Scanning Electron Microscopy (SEM). Particle configuration, aggregation, and fabric have to be indirectly inferred from the evolution of the distribution of the pore size. In order to exploit the information gained from the MIP test, assumptions on the mechanism of intrusion and extrusions have been made over the years (e.g. capillary tube model and ink-bottle model). On such basis, brainy exercises of logic have been performed in order to extrapolate the microstructure form the pore size distribution. For example, difference in the

intruded volume upon the 1st and 2nd intrusion has been attributed to constricted porosity Delage et al. (1983), entrapped volume after 1st extrusion has been associated with the volume of the inter-aggregate porosity (Romero et al., 2011), and bi-modal pore size distribution has been considered as an evidence of the existence of aggregates.

On the other hand, although SEM technique allows a direct view of a previously dehydrated sample surface, it has not been considered suitable for the purpose of the research. SEM imaging is believed to be subjected to a high level of bias both during the image process and in the image interpretation. The duty of providing direct images supporting the conclusions of such thesis is postponed to future works, where alternative imaging techniques (e.g. x-ray micro- or nano-tomography) will be investigated. 3D imaging should provide images of particle configuration from the core of a sample (not from the surface) and without previous dehydration (freeze-drying).

The first part of this chapter presents a state of the art of MIP including experimental procedures (measurement of the volume of mercury intruded and techniques for sample preparation) and the interpretation of MIP data based on the assumptions on the mechanisms of mercury intrusion and extrusion. It is worth highlighting that such a review transcends the traditional 'geotechnical' approach. Indeed, It is based on papers that, although dated, may give a fresh approach to the topic.

In the second part of the chapter, sources of error in MIP measurement have been investigated experimentally. Different procedures of freeze-drying have been investigated, tested, and compared. An error analysis has been carried out with respect to the measurement of the intruded volume and the parameters controlling the process of intrusion/extrusion.

In the final part of the chapter, a conceptual model of intrusion and extrusion is put forward and a numerical code to model the intrusion/extrusion process is presented. The aim of such a model is to provide a numerical validation by 'virtual' tests of the different conceptual models adopted when interpreting MIP

data. The model is presented only in its embryonic stage and its full validation is part of future works.

2.2 State of the art

2.2.1 Experimental techniques

Method of intrusion

The basis of the mercury intrusion method was introduced originally by Washburn (1921). The method rests on the physical principle that a non-wetting fluid will not spontaneously intrude the pores of a medium but will do so if sufficient pressure is applied.

When a change in pressure of mercury surrounding a soil sample is applied, a range of pores is intruded by the mercury. The maximum and minimum diameter of the pores intruded upon a given pressure change can be related to pressure at the start and the end of the pressure step respectively according to Washburn's equation (Equation 13):

$$d = -\frac{4 \cdot \gamma \cdot cos\theta}{P} \qquad [13]$$

where *d* is the diameter of the intruded pores, *P is* the applied pressure, γ is the mercury surface tension, and θ is the contact angle. Equation [13 makes the implicit assumption that pores are cylindrical and, hence, the air-mercury interface is a spherical cap.

The volume of mercury intruded upon a given pressure step is therefore associated with the range of pore diameters intruded. By pairing the cumulative volume intruded and the current minimum pore diameter (associated with the current mercury pressure applied), the cumulative pore volume distribution with respect to pore diameter can be built up. According to Diamond (1970), the surface tension value of 0.484 N/m at 25 °C (Kemball, 1946, Nicholas et al., 1961) can be assumed. Penumadu and Dean (2000) assumed the mercury surface tension to be 0.484 N/m. They also elaborated the data by assuming a different mercury surface tension (0.473 N/m) and showed that the difference in the estimated intruded volume was negligible.

The usual value employed for the contact angle between mercury and kaolinite particles is 147°, which was determined by Diamond (1970). In Diamond's research, the contact angle had been indirectly measured using the sessile drop method (method described by Padday (1957)). Other measurements of mercury contact angles between mercury and kaolinite clay are reported in Penumadu and Dean (2000), who gives a value of 160° measured by means of a goniometer with high-magnification optics.

Measurement of intruded volume

Several factors affect the volume measurement during a porosimetry test. Such factors must be considered when analysing porosimetry data. As highlighted in Diamond (1970), the porosimetry will only give the volume of pores that are accessible from the exterior. Even if all of the pore space is accessible from the outside some of them may be accessible only through entryways of smaller diameter. Those pores will not be intruded until sufficient pressure is applied to intrude the entryways. Hence, all of the volume of such pores will be allocated to diameter class of the most restricted part of the entryway.

Since the test involves a mass moving of mercury into a confined pore space, the process is not instantaneous. Therefore "care must be taken to insure completion of the intrusion process at a given pressure before the next pressure increment is applied" (Diamond, 1970). According to Webb (2001) the time for equilibration varies with the nature of the pores system and is not uniform from pressure to pressure within a given run.

Further corrections are also required to take into account the compressibility of mercury (Diamond, 1970), the compressibility of the system (Webb, 2001), and the mercury density changes due to heating (ASTM, 1984).

Finally according to Diamond (1970), a small but finite residual amount of air remains trapped within the penetrometer in the initial evacuation step. A correction for the decreasing volume of this trapped air at each increment of increasing pressure might be used. However "when large pores are not of

interest (pores larger than 50 μm diameter) this correction may be safely ignored" (ASTM, 1984).

Dehydration technique

Mercury intrusion tests have to be performed on dehydrated samples. Techniques such as oven drying should be avoided to avoid altering the pore volume of the specimen. Since the pioneering work of Diamond (1970), several procedures have been developed for specimen dehydration with minimum disturbance of the pore structure. All of these procedures consist in rapid freezing of small sized samples in cryogenic liquid (with the aim of avoiding the 9% of volume increasing of ice) and subsequent sublimation in a controlled vacuum chamber (lyophilisation).
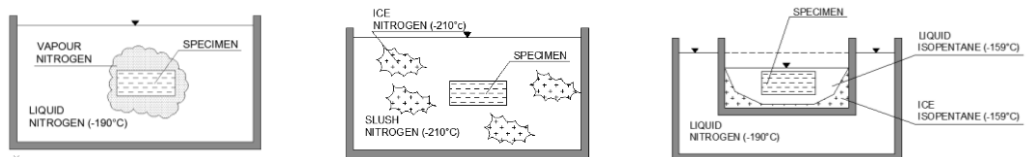
A) liquid nitrogen   B) slush nitrogen   C) isopentane + liquid nitrogen

Figure 21: Specimen freezing techniques

Delage and Pellerin (1984) showed that submerging clay samples in liquid nitrogen at its melting point (-196 °C) is not sufficient to allow crystalline ice formation within the sample (Figure 21a). Heat transfer between the soil and the nitrogen is slowed down by a gaseous layer of boiling nitrogen which occurs all around the immersed sample.

Alleman et al. (1985) suggested using liquid nitrogen in slush form (Figure 21b). Approximately 200 ml of liquid nitrogen must be cooled down to its triple point (-208 °C) by applying a pressure lower than 125 mbar in an insulated vessel. According to Alleman "It takes approximately 10 minutes to obtain nitrogen in the slush form. The vacuum is then broken and specimen is quickly deposited into the slush nitrogen using pre-dipped fine forceps. This action should not be accompanied by any boiling motion around the specimen. If

boiling does occur, this is an indication that the nitrogen has warmed or that the sample is excessively sized."

Another possibility to freeze the specimen consists of submerging the samples in a container of Freon 22 (Delage et al., 1982) or Isopentane (Tarantino & De Col, 2008) as shown in Figure 21c. Freon or Isopentane are cooled close to their melting point (-145 °C or -159 °C respectively) by liquid nitrogen (-190 °C). Immersion of small pieces of soil is made when Freon (or Isopentane) starts freezing. With a sample of sufficiently small mass of the sample the amount of heat transferred by the sample during immersion is not enough to bring the temperature of Freon (or Isopentane) up to its boiling point. Freezing takes place in the liquid phase and heat transfer is much faster than during direct immersion in liquid nitrogen.

2.2.2 Conceptual model of mercury intrusion/extrusion in porous material

Intrusion-extrusion hysteresis

Hysteresis occurs in mercury intrusion and extrusion. At a given pressure, the cumulative volume recorded on the extrusion curve is greater than the one recorded on the intrusion curve (Lowell & Shields, 1981). Hysteresis between the intrusion and extrusion is always observed during mercury measurement. There are different sources of hysteresis and these are discussed hereafter.

Contact angle hysteresis

Contact angle hysteresis is a well-documented phenomenon. Intrusion occurs with an advancing angle ϑ_a and extrusion with a receding angle ϑ_r. Therefore, the pressure required for mercury to extrude from pores with a receding angle ϑ_r is less than the on required to re-intrude into the same pores with an advancing angle ϑ_a. Consequently, the superimposition of extrusion curves using ϑ_r with second or subsequent intrusion curves occurs as a function of pore radii and not pressure (Lowell & Shields, 1981). However,

some hysteretic effects cannot be explained by the contact angle hysteresis (Giesche, 2006):

a) Contact angle hysteresis cannot explain why some mercury remains trapped in the pore system after complete depressurization.

b) Extrusion and re-intrusion curves should have a similar shape when plotted on a logarithmic pressure or pore size scale. However, data in the literature frequently show only a marginal overlap between these curves.

c) No volume changes should be observed, when scanning between the hysteresis branches (extrusion and intrusion curve). Yet, frequently those scans within the hysteresis-range are not constant with respect to pore volume.

Washburn hypothesis limitations

The conventional method of analysis of mercury porosimetry data, i.e. Washburn's hypothesis, is based on the model of parallel nonintersecting cylindrical pores. According to such hypothesis, a porous material will exhibit hysteresis between intrusion and extrusion only due to different extrusion and intrusion pressure in turn associated with contact angle hysteresis.

However, hysteresis is also associated with differences in intruded and extruded volume at the mercury same pressure. Intrusion of mercury occurs within an interconnected network of pores which are not readily accessible to mercury at every stage of the penetration process. Furthermore, the observed capillary pressure hysteresis between the intrusion and extrusion curves and the permanent retention of mercury cannot be predicted by the capillary tube model (Ioannidis & Chatzis, 1993).

Percolation model

Percolation is a mathematical theory dealing with the passage of a fluid through a porous medium simulated as a lattice of interconnected pores. Percolation models are generally classified as "site percolation" or "bonding percolation", depending on whether the connectivity is defined by square

sharing sites (the fluid passes through squares sharing sites) or adjacent bonds.

The main concept behind percolation theory is the existence of a percolation threshold, i.e. the degree of saturation at which the system is connected from one side to the other. In mercury intrusion simulation, threshold injection pressure is a term used for the pressure at which there is an abrupt change of gradient of the initial injection curve and at which there is a significant invasion of a sample with mercury. Threshold injection pressure, being related to throat size, may be affected by boundary effects as coordination number and presence of non-random heterogeneities in the pore system (Wardlaw & McKellar, 1981). For a given pore size distribution, the threshold injection pressure will be less for a network of larger coordination number than for one of smaller coordination number (Wardlaw & McKellar, 1981).

The percolation model cannot be applied if the pore network is arranged as non-random distribution of pores (ganglia of pore of the same size). Depending on whether small pores or big pores form a cluster, the threshold pressure could be lower or greater than the one of a random distributed network (Wardlaw & McKellar, 1981).

Ink bottle theory

It is generally accepted that a good representation of pore space in porous materials is a matrix of pores (bodies) interconnected through narrow pore throats. A large pore can be shielded by a smaller one during intrusion and a small one can be shielded by a bigger one during extrusion. Therefore, in a body-throat system, mercury intrusion is controlled by the capillary resistance of pore throats whereas mercury extrusion is controlled by the capillary resistance of pore bodies (Ioannidis & Chatzis, 1993). This phenomenon will affect both the intrusion and the extrusion stages. During the intrusion, the intruded volume related to a given pore size will be less than the actual one because of throats. In contrast, the extruded volume for the same given pore size will be more than the actual one because of bodies.

Wardlaw & McKellar (1981) have photographed the trapped mercury in a glass micro-model of pore and throat chains with different pore /throat ratios (Figure 22). For ratios that are greater than 6, mercury trapping occurred even if the final releasing pressure was lower than the nominal receding pressure of the bigger pore. If the ink-bottle effect is the only phenomenon involved in volume hysteresis, no mercury would have remained trapped upon the releasing of the lower pressure.
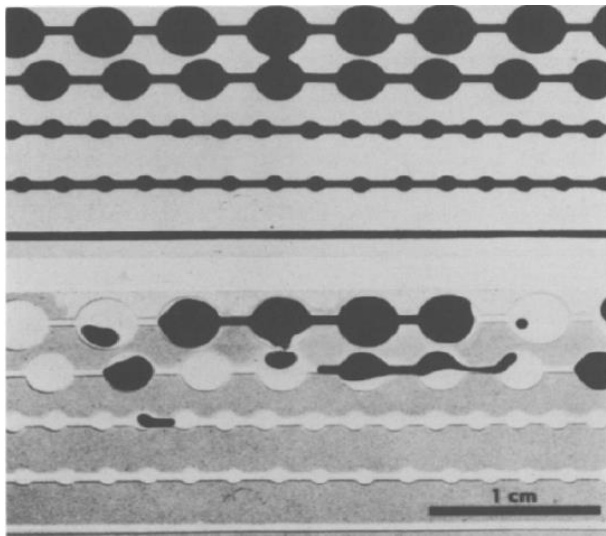
Figure 22. Glass model for ink-bottle effects on trapped mercury (Wardlaw & McKellar, 1981)

Snap-off

Trapped mercury is defined as the mercury that remains entrapped in the sample after an initial intrusion-extrusion cycle. After a complete cycle of intrusion and extrusion the amount of trapped mercury depends on the phenomenon called snap-off.

Extrusion of mercury from a "fully saturated" porous medium is an imbibition process, during which gas at low pressure displaces mercury. However, the onset of retraction is contingent on the existence of mercury-gas interfaces that can retreat as the pressure is decreased.

At the end of the intrusion, where mercury saturation tends to unity, there exist tiny pockets of compressed air sheltered in regions of pore wall roughness features which act as nuclei for mercury disconnections during retraction. Mercury retraction is a quasi-static imbibition process in which low-pressure air (wetting fluid) displaces mercury (non-wetting fluid). When the external pressure decreases, the mercury menisci that occupy pore wall roughness begin to retract. This eventually leads to the formation of collars around various mercury threads occupying long and narrow pores (throats). When a thread surface becomes unstable the mercury thread collapses. This mechanism is referred to as snap-off (Tsakiroglou et al., 1997).

Snap-off and consequent trapping of mercury can also occur because of the structure of an interconnected network. For a non-wetting phase to empty, there must be a continuous unbroken line of non-wetting phase to the outside surface.

In a two-dimensional network of pores and throats, access throats will empty first as pressure begins to reduce in the extrusion process. In fact, the smaller the pores, the higher is the extrusion pressure causing the pore to empty (Matthews et al., 1995). Therefore there is no interconnected routes available to mercury to escape and the pressure of mercury behind 'broken' access throats will no longer be affected by the external pressure.

Factors that affect snap-off during extrusion from a porous material are:

- Pore/throat ratio
- Pore coordination number
- Random and non-random sorting (Figure 23)

Pore/throat ratio

Wardlaw & McKellar (1981) showed how the pore/throat ratio affects the occurring of snap-off. Their experiments have proved that the snap-off is likely to occur at ratios bigger than 6 and that tendency to snap-off increases with the increasing pore/throat ratio.
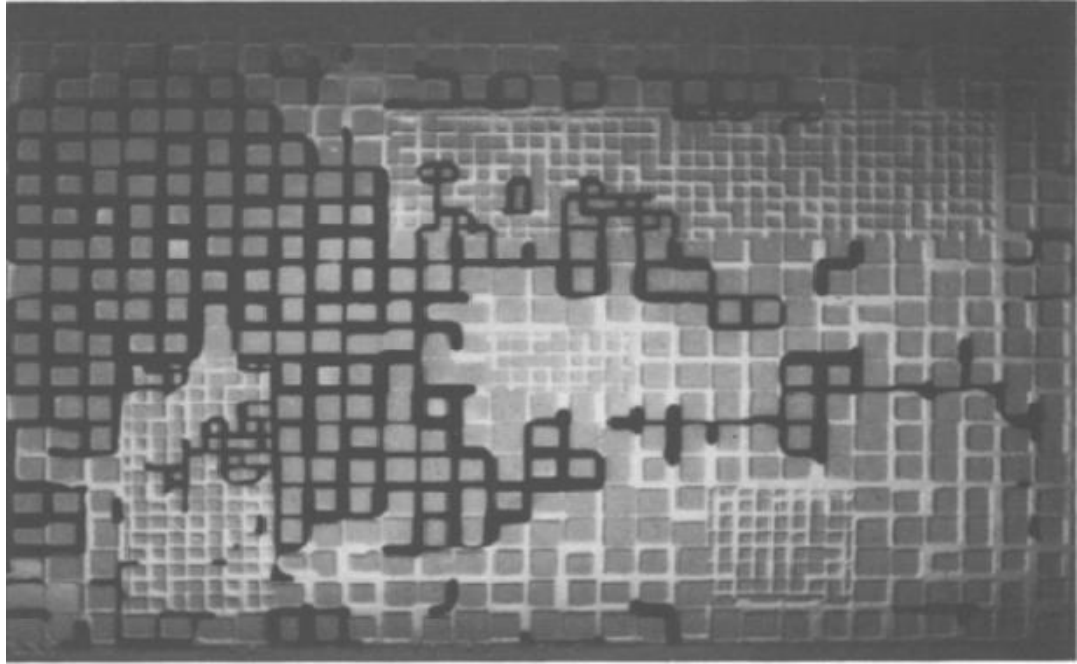
Figure 23. Glass micro-model with non-random heterogeneity. Pressure reduction after almost-full sample saturation (Wardlaw & McKellar, 1981).

Pore coordination number

The coordination number of a pore system is defined as the average number of throats connecting each pore (Wardlaw & McKellar, 1981). It has been shown that the final trapped mercury decreases as the coordination number of the network increases (Wardlaw & McKellar, 1981).

Random and non-random sorting

Experiments carried out by Wardlaw & McKellar (1981) showed that the trapped mercury is sensitive to the distribution of pores in the sample/model. The existence of ganglia of big heterogeneous pores (non-random sorting) causes an increasing in the trapped mercury. At the stage where pressure has been reduced below the threshold value for the emptying of the clusters of larger element, these have already been disconnected by snap-off and extensive residual mercury is retained.

Snap-off factor or energy barrier

During the extrusion process, new mercury interfaces have to be created as the mercury retracts from the pore system. This process requires additional energy and an "energy-barrier" is expected to affect the process. The energy barrier represents the degree to which the extrusion pressure (additional pull) has to be lowered relative to the corresponding intrusion pressure until the mercury network breaks apart and mercury can retreat from a specific pore (Giesche, 2006). In general, it has been shown that the snap-off factor for a cylindrical pore depends on the pore length; the longer the pore the smaller the snap-off factor. As a result, long pores are associated with a small increase in the energy amount required to cause snap-off (Giesche, 1997). Even more relevant is the conclusion drawn by Tsakiroglou et al. (1997) who simulated the snap-off factor for lenticular throats (Figure 24). They concluded that the number of filled throats connected with a pore deeply affects the ability of the pore to empty in addition to its size and the size of the connecting throats. A pore connected to the mercury network by only one filled throat (and three empty throats) is drained at a higher pressure during the extrusion (earlier on) compared to a pore connected via 2 or 3 filled throats (Tsakiroglou et al., 1997).
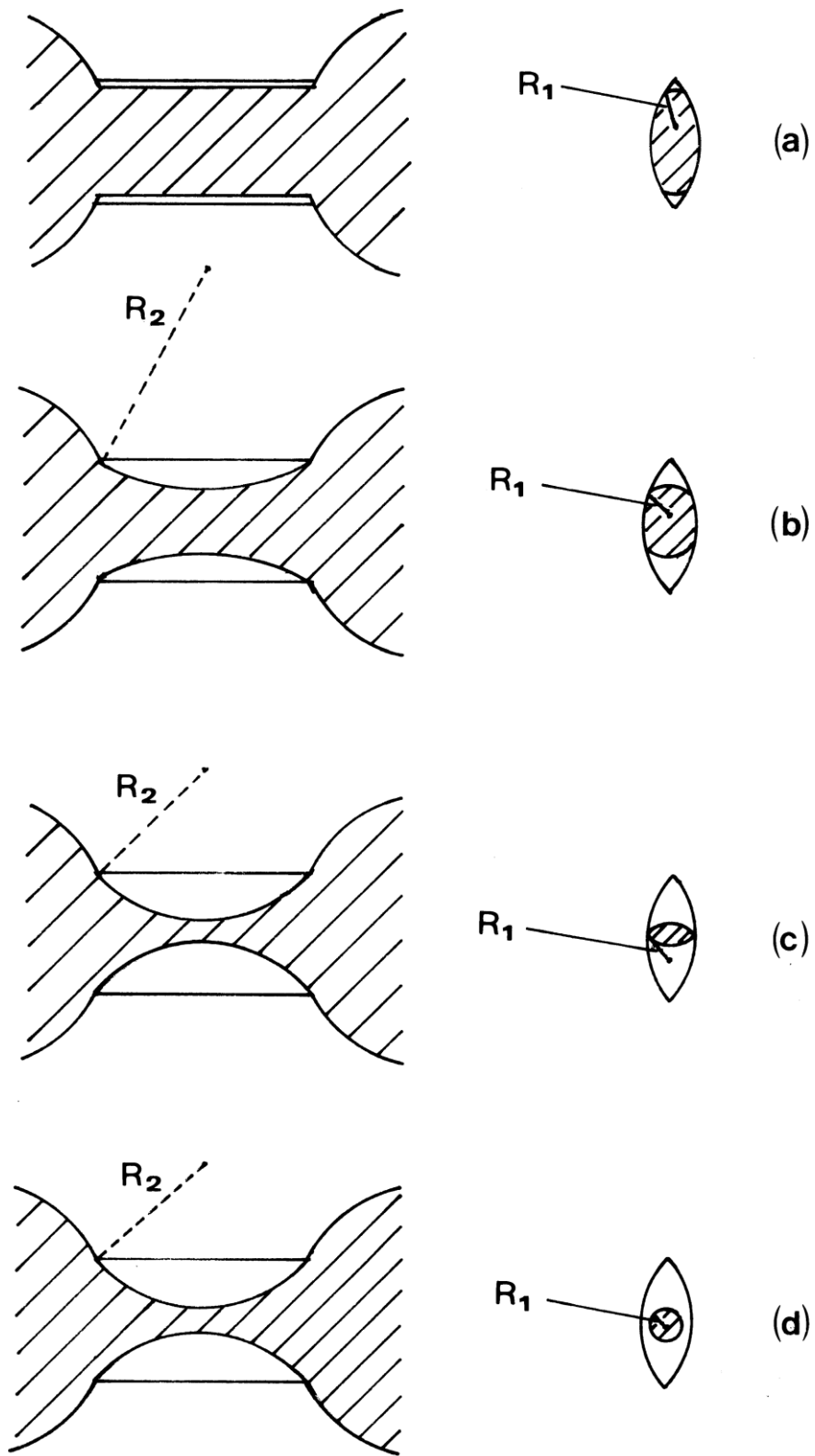
Figure 24. Consecutive stages of snap-off in a lenticular throat connected with two chambers (Tsakiroglou & Payatakes, 1998)

2.3 Experimental procedures

2.3.1 Sample preparation: freeze-drying technique

Two different techniques were used to freeze water within the samples. These are based on slush nitrogen and isopentane as freezing fluid respectively.

Slush nitrogen technique

Nitrogen has been used because is not flammable (unlike many other cryogenic liquids) and because of its low freezing temperature (-210 C°). The low temperature should maximize the speed of freezing of water within the sample. The procedure adopted was as follows:

i)   An expanded polystyrene vessel with approximately 150 ml of liquid nitrogen was cooled down in an insulate chamber by applying an absolute pressure of approximately 0.6 kPa.

ii)   The vacuum was removed 30 minutes after all the liquid nitrogen became ice. When the vacuum was removed, the ice was expected to melt partially and ice and liquid were expected to coexist for a while (slush nitrogen). In reality, all the ice instantaneously melted down to liquid. It is assumed that the coexistence of ice and liquid could not be achieved because of the small amount of liquid and, hence, the low thermal inertia of the system. A bigger amount of liquid would have been required to make slush nitrogen last longer. However, it was impossible to use a bigger dewar because of the reduced size of the vacuum chamber.

iii)   A single specimen of clay (approx. 1 cm^3) was then rapidly submerged in the nitrogen.

Figure 25 shows phases of nitrogen at each stage of the sample freezing. Liquid nitrogen at atmospheric pressure has a temperature of about 78 °K (-195 °C) and lies on the boiling line, i.e. the line where the liquid and the vapour

phases coexist (point A in Figure 25). At this stage nitrogen is evaporating because of the heat supplied by the environment that is at about 293 °K (+20 °C).

When vacuum is applied, the pressure within the nitrogen drops instantaneously. As it may be seen on the phase diagram, starting from point A, a vertical drop of pressure without any phase transformation is not possible. For nitrogen pressure to decrease, temperature as to decrease as well by following the boiling line down to the triple point (point T in the figure). Once the triple point has been reached, the nitrogen cannot reduce its pressure anymore without a complete phase transition. As a matter of fact, at pressures lower than the triple point only two phases can exist, solid and vapour. So, all liquid will rapidly transform into solid phase that remains in equilibrium with the vapour phase. When liquid no longer exists, the ice-vapour system will reduce its pressure and temperature along the ice-vapour branch (sublimation line) of the phase diagram (point B).

Finally, when the pressure is quickly restored to environmental pressure (about 1 atm), the nitrogen will reach equilibrium at point A (boiling line at atmospheric pressure). Before reaching point A the system has to melt down the solid nitrogen, and therefore any energy supplied to the system will be used to melt down the ice (which is in a metastable state), keeping the temperature constant (transient in Figure 25)

This condition of ice-liquid-vapour coexistence (slush nitrogen) could not be achieved in practice in the sense that no ice was observed in liquid nitrogen and nitrogen ice apparently entirely melted into liquid. Although, the ice phase was no longer present when sample was submerged, no boiling was observed around the sample, the temperature of the system was cold enough to avoid evaporation. In other words, although the temperature increases because of the heat that has been supplied by the sample (no more ice was present to dissipate the supplied energy), the temperature was still less than -195 °C (point A has not been reached). Thus no boiling was generated.
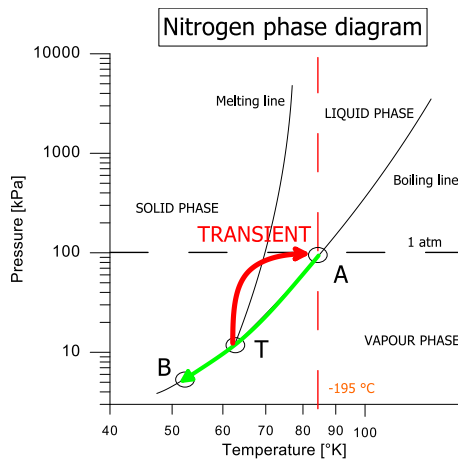
Figure 25: Nitrogen phase diagram in water freezing process

Nitrogen-isopentane technique

Freezing technique using isopentane has been widely used by the scientific community because isopentane melting point is easily reachable. Melting point of isopentane (-159 °C) is reached by submerging a metallic reservoir of about 100 ml of liquid isopentane in a dewar of liquid nitrogen (-195 °C). After immersion, the isopentane starts freezing from reservoir walls to the centre. When all the isopentane but a small area in the middle is frozen, a piece of soil (1cc) is submerged for a purposeful time.

Figure 26 shows the phase diagram of isopentane during the freezing procedure. Isopentane boiling point at environmental pressure (1 atm) is at about 301 °K (28 °C). At a room temperature of 20 °C and atmospheric pressure, isopentane is therefore in its liquid phase (point A in the figure). If isopentane is placed in liquid nitrogen, isopentane is cooled down (green arrow in the figure) until the melting line is reached (point C). At this stage, temperature remains constant until the liquid phase is entirely converted into ice. Because of the cooling action of nitrogen, energy is subtracted from the liquid isopentane, so ice isopentane will start to form. When the 'hot' soil sample is submerged into liquid isopentane at its freezing point (point C), sample will supply heat to the system, ice melts back to the liquid phase. As long as ice isopentane is still present in the system, temperature will remain at the freezing point and boiling is therefore avoided.
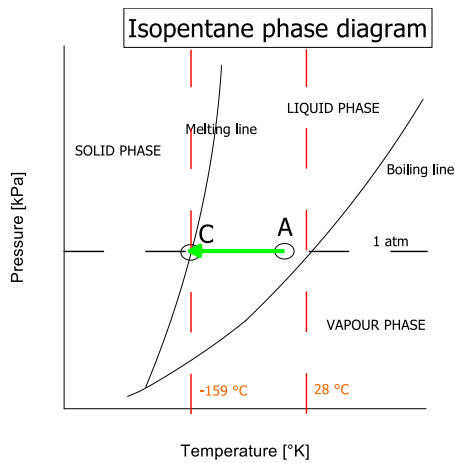
Figure 26:Isopentane phase diagram in water freezing process

Lyophilisation

In the lyophilisation process, the ice within the sample is removed by its direct conversion to vapour phase (sublimation), i.e. without passing through the liquid phase. Sublimation is an endothermic phase transition and it requires additional energy to be inputted. The sample therefore needs to be heated to allow ice phase change. When heat is added to the ice and temperature increases, sublimation from ice or evaporation from liquid can take place, depending on the pressure of the system at the phase transition. If the pressure is higher than the pressure at the triple point, the ice will meet the melting line first and then the evaporation line, eventually transforming into vapour (evaporation in Figure 27). In contrast, if the pressure is low enough (below the triple point pressure) the ice will meet the sublimation line and it will sublimate into vapour (sublimation in Figure 27). Accordingly, during the initial phase, the pressure should be reduced fast enough and heat should be supplied slow enough to maintain the system far from the melting line of the phase diagram.

Heat required for sublimation is supplied by conductivity of the metal shelf, where the sample is placed, and also by convection. To slow down the heating of the soil specimen, an iron disk of about 500 gr previously cooled in liquid nitrogen is placed in direct contact with the sample. Because the thermal capacity of the iron disk is significantly higher than the thermal capacity of the sample, the temperature of the specimen remains closer to the temperature of

the iron disk. To calculate the temperature variation of the iron disk, which is assumed to coincide with the temperature of the soil specimen, the three following simplifying assumptions were made:

- The metal is non-deformable and the thermal flux equals the rate of change of internal energy;

- The thermal flux due to the heat conduction is equal to zero, i.e. the thermal conductivity of iron is very high ($k\rightarrow\infty$), which means no ΔT in radial direction.;

- The heat transfer coefficient, h, is constant and independent of the temperature difference between the iron disk and the environment.
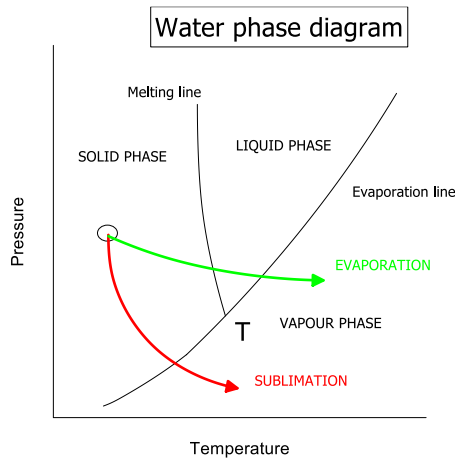
Figure 27: Water phase diagram

Under these assumptions, a solution of the Newton's cooling law can be derived as shown in Equation 14. This equation gives the evolution of temperature T as a function of time т, where L is the height of the iron cylinder, c_p is the specific heat capacity at constant pressure, and h is the heat transfer coefficient, which has been back-calculated from two known data points.

$$T(\tau) = T_{enviromental} + (T_{initial} - T_{enviromental})e^{-\frac{h}{c_p \rho L}\tau} \qquad [14]$$

The path of the sample in terms of temperature and pressure from the freezing point to lyophilisation was then calculated and is shown in Figure 28. The initial plateau corresponds to the time required to move samples from the nitrogen to the freeze dryer. It can be seen that the estimated cooling path remains far from the melting line. This gave reasonable confidence that phase transition to vapour phase was achieved without any intermediate transition to liquid phase.
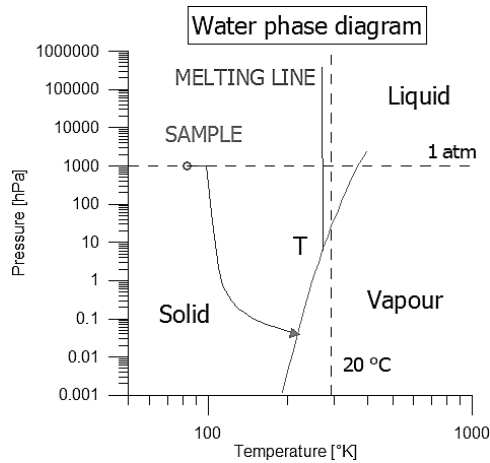
Figure 28: Lyophilisation path

2.3.2 Mercury intrusion porosimetry: errors in volume measurement

Mercury intrusion porosimetry has been carried out using a Poremaster–60 produced by Quantachrome Instruments. The machine is designed to intrude pore diameters in the range from 1000 to 0.007 µm corresponding to an intrusion pressure from 1.5 kPa to 420 MPa respectively. For pressures up to 340 kPa the machine operates on a different station than for higher pressures, those stations are called the low pressure station and the high pressure station respectively. The porosimetry output raw data consists of the cumulative intruded volume, V_i and the corresponding pressure applied, P_i . To derive cumulative pore-size distribution in terms of volume intruded per unit volume of solids versus pore entrance diameter, the following parameters have been adopted:

- Mercury surface tension, γ=0. 484 N/m (Diamond, 1970)

- Mercury-kaolin contact angle, θ=147° (Diamond, 1970)

- Specific gravity of the kaolin, G_s=2605 g/cm³ (Tarantino & De Col, 2008)

Error associated with volume transducer accuracy

A capillary stem is used in the porosimeter to measure the volume of mercury intruded into the pore space of the soil specimen. The capillary stem is made of glass (an electrical insulator) and is filled with mercury (an electrical conductor) whereas the outer surface of the capillary stem is plated with metal (again an electrical conductor). The combination of two concentric electrical conductors separated by an insulator produces a co-axial capacitor, whose capacitance is controlled by the level of mercury in the capillary stem. In the porosimeter, the capacitance of the stem is monitored by a capacitance detector that produces an electrical signal that is proportional to capacitance. Capacitance measurement is related to mercury level via the stem diameter and the equation governing coaxial capacitors. The ratio between the mercury volume change and voltage is called the penetrometer constant and is assessed by calibration.
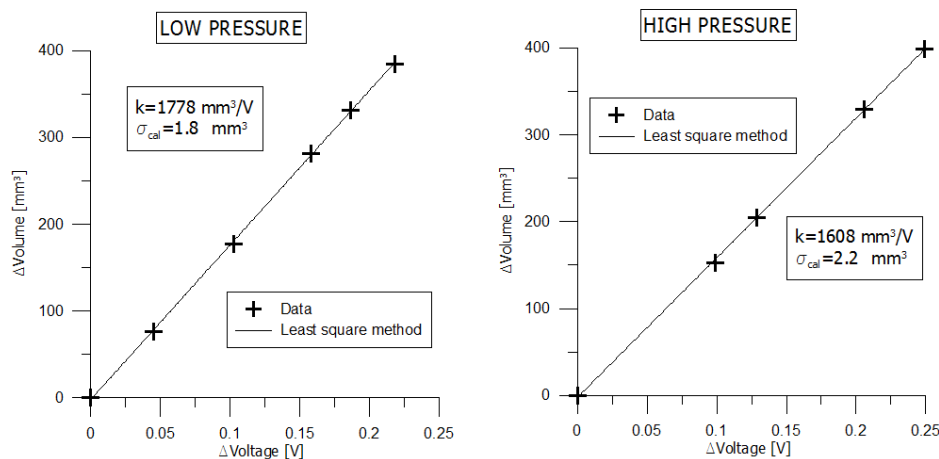
Figure 29: Porosimeter calibration data

The calibration of the penetrometer constant was carried out with 11 readings of the level of the mercury in the stem (6 in the low pressure station

and 5 in the high pressure station) by means of a ruler with an accuracy equal to ±0.5 mm as suggested by the manufacturer.

Figure 29 shows the mercury volume change in the capillary stem against the electrical signal related to the capacitance. The penetrometer constant is the slope of the calibration curve, that was assumed to be linear. The standard deviation of the error, σ_{cal}, is then defined as the square root of the variance (Equation 15), where the variance is the average squared deviation of each Δ_{VOLUME} measured with respect to the $\hat{\Delta}_{VOLUME}$ estimated via the calibration constant. The total standard deviation of the errors, considering low pressure data and high pressure data all together, was estimated equal to 2.0 mm^3.

$$\sigma = \sqrt{\frac{\sum_{i=1}^{N}(\Delta_{VOLUME_i} - \hat{\Delta}_{VOLUME_i})^2}{N}} \qquad [15]$$

Error associated with rate of mercury intrusion

Work is inputted during pressure increase and part of that work is dissipated as the system heats. The increase in temperature causes the mercury density to decrease in turn causing an apparent (negative) volume intruded into the stem. The higher the rate of mercury intrusion, the higher is the heat dissipated and, hence, the apparent spurious change in volume.
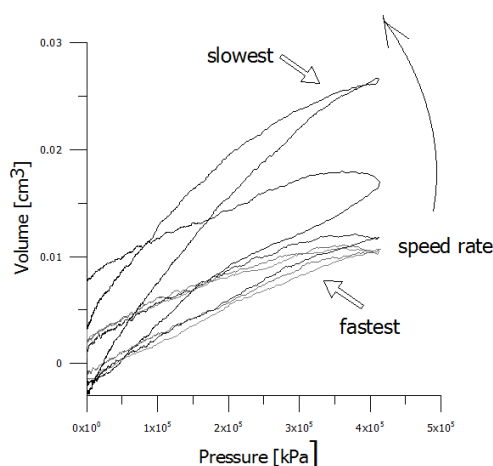
Figure 30: Different speed ratios

Several blank tests (test without sample) were therefore carried out to investigate the effects of the rate of mercury intrusion (Figure 30). As mentioned above, the test showing a higher intruded volume is the slowest one, characterised by the lower change in density due to heat dissipation.

Error associated with compressibility of the system

Errors caused by cell compressibility and mercury compressibility also affect the measurement of the intruded volume. Both cell and mercury volume change depends on the value of the pressure applied. Indeed, the greater the pressure, the larger is the effect of system compliance. Errors linked to compressibility will result in an additional apparent (positive) volume intruded during the test. This error was taken into account by performing a blank test.

Regarding sample compressibility, no effect should be seen if all the pores were intruded instantaneously (effective stress would not change). However, a small amount of pores within the sample are inaccessible to mercury and are not intruded. As a result, some (unknown) compression of the soil specimen may occur.

Blank test (to assess spurious changes in intruded volume)

Results of the blank test are a series of measured volume changes that can also be expected to occur during actual intrusion/extrusion of mercury in/from the soil sample. The blank test can either return an apparent intrusion (compressibility of the system is dominant) or an apparent extrusion of mercury (temperature effects are dominant). To check the reliability of the blank test, the correction is applied to a test that had been carried out without any sample (Figure 31). The average error related with the accuracy of the correction applied is ± 2.5 mm^3. The volume intruded should be equal to zero after applying the correction. And it represents the accuracy associated with the correction.

In conclusion by adding the errors from calibration analysis and from the blank test an error of about 4.5 mm^3 in the measurement of the intruded void volume was assessed.
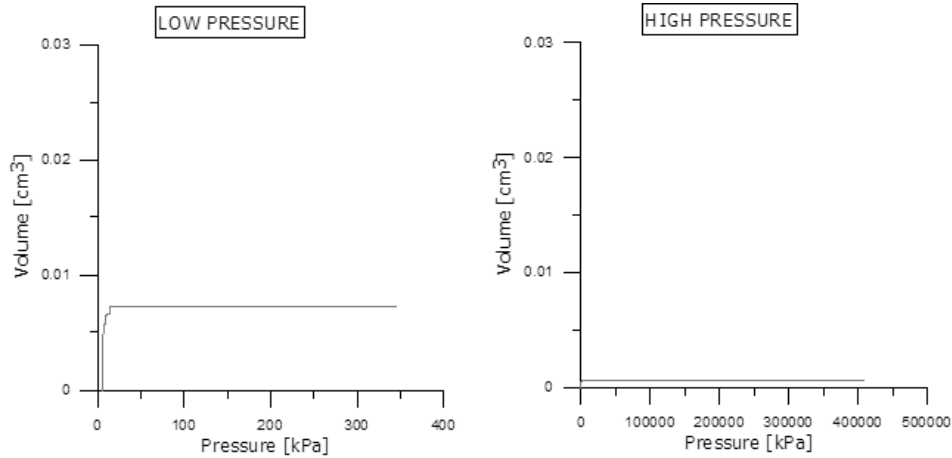
Figure 31: Blank test corrections

Combined error in the estimation of intruded void ratio

The mercury intruded volume, V_v, has been made dimensionless by referring it to the volume of solids, V_s. The value of void ratio (V_v/V_s), e_{MIP}, estimated by the porosimetry, can be directly compared with the void ratio determined in a traditional way by measuring dry mass and total volume.

The void ratio of the specimen is calculated as shown in equation 16, where G_s is the specific gravity of the clay, V_v is the volume intruded, and M_s is the mass of the dehydrated specimen.

$$e = \frac{V_V}{V_S} = \frac{V_V}{(M_s/G_S)} = \frac{V_V}{M_s} G_S \qquad [16]$$

The error associated with the void ratio measurement can be calculated by differentiating Equation 16 as shown in Equation 17, where dV is the error in the volume measurement associated with the porosimeter, reported in the previous page ($dV \sim 4.5$ mm^3), and dM_s is the error associated with the balance accuracy (less than 10 mg for class I balances).

$$de = \left(\frac{G_S}{M_s}\right) dV + \left(\frac{V_V}{M_s^2} G_S\right) dM_s = \left(\frac{G_S}{M_s}\right) dV + e \frac{dM_s}{M_s} \qquad [17]$$

By using Equation 17, and assuming a nominal mass of solids M_s=0.3 g and a nominal void ratio e= 1.2 an average value of the error made during the porosimetry test was estimated to be Δe= $\pm$0.043 less than 3.6% of the amount of the measurement.

Error associated with the adopted freeze-drying technique

Two different freezing techniques were shown. In Figure 32 the cumulative trend of the void ratio of two identical samples dehydrated respectively by means of nitrogen-isopentane and slush nitrogen freeze-drying technique are compared. The difference between the two measured void ratios was shown to be within the estimated error of the test itself. Both dehydration techniques can be considered satisfactory.
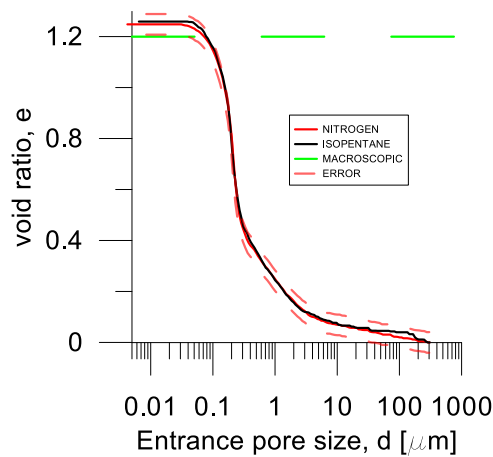
Figure 32: Comparison of different freezing techniques

2.4 Numerical model

The numerical model was mainly developed to understand, interpret or validate assumption made when interpreting MIP data. Pore size distribution obtained from MIP analyses is known to be affected by several factors (e.g. ink-bottle). A numerical model could be an interesting tool to investigated the difference between a given pore size distribution and the one obtain upon MIP. Furthermore, upon mercury extrusion, the volume of mercury that remains entrapped has been associated with the volume of intra-aggregate porosity in compacted soils. A numerical model could be used to support or not such assumption. Indeed, it could be used to simulate the intrusion and extrusion of a given bi-modal pore size distribution resulting from an aggregated microstructure and the simulated volume of entrapped mercury investigated. Finally, a second intrusion has sometimes been used to investigate the micro-porosity of bi-modal pore size distribution. A numerical simulation could help to understand which information is possible to infer from the different volume intruded between the first and the second intrusion.

As a result, attention was paid to the modelling of hysteresis and mercury entrapment.

Mercury is trapped where snap-off occurs and where blobs of mercury become disconnected and isolated from the rest of the mercury. Snap-off is facilitated when individual pores have a large pore to throat size ratio and, on a larger scale, when domains of a large pores occur as isolated regions surrounded by smaller pores (Wardlaw & McKellar, 1981).For a single sample, the amount of trapped mercury is affected more by the pore-throat ratio and by the non-random distribution than the coordination number (Wardlaw & McKellar, 1981).

The hysteresis between the first intrusion and the extrusion curves is due to 3 different factors:

- Contact angle hysteresis
- Ink bottle effect and interconnected pores

- Snap-off

During a second (or subsequent) intrusion, mercury, that is present in the sample, at a specific pressure, can be considered as being distributed in two different ways. There is the mercury that occurs as connected, which increases as pressure is increased, and there is the disconnected (trapped) mercury. This mercury resides in spaces that have not been reinvaded at the pressure in question because of the small size of the connecting throats.

Moreover, between the second (or subsequent) intrusion and the extrusion curves the differences in terms of diameters are due to the contact angle hysteresis and the ink-bottle effects. The ink bottle effect causes an underestimation of the volume for a given diameter during intrusion and an overestimation during extrusion.

The differences between the second (or subsequent) intrusion and the first intrusion curves are due to the trapped mercury caused by snap-off. Hence the differences between the two curves are in somehow related with the pore/throats ratio and the non-random distribution of pores.

The first intrusion mercury gives the amount of the connected pores for a given pressure, but with an underestimation of the volume because of the ink-bottle effects.

2.4.1 Conceptual model

Pore volume

Pores have been assumed to have a cylindrical symmetry with different sizes. The volume, v_j, of each pore has been considered to be proportional to its diameter d_j, its length l_j and a shape factor C_j (Figure 33a):

$$v_j = C_j l_j d_j \qquad [18]$$

Each diameter class, *i*, is identified by the diameter, d_i, defined as the mean value between the lower and the higher diameters belonging that class. By considering the class small enough to assume that the difference between the

mean diameter, d_i, and the pore diameter, d_j, is negligible it is possible to adopt $d_i \cong \frac{\sum_{j=1}^{n} d_j}{n_i}$ within the same class

Then, by considering a class i with n_i pores of mean diameter equal to d_i, the total volume ΔV_i related to that class has been defined as:

$$\Delta V_i = \sum_{j=1}^{n} v_j = \sum_{j=1}^{n} (C_j l_j d_j) = C_i L_i n_i d_i \qquad [19]$$

where $C_i = \sum_{j=1}^{n} C_j$ and $L_i = \sum_{j=1}^{n} l_j$. Hence ΔV_i in each class is considered to be proportional to the mean diameter d_i and a constant value A_i that includes the number, the total length L_i and the shape factor of the pores C_i of that class:

$$\Delta V_i = A_i d_i \qquad [20]$$
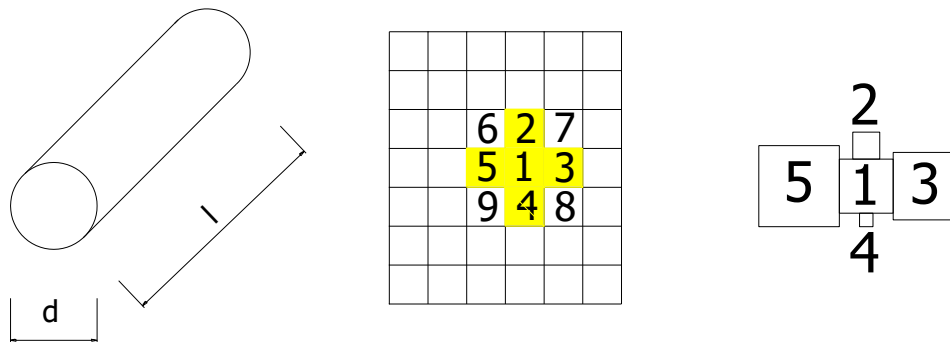
a) *Ideal pore*   b) *Matrix of pores*   c) *Pore cordination*

Figure 33. Pore conceptual model

Pore coordination

Despite the threshold value of intrusion/extrusion has been calculated by the Washburn equation, the network does not stand under the Washburn hypothesis of non-intersecting cylindrical pores. According to the site percolation model the system has been assumed as a network of intersecting pores, by considering a two-dimensional square mesh of pores, where each pore results to be connected with four other pores (Figure 33b). Under such

assumption, pore 1 is connected to pore 2,3,4 and 5, but is not connected to pore 6,7,8 and 9.

Pore sizes

In a porous material, pores are usually modelled as a system of pore bodies and pore throats. In the model, pores have been assumed with different sizes in order to simulate the existence of pore bodies and the existence of pore throats. In this way each pore can be considered as a throat of a bigger connected pore, or as a body of a smaller connected one (Figure 33c). Pore 1 will act as throat for pore 5 and 3 but as body when compared to pore 2 and 4.

Pore threshold value

The threshold value of intrusion (or extrusion) has been calculated according to the Washburn equation (equation 13) for a cylindrical pore, where γ is the mercury surface tension and ϴ the advancing (or receding) angle. Once that the threshold value has been overcome the intrusion (or extrusion) of the pore is instantaneous, regardless the pore length.

$$P = -\frac{4 \cdot \gamma \cdot \cos\theta}{d} \tag{21}$$

Snap-off

During mercury porosimetry, despite vacuum is applied, air still resides in the system cavities and imperfections. When the external pressure decreases, the mercury menisci that occupy pore wall roughness features begin to retract. This, eventually, leads to the formation of collars around various mercury threads occupying long and narrow pores. When a thread surface becomes unstable the mercury thread collapses and the snap-off occurs. The condition sine qua non for snap-off to occur is to have air entrapped in the system. Using a simplified model, as it is, the presence of air can hardly be modelled. Thus, in the model, the snap-off has been caused by leaving a certain amount of unsaturated pores around the system, with an intrusion pressure higher than the maximum applied pressure during intrusion. Of course the effects of the

sorting and the amount of the unsaturated pores will affect the response of the model and a further investigation will be required.

Consequently, extrusion will occur in a saturated pore not only if the threshold value has been overcome but if the pore has at least one meniscus (it must be connected at least to an unsaturated pore) and if the pore still has a continuous mercury path to the exterior.

Intrusion, on the other side, occurs when the threshold value has been overcome in an unsaturated pore that, again, is connected to the exterior through a continuous mercury path.

Additional energy is required to create new menisci. Pore de-saturation requires less energy if the pore is connected with only one de-saturated pore than if it is connected with two or three, because less menisci need to be created. In the model this effect has not been considered, thus no hierarchy between pores of the same size has been implemented.

Pore sorting

The pore sorting can be made both randomly and non-randomly.

2.4.2 Development of the numerical model

Model parameters

$s \rightarrow$ number of pore classes

$n \rightarrow$ dimension of the square mesh of pores (nxn)

$l \rightarrow$ number of intrusion/extrusion steps

$\gamma \rightarrow$ mercury surface tension [N/m]

$\Theta_i, \Theta_e \rightarrow$ intrusion and extrusion contact angle [rad]

Pores size distribution and random pore sorting

For a given pore size distribution, in terms of cumulative intruded volume and respective pore diameters, the code creates a new array of diameters, $d\_eq_{S,1}$, that are equi-spaced in a logarithmic scale. For each new computed

interval of diameter, the code calculates the respective cumulative volume, $V_{S,1}$, through a linear interpolation between the two closer input volume values. For each diameter interval the incremental volume, $\Delta V_{S,1}$, and the mean diameter $d_{S,1}$ is then computed.

A matrix $R_{n,n}$ has been created with random values between the maximum and the minimum value of $V_{S,1}$. Then a matrix $K_{n,n}$ has been created, where, according to the input pore size distribution, each value has been calculated as the respective diameters of the $R_{n,n}$ volumes.

According to equation 20 the array A_S, has been created. The elements of the array are the constant factors that relates each input diameter, $d\_eq_{S,1}$, with its volume, $V_{S,1}$. For each class I, the constant factor A_i is defined as shown in equation 22:

$$A_i = \frac{\Delta V_i}{d_i} \qquad [22]$$

To compute the volume related to each pore of the new distribution $K_{n,n}$ a new array, A_new_S, has been created. It is defined as the ratio between A_S, and the absolute frequency of the diameters, f_i, belonging to one class, as shown in equation 23:

$$A\_new_i = \frac{A_i}{f_i} \qquad [23]$$

In this way the values of *A_new* do not include any dependency on the number of the pores, but they depend only on the length and the shape of pores.

Simulation tools

A matrix $P\_ent_{n,n}$ and a matrix $P\_rec_{n,n}$, has been created, with the threshold value of intrusion and extrusion, respectively, per each diameter of the related matrix $K_{n,n}$.

Three new matrixes $Saturation_{n,n}$, $Desaturation_{n,n}$ and $Saturation2_{n,n}$ have been created in order to indicate the pressure step at which each pore saturates, de-saturates and re-saturates.

Finally to manage the intrusion and extrusion problem a new matrix $L_{n,n}$ has been created. At each step of intrusion and extrusion, that matrix indicates the condition (saturated or unsaturated) of the respective pore of the matrix $K_{n,n}$.

Intrusion process

For each step z of intrusion pressure the system scans the pores i,j of the matrix K, looking for the pores that satisfy the following conditions:

- $L_{ij}=0$ (unsaturated pore)

- The pore i,j is connected at least with one saturated pore, or lies on the borders

- $P\_ent_{ij}<$pressure of intrusion at the z step.

If such conditions result satisfied L_{ij} turns to 1 (saturated pore) and the element $Saturation_{ij}$ records the z step. At each step z of intruded pressure, the system keeps scanning all the K_{ij} elements as long as no more pores saturate. When in two following iterations the number of new saturated pores is zero the intrusion pressure is increased and the iteration of the pore scanning starts again for a new z step of intrusion pressure.

In Figure 34 a possible intrusion configuration for a given step z is reported. Asses that pore 1 is unsaturated, the system checks whether pore 1 is connected to a saturated pore (pore 3 in Figure 34) and whether the intrusion pressure of pore 1 is lower than the injection pressure at step z, then it will saturate the pore.

On the other hand, the system will not saturate pore 2 because, although it is unsaturated, it is not connected to any saturated pores.
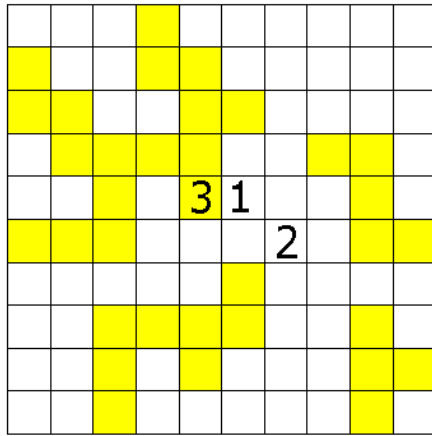
Figure 34. Intrusion process. Saturated pores reported full

Extrusion process

For extrusion process, the biggest issue is to check if the pore is connected to the exterior through a continuous path of mercury. To solve the problem a function to solve mazes has been implemented. As output for each step of the iteration the maze-solver function returns which pore is connected and which is not. Then for each step z of extrusion pressure the system scans the pores i,j of the matrix K, looking for the pores that satisfy the following conditions:

- $L_{ij}=1$ (saturated pore)

- The pore i,j is connected at least with one unsaturated pore

- The pore i,j is connected to the exterior through a continuous path of mercury (output of the maze-solver function)

- P_rec$_{ij}$>pressure of extrusion at the z step.

If such conditions result satisfied L_{ij} turns to 0 (unsaturated pore) and the element Desaturation$_{ij}$ records the z step. At each step z of intruded pressure, the system keeps scanning all the K_{ij} elements as long as no more pores de-saturate. When in two following iterations the number of new unsaturated pores is zero the extrusion pressure is decreased and the iteration of the pore scanning starts again for a new z step of extrusion pressure.
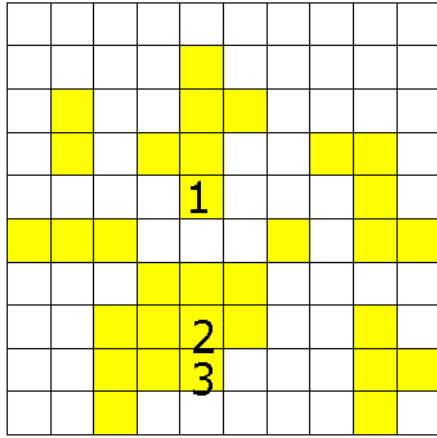
Figure 35. Extrusion process. Saturated pores reported full.

In Figure 35 a possible intrusion configuration for a give step z is reported. Asses the pore 1, 2 and 3 are saturated, the system checks whether each pore is connected at least to an unsaturated pore and whether is connected to the exterior through a continuous path. Pore 1 is not connected to the exterior through a continuous path and pore 2 is not connected to any unsaturated path. Therefore, none of the 2 pores will be extruded. On the other hand, pore 3 is saturated, connected to at least one unsaturated pore and connected through a continuous path to the exterior. The system will check if the extrusion pressure of pore 3 is higher than the external pressure at step z, and in case it will desaturate the pore.

Second intrusion process

During 2nd-intrusion one pore to re-saturate needs to be connected through a continuous path of mercury to the exterior. Also in the 2nd-intrusion process the maze-solver function has been used. Then for each step *z* of 2nd-intrusion pressure the system scans the pores i,j of the matrix K, looking for the pores that satisfy the following conditions:

- $L_{ij}=0$ (unsaturated pore)

- The pore i,j is connected to the exterior through a continuous path of mercury (output of the maze-solver function)

- P_ent_{ij}<pressure of 2nd-intrusion at the z step.

If such conditions result satisfied L_{ij} turns to 1 (saturated pore) and the element Saturation2$_{ij}$ records the z step. At each step z of 2nd- intruded pressure the system keeps scanning all the K_{ij} elements as long as no more pores saturate. When in two following iterations the number of new saturated pores is zero the 2nd-intrusion pressure is increased and the iteration of the pore scanning starts again for a new z step of 2nd- intrusion pressure.

2.5 Conclusions

In this chapter the procedure for sample preparation for MIP test have been tested. Two different techniques of freeze-drying have been compared on saturated samples of kaolin clay. The results in terms of water expansion were comparable and the one using isopentane has been chosen as the freeze-drying technique for this research work, because of it is easier to put in practice.

In the case of saturated samples some expansion of the volume of voids has been found. Such problem is not generally reported in the traditional literature but has been found consistent with some published data (e.g. Delage & Lefebvre (1984). Expansion disappears where the freeze sample is partially saturated.

Errors due to accuracy of the transducer and test procedure have been evaluated and found to be negligible when compared with the repeatability of the sample itself.

Different conceptual models of intrusion have been presented. Since none of them has been tested with the numerical code proposed, the data interpretation of the MIP tests will be carried out in the more traditional way, taking into consideration only the first intrusion and assuming the pores in the sample as cylindrical.

Chapter 3. A micromechanical conceptual model for non-active clays

3.1 Introduction

The aim of this chapter is to develop a conceptual micromechanical model for non-active clays to lay the basis for discrete element modelling of clays.

The key step is to recognise the mechanical and electro-chemical inter-particle forces governing the behaviour of the clay particle assembly. Previous work on clay suspension has shown that the charge of the particle edge plays a crucial role in controlling particle arrangement and rheology of the suspensions. It would therefore be reasonable to assume that edge charge plays similar role in consolidated clays. Studies on clay suspensions have also highlighted the role played by the Coulombian interactions and similar effects would be expected in consolidated clay.

The approach to investigate edge charge and Coulombian interaction effects was designed as follows:

i) compare the 1-D mechanical response of clays with active (positive) and de-activated (negative) edge charge and of clays with stronger or weaker Coulombian interactions;

ii) compare microstructure and its evolution along loading and unloading paths using MIP;

iii) formulate assumptions about particle interactions and particle configurations controlling the macroscopic response of the clay.

Special attention was paid to reversible and non-reversible compression mechanisms, i.e. the evolution of the pore size distribution of samples lying on the normal consolidation and the unloading-reloading line at the same level of stress.

This experimental investigation is instrumental in the formulation of a micro-mechanical conceptual model. To demonstrate the potential of the conceptual model to be used as a basis for DEM formulations, an 'embryonic' DEM model has been developed to test its capability to reproduce, at a qualitative level, major features of the response of clays in 1-D compression.

3.2 Electrochemistry of kaolin clay particles

3.2.1 Electrical charges on kaolin surface

As highlighted in the literature review chapter, charges on kaolin surface are the result of permanent charges (isomorphic substitution on particle faces) and pH-dependent charges (protonation or deprotonation of hydroxyl groups of edges). The overall surface charge on the basal planes is always considered to be negative (Wang & Siu, 2006) because of the isomorphic substitution, but its magnitude is pH-dependent. Unlike the face, the sign of edge charge is pH-dependent.

The point of zero charge of the edges (PZC) for kaolin is placed between pH values of 5 and 6. Accordingly, the edges of kaolinite particles become positively charged when kaolin is mixed with acidic solutions and negatively charged when kaolin is mixed with alkaline solutions. Neutralization of positive edges in alkaline solutions occurs because of deprotonation of the edges, where hydroxyl anions (OH^-) are present. Sodium-hexametaphosphate is also known to be a very efficient dispersant for clay solutions because of the high negative charge of polyphosphate anions. When sodium hexametaphosphate, $(NaPO_3)_6$, is added to clay solutions, the neutralization of the positive broken edges is due to the polyphosphate anions (Andreola et al., 2004, Choi et al., 1993) with the same mechanism described for hydroxyl anions.
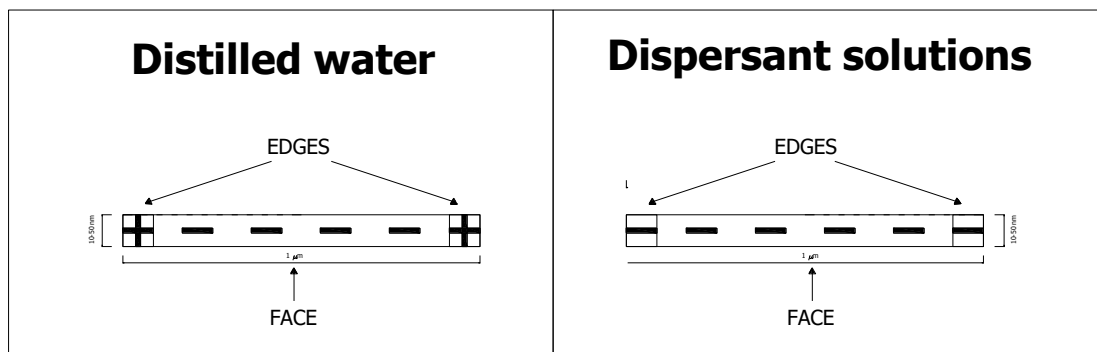
Figure 36. Surface electrical charge on kaolin particles

In general, when kaolin clay powder is mixed with distilled water, an acid reaction occurs. The pH of the suspension (kaolin + distilled water) drops form values of about 7 to values below 5. Therefore kaolinite in suspension with distilled water is usually associated with suspensions of kaolin in acidic solutions. On the other side, when kaolin is mixed with alkaline solutions (solutions of KOH or NaOH) or with dispersant solutions (($NaPO_3$)$_6$), particles edges become negatively charged (Figure 36).

3.2.2 Interparticle electrochemical interactions in kaolin suspensions

As defined by Van Olphen (1977), the "net potential curve of particle interaction is constructed simply by adding the attractive and the repulsive potential at each particle distance, considering the attractive potential negative and the repulsive potential positive". The forces involved in such particulate suspension are generally assumed to be Van der Waals forces, Coulombian interactions between particle charges and hydration forces. According to Van Olphen (1977), in hydrophobic suspensions as clay suspensions are, the hydration forces can be significant only up to a few molecules of water from the particle surface when compared to Van der Waals forces. Because of that, hydration forces are generally considered to be negligible. Interaction between clay particles in suspension is generally explained by the balance between Coulombian interactions (which may be either attractive or repulsive) and Van der Waals attraction. This theory is often referred to as DLVO theory (Derjaguin & Landau, 1941, Verwey et al., 1948).

Coulomb interaction between particle surfaces depends on the electric field generated by the particle charges. The interaction can be attractive if the surfaces are charged with opposite sign or repulsive if the sign of the charges is the same. For clays suspensions, the Coulombian interaction is computed using the double layer theory, which takes into account the electric charges distribution of the ions dissolved in an electrolyte solution. An extended presentation on how to compute the Coulombian interaction between two parallel surfaces is shown in appendix A.

In general, Coulombian interaction forces depend on the dielectric constant of the pore fluid, the electrolyte concentration, and the particle distance.

Particles are considered to interact in two different modes (Figure 37):

i)   Face-to-face interaction: The forces involved in this interaction are Coulombian repulsion (clay faces are always negative regardless the pH of the suspension) and Van der Waals attraction. In an electrolyte-free suspension, Coulombian repulsion is always greater than Van der Waals attraction, and therefore the nature of the face-to-face interaction is always repulsive.

ii)   Edge-to-face interaction. The forces involved in this interaction are Coulombian attraction between the negative clay faces and the positive edges (edges are positive charged as long as the solution is not alkaline or any dispersant is added), and Van der Waals attraction. Thus the nature of the edge-to-face interaction is attractive when kaolin is suspended in an acidic solution (or distilled water).

In an electrolyte free suspension, Van der Waals forces are considered to be relevant (compared to the Coulombian forces) only at distances smaller than 10-20 nm (Mitchell & Soga, 2005, Van Olphen, 1977). Therefore, particle distance is mainly controlled by the Coulombian interactions.
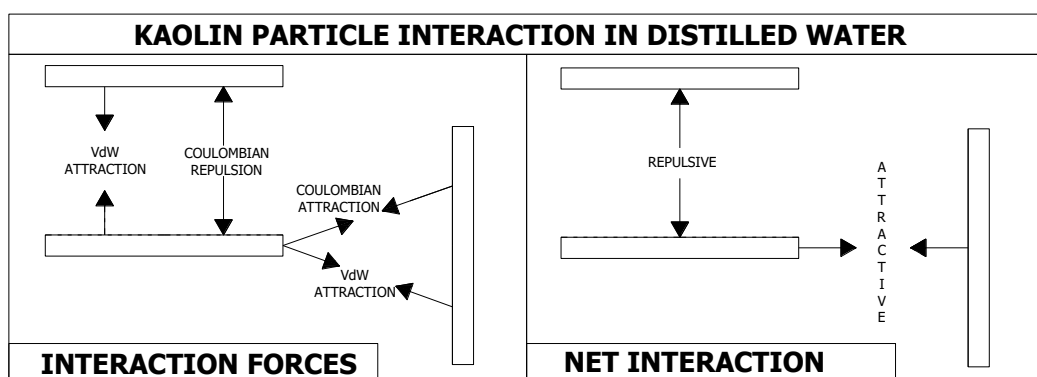
Figure 37. Electrochemical interaction forces of kaolin particles in distilled water

For the case where kaolin clay is mixed with alkaline solution (or dispersant), particle edges are negatively charged, as the particle faces. Therefore (Figure 38):

i) Face-to-face interaction is repulsive due to the net balance between the Coulombian repulsion and the Van der Waals attraction.

ii) Edge-to-face interaction is repulsive as well. In this case, since both faces and the edges of the particles are negatively charged, Coulombian interaction is repulsive in nature and therefore particles repel each other. As in the face-to-face interaction, as long as the electrolyte concentration of the solution is negligible, Coulombian repulsion overwhelms Van der Waals attraction, giving rise to a repulsive interaction.
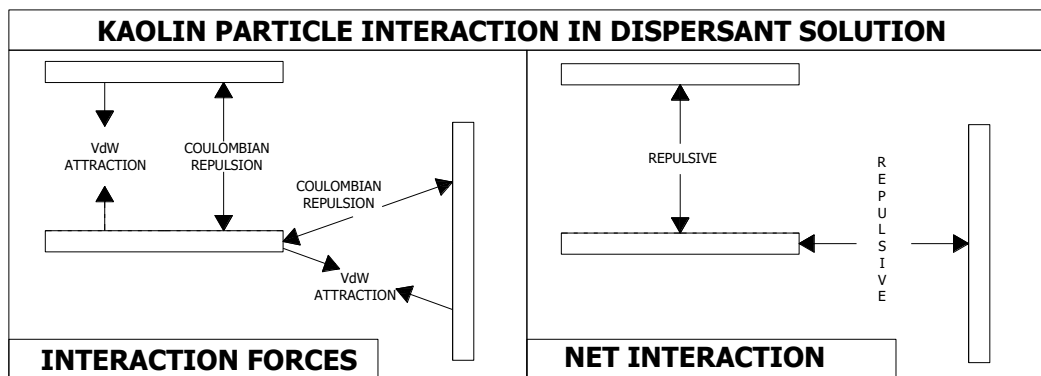
Figure 38. Electrochemical interaction forces of kaolin particles in dispersant solutions

3.3 Experimental investigation of edge charge effect on compression behaviour

3.3.1 Sediment final volume of kaolin suspensions with activated and de-activated edge-to-face attractive interaction

Figure 39 shows the final void ratio of kaolin clay at the end of a sedimentation test (Wang & Siu, 2006). It can be observed that the change in pH affects the response of the suspensions. Since the response changes at pH equal to the PZC value, such difference is usually associated with the change in the electrical charge of particle edges.
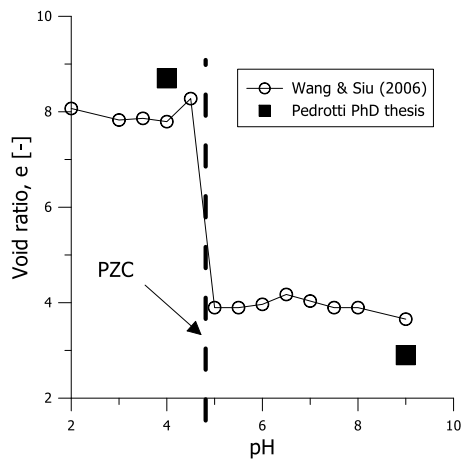
Figure 39. Final void ratio of kaolin suspension at different pH.

For the case of pH<pH_{PZC} (active edge-to-face attractive interaction), particle configuration is assumed to be dominated by the edge-to-face interactions, which lead to a very open structures (Figure 39). For the case of pH>pH_{PZC} (de-activated edge-to-face attractive interaction), non-contact interactions between dispersed sub-parallel particles lead to a closer particle configuration (Figure 39).

Typical colloidal problems involve suspensions characterised by clay fraction less than the 5% (weight of clay/weight of solution). On the other side, clays in soil mechanics problems are characterised by a clay fraction greater

than 100%. The question then arises as to whether pH values of the pore-water lower or higher than pH at the PZC give rise to the same step change in the mechanical response of 'consolidated' clays.

3.3.2 1-D consolidation of kaolin samples with activated and deactivated edge-to-face attractive interaction

One-dimensional compression tests on kaolin samples reconstituted from slurry were therefore carried out to investigate the role of edge-to-face attraction. To this end, kaolin samples were prepared with demineralised water and a dispersant (pH ~9), i.e with pore-water having pH lower and higher than the PZC. The dispersant modifies the charge of particle edge from positive to negative values, therefore 'deactivating' the edge-to-face attraction between clay particles.

Speswhite kaolin with plastic limit w_P=0.32 and liquid limit w_L=0.64 was chosen for the tests presented herein. The grain size distribution showed it to have 0.20 silt fraction and 0.80 clay fraction. Two different pore fluids were used for this set of experiment: i) distilled water and ii) dispersant solution. Distilled water was corrected to obtain a pH equal to 4 by adding few drops of very dilute solution of hydrochloric acid (HCl solution). The total concentration of hydrochloric salt (HCl) at the end of the preparation was always very small (less than 0.0001M). Separate sedimentation tests on kaolin clay mixed with an electrolyte solution of sodium chloride, NaCl, at different concentrations showed that the amount of Cl^- anions corresponding to a 0.0001M HCl solution has negligible effects on particle interactions.

A solution of potassium hydroxide (KOH) with a molar concentration smaller than 0.01 M was used as dispersant. Such amount of electrolyte was sufficient to raise the pH of a pore-water in the kaolin slurry (water content equal to 0.6) to values higher than 9. Potassium hydroxide in water dissociates in K^+ cations and OH- anions. The amount of K^+ cations introduced in the system via KOH is equivalent to the amount of Na^+ cations introduced by adding 0.01M of NaCl. Under the hypothesis that K^+ and Na^+ cations affect response of the

suspension in the same way (same hypothesis made by the DLVO theory), the introduced amount of K^+ cations can again be considered negligible.

In order to have the two samples starting from the same particle configuration, and therefore avoiding microstructural differences that may arise from different sample preparation, oven-dried kaolin clay was placed in the oedometer cell. After placing the oedometer cap on the kaolin powder (corresponding to a vertical pressure of about 1 kPa) the sample was fully saturated with one of the two solutions (distilled water or water with dispersant) and vertical displacements were monitored ("saturation" in Figure 40). After saturation, the two samples were loaded in steps up to 2220 kPa vertical stress and then unloaded in steps to 1 kPa. Samples were allowed to fully consolidate under each loading and unloading steps.

As vertical displacement was monitored during the test, the void ratio could be back-calculated at any stage of the test from the final water content measured at the end of the test.
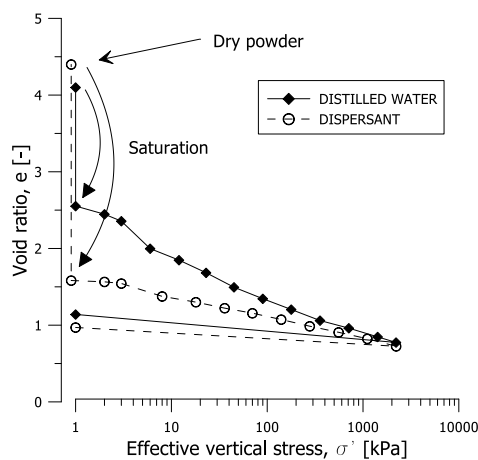
Figure 40. Mono-dimensional compression on kaolin mixed with water at different pH.

Figure 40 shows the 1-D consolidation of the sample saturated with distilled water and the sample saturated with dispersant solution. After saturation, an immediate volumetric collapse was recorded. However, the two samples showed a different amount of collapse. The dry kaolin had an initial void ratio

e higher than 4. After saturation with distilled water, the sample collapsed to a void ratio *e* of about 2.6 (incidentally, *e*=2.6 corresponds to a water content *w* equal to 1.00 in turn equal to $1.5w_L$) whereas the sample prepared with the dispersant collapsed to a void ratio of about 1.5. Upon loading, the sample saturated with distilled water showed it to be much more compressible whereas the sample saturated with dispersant showed an overconsolidated-like behaviour. At any given vertical stress, the sample prepared with distilled water always showed a more open structure than the sample prepared with dispersant. The difference in void ratio reduces with increasing vertical stress. At the maximum vertical stress (2220 kPa), the two samples show a similar void ratio and the swelling upon unloading appears to be very similar.

If the electrochemical interactions have an effect on the macroscopic behaviour of clays, such effect must be driven by a different microstructure (i.e. different particle arrangements and/or different interparticle forces). Observation of pore size distribution should therefore help understand the modes by which micromechanics controls macroscopic behaviour.

3.4 Microstructure of kaolin clay with active and deactivated edge-to-face attractive interaction

The pore-size distribution of samples prepared with distilled water and dispersant respectively and consolidated to two different vertical stresses and then unloaded was measured to investigate the role of edge-to-face attraction. Figure 41a and Figure 41b show the loading paths of the samples prepared with distilled water and dispersant tested for the MIP. After consolidation samples were dehydrated by the freeze drying technique, using liquid nitrogen and isopentane as described in chapter 2

| A) Sample prepared with distilled water | B) Samples prepared with dispersant |
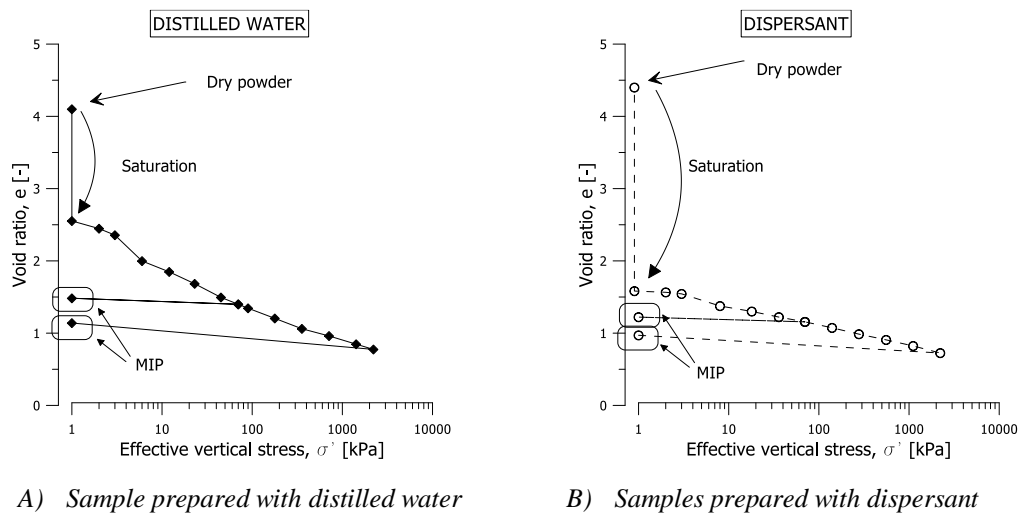
Figure 41. Sample preparation paths for mercury intrusion porosimetries (MIP)

Mercury intrusion porosimetry was carried out using a POREMASTER−60 produced by Quantachrome Instruments. The equipment is designed to measure pore entrance diameters in the range from about 1000 μm to 0.003 μm corresponding to 1.5-420000 kPa mercury intrusion pressure respectively. For pressure up to 340 kPa the machine operates on a station different from the one used for high pressures. These stations are called low pressure station and high pressure station respectively. The input parameters used for the interpretation of the test are as follows:

- Mercury surface tension, γ: 0.484 N/m (Diamond, 1970)
- Mercury-kaolin contact angle, θ:147° (Diamond, 1970)

- Specific gravity of the kaolin, G_s: 2,605 g/cm^3 (Tarantino & De Col, 2008)

Figure 42 shows the pore size distributions of the 4 samples highlighted in Figure 41. The samples prepared with demineralised water as pore fluid are named "water" whereas the samples prepared with the dispersant as pore fluid are named "dispersant". Two samples were compressed to 70 kPa and then unloaded (water-70url and dispersant-70url). Other two samples were compressed to 2220 kPa and then unloaded (water-2220url and dispersant-2220url). Sample reported in Figure 42 were named "url" since unloading was carried out under drained conditions and the samples therefore lied on the unloading-reloading line (url) at the end of the oedometer test.
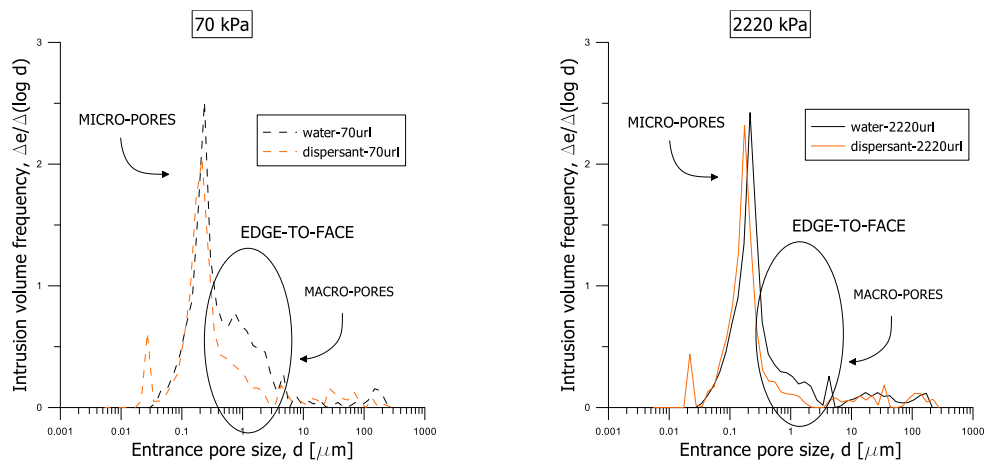
A) Pore size distribution of samples consolidated at 70 kpa.

B) Pore size distribution of samples consolidated at 2220 kpa.

Figure 42. Pore size distribution of consolidated kaolin saturated with distilled water and dispersant.

For the sake of completeness, it is worth noting the small peak at about 20 nm, in the two dispersant samples. Such peak is believed to be a random artefact of the MIP machine, which is made by a scatter of only one single point in the raw data, and not to be considered as an actual pore of the sample.

Key experimental finding no. 1:

Two different classes of pores can be identified in the pore size distribution, micro-pores (i.e. pores smaller than the modal value) and macro-pores (i.e. pores larger than the modal value)

No difference in the micro-pores distribution can be detected between the sample prepared with demineralised water and the one prepared with dispersant. On the other hand, macro-pores distribution is significantly different between the sample prepared with demineralised water and the one prepared with dispersant. For the case of sample prepared with dispersant, the macro-porosity almost disappears, indicating that such class of pores is the one controlled by the edge-to-face attractive interaction.

In summary:

$\Rightarrow$ Micro-pores: these pores are smaller than the modal value and are not controlled by the presence of the edge-to-face attraction

$\Rightarrow$ Macro-pores: these pores are greater than the modal value and are controlled by the presence of the edge-to-face attraction.

3.5 Microstructure of kaolin clay along reversible and non-reversible compression paths

3.5.1 Pore-size frequency distribution

Reconstituted kaolin from slurry was consolidated at 2 different vertical stresses 70 kPa and 2220 kPa. Slurry was prepared by mixing oven-dried kaolin with distilled water, at water content, w, equal to 1.00, which corresponds to $w=1.5w_L$. Before mixing the dried kaolin with distilled water, the pH of the distilled water was adjusted to 4, following the same procedure described in the previous section.

For each vertical stress (70 and 2220 kPa) two different samples were prepared, one lying on the normal consolidation line (ncl) and the other on the unloading-reloading line (url). For the ncl samples, once the desired vertical stress was attained, quick unloading was performed to generate undrained conditions. To achieve undrained conditions, the time over which load is removed should be significantly shorter than the time of consolidation. Because the time required for removing the load cannot be reduced beyond a certain limit, the time of consolidation was indeed increased by increasing the drainage length. To this end, a layer of para-film™ was placed at the bottom of the sample in order to seal the bottom porous stone. Since water flow was permitted only at the top of the sample, the drainage length could be doubled and the consolidation time then incremented by 4 times.

The undrained unloading consisted in one single step, from the higher vertical stress to 1kPa. For url samples a drained unloading was performed following the same procedure described in the previous section. Figure 43a shows the state of the samples removed from the oedometer and tested for MIP.

An additional series of samples consolidated to 70kPa, 178 kPa, 711 kPa and 2220 kPa were prepared. All samples were unloaded under drained conditions (url). The state of the samples is shown in Figure 43b. In Figure 43b

an additional sample called "slurry" is reported. Such sample was prepared from slurry and no vertical stress was applied.
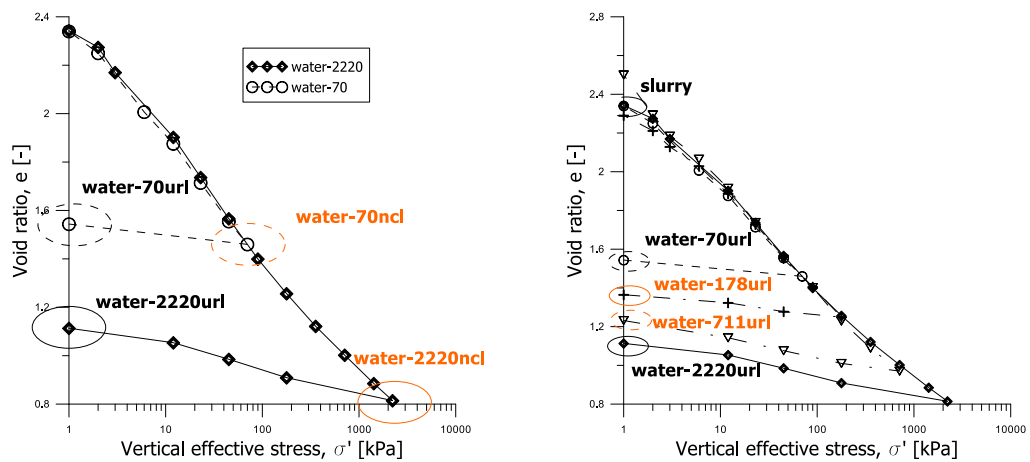
A) *Consolidation path for ncl and url kaolin samples at 70 and 2220 kpa.*

B) *Consolidation path for url kaolin samples at 70, 178, 711and 2220 kpa, plus slurry.*

Figure 43. Mono-dimensional compression on kaolin mixed with water. .Ellipses indicated samples tested in MIP

After removal from the oedometer, all samples were dehydrated by freeze-drying technique and an MIP test was performed, as described in the previous section. Figure 44 shows the pore size evolution upon unloading of samples consolidated to 70 kPa and 2220 kPa. It can be observed that the unloading does not change the shape of the pore size distribution. However, a clear shift rightward is observed upon unloading, i.e. the whole distribution shifts towards bigger pore diameter. This is observed for both the samples loaded to 70 kPa and 2220 kPa respectively

Figure 45 shows the pore size evolution associated with the accumulation of plastic deformation (samples have been all brought to 1 kPa after being pre-consolidated to different vertical stresses. Figure 45a shows clearly that the pore size distribution of the sample pre-consolidated to 70 kPa has the same micro-pores as the sample pre-consolidated to 2220 kPa. On the other hand,

the frequency of the macro-pores reduces significantly after the sample undergoes plastic deformation.
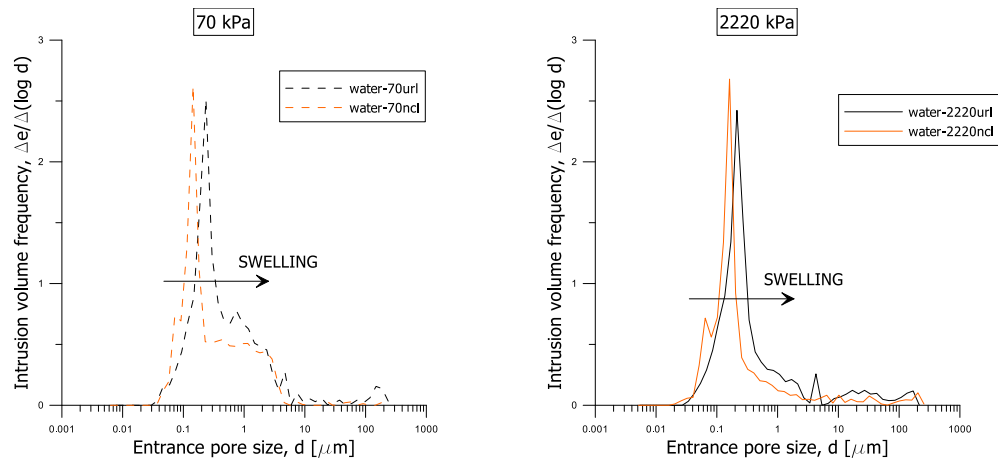
A) *Kaolin consolidated at 70 kpa (url and ncl)*

B) *Kaolin consolidated at 2220 kpa (url and ncl)*

Figure 44. Pore size evolution during swelling

Figure 45b just adds more samples to those shown in Figure 45a. Micro-pores remain the same for a range that goes from slurry (no load applied) to the maximum vertical stress of 2220 kPa. Again, the volume change associated with the yielding is clearly visible in the evolution of the macro-pores. The higher the consolidation stress the smaller is the frequency for a given macro-pore diameter.
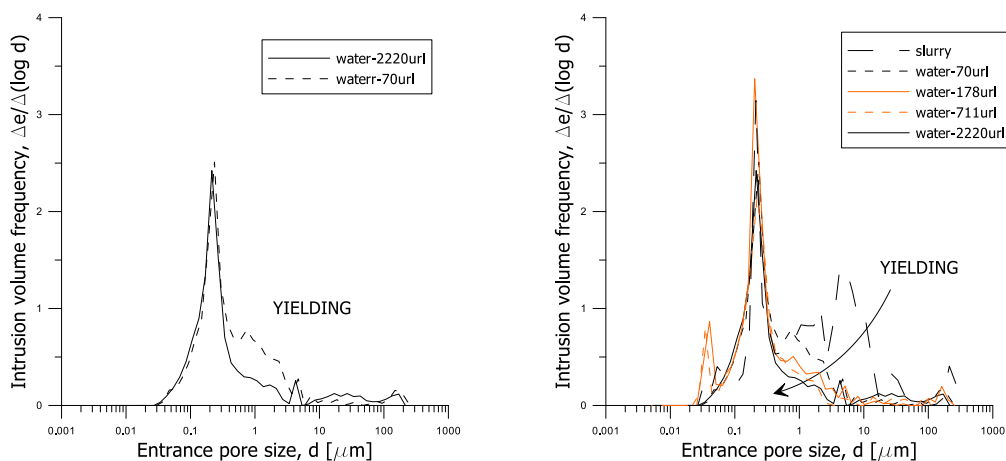
A) *Kaolin consolidated at 70 and 2220 kpa*

B) *Kaolin consolidated at different vertical stress*

Figure 45. Pore size evolution during consolidation at different maximum vertical stress.

3.5.2 **Pore-size cumulative distribution**

The evolution of the macro-pores upon loading and unloading can be better appreciated when the cumulative pore-size distribution is considered. Figure 46 shows the cumulative pore size distribution of the samples in Figure 45b. The total volume associated to the micro-pores remains essentially unaltered regardless of the vertical stress. On the other hand, starting from slurry, any increase in the vertical stress causes a reduction of the total volume associated with the macro-pores. Since all the samples lie on an url line at 1 kPa, any difference Δe in void ratio is associated with plastic deformation accumulated when moving from one pre-consolidation stress to another.
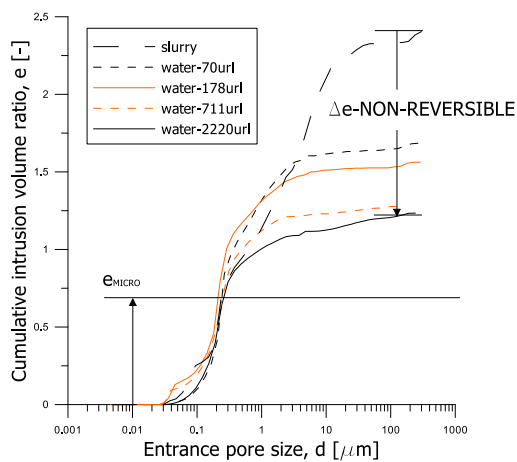
Figure 46 Cumulative pore size distribution for kaolin samples consolidated at different vertical stress

In order to visualize the class of pores responsible for reversible and non-reversible volume changes, it is convenient to compare the cumulative pore size distributions of three samples (Figure 47): 1) sample consolidated to 70 kPa and unloaded under drained conditions (water-70url), 2) sample consolidated to 2220 kPa and unloaded under undrained conditions (water-2220ncl) and 3) sample consolidated at 2220 kPa and unloaded under drained conditions (water-2220url). The state of the three samples is visualised at the bottom-right corner of Figure 47.

Change in volume between sample 1 and 2 is a sum of a reversible and non-reversible deformation (stress path is url+ncl). Change in volume between samples 2 and 3 is only associated with reversible deformation (stress path on url). Therefore, the change in volume between sample 1 and 3 is the non-reversible deformations accumulated between the two different pre-consolidation stresses.

Although reversible volume change (associated with the path 2-3) affects both micro-pores and macro-pores, it can be observed that the total reversible volume change is essentially dominated by the volume change of the macro-pores. As a first approximation, the reversible volume change can therefore be associated with the reversible volume change of the macro-pores.
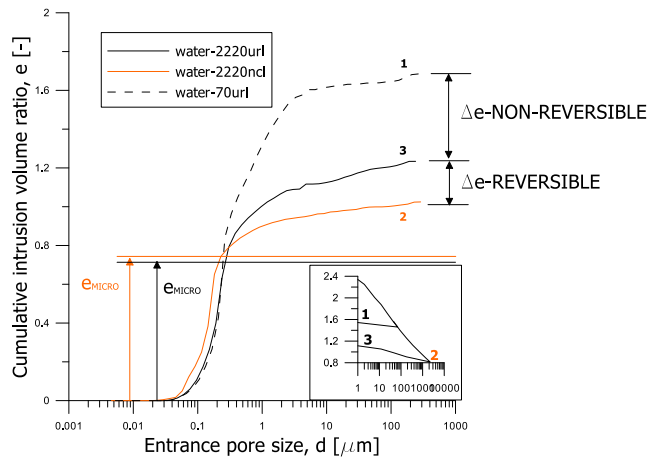
Figure 47 Cumulative pore size distribution for kaolin during an loading-unloading cycle.

3.5.3 Pore classes controlling reversible and non-reversible compression

Key experimental finding no. 2: reversible volume change

The reversible volume change involves the entire pore size distribution. According to Figure 44, samples moving along the url show a shift of the pore size distribution towards bigger pores. It should be noted that the reversible volume change is practically controlled by the volume change of the macro-

pores rather than the one of the micro-pores, the latter seems to be negligible quantitatively (Figure 47).

$\Rightarrow$ Reversible volume changes involve both micro-pores and macro-pores

Key experimental finding no. 3: non-reversible volume change

According to Figure 45 and Figure 46, micro-pores remain unaltered regardless of the different pre-consolidation stress attained. Only the volume associated with the macro-pores is reduced when plastic changes occur.

$\Rightarrow$ Non-reversible volume changes only involve the macro-pores

3.6 Micro-mechanical conceptual model for non-active clay

3.6.1 Particle configuration

In the tests described in Figure 40 and Figure 42, the mechanical macro-behaviour and the pore size distribution of samples with distilled water or dispersant as pore-fluid have been compared. Dispersant has been used in order to eliminate the positive charge of the particle edges and, hence, de-activate the edge-to-face attraction. Assuming that i) the permittivity of distilled water and water + dispersant are the same (and equal to the permittivity of water) and ii) the salt concentration in the water + dispersant is negligible as in the distilled water, the differences observed between the two samples have to be associated to the electrical charge of the edges.
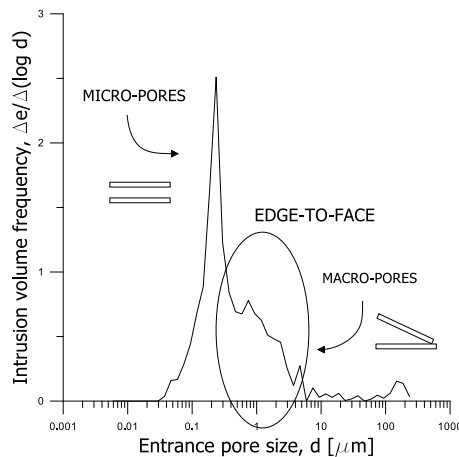
Figure 48. Pore size distribution and particle configuration in a kaolin clay sample

Positive edges are responsible of the edge-to-face attraction and, hence, responsible for a particle contact configuration. When the positive charge of the edges is turned into a negative one, the net interaction between edges and faces becomes repulsive. Therefore the only feasible particle configuration is a particle non-contact configuration since no attractive forces exist (Figure 48).

In a 2-D model a kaolin clay particle (Figure 49) could be considered as rectangular in shape. The particle length, according to the equivalent Stokes'

diameter calculated by sedimentation tests, would be about 1μm and the thickness would be of the order of 1/10 of the length. Edges should be considered different than faces, since they have a different electrical charge.
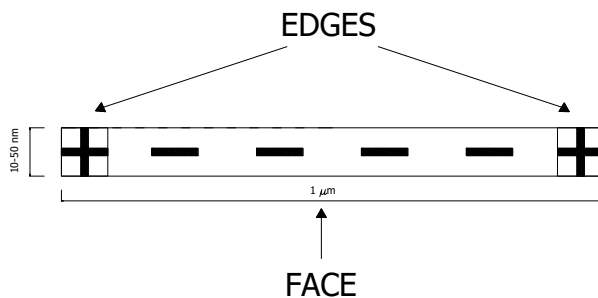
Figure 49. 2-D for kaolin clay particle

According to Key Finding No. 1, two classes of pores have been identified and therefore two different particle configurations has to be considered accordingly (Figure 50):

1) Non-contact configuration

2) Contact configuration
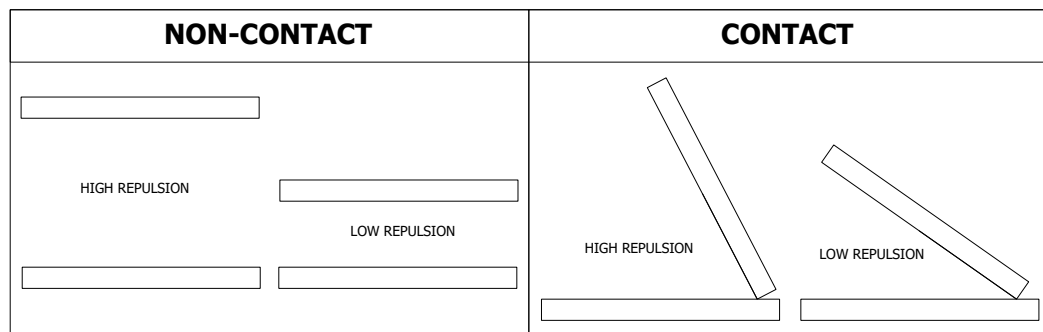
Figure 50. Particle configurations

3.6.2 **Micro-mechanisms controlled by clay particle interaction**

According to evolution of porosity upon reversible and non-reversible volume changes (showed in the previous section), it was inferred that reversible volume changes involve both micro pore and the macro-pores (Key Finding No. 2). As a result, reversible interactions must be expected both in contact and non-contact configuration (Figure 51a).

On the other hand, non-reversible volume changes involve only the macro-pores, which seem to disappear upon loading in the sense that they turn into micro-pores. As a result, a non-reversible interaction would be expected to control contact configuration (Figure 51b).

A) reversible volume change   B) non reversible volume change
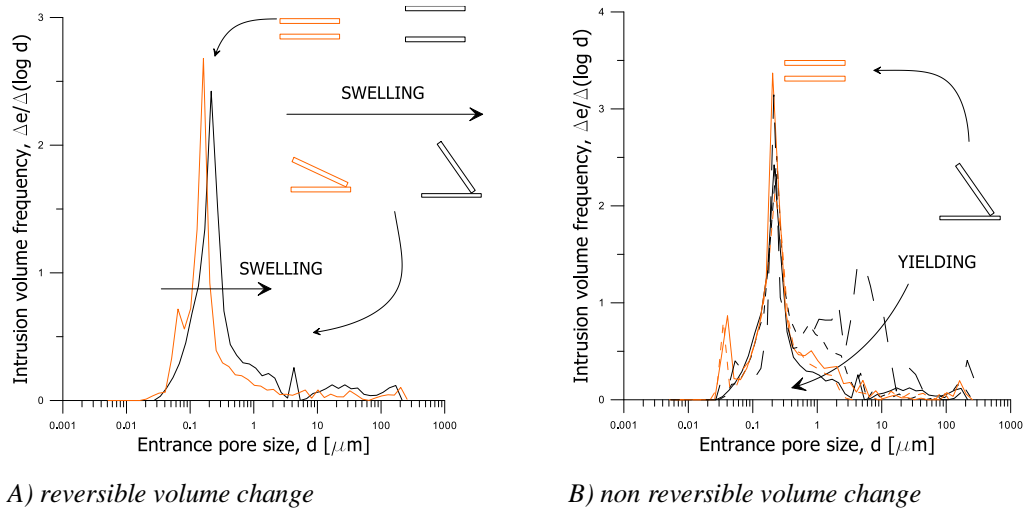
Figure 51. Pore size distributions underpinning reversible and non-reversible volume changes

3.6.3 Conceptualisation of the reversible interparticle interaction

Reversible interaction has been inferred to be present in both: i) non-contact configuration (Figure 52a) and ii) contact configuration (Figure 52b).

A)   Non-contact configuration   B)   Contact configuration
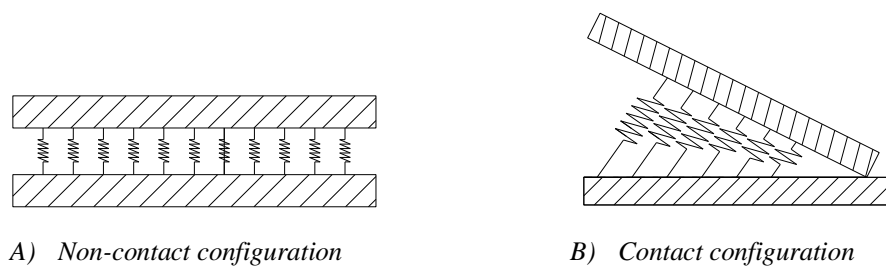
Figure 52. Particle configuration

i)   Non-contact configuration refers to all particles that are not in contact and face each other in a parallel or sub-parallel configuration. The particle distance is controlled by the repulsion existing between the two faces having the same electrical charge and such an interaction can be modelled by springs (Figure 52a).

Compression and decompression of such springs is associated only with reversible mechanism of volume change.

ii)   Contact configuration refers to all particles that are in contact. Contact between particles is here assumed to be associated only with the edge to face. The contact configuration is therefore caused by the edge-to-face attraction. Nevertheless, the mutual distance or rotation between two particles in such configuration is controlled, as in the non-contact configuration, by the repulsion between the two faces, and it is considered to be again a reversible mechanism.

By modelling two particles facing each other as parallel circular plates, the repulsive force, F [N], is computed as shown in Equation 24 (derivation detailed in Appendix):

$$F = \frac{\pi \cdot a^2}{8 \cdot \varepsilon} \rho^2 \left(\frac{d}{\sqrt{a^2 + d^2}} - 1 \right)$$ [24]

where a is the radius of the plates [m], d is the plate distance [m], ρ is the electrical charge distribution on the two plates [C/m^2] and ε is the permittivity of the media between the two plates [F/m], which is defined as the vacuum permittivity times the relative permittivity.

As shown in Figure 53, the smaller the distance between the plates, the higher is the repulsive force developed. Consequently, the higher the applied stress is, the closer the two particles in non-contact configuration are.

The relation between the repulsive force and the distance (stiffness of the spring) is non-linear, i.e. stiffness changes with the distance of the plates (slope of the curve in Figure 53).

In an hypothetic case where load is increased from 1 kPa to 2220 kPa and then back to 1 kPa, it is possible to see that the particle distance decreases with the increasing of the applied load and then increases back when the load is removed (point 1,2 and 3 in Figure 53).

Since the particle distance in both the non-contact and contact configuration is controlled by the spring simulating the compression and decompression of the repulsive field, a reversible behaviour has to be expected if particle configuration does not change.
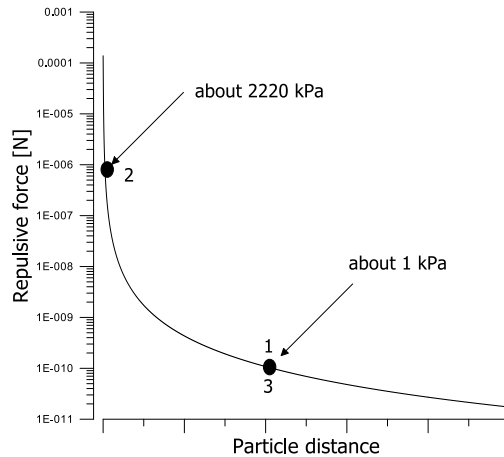
Figure 53. Coulombian repulsive force between two parallel plates

3.6.4 Conceptualisation of the non-reversible interparticle interaction

Non-reversible response has been found to involve only the macro-pores and, hence, the pores associated with the contact configuration.

When particles are in contact configuration, two are the mechanisms assumed to take place: i) relative tilting and ii) contact disengagement. The relative titling has been already discussed in the previous section and it is assumed to be the one responsible for reversible behaviour associated with the contact configuration.

In order to investigate the mechanisms of contact disengagement, two particles in contact configuration can were considered as shown in Figure 54. The contact was assumed to be simulated by a frictional constraint in horizontal direction (parallel to particle face) and a unilateral constraint in vertical direction (orthogonal to particle face) (Figure 54b). The former is controlled by a particle-to-particle friction mechanism whereas the latter

prevents penetration between two particles and leaves the two particles free to move apart. For sake of simplicity, the frictional constraint was assumed to have a perfectly plastic behaviour. If a threshold shear force is not exceeded, the constraint behaves as a simple bearing in horizontal direction. When the threshold shear force is exceeded, the constraint turns into a roller.

A)   B)
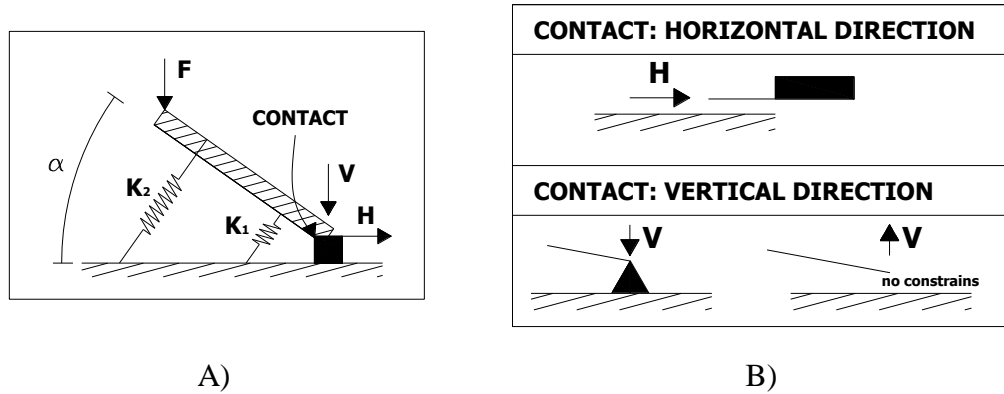
Figure 54. Mechanical sketch of edge to face interaction

Between the two particle faces, a bed of repulsive springs has to be considered to simulate repulsive forces due to same charge.

Since the stiffness of the spring depends on inter-particle distance, the springs should have different stiffness. The closer the spring is to the contact, the stiffer is its response.

The bed of springs plays a double role:

i)   It controls the mutual particle tilting (reversible interaction)

ii)   It controls the reactions generated at the contact

In order to understand the mechanisms involved the disengagement of the contact, the evolution of vertical and horizontal forces at the contact was investigated analytically. The two forces (horizontal mobilized force, H, and vertical force; V, depend on the external force applied, F, on the stiffness of the springs and on the angle formed by the two particles, α.
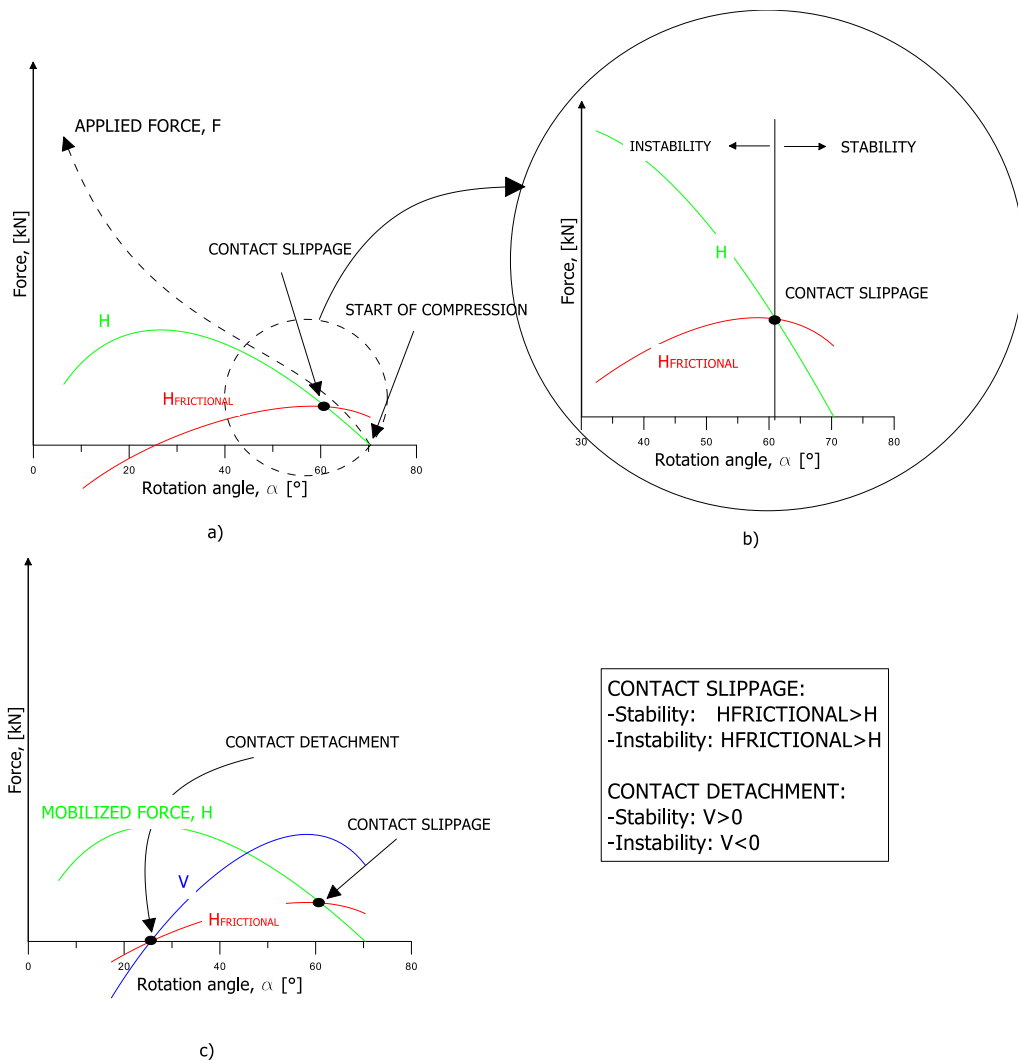
Figure 55: Contact mechanisms

The vertical force, V, is computed as the sum of the reaction associated with by the external force-springs system, V_{SYSTEM}, and the mutual attraction existing between the edge and the face, acting directly at the contact, V_{EF} (Equation 25).

$$V = V_{SYSTEM} + V_{EF}$$

[25]

$$H_{FRICTIONAL} = V \cdot \mu$$

When the applied external force is equal to zero ($V_{SYSTEM}=0$), the vertical force, V, is not equal to zero because attraction between the two particles exists, V_{EF}.

As long as the contact exists, the constraint at the contact can be thought as a hinged fixed bearing (Figure 54a). In Figure 55a, the evolution of the forces involved in the contact mechanism versus the inter-particle, α, is reported. For a given starting inter-particle angle (in this example assumed to be equal 70°), increasing the applied force, F causes the inclined particle to tilt and the inter-particle distance to reduce (dashed line in Figure 55a). The rotation of the particles causes i) the vertical force, V, to reduce and ii) the mobilized horizontal force, H, to increase.

The two mechanisms considered here, are frictional sliding and detachment.

i) The frictional mechanism has been assumed here to be perfectly plastic. The threshold shear force in Figure 55b ($H_{FRICTIONAL}$ in Equation 25) was computed as the product of the vertical mobilized force, V, and the frictional constant, µ. No horizontal displacement will occur as long as the mobilized horizontal force, H, is less than the frictional resistance. Slippage occurs when the mobilized force becomes greater than the frictional resistance (contact slippage in Figure 55b).

ii) The detachment mechanism, on the other side, depends only on the mobilized vertical reaction. Since the constraint at the contact is unilateral, when the vertical force becomes equal to zero the particles move apart since no constraint is preventing detachment. However the detachment mechanism seems to be more unlikely since it appears to occur always at rotation angles smaller than the contact slippage (Figure 55c).

Regardless of the mechanism of contact disengagement (by detachment or slippage), the associated decrease in volume has to be considered as non-reversible, since upon unloading the contact is assumed to not be restored.

3.6.5 Summary of micro-mechanisms associated with contact and non-contact configuration

The micro-mechanisms occurring along a loading and unloading path (Figure 56) are summarised in Figure 57. Non-contact configuration is considered to be associated only with reversible mechanisms. The external load is counterbalanced by repulsion forces (virtual spring) upon reversible compression paths, with the particles getting closer or moving away with compression and decompression respectively.
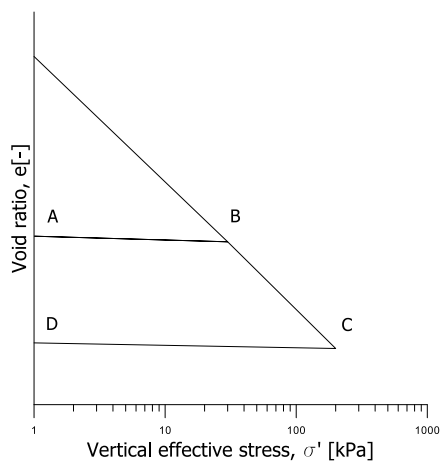
Figure 56. Loading-unloading path

On the other hand, contact-configuration gives rise to both reversible and non-reversible mechanisms. From point A to point B, all the particles in contact configuration act in reversible manner. No disengagement of contacts occurs, and particle relative displacements are only associated with compression and decompression of the electric field between faces (as in the non-contact configuration). At point B, plastic deformation begins to occur. There will be particles in closer configuration (low inter-particle angles) that are prone to slide if locally subjected to high forces depending on the internal distribution of force chains. When plastic deformations begin, some contacts will start to disengage (slippage in Figure 57) while more open contacts keep behaving in a reversible way. The more the load is increased, the higher is the number of contact being disengaged. Once that contact has been disengaged, particles

tend to dispose in a sub-parallel configuration and, from this point on, the mechanical behaviour will become reversible (non-contact configuration). In summary, plastic deformations are associated with the disengagement of the contact, which is considered to be non-reversible.
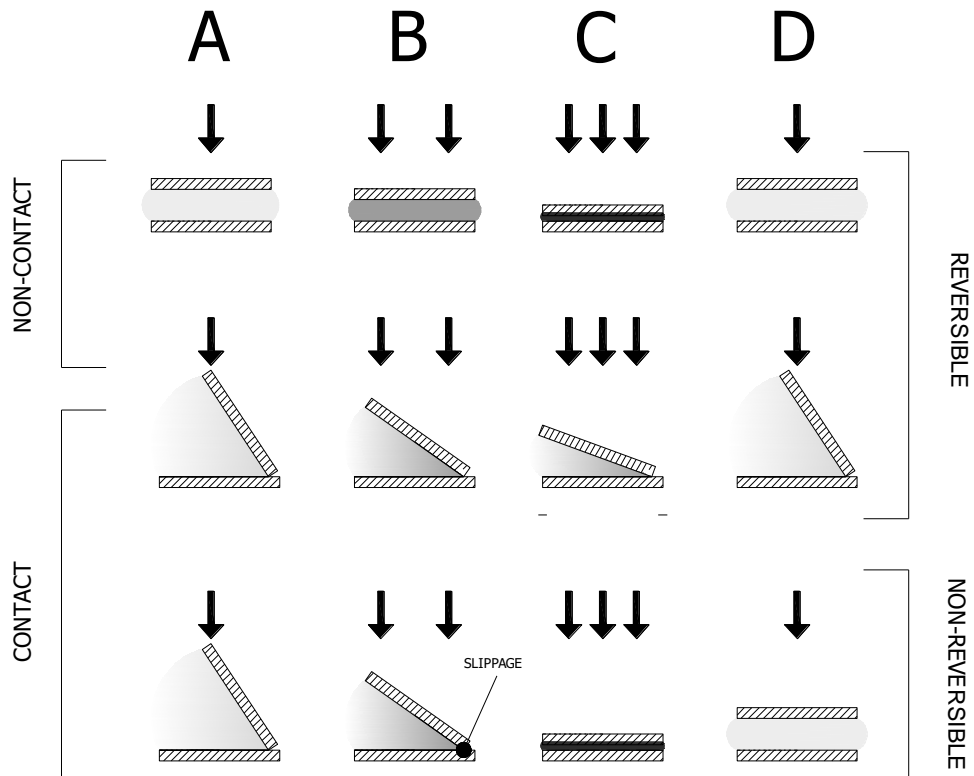
Figure 57. Micro-mechanism associated to contact and non-contact configuration

3.7 Experimental validation of the micro-mechanical conceptual model

The assumption made in the previous sections is that kaolin particles may exist in two different configurations, contact and non-contact respectively. Reversible compression is associated with the Coulombian repulsion in both contact and non-contact configuration whereas non-reversible compression is associated with the disengagement of particle contact.

Particle configuration and micro-mechanical interactions are assumed to be controlled by electro-chemical forces in turn controlled by pore-fluid chemistry. As a result, a change in pore-fluid chemistry should give rise to a change in both microstructure (pore-size distribution) and macro-behaviour that the conceptual model should be able to predict at a qualitative level.

3.7.1 Effect of dielectric constant on inter-particle forces

Figure 58a shows the trend of the repulsive force versus the particle distance for three fluids having different permittivity. It can be observed that the repulsive force is inversely proportional to the particle distance and that this relationship is dielectric permittivity-dependent. For any given applied force, the distance between particles in air will be greater than that in acetone and, in turn, the distance between particles in acetone is greater than that in water. Particles would therefore be expected to have a more open structure in air than acetone or water (Figure 58b)

Figure 59a shows the trend of the repulsive force versus particle distance for three difference particle size (0.5 μm, 1.0 μm and 2.0 μm). It can be observed that the repulsive force is proportional to particle size. For any given applied force, the smaller the particle distance, the less is the repulsion and, hence, the particle distance for a given external stress applied (Figure 59b).
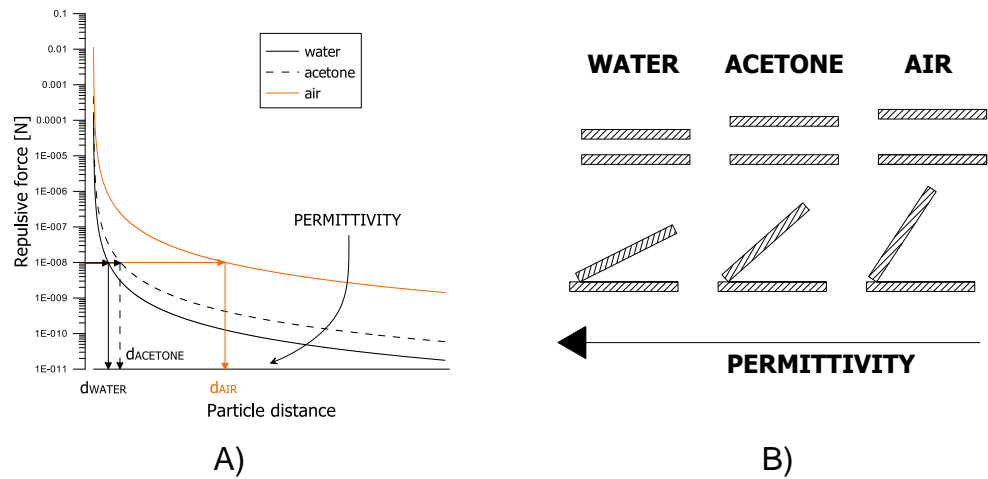
Figure 58. Repulsive force for three different pore fluids: water, acetone and air
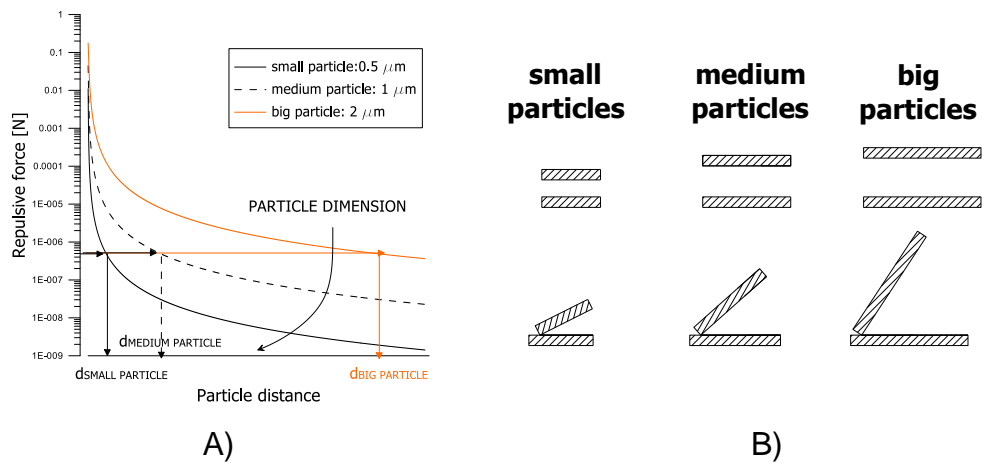
Figure 59. Repulsive force for three particle size

3.7.2 Response of clay saturated with fluids having different dielectric permittivity as predicted by the conceptual model

In Figure 60 particles will be either in contact and non-contact configuration, with the mutual distance controlled by the repulsive force. For the sake of simplicity only particles in contact configuration are reported. Since the repulsion between particles is higher in the sample having lower permittivity (e.g. air), a more open configuration is expected for the air-saturated sample (Figure 60b) as compared to the water-saturated one (Figure 60a).

If the stress is increased to a value lower or equal than the pre-consolidation stress (A to B in Figure 61), a reversible compression is achieved and no inter-particle slippage is expected. The only change in volume is assumed to be the

one related to the (reversible) rotation of particles around the contact point and sub-parallel particles moving closer (the latter mechanism is not shown in Figure 60). The rotation of the particles is controlled by the springs existing between the two faces, which have a stiffness that depends on the mutual particle distance and on the permittivity of the pore fluid.

A) High permittivity (water-like)   B) Low permittivity (air-like)
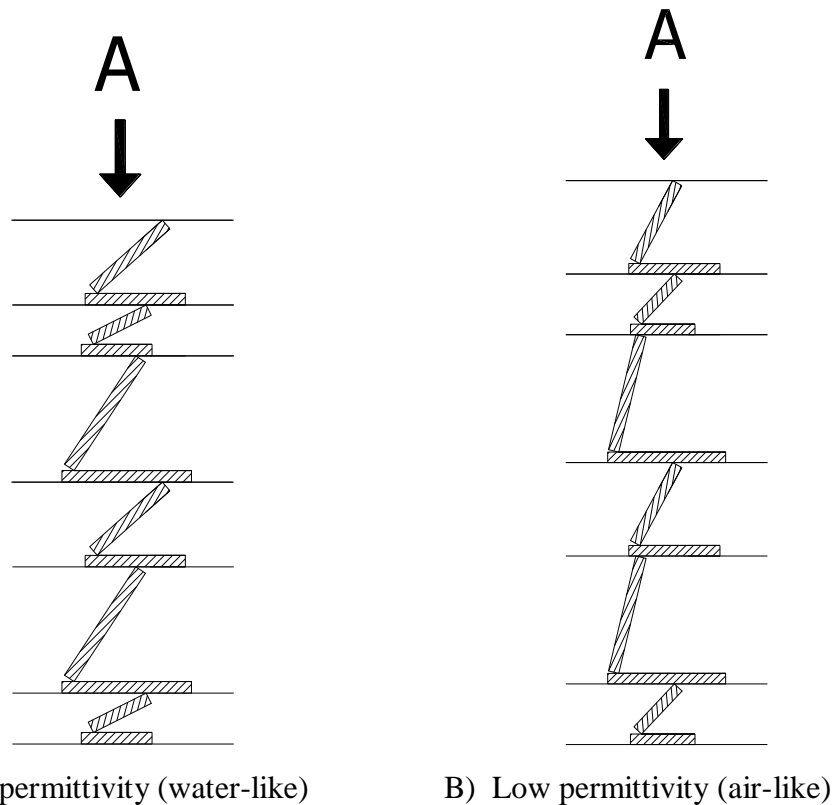
Figure 60. Particle initial configuration

When the load is increased beyond the pre-consolidation stress (B to C in Figure 61), some slippage has to be expected. Some particles move from a contact configuration to a non-contact configuration (Figure 61), causing a significant decrease in the volume of voids.

When the load is decreased again (from C to D Figure 61), only the particles that are still in a contact configuration will essentially contribute to the swelling (as shown in Figure 47). The contribution to swelling of the particles in non-contact configuration will be very small as discussed in the previous section and it can therefore be neglected for the sake of simplicity.

A) *High permittivity (water-like)*   B) *Low permittivity (air-like)*
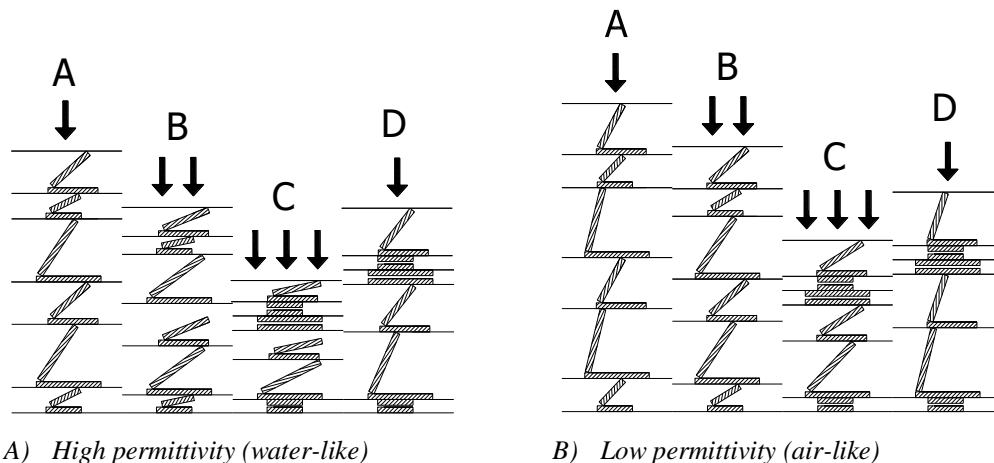
Figure 61. Conceptual model for consolidation test.

3.7.3 Experimental tests

1-D compression

1-D compression tests were carried out to investigate the effects of dielectric permittivity on the micro- and macro response of kaolin. Three different pore fluids were considered: water, acetone and air.

Oven-dried powder was placed in the oedometer cell. After the oedometer cap was placed on the sample (about 1 kPa), the sample was fully saturated with water or acetone or left dry for the case of air. When fluid was added to the cell, a consolidation took place. At the end of the consolidation each sample was loaded in steps to the maximum vertical stress (Figure 62).

When the pore fluid was changed from air to acetone or from air to water, the interparticle repulsive forces are expected to reduce (Figure 58). Indeed, for the same initial stress (1 kPa), the sample having water as pore fluid attained a much closer structure (e=2.55) than the sample having acetone as pore fluid (e=3.51).

This difference is maintained along first loading since kaolin mixed with water always shows a much closer structure than acetone and air. Accordingly,

to the conceptual model, the sample in air is more compressible than the others, because of the more open structure.
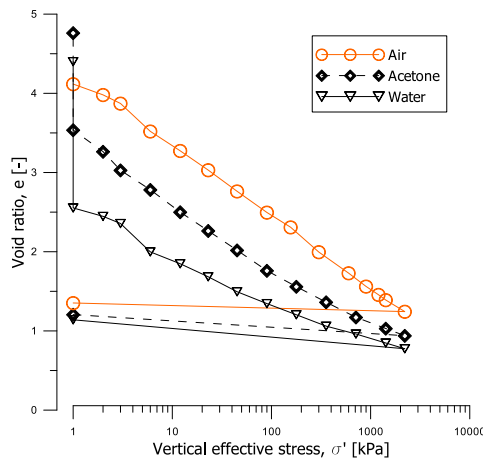
Figure 62. 1-D consolidation of kaolin clay sample saturated with three different fluids

Upon unloading, swelling occurred for the three samples. The amount of reversible volume changes that has been recorder is larger for kaolin mixed with water and smaller for the case of kaolin mixed with acetone and air. This trend is in agreement with the prediction of the conceptual model if contact configuration is taken in account. As reported in Figure 58 and Figure 59 at higher dielectric constants the relation between applied force and displacement is less rigid for lower dielectric constants. Therefore, for a given delta force, the mutual rotation between two particles in water is expected to be higher than for two particles in air. Since the elastic response is controlled by the 'elastic' rebound around the inter-particle contact, a higher swelling for particles in water is expected.

Pore-size distribution

The pore size distribution of the samples having different pore fluids was investigated using MIP. A different dehydration technique was used for the three samples. For samples saturated with air (dry samples), no dehydration was performed. For samples saturated with acetone, dehydration was achieved by oven drying for at least 24 hours. For samples saturated with water, the freeze-drying technique (as described before) was used.

Microstructure of samples in acetone, differently from samples containing water, is believed to be slightly affected by the process of oven-drying. Acetone surface tension is 0.0252 N/m at 20°, while water surface tension is three times higher, 0.0728 N/m. Moreover, the surface tension of acetone decreases with temperature (0.0211 N/m at 57°, which is the boiling point). If the contact angle between acetone and clay is considered to be conservatively equal to 0°, and a conservative pore size of 0.2 μm is considered, the maximum suction developed at the air-entry value is 252 kPa at 20° and 210 kPa at 57°. This suction is considerably smaller than the maximum pre-consolidation stress attained during the consolidation process and is expected to generate negligible mechanical effects.
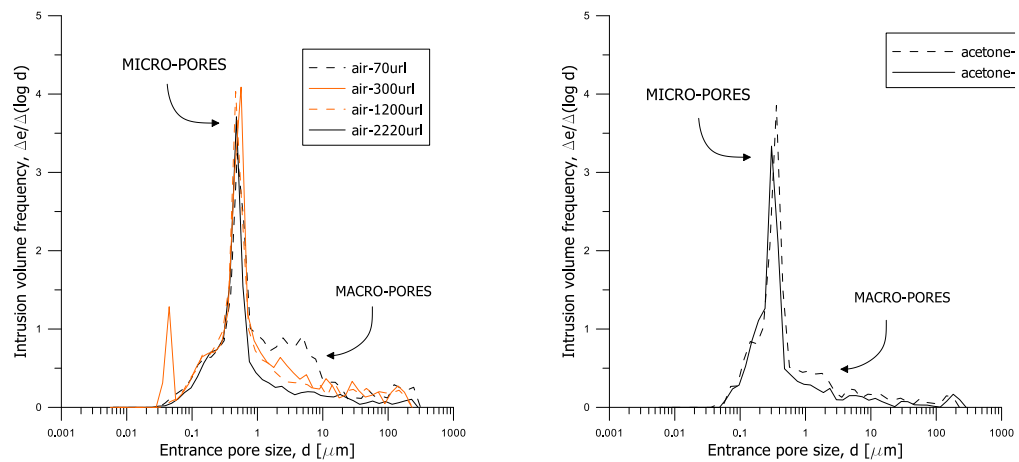
A) *Pore size distribution of air-saturated samples consolidated at different vertical stress.*

B) *Pore size distribution of acetone-saturated samples consolidated at different vertical stress*

Figure 63. Pore size distribution at different vertical stress. Air (a) and acetone (b)

The pore size distributions of samples in air and acetone are shown in Figure 63a and Figure 63b respectively. It can be noted that the distribution of pores are similar in a qualitative way. Air-saturated and acetone-saturated samples show a mono-modal size distribution, the branch associated with the micro-pores remains the same regardless of the applied stress, and macro-pores reduces in size and frequency when the vertical stress is increased. These features were also observed in water-saturated samples (Figure 45b), suggesting that the same micro-mechanisms occur for the three pore-fluids.

A comparison of the pore-size distribution of samples saturated with the three different pore fluids at the same vertical stress is reported in Figure 64a (70 kPa) and Figure 64b (2220 kPa). There are two major points than can be observed:

i)   The modal pore size (micro-pores) of the three samples is shifted as the pore-fluid is changed. Modal pore-size of water-saturated samples is smaller than the acetone-saturated and air-saturated samples. The trend is indeed in agreement with the one showed in Figure 58a. This is clear evidence that the particle distance in the non-contact configuration is controlled by the electrical repulsion existing between the faces that, in turn, depends on the permittivity of the fluid. It is worth noticing that not only the modal pore size is shifted but the whole pore-size distribution.

ii)   The macro-pores are shifted both in terms of pore size and frequency, with the higher pore-size and frequency recorded for the air-saturated samples. This is in agreement with the prediction of the conceptual model. Samples in air have a contact configuration more open than samples in water (shift in the diameter size). As a result, air-saturated samples have a higher frequency of pores than water-saturated samples at larger pore diameter.
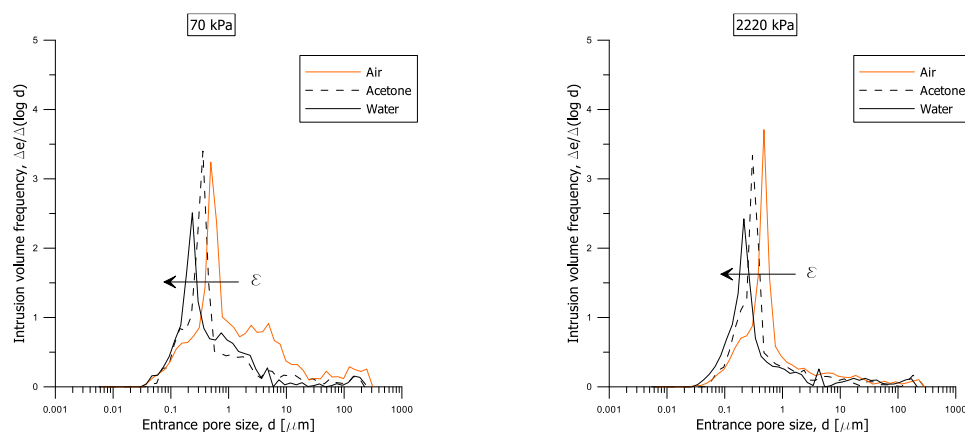
A) *Pore size distributions of samples consolidated at 70 kpa*

B) *Pore size distributions of samples consolidated at 2220 kpa*

Figure 64. Pore size distribution of samples consolidated at 70 kPa (a) and 2220 kPa (b) having different pore fluids.

3.8 'Embryonic' discrete element model

A simplified Discrete Element Method (DEM) model was developed to demonstrate the potential of the conceptual model to be turned into a full DEM model. In order to evaluate the void volume changes, only particles in contact configuration were considered. Once particles move from contact to non-contact configuration, the void volume associated with contact configuration is assumed to be equal zero (i.e. change in volume of voids associated with particle in non-contact configuration is considered to be negligible compared to the change in volume associated with particle in contact configuration).

Particle-to-particle interactions are assumed to be the ones illustrated in the previous sections. For a given load the inter-particle distance is controlled by the repulsive force existing between the faces. As shown in Equation 24, the repulsive force is controlled by the pore-fluid permittivity, ε, and the particle dimensions, *a*.

The model

50 pairs of particles have been included in the 1-D DEM shown in Figure 60. Particles were assumed to have a log-normal distribution with mean diameter of 1 μm and standard deviation of 0.2 μm. Each pair of particles was assumed to start from a contact configuration and the initial inter-particle angle was computed in order to each set of particles in equilibrium with the applied force.

The loading path considered in the simulation is the same as shown in Figure 56. Three different pore fluids have been considered (air, acetone and water) having different relative dielectric permittivity (1, 24 and 80 respectively).

Calibration

According to Equation 24 the repulsive force existing between the particles depends on the permittivity and on the surface charge of the particle (Figure 65). Permittivity is given by the pore fluid, but the surface charge it is not.

Surface charge is not easily measurable but it is known to reduce with dielectric permittivity of the pore-fluid (Mitchell & Soga, 2005).
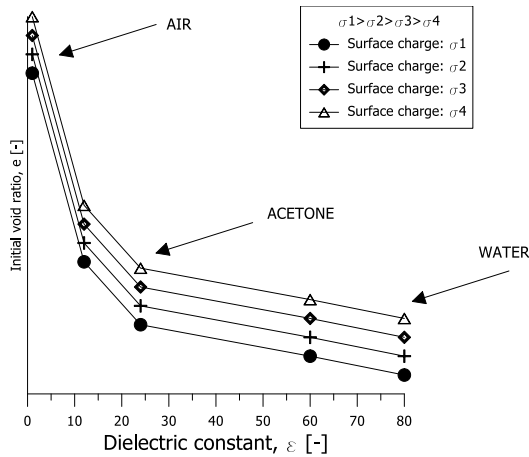
Figure 65. Qualitative trend of the initial void ratio as function of the dielectric constant (ε) and surface charge (σ).

Initially the electrical charge was calibrated to match exactly the initial experimental void ratio. However, this resulted in compression curves derived from the simulations that were not fully consistent with the curve determined experimentally in normal compression. It was then decided to calibrate the surface charge by seeking the best compromise between an acceptable simulation of the initial void ratio and a satisfactory simulation of the entire compression curve (Figure 66).

According to Equation 25, the external force at which two particles in contact configuration slip is controlled by particle repulsion and by the adhesion at the contact (V_{EF} in Equation 25). Such adhesion depends on the van der Waals attraction and the edge-to-face Columbian attraction. No clear information exists on the trend of such adhesion when the pore fluid is changed. As shown by Mitchell & Soga (2005), van der Waals attraction has a non-monotonic trend in the range of permittivity between 1 and 80. It shows a minimum at a permittivity of about 20 (acetone) and two maximums at permittivity of 1 (air) and 80 (water). On the other hand, edge-to-face attraction due to Coulombian forces is known to increase as the permittivity decreases.

	Dielectric constant [-]	Electrical charge [C]
Air	1	1150
Acetone	24	800
Water	80	200
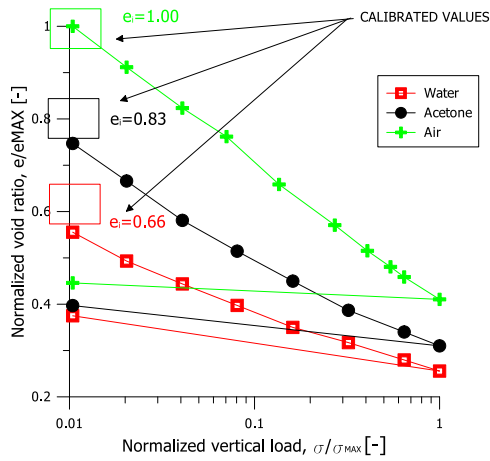
A) *Calibration of surface electrical charge against initial void ratio experimental result*

B) *Calibrated values of electrical charge*

Figure 66. Surface electrical charge calibration for different dielectric constant.

For given initial conditions, changing the adhesion at the contact (V_{EF}) changes the load interval at which the yielding (particle slippage) occurs. The higher is the contact adhesion, the higher is the load at which slippage between two particles occurs. In order to have the three samples yielding at the same vertical stress, adhesion forces (V_{EF} in equation [25]) have been chosen by imposing the minimum void ratio derived from the simulation matched experimental void ratio (Figure 67).

	Dielectric constant [-]	V_{EF} [KN]
Air	1	68
Acetone	24	79
Water	80	86
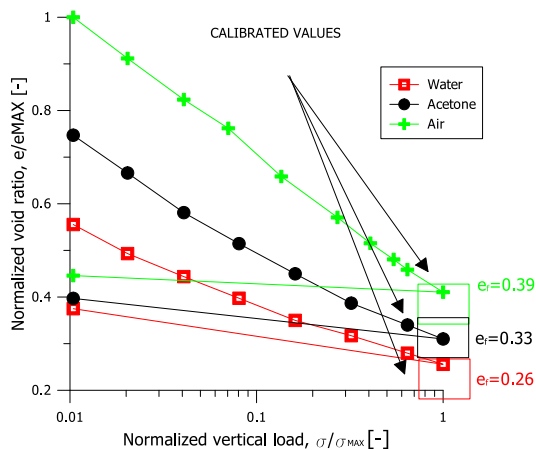
A) *Calibration of adhesion against final void ratio experimental result*

B) *Calibrated values of contact adhesion*

Figure 67. Contact adhesion calibration for different dielectric constants

Discrete element model: results and discussion

In Figure 68a, the result of the 1-D DEM model is reported. The test was performed on 50 pairs of particles having different dimension. Air-saturated, acetone-saturated, and water-saturated samples were considered. The volume of voids at each step was calculated by considering only the pair of particles in contact configuration and considering only the vertical dimension.

A) *Embrionic DEM - oedometer test*   B) *Swelling*
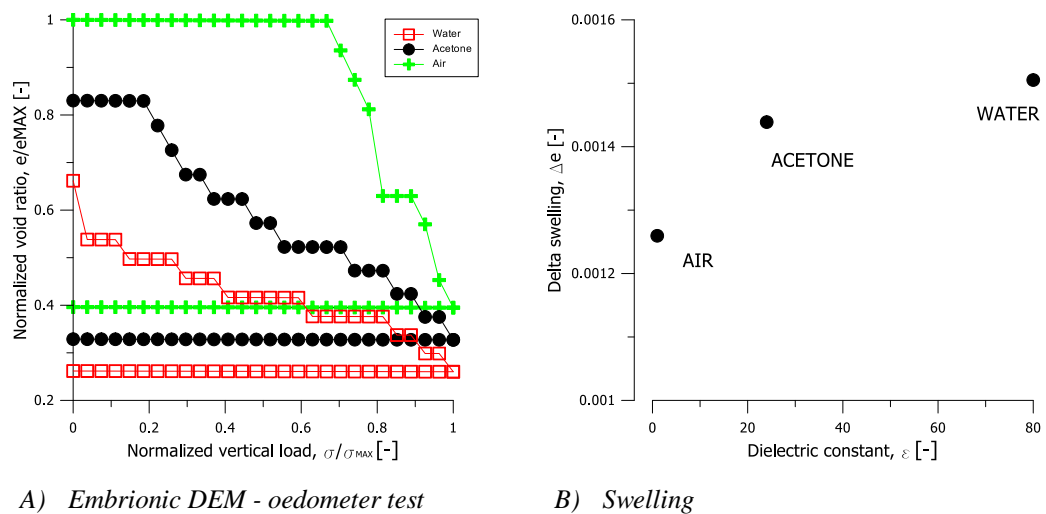
Figure 68. DEM simulation

Two main results were achieved:

i)   During the loading path (B-C) the clay particles saturated with the fluid having lower permittivity maintains a more open structure than the clay particles saturated with the fluid having higher permittivity. The sample with the fluid having the lowest permittivity was shown to be the most compressible.

ii) Upon unloading the sample saturated with the fluid having higher permittivity (water) showed a larger swelling than the sample saturated with the fluid having lower permittivity (air). This is in agreement with the 'elastic' response of samples shown in Figure 62.

3.9 Conclusions

A microstructural conceptual model has been proposed and experimentally validated.

The conceptual model is based on the assumption that particles can be present in two configurations:

i)   Contact

ii)   Non-contact

Particles interact to each other by means of electrochemical forces existing between the surfaces. Such forces have been schematized as springs, which control the particle mutual distance.

Moreover, reversible and non-reversible mechanisms have been associated with the two configurations. Slippage at the particle contact was inferred to be the mechanisms controlling the non-reversible volume change. On the other hand, reversible mechanisms have been associated with both contact and non-contact configuration. However, reversible volume change of contact configuration has been found to be the main contributors to reversible volume change.

A simplified DEM model has been formulated and validated against experimental data. The model showed to be capable of simulating qualitatively the different compressibility upon loading of water-, acetone, and air-saturated samples.

Appendix

A 1. Electric potential

Poisson equation (Equation 4) was derived in Chapter 1. Such an equation gives the spatial evolution of an electric potential, φ, in a dielectric medium, ε, having a distribution of electric charges with density ρ.

$$\text{POISSON'S EQUATION: } \nabla \cdot E = \nabla(-\nabla\varphi) = -\nabla^2\varphi = \frac{\rho}{\varepsilon} \qquad [26]$$

Two are the cases to be considered:

iii)   Zero electric charge distribution in the media ($\rho = 0$)

iv)   Electric charge distribution that follows a Boltzmann's distribution

If the charge density ρ is equal to zero, Poisson's equation turns into Laplace's equation (Equation[27]).

$$\text{LAPLACE'S EQUATION: } \nabla^2\Phi = 0 \qquad [27]$$

Analytical solutions of Laplace's equation exist in two and three dimensional problem. Such solutions are generally computed by using the Green's function. For the case of an electrical field, for a known and quite simple geometry, solutions of the Laplace's equation can be inferred directly from the definition of the electric potential (Equation [28]), which involves little computational efforts:

$$\varphi(z) = \frac{1}{4\pi\varepsilon} \int \frac{\sigma(x)}{|x - z|} dx \qquad [28]$$

where σ is the charge distribution on the surface, z is the distance from the surface and x is the spatial coordinate on the surface.

For the case of an electric field generated by a disk having radius *a* with a uniform surface charge distribution σ_S in a free-electrolyte medium having dielectric constant ε, the electric potential $\varphi(z)$ is defined by Equation 29:

$$\varphi(z) = \frac{\sigma_s}{2\varepsilon}\left[\sqrt{(a^2 + z^2)} - |z|\right] \qquad [29]$$

On the other hand, when the medium is a polar fluid, e.g. water, and electrolytes are dissolved in it, a distribution of cations and anions is generated. The charge distribution ρ within the medium cannot be considered to be nil.

In order to solve the Poisson's equation (Equation[26) it is necessary to assume an ion distribution in the medium. The double layer theory describes the distribution of ions around particles in suspension (Gouy, 1910, Chapman, 1913, Derjaguin & Landau, 1941, Verwey et al., 1948, Van Olphen, 1977, Mitchell & Soga, 2005, Stern, 1924). According to this theory, ions around particles in suspension are distributed in two charged layers, in order to neutralize the surface charge of the particles (Figure 7).

Figure 8 shows the electric potential, φ, as a function of the distance from the surface according to the Gouy-Chapman theory. The potential has a maximum value at the surface, and it decreases roughly exponentially with the surface charge.
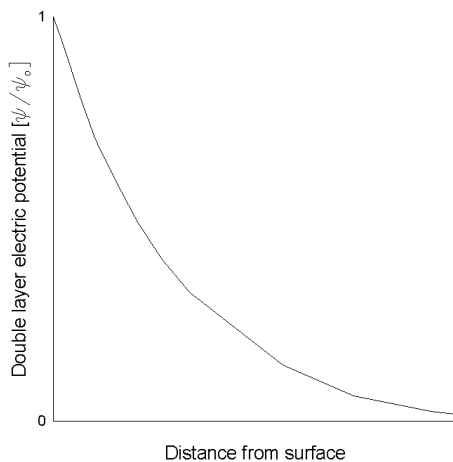
Figure 69: Variation of electrical potential with distance from a charged surface (Mitchell & Soga, 2005)

The potential at the surface (φ_0), the potential at the limit of the Stern layer, and the ζ potential are different from a theoretical point of view since they are computed at different distance from the surface. Nevertheless, the ζ potential

is often the only potential that is possible to measure in colloidal science. As a result, the Stern layer is almost never considered in calculations or it is included in the particle surface (so-called "solid water").

The concentration of ions (ions/m^3) in a force field at equilibrium with electric potential φ is assumed to have a Boltzmann distribution (Equation[30]):

$$n_i = n_{i0} \exp\left(\frac{-v_i e\psi}{kt}\right) \qquad [30]$$

where n_i is the concentration of the ions with valence v_i. n_{i0} is the concentration at the equilibrium in the solution, k is the Boltzmann constant (1.38x10^{-23} J K^{-1}), T is the temperature (K) and e is the electronic charge (1.602x10^{-19} C).

The distribution of charges (Equation 31) depends on the distribution of the free-ions, n_i, in the double layer (Equation[26]):

$$\rho = e \sum_i v_i n_i \qquad [31]$$

By substituting the Boltzmann's equation into the Poisson's equation the Poisson-Boltzmann's equation is derivate:

$$\nabla^2 \varphi = \frac{2n_0 ve}{\varepsilon} \sinh\left(\frac{ve\varphi}{kT}\right) \qquad [32]$$

For the case of free-electrolyte solution (Laplace's equation) the case of a single charged surface is enough to characterize the problem, in the case of an electrolyte solution a single double layer is not representative of the actual condition of the ions distribution. Different double layers of adjacent particles will overlap, and thus a different charge distribution, ρ, has to be expected.

Numerical and mathematical relationships about the solution of the differential equation for the electric double layer in these particular boundary conditions are reported by many authors, including Van Olphen (1977) and Mitchell & Soga (2005).

According to the Gouy-Chapman theory (Gouy, 1910, D. L. Chapman, 1913) a simplified solution for the electric potential, φ, between two plates can be expressed as follows:

$$\varphi(z) \sim 2\left(\frac{4kT\gamma_0}{ve}\right)\exp(-Kz) \qquad [33]$$

where *1/K* is defined as the centre of gravity of the diffuse layer and γ_0 is given by:

$$\gamma_0 = \frac{\exp\left(\frac{ve\varphi_0}{2kT}\right) - 1}{\exp\left(\frac{ve\varphi_0}{2kT}\right) + 1} \qquad [34]$$

Traditionally, the electric potential generated by clay particles in a liquid solution it has always been computed using one of the solutions of the Boltzmann-Poisson equation (i.e. Equation 33).

However, when the electrolyte concentration is very small, it is possible to demonstrate that the electric potential computed by the Gouy-Chapman's equation tends to overlap with the exact solution given by Equation 6 (which has been derived from the Laplace's equation by assuming no electrical charge distribution in the medium).

For a given set of surface electrical potential and particle geometry, it is possible to compute i) the electric potential for a liquid medium having different dielectric constant (i.e. air, acetone and water) but no electrolytes dissolved in it (Figure 70a) and ii) the electric potential for a medium made of water and a very small amount of electrolyte (Figure 70b). The electrolyte considered in Figure 70b was NaCl with a molar concentration of 10^{-3}, 10^{-4} and 10^{-5} M.
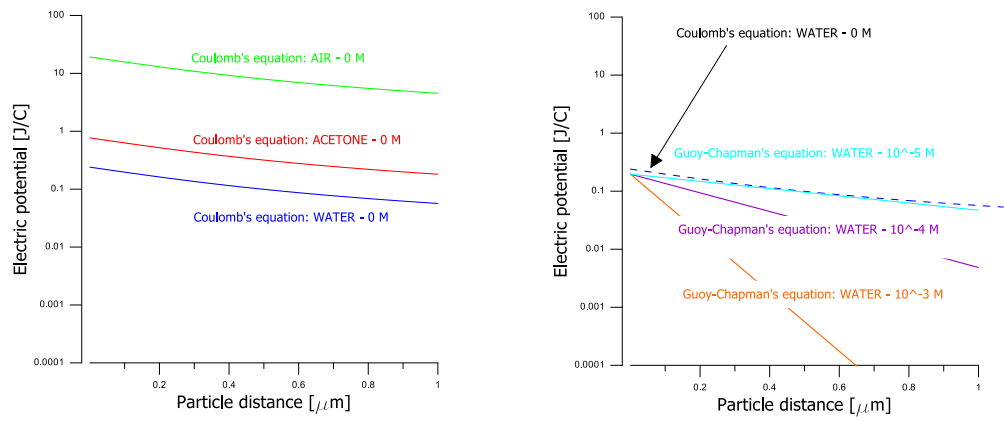
A) *Electric potential trend for medium at different dielectric constant (Coulomb's equation)*

B) *Electric potential for water at different electrolyte concentration (Gouy-Chapman's equation)*

Figure 70. Computation of electric potential for different dielectric medium.

As shown in Figure 70b, when the electrolyte concentration of the medium tends to zero, the difference between the Gouy-Chapman's solution and the Coulomb's equation becomes negligible. Therefore, under laboratory condition, where distilled water is used and no electrolyte is added to the water-clay mixture, it is more convenient to employ the Coulomb's equation under the simplifying hypothesis of zero or negligible electrolyte concentration. Moreover, the double layer theory, and in this case the Gouy-Chapman equation, it is often misused to compute the electric repulsion for the case of apolar or polar aprotic medium. In such media, the electrolyte dissolution is zero or very small respectively, and a Boltzmann's distribution of the ions therefore seems to be an unlikely assumption. On the other hand, if the electric potential is compute by using the Coulomb's equation, the only assumption that needs to be introduced is the low electrolyte concentration in the medium, which can be indeed controlled.

A 2. Repulsive forces between two electrically charged particles

When a shell with an electrical charge is submerged into an electric field, it has an electric potential energy, U [J]. The potential energy is generally defined as $U = \varphi^* Q$, where φ [J/C] is the electric potential and Q [C] is the electrical charge of the surface of the particle. Equation[35 gives the potential energy

U(z) for an electric potential φ, defined according to Equation 29, and an electrical charge distribution, ρ_S [C/m^2]:

$$U(z) = (\frac{\rho_S}{2\varepsilon}\left[\sqrt{(a^2 + z^2)} - |z|\right]) \cdot \rho_S \cdot \frac{\pi \cdot a^2}{4} \qquad [35]$$

Under the assumption that the electric force is conservative, the work done to bring one particle from a point z_1 to a point z_2 is defined as the difference between the potential energy in z_1 and z_2. From the definition of work, it is therefore possible to derive the force F, required to bring the particles to a given distance:

$$W_{\Delta z} = \int F dz = - \Delta U(z)$$

$$[36]$$

$$F = \frac{W_{\Delta z}}{\Delta z} + C = - \frac{\Delta U(z)}{\Delta z} + C$$

where C is the constant of integration. This is assumed to be equal to 0 under the boundary condition of force, F, equal to zero at infinite distance ($z \to \infty$). If $\Delta z \to 0$, $F = -\frac{\partial U}{\partial z}$ and therefore:

$$F = \frac{\pi \cdot a^2}{8 \cdot \varepsilon} \rho^2 \left(\frac{z}{\sqrt{a^2 + z^2}} - 1\right) \qquad [37]$$

where z is the particle distance assumed to be positive when two particles move apart.

Chapter 4.   A particle-based micromechanical conceptual model for partially saturated non-active clays and an alternate approach to constitutive modelling

4.1 Introduction

This chapter presents an experimental investigation on microstructure of kaolin in partially saturated state. To this end, 1-D compaction tests have been coupled with MIP tests. Partially saturated samples in compacted state generally show a bi-modal pore size distribution and, over the last 30 years, this has been associated with an aggregate configuration of particles. Such conceptual models have gained great success since the end of the 90s. The most advanced and successful hydro-mechanical frameworks for partially saturated clays have been based on the assumption that aggregates form the 'elementary unit'. Constitutive models informed by the aggregate-based microstructural concept, which often incorporate microstructural variables or parameters (Tarantino, 2007, Alonso et al., 2012, Gallipoli et al., 2003), have proven to model successfully macroscopic behaviour of partially saturated soils. However, a convincing experimental validation of the assumption that aggregates are the 'elementary' units controlling the macro-mechanical response still appears to be missing.

Several contributions have been focusing on demonstrating the aggregate nature of clays under saturated and partially saturated conditions including

Delage & Lefebvre (1984), Delage et al. (1996), Delage et al. (2006), Romero et al. (1999), Romero & Simms (2008), Romero et al. (2011), Tarantino & Tombolato (2005), Tarantino & De Col (2008).

However, inspection of pore-size distribution during mechanical or hydraulic paths reveals a number of contradictory aspects. As highlighted in the chapter on the literature review, the main issue concerns the role and the evolution of the macro-porosity. Such a class of pores does not change its modal pore size but only its frequency upon hydro-mechanical loading. This is not very consistent with the assumption that macro-porosity evolves in response to slippage between aggregates. If aggregates behave like sand grains as a first approximation, the inter-aggregate porosity (porosity between the aggregates) should reduce in size when the soil undergoes plastic volumetric deformation. A shift in modal size of the macro-pores towards smaller values would therefore be expected, which is instead not observed.

In addition, such 'macro-pore' size is the only one being present in samples compacted at low water contents. This leads to the paradox that the soil compacted at low water contents is made of inter-aggregate pores without intra-aggregate pores and, hence, aggregate themselves being present.

More in general, discrepancies arise when conceptual microstructural models for saturated and partially saturated soils. For example, Delage & Lefebvre (1984) observed that mono-modal pore-size distribution in natural clay is associated with an aggregate structure with inter- and intra-aggregate pores being represented by the pores larger and smaller than the modal size respectively. On the other hand, mono-modal pore-size distribution in unsaturated soils is often associated with a non-aggregate microstructure (matrix-like).

In this chapter, an attempt will be made to unify the microstructural conceptual models for saturated and unsaturated states and possibly identify, via the microstructure, the continuity between saturated, unsaturated and dry states.

4.2 An alternate hypothesis about the double porosity of compacted kaolin clay

4.2.1 Pore size distribution of water-saturated and air-saturated clay

The nature of the pore fluid is traditionally identified with respect to water. Samples fully saturated with water are referred as 'saturated' and samples fully saturated with air are referred as 'dry'. This definition somehow implicitly assumes that it is the water that essentially matters and that air has a neutral effect on the soil response.

It has been shown in Chapter 3 that inter-particle distance and, hence, pore-size distribution and 1-D compression behaviour are controlled by the dielectric permittivity of the pore-fluid, regardless of whether the fluid is polar or a-polar. The lower the dielectric permittivity of the fluid, the higher is the repulsion between particles. Particles having water as the pore fluid, which has relative dielectric permittivity equal to 80, were closer than particles having air as pore fluid (relative dielectric permittivity equal to 1). The inter-particle distance controlled by dielectric permittivity was then shown to have a direct effect on compression behaviour.

The continuity observed in the pore-size distribution and 1-D compression response of clay saturated with fluids having different dielectric permittivity (air, acetone, and water) seems to suggest that water and air have same micro-mechanical control of inter-particle interaction in the sense that they control inter-particle (Coulombian) repulsion in a similar way via their permittivity.

In this perspective, air and water should be given same 'status'. Saturated samples will therefore be referred herein to as 'water-saturated' and dry samples will be referred to as 'air-saturated'. A similar nomenclature will be adopted for the partially saturated samples, which will be referred to as 'air-water saturated'.

If a continuity exists between dry and saturated states, micro-mechanical models for partially saturated clays should be able to encompass the whole range of degrees of saturation from S_R=0 to S_R=1. For this reason, the starting point of the microstructural investigation will be the comparison of the pore-size distributions of water-saturated, air-saturated, and air-water saturated clays.

So far, little attention has been paid to dry clays and clays having low degree of water-saturation. Most of the microstructural investigations have been focusing on clays with relatively high degree of water-saturation or being fully water-saturated. Another aspect that has not been tackled in depth are the micro-mechanisms giving rise to mono-modal or bi-modal pore-size distributions and the micro-mechanisms controlling the transition from mono-modal to bi-modal pore-size distributions or vice versa (Romero et al., 1999, Romero et al., 2011, Tarantino, 2009, Tarantino, 2010, Delage & Lefebvre, 1984).

Experimental procedures

Speswhite kaolin with plastic limit w_P=0.32 and liquid limit w_L=0.64 was chosen for the tests presented in this paper. The grain size distribution showed it to have 0.20 silt fraction and 0.80 clay fraction

Two 1-D compression tests were performed in order to prepare air-saturated and water-saturated samples:

i)   To prepare the water-saturated sample (Figure 71), kaolin was reconstituted from slurry (w=1.00=1.5w_L) and consolidated to 2220 kPa vertical stress. Once the maximum vertical stress was reached, an undrained unloading was performed to preserve the water content at the same value as on the Normal Consolidation Line (ncl). To ensure an undrained condition, a layer of parafilm^{TM} was placed at the bottom of the sample in order to seal the bottom porous stone. Since drainage was allowed only at the top of the sample, the drainage length could be doubled and the consolidation time incremented by four times with

respect to the case of drainage at both ends. The undrained unloading consisted in one single step, from 2200 kPa to 1kPa vertical stress. The unloading was carried out as fast as possible and no time for consolidation was allowed.

ii) To prepare the air-saturated sample (Figure 71), oven-dried kaolin powder was prepared by compacting up to 2220 kPa in the oedometer cell.

In order to perform an MIP test, samples have to be dehydrated with minimal disturbance of the microstructure. A freeze-drying technique was therefore used to dehydrate the sample reconstituted from slurry using liquid nitrogen and isopentane as previously described. No dehydration was needed for sample compressed from dried powder.

Mercury intrusion porosimetry was carried out using a POREMASTER–60 produced by Quantachrome Instruments. The machine is designed to measure pore diameters in the range of about 1000 to 0.003 µm corresponding to mercury pressure of 1.5-420,000 kPa respectively.
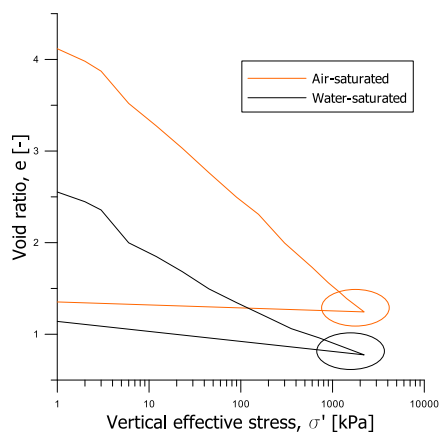
Figure 71. 1-D consolidation of kaolin clay reconstituted from slurry (water saturated) and dried kaolin (air-saturated). Circles indicated sample tested in MIP.

For the pore size distribution of air-water saturated samples (unsaturated samples), MIP data presented by Tarantino & De Col (2008) were considered. The samples were compacted to 1200 kPa vertical stress with water content

ranging from 0.08 to 0.32 (Figure 72), and dehydrated by freeze-drying technique as described above.
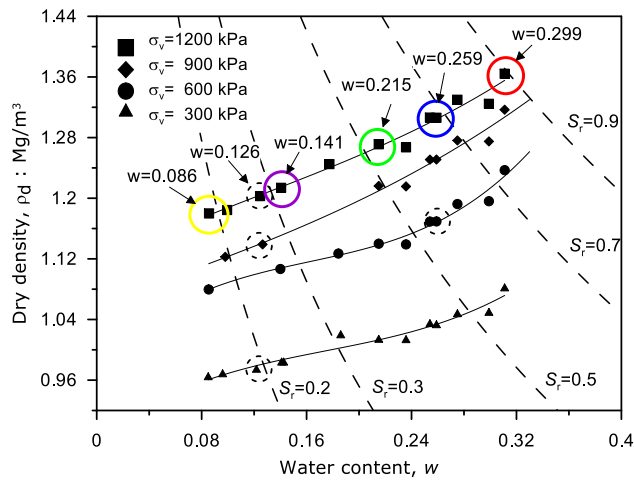
Figure 72. Post compaction dry density against water content of statically compacted kaolin. Circles indicate sample tested in MIP tests. (Tarantino & De Col, 2008)

Results

Figure 73 shows the pore size distribution of water-saturated kaolin and air-saturated kaolin both compressed to 2220 kPa vertical stress (as reported in Figure 71). The kaolin sample reconstituted from slurry (water-saturated), taken on the ncl, shows a mono-modal pore size distribution with the diameter modal value of about 0.16 μm (Figure 73). On the other hand, dry powder (air-saturated) shows a modal value of 0.50 μm (Figure 73).
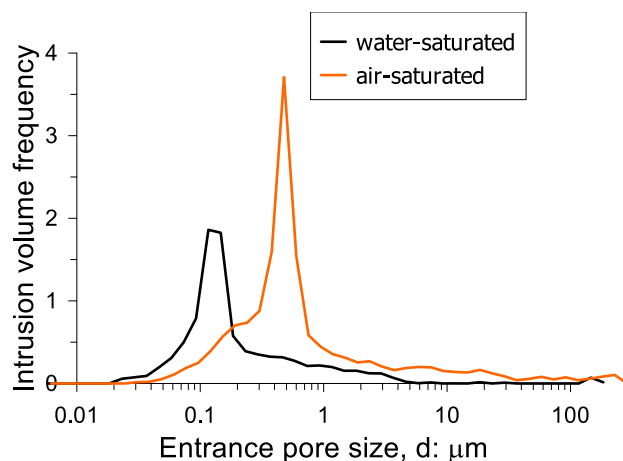
Figure 73. Pore size distribution of ncl sample of water-saturated and air-saturated kaolin

Figure 74 compares the pore size distribution of water-saturated and air-saturated kaolin with the pore size distributions of air-water saturated kaolin samples compacted to 1200 kPa vertical stress at different water contents (compaction data from Tarantino & De Col (2008).

The most striking aspect is that the two modal values of the frequency pore size distribution of the compacted air-water saturated samples occur essentially at the same pore size regardless of the compaction water content. The pore size of the micro-pores (generally referred to as "intra-aggregate pores") corresponds to the dominant pore size of the water-saturated samples (reconstituted from slurry) whereas the modal diameter of the macro-pores (generally referred to as "inter-aggregate pores") corresponds to the dominant pore size of the air-saturated sample. The straightforward conclusion that could be drawn from Figure 74 is that macro-pores are filled with air and micro-pores are filled with water. This is an unusual view of micro-structure of unsaturated compacted soils and therefore further investigation was envisaged.
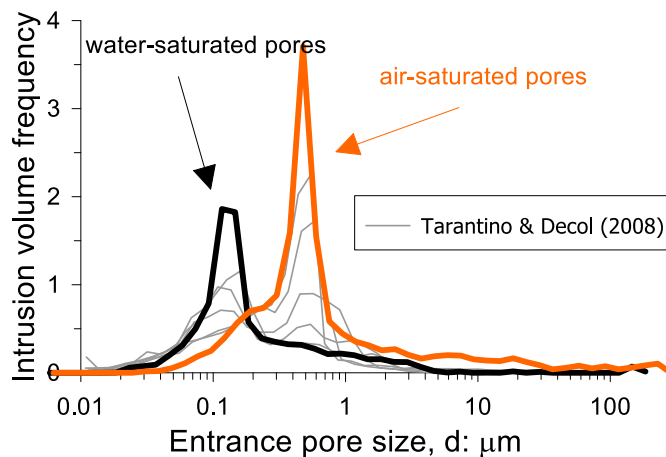
Figure 74. Pore size distribution of ncl sample of reconstituted kaolin and compressed kaolin dry powder compared with compacted kaolin pore size distributions.

4.2.2 **Nature of the pore fluid in the macro-pores**

When water is removed from a clay sample by oven-drying, suction attains very high values and generates irreversible compression. The class of pores where water is present would therefore be the class of pores affected by oven-drying.

Kaolin samples were prepared at water content of 0.12 and 0.22 and compacted to 1200 kPa vertical stress. For each water content, two different dehydration techniques were considered, freeze-drying (already described in the previous sections) and oven drying.

As shown in Figure 75 and Figure 76, the macro-pores are unaffected by the dehydration technique whereas a shift towards smaller diameter can be observed for the micro-pores. The macro-pores, because of their bigger dimensions, should be more compressible than micro-pores. When suction increased, significant non-recoverable compression of the macro-pores should have occurred if water was present in the macro-pores. This evidence seems to support the assumption that macro-pores are filled with air and water is only located into the micro-pores.
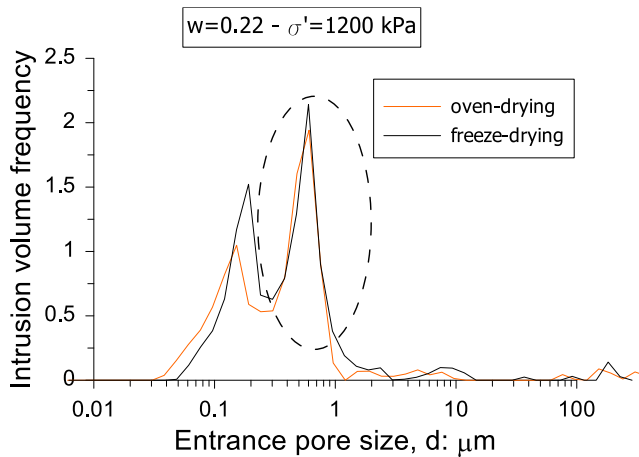
Figure 75. Compacted kaolin at water content 0.22 and 1200 kPa vertical stress. Sample prepared with oven-drying and with freeze-drying technique.
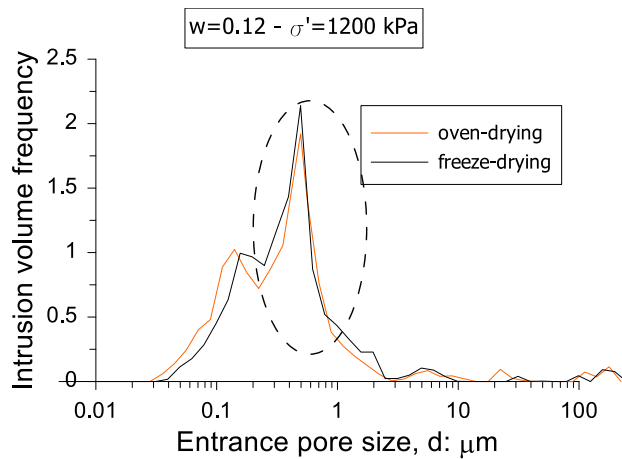
Figure 76. Compacted kaolin at water content 0.12 and 1200 kPa vertical stress. Sample prepared with oven-drying and with freeze-drying technique.

4.2.3 Nature of the pore fluid in the micro-pores

Pore-fluid in the micro-pores upon wetting from air-saturated state

If the micro-pores are fully saturated with the wetting fluid (water), the size of the micro-pore should be controlled by the nature of the wetting fluid. It has been shown in Chapter 3 that inter-particle distance is controlled by the dielectric permittivity of the pore fluid. It would therefore be expected that replacing water with a wetting fluid having different dielectric permittivity will cause the micro-pores to change their modal size. Again, if the macro-pores are only filled with air, no differences should be observed in the pore-size distribution of the macro-pores when replacing water with another wetting fluid.

To this end, kaolin samples were mixed with acetone (instead of water) at different acetone contents and compacted to the same vertical stresses as the samples investigated by Tarantino and De Col (2008) shown in Figure 74.

As the dielectric permittivity of acetone is about 24, the distance between particles soaked with acetone must be higher than the ones soaked with water and smaller than the particles 'soaked' with air (Figure 77). A shift towards higher pore size would therefore be expected for the micro-porosity.

Compacted samples are here assumed to be associated with a hydraulic main wetting path. To prepare compacted samples, water is added to dry powder and initially dry pores are therefore saturated with a wetting fluid for the first time upon the addition of water.
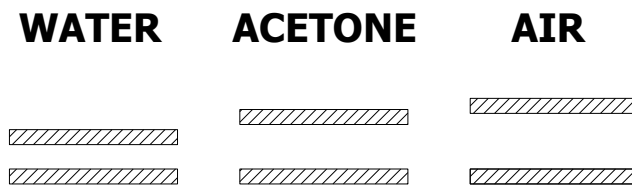
WATER   ACETONE   AIR

Figure 77. Particle 'non-contact' configuration for different pore fluids.

Experimental procedures

A set of compacted samples was prepared as described in Tarantino & De Col (2008) but using acetone instead of water (air/acetone saturated samples). Air/acetone saturated powders were prepared at 0.10, 0.20 and 0.30 acetone content (mass of acetone/mass of solid). Afterwards the sample was compacted to 300, 600, 900 and 1200 kPa vertical stress. Although no drainage was allowed during test and proper sealing was provided, the acetone content did not remain constant during static compaction because of the high volatility of acetone. In order to reduce the amount of evaporation of acetone none of the compaction tests took more than 30 minutes. The acetone content was therefore taken at the end of the test. Figure 78 shows the samples prepared by compaction in the compaction plane in terms of void ratio, e, against acetone content, w.

An acetone-saturated sample was also prepared to obtain a reference pore-size distribution for the samples compacted with acetone (air/acetone saturated samples). Oven-dried kaolin was initially placed into the oedometer cell. Once that the powder was in place and the cell set up, the sample was gently saturated with acetone. When the induced consolidation ended the sample was further consolidated one-dimensionally up to a maximum of 2220 kPa vertical stress.
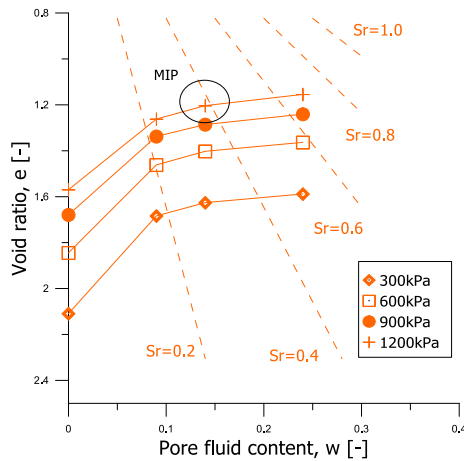
Figure 78. Compaction plan for kaolin compacted with acetone

MIP tests were performed on the kaolin clay sample compacted to 1200 kPa at nominal acetone content of 0.20 (circled in Figure 78) and the acetone-saturated kaolin sample consolidated to 2220 kPa vertical stress (circled in Figure 79).

The dehydration of samples saturated with acetone was performed by oven-drying technique. As describe in chapter 3, microstructure of samples in acetone, in contrast with samples prepared with water, was assumed to be slightly affected by the oven-drying. This is because much lower suctions develop in presence of acetone in the soil pores. Acetone surface tension is 0.0252 N/m at 20°, which is three times lower than surface tension of water (0.0728 N/m at 20°). This surface tension decreases with temperature down to 0.0211 N/m at 57°, which is the boiling point of acetone. Since the modal pore-size of micro-pores of samples prepared with acetone is about twice the modal pore-size of the macro-pores prepared with water, suctions developed in presence of acetone are about 6-7 times smaller than suctions developed in the presence of water.

To capture an order of magnitude of the suction developed in presence of acetone, let us consider a conservative contact angle between acetone and clay equal to 0° and a pore size of 0.2 μm (the micro-pore modal pore diameter

of acetone/air saturated samples, which is about twice the micro-pore modal pore size of water/air saturated samples). The suction developed in presence of acetone is 252 kPa at 20° and 210 kPa at 57° (compared to the 1450 kPa that is developed in presence of water occupying the micro-pores). This level of suction is much smaller than the total stresses applied during compaction or consolidation.

Results

Figure 79 shows the 1-D compression test of water-saturated, acetone-saturated, and air-saturated samples. As previously discusses (see Figure 77), the void ratio of acetone-saturated sample lies in between the void ratios of water-saturated and air-saturated sample at the same effective vertical stress. Figure 80 shows the pore size distribution of the three samples consolidated to 2200 kPa. The three PSDs all show a mono-modal shape. It is possible to see that the three PSDs are shifted depending on the nature pore fluid and that the modal value of acetone-saturated sample, as expected, is greater than the modal value of water-saturated samples and smaller than the modal value of the air-saturated one.
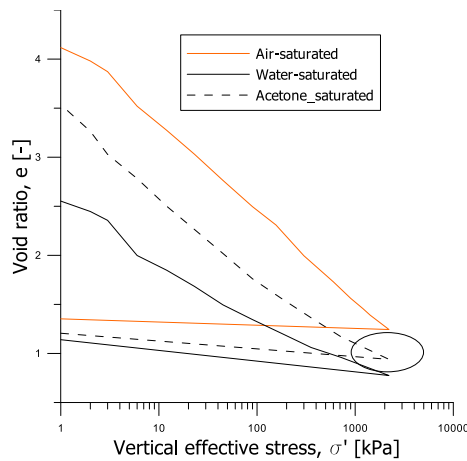
Figure 79. 1D consolidation for water-saturated, acetone-saturated and air-saturated kaolin. Circles indicated sample tested in MIP.
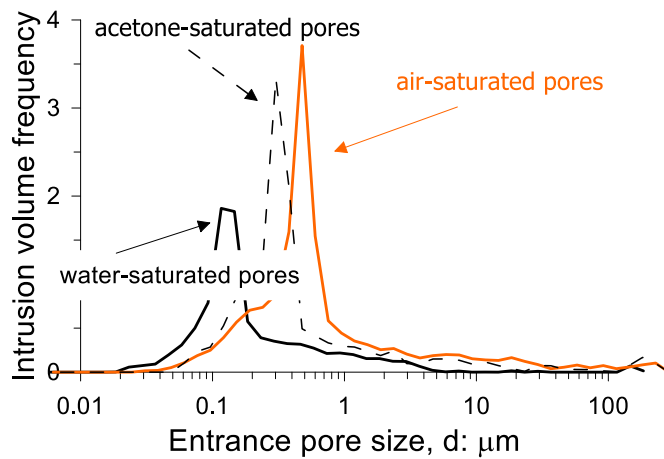
Figure 80. Pore size distribution of sample of kaolin water-saturated, acetone-saturated and air-saturated.

Before inspecting the PSD measured for the acetone/air saturated sample (sample compacted with acetone instead of water), it might be interesting to anticipate the shape PSD according to the assumption that micro-pores are saturated with the wetting fluid (acetone) and macro-pores are saturated with air. One should expect the modal size of the micro-pores coincides with the modal size of the acetone-saturated sample in Figure 80 and that modal size of the macro-pores coincides with the modal size of the air-saturated sample in Figure 80.

Figure 81 shows indeed that the pore size distribution of the air/acetone saturated sample (sample compacted with acetone) shows it to be bi-modal with the micro-pore modal size coinciding with the modal value of the acetone-saturated samples. The micro-pore modal size is clearly shifted on the right with respect to the micro-pore size of the water/air saturated samples. At the same time, no change in the macro-pore size between water/air saturated sample and acetone/air saturated sample is observed and this can be considered as a further evidence of the absence of any kind of fluids other than air in the macro-porosity.

The pore-size distribution of the air/acetone saturated samples is therefore the combination of the pore size distributions of the acetone-saturated and air-saturated samples respectively. Similarly, to the water/air saturated samples,

the two classes of pores present in a compacted sample are the consequence of the two different pore fluids coexisting within the sample, which cause particles to have different distances due to the different dielectric permittivity.
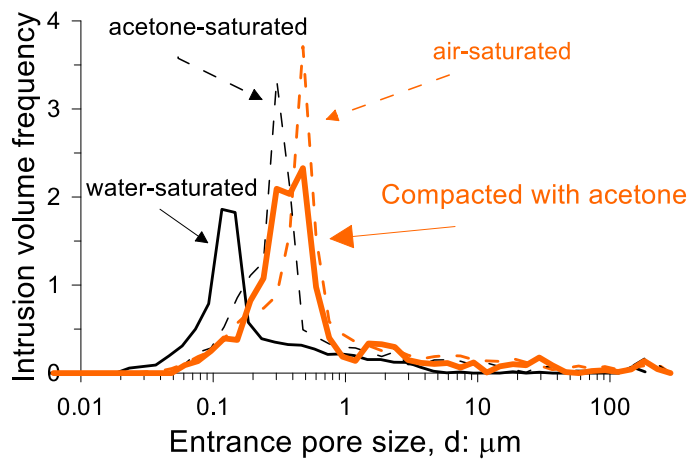
Figure 81. Pore size distribution of kaolin compacted with acetone, compared with pore size distibution of water-saturated, acetone saturated and air-saturated samples.

Suction generated by air-acetone menisci is expected to be at least 1/3 of the one generated by air-water menisci, since the air-acetone surface tension is 1/3 of the air-water surface tension. If as generally assumed, the macro-porosity is controlled by the menisci existing between the aggregates, lowering the suction should imply a change in the stability of the aggregate. The fact that no change in the macro-pore size between water/air saturated sample and acetone/air saturated sample must be considered as a further evidence of the absence of any kind of fluids other than air in the macro-porosity.

Pore-fluid in the micro-pores upon drying from water-saturated state

As shown in Figure 75 and Figure 76, water appears to present only in the micro-pores as only the micro-pores are affected by oven-drying. When such water is removed from the sample, the micro-pores desaturate and eventually dry out completely. To investigate the behaviour of water-saturated micro-pores upon drying, the evolution of the void ratio and pore size distribution of a sample reconstituted from slurry and then dried was considered.

Experimental procedure

Void ratios of samples of kaolin clay consolidated at 100 kPa and then let dry to different target water contents have been taken from Tarantino (2010). Experimental data for a range of water contents from 0.55 to 0.01 are reported in Figure 82.
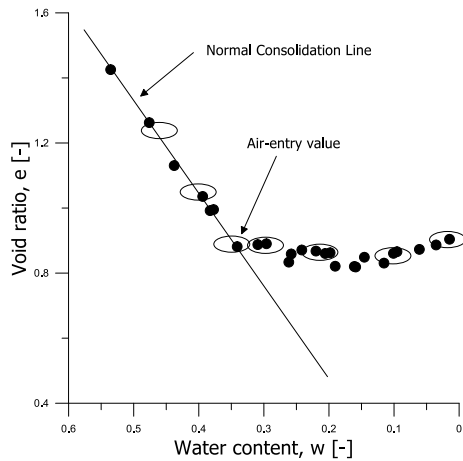
Figure 82. Volume deformation of reconstituted kaolin from slurry upon drying (circles=MIP tests)

MIP tests were performed on samples of kaolin consolidated and dried to target water contents adopting the same procedure described in Tarantino (2010). Seven samples were prepared having water contents of 0.01, 0.09, 0.21, 0.28, 0.32, 0.40 and 0.47. When samples reached the target water content, freeze-drying was performed to dehydrate the samples in order to perform a MIP test. Freeze-drying technique and MIP test procedure were performed as already described in the previous sections.

Results

As shown by data presented in Figure 82, upon drying kaolin reconstituted from slurry shrinks until the air-entry value is reached and the sample starts to de-saturate (at about w=0.32 corresponding to a suction of about 900 kPa according to Tarantino 2010). When desaturation starts no further reduction in the void ratio can be spotted but a slight swell at very low values of degree of saturation (Figure 82)

Pore size distributions of sample reconstituted from slurry and then dried to water content ranging from 0.47 to 0.01 are reported in Figure 83.
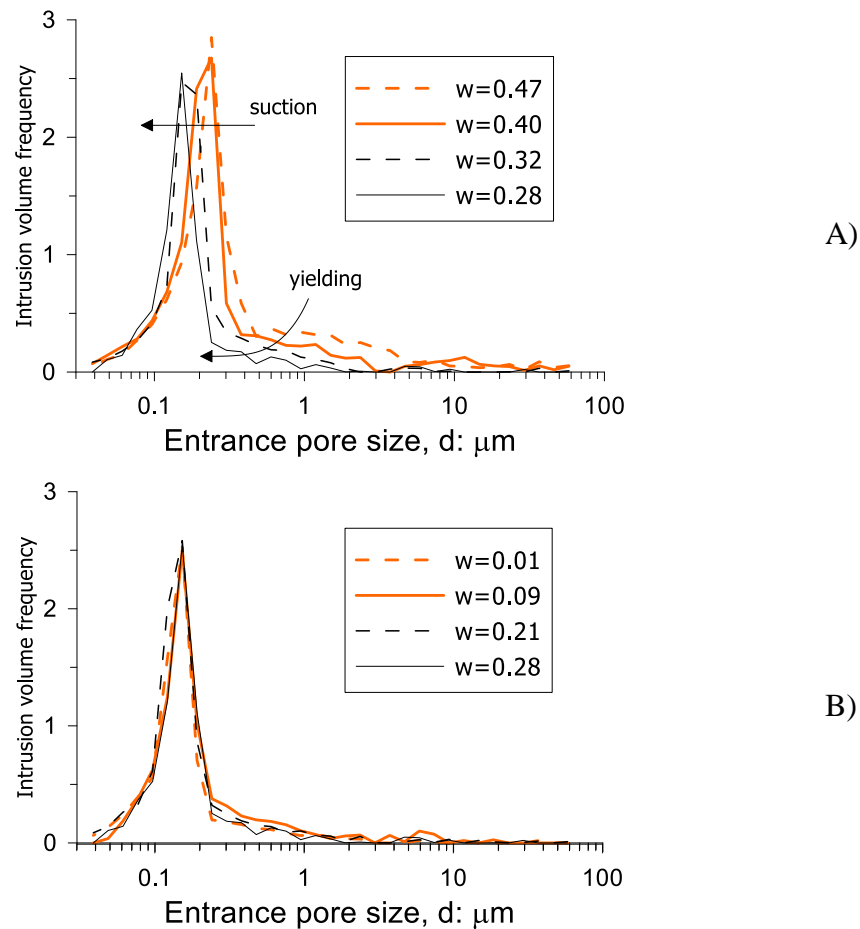
Figure 83. Pore size distribution of reconstituted sample from slurry upon drying. A) saturated samples. B) partially saturated samples.

In Figure 83a pore size distributions of saturated and quasi-saturated specimens are reported (water content from 0.47 to 0.28). It is possible to note that the decrease in water content (and an increase in suction) causes the pore size distributions to shift to the left. Two possible trends can be detected: i) the modal values (micro-pores associated with non-contact configuration) become smaller and ii) pore distributions on the right-side of the modal value (macro-pores in fluid-saturated samples) decrease in frequency. Such behaviour can be associated with yielding and this is consistent with the data in Figure 82 showing that the void ratio of the samples with water content higher than 0.32 lies on the ncl.
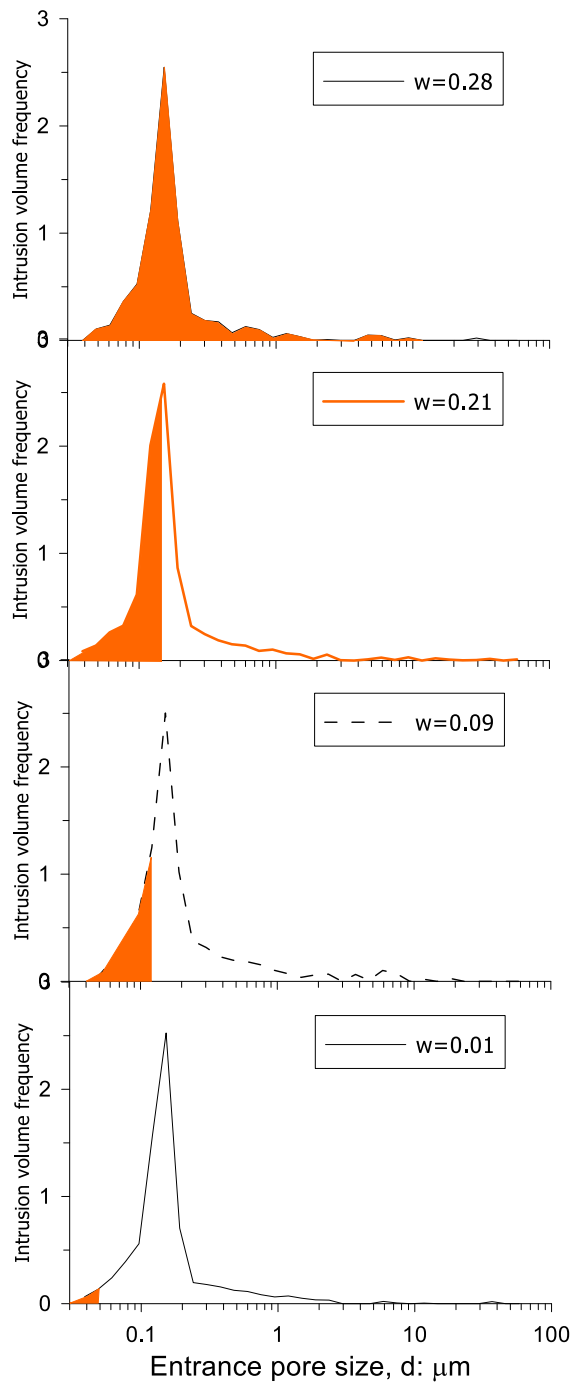
Figure 84. Evolution of pore size distribution of reconstituted kaolin from slurry upon drying and comparison with the water void ratio. Partially saturated samples.

Samples having water content equal to 0.47, 0.40, 0.32 and 0.28 are all saturated. Therefore, even if menisci are present on the external boundary of the sample, they do not recede into the sample. Their position is virtually steady. The loss of water caused by the drying compels the whole sample to

shrink. Since the degree of saturation is equal to 1, any increase in suction generates a decrease in the meniscus curvature which can be accommodated by a reduction of the pore size.

The pore size distributions of specimens after desaturation (when the air-entry value has been exceeded and the degree of saturation starts decreasing) is shown in Figure 83b. Pore size distributions do not show any difference, they all look very similar. The micro-pores are not subjected to any kind of variation despite the fact that the water content has been reduced from 0.28 to 0.01 and the degree of saturation has been dropped from values of about 0.90 to almost 0. Therefore, when a water-saturated micro-pore is subjected to an increase in suction, it shrinks as long as it remains saturated. At the air-entry value, micro-pores gradually de-saturates preserving their pore size at the air-entry value, as shown in Figure 84.

Possible mechanisms of micro-pore response upon drying

To explain the response of initially water-saturated pores upon drying, two possible mechanisms have been considered. Figure 85a shows the cumulative pore-size distribution of the data presented in Figure 83a. An 'air-entry pore size' d_{entry} associated with a PSD was defined by considering the intersection between the tangent to the curve at the modal value (inflection point) and the x-axis as shown by the graphical construction in Figure 85a for the arbitrary value of w=0.40 . The air-entry pore size for each sample was then associated with the suction to which each sample was subjected (according to the data by Tarantino (2010). The data points are shown as solid circles in Figure 85b.

The maximum suction that each air-entry pore size can sustain was then calculated using the Washburn's equation (Equation 38).

$$s = \frac{4\gamma}{d_{entry}} cos\theta \qquad [38]$$

This equation is also shown in Figure 85b as continuous line.
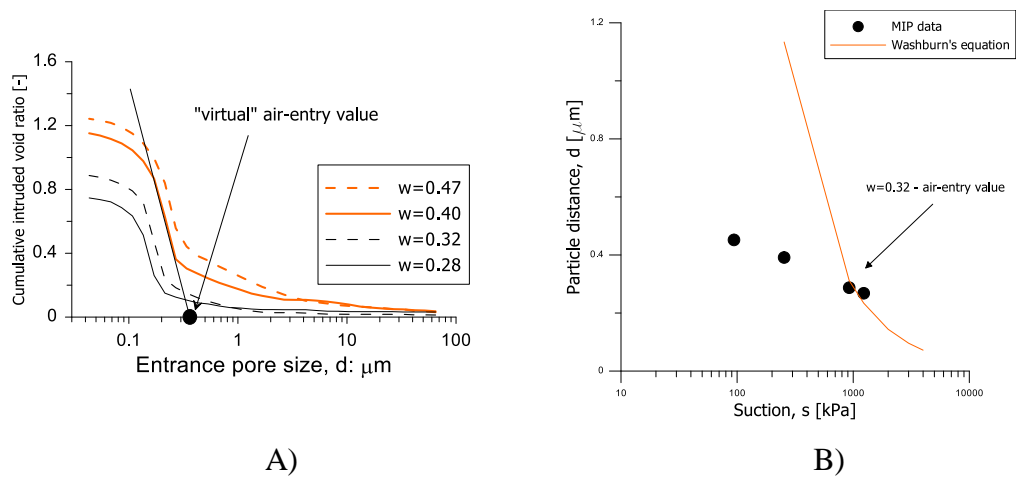
Figure 85. Particle distance versus suction from microscopic and macroscopic data. a) virtual air-entry value computation. b) Particle distance trend comparison.

It is interesting to note that that the experimental data and the Washburn's equation intersect at around 900 kPa, which is very consistent with the value of suction at which the sample starts desaturating macroscopically.

For a given particle distance, d, the Washburn's equation shows the maximum suction that the air-entry pore can develop before the menisci start receding into the inner pores. On the other side, the experimental data show the suction required to hold the particles at such distance, i.e. the suction required to equalise the interparticle repulsion. The region where the maximum suction is higher than the actual suction can be considered as the region where the pores remain saturated. In this area, any increase in suction corresponds to a decrease in particle distance.

Beyond the macroscopic air-entry value, where the maximum suction that the air-entry pore can sustain is smaller than the actual suction, menisci will start receding into the smaller micro-pores.

If pores became totally dry, they would swell up to dimensions equal to macro-pores (air-saturated pores), as indeed suggested by Tarantino (2010). The pore size distribution of a sample subjected to a drying path would then show two different classes of pores. The first would correspond to the pore

size of water-saturated pores (which reduces as suction increases) whereas the second would correspond to pore that are totally dry (air-saturated).

This response is not observed. When a reconstituted sample is subjected to an increase in suction (drying path)

i)   Water-saturated pores reduce in size as suction increases until the meniscus does not recede into the pores

ii)   Pores that were water-saturated and are now dehydrated stop shrinking.
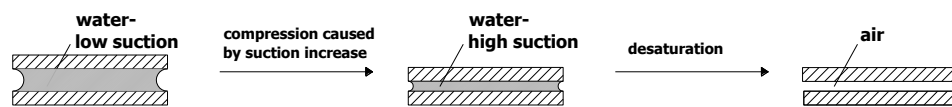
Figure 86. Drying mechanism

The no change in size of micro-pore as they de-saturate could tentatively be explained by invoking Van der Waals effect or a mechanism similar to the one suggested by Fisher (1926), or a combination of both.

Van der Waals forces are considered to be relevant when particle distance is at least few tens of nanometres (Figure 87). When such particle distances are reached, energy of interaction is at a local minimum (commonly called energy trap) and thus in equilibrium, as described by the well-known DLVO theory (Gouy, 1910, D. L. Chapman, 1913, Derjaguin & Landau, 1941).
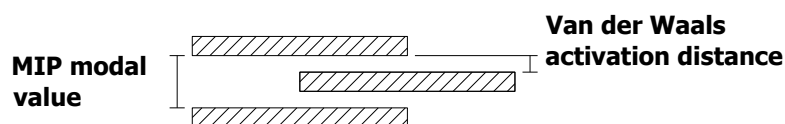
Figure 87. Possible explanation for Van der Waals activation

On the other hand Fisher (1926) demonstrated that the interparticle forces caused by the presence of menisci at the inter-particle contact between two spherical particles does not change significantly when the meniscus recedes. Similarly, it is possible to demonstrate that the total force exerted by the meniscus forming between two plate-like particles does not change when the meniscus recedes.
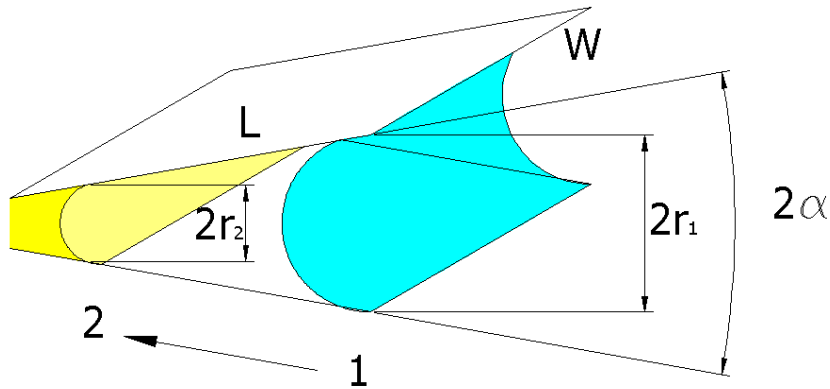
Figure 88. Mensicus receding between two sub-parallel particles

When the meniscus recedes, the suction increases and the wet area decreases.

Let us consider the case of two clay particles having width *W* and length *L* forming an angle 2α as shown in Figure 88. If $2r$ is the particle distance at the meniscus contact, the forces F_1 and F_2, associated with the meniscus in position 1 and position 2 respectively, can be computed as follows:

$$F_1 = s_1 W L_1 \cos \alpha \qquad\qquad F_2 = s_2 W L_2 \cos \alpha$$

$$L_1 = \frac{r_1}{\sin\alpha} \qquad\qquad L_2 = \frac{r_2}{\sin\alpha}$$

$$s_1 = \frac{2\gamma}{r_1} \qquad\qquad s_2 = \frac{2\gamma}{r_2} \qquad\qquad [39]$$

$$F_1 = \frac{2\gamma}{r_1} W \frac{r_1}{\sin\alpha} \qquad\qquad F_2 = \frac{2\gamma}{r_2} W \frac{r_2}{\sin\alpha}$$

$$F_1 = F_2 \rightarrow \frac{2\gamma}{\sin\alpha} W = \frac{2\gamma}{\sin\alpha} W \qquad\qquad [40]$$

Equation 39 is an identity. This implies that, for any angle between the two particles, the applied force remains constant when the meniscus recedes. This implies that once that the meniscus starts receding no shrinkage or swelling is to be expected (Figure 89).
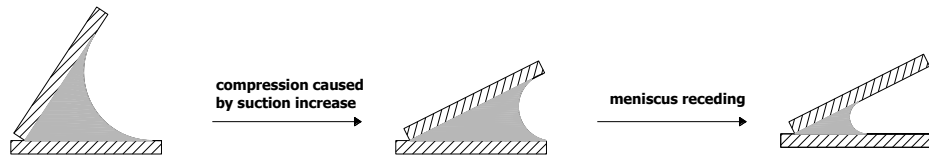
Figure 89. Conceptual model for no change in pore-size upon desaturation of the pore

4.3 A particle-based microstructural conceptual model for partially saturated soils

According to the experimental data presented above, a microstructural conceptual model is formulated here based on the assumption that microstructure is controlled by particle-to-particle interaction. The features of the model can be summarised as follows:

i)   samples born air-saturated are only formed by macro-pores
ii)   samples born water-saturated are only formed by micro-pores
iii)   macro-pores (born air-saturated) that are wetted become micro-pores
iv)   micro-pores (born water-saturated) that are dried remain micro-pores

Pores that are born water-saturated and air-saturated can be associated with 'virgin' states. In particular, water-saturated pores are associated with reconstituted-from-slurry state and air-saturated pores are associated with initially dry powder. When both air-saturated and water-saturated pores are present, it follows that:

v)   the mechanical response of the saturated part can be associated with the response of the saturated clay in reconstituted state (clay prepared from slurry) and the mechanical response of the dry part can be associated with the response of the dry (air-saturated) powder.

According to the microstructural conceptual model laid down in the Chapter 3, the water-saturated and air-saturated clays are characterised by a mono-modal PSD. The pores on the left-hand side of the modal value are associated with non-contact configuration and pores on the right-hand side of the modal value are associated with contact configuration (Figure 90). The difference in size of the two peaks (water-saturated and air-saturated pores) is here assumed to be due to the different dielectric permittivity of the pore fluids, which controls the inter-particle distance and, hence, the inter-particle volume.
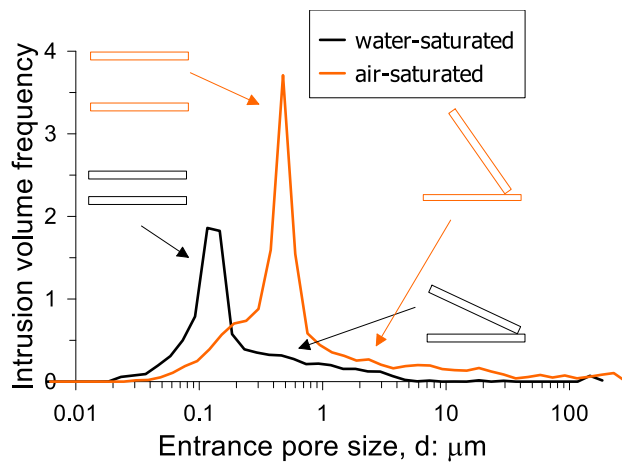
Figure 90. Classes of pores according to the particle configuration for water-saturated and air-saturated samples

If an air-water saturated compacted sample is assumed to be made by pores that are water saturated and pores that are air-saturated, four classes of pores are to be expected (2 classes of pores per each pore fluid) as shown in Figure 90:

- Porosity related to particles in non-contact configuration saturated with water (approximately a log-normal distribution centred around the peak of the micro-pores)
- Porosity related to particles in contact configuration saturated with water (tail on the right-hand side of the smaller peak)
- Porosity related to particles in non-contact configuration saturated with air (approximately a log-normal distribution centred around the peak of the macro-pores)
- Porosity related to particles in contact configuration saturated with air (tail on the right-hand side of the bigger peak).

For the sake of simplicity and to be aligned with the traditional nomenclature, all the pores related to the first peak, which are related to water-saturated pores, will be referred to as micro-pores and the ones related to the second peak, which are related to the air-saturated pores, will be referred to as macro-pores.
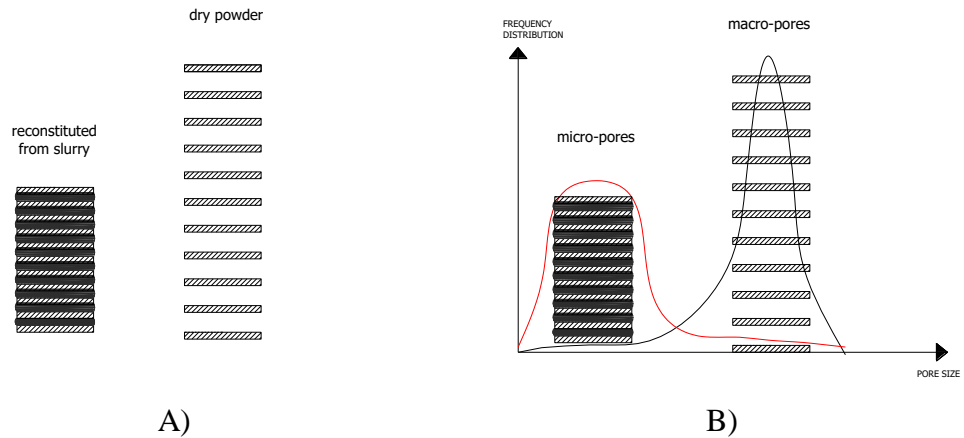
Figure 91. Schematic representation of samples reconstituted from slurry and dry powder. a) particle arrangement. b) PSD conceptual model.

Accordingly a sample reconstituted from slurry and a sample of dry powder can be schematized as reported in Figure 91a and the respective PSD as in Figure 91b. For the sake of simplicity, only particles in non-contact configuration are shown in the figure.
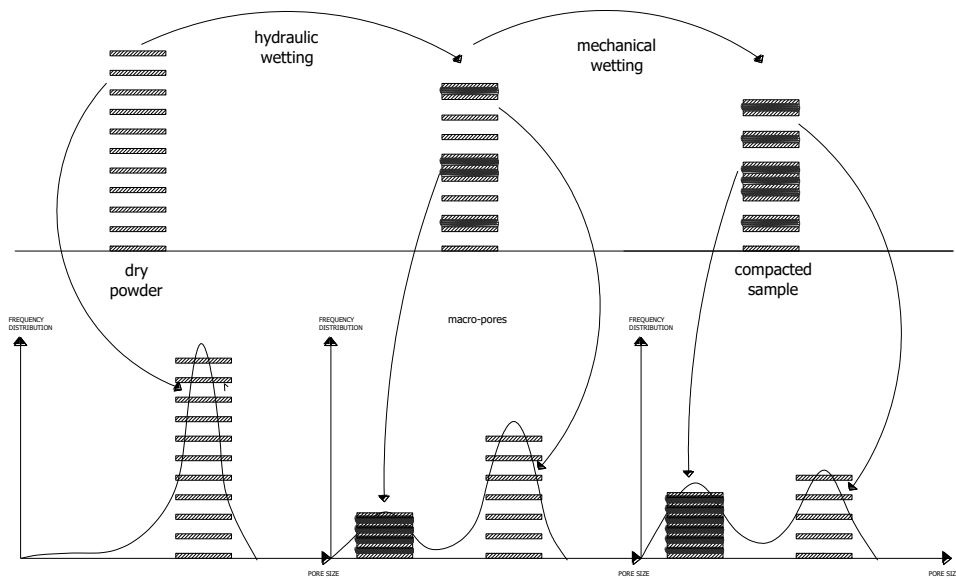
Figure 92. Compacted sample formation

Applying the same criteria, the formation of a compacted sample can be schematised as in Figure 92. A compacted sample can be considered as a

sample born air-saturated, then partially wetted (hydraulic wetting) and finally mechanically compressed (mechanical wetting). As it is possible to see, the micro-porosity increase both upon hydraulic and mechanical wetting as the degree of saturation increases.

Three different mechanisms for the evolution of the pores size must be considered upon compression (Figure 93):

i)   Pores that are water-saturated behave as they were on the water-saturated compression curve, showing the same reversible and non-reversible mechanisms as water-saturated samples (particle slippage and tilting).

ii)   Pores that are air-saturated and remain air-saturated behave as they were on the air-saturated compression curves showing the same reversible and non-reversible mechanisms as air-saturated samples (particle slippage and tilting).

iii)   Air-saturated pores that during load undergo on mechanical wetting and become water saturated change from macro-pores to micro-pores.
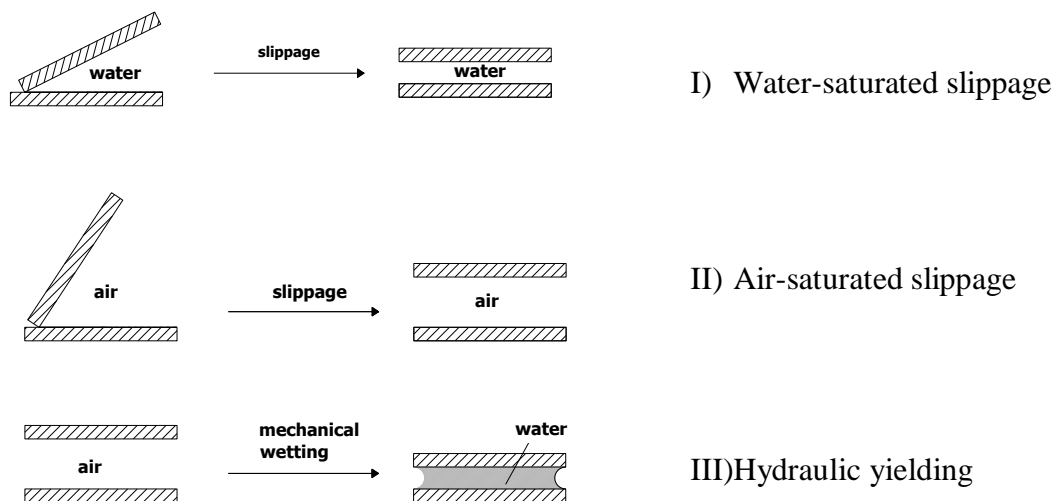
Figure 93. Non reversible mechanisms according to the particle-based model

Since the first two mechanisms are the ones that exist in air-saturated and water-saturated conditions, and they have been extensively explained in the previous chapter, for the sake of simplicity only the third mechanism will be the focus of the rest of the chapter.

4.4 Revisiting pore-size distribution data from the literature

Figure 94 compares the particle-based conceptual model with the traditional aggregate-based model. This section will show that particle-based conceptual model is equally capable of explaining, at a qualitative level, distinctive features of the microstructural and macroscopic response of unsaturated compacted clays.
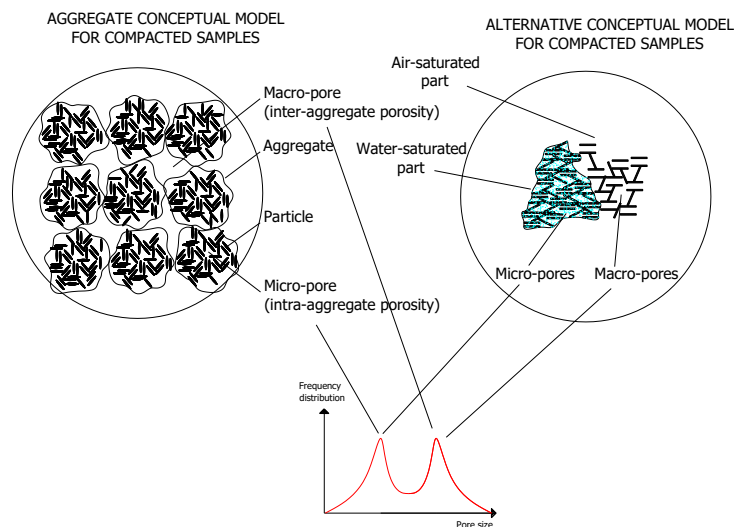
Figure 94. Comparison between traditional "aggregate-based" model and the proposed alternate "particle-based" conceptual model.

4.4.1 Bi-modal pore-size distribution of clays compacted at different water contents

A compacted sample is unsaturated and this gives rise to a class of pores associated with the presence of water and a class of pores associated with the presence of air.

The frequency of the two classes of pores will depend on the amount of water present in the sample and, hence, on the degree of saturation. According to

the particle-based microstructural model, the higher the water content, the higher is the number of micro-pores to be expected as shown in Figure 95.

(A)   *(B)*
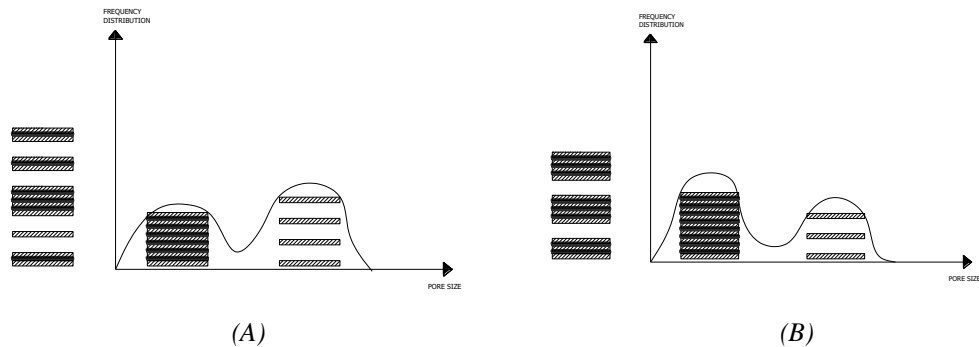
Figure 95. Anticipated pore size distribution for samples compacted at different water content. (a) lower water content; (b) higher water content.

Figure 96 shows two samples of kaolin compacted at water contents of 0.22 and 0.28 (data Tarantino & De Col 2008). The pore space occupied by water is also visualised in Figure 96 (shaded area) and was derived by assuming that the measured pore-water volume saturates the smallest pores.
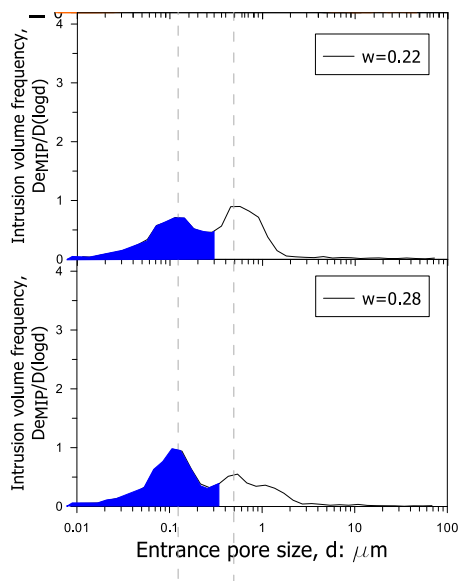
Figure 96. Evolution of pore size distribution of compacted kaolin at different water content and 1200 kPa of vertical stress and comparison with water void ratio. Data taken from Tarantino & De Col (2008)

It can be observed clearly that water only occupies the micro-pores, which is consistent with the assumption that micro-pores are the water-saturated pores in the particle-based microstructural conceptual model. It can also be observed that the higher the water content (w=0.28) the higher is the frequency of the micro-pores, which is consistent with the prediction of the particle-based microstructural model as shown in Figure 95.

4.4.2 Compacted samples with mono-modal pore size distribution

If a sample is compacted at very high water content (close to optimum), most of the pores will be saturated and the air-saturated pores will only be small fraction of the total pores. The pore-size distribution would therefore appear as in Figure 97a. On the other hand, if a sample is compacted at very low water content, most of the pores will be dry (air-saturated) and the water-saturated pores will only be small fraction of the total pores. The pore-size distribution would therefore appear as in Figure 97b.

(A)   *(B)*

Figure 97. Anticip0ated pore size distribution of samples compacted at (a) very high or (b) very low water content.

Figure 98 shows the pore-size distributions of two samples compacted at very low or very high (close to optimum) water content respectively (Tarantino & De Col (2008). These are consistent with the pore size distributions depicted in Figure 96 based on the particle-based microstructural model.
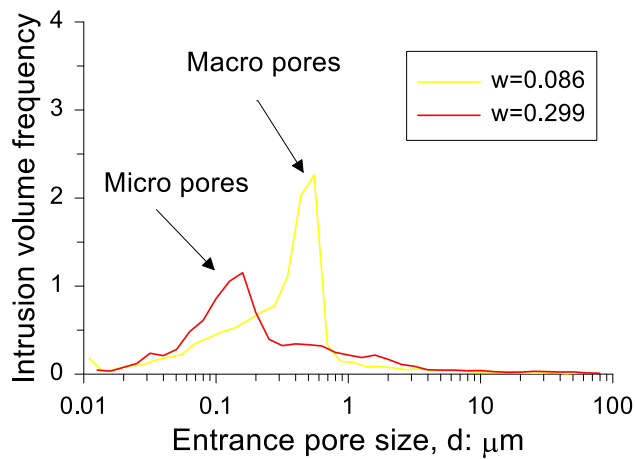
Figure 98. Pore size distribution of kaolin clay compacted at very high or very low water content respectively (Tarantino & De Col, 2008)

4.4.3 Evolution of pore size distribution upon wetting

If water content is increased in a compacted sample, the following mechanisms would take place according to the particle-based microstructural model:

i)   Micro-pores, which are water-saturated, will swell because of the reduction in suction (Figure 99a).

ii)   A part of macro-pores will become water-saturated. The pore fluid 'switches' from air to water, and therefore the pore size is expected to change as consequence of the changing in the inter-particle forces (Figure 99b).

iii)   A part of the macro-pores, which are air-saturated, remains unaltered as long as they remain dry.

Consequently, the following evolution of the pore size has to be expected in a compacted sample when wetted (Figure 100). The air-saturated macro-pores should reduce their frequency with no change in modal size whereas the water saturated micro-pores should increase their frequency with the modal size also increasing according to the mechanism in Figure 99a.
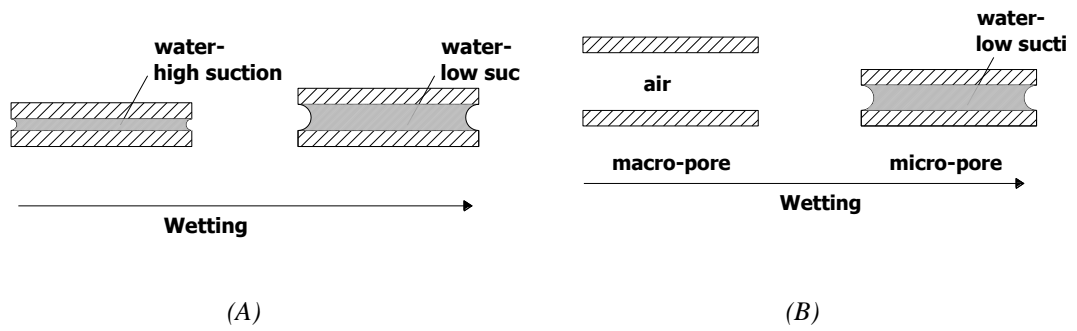
Figure 99. Micro-mechanisms upon wetting: (a) volume increase of initially saturated pores and (b) volume decrease of initially air-saturated pores subjected to wetting.
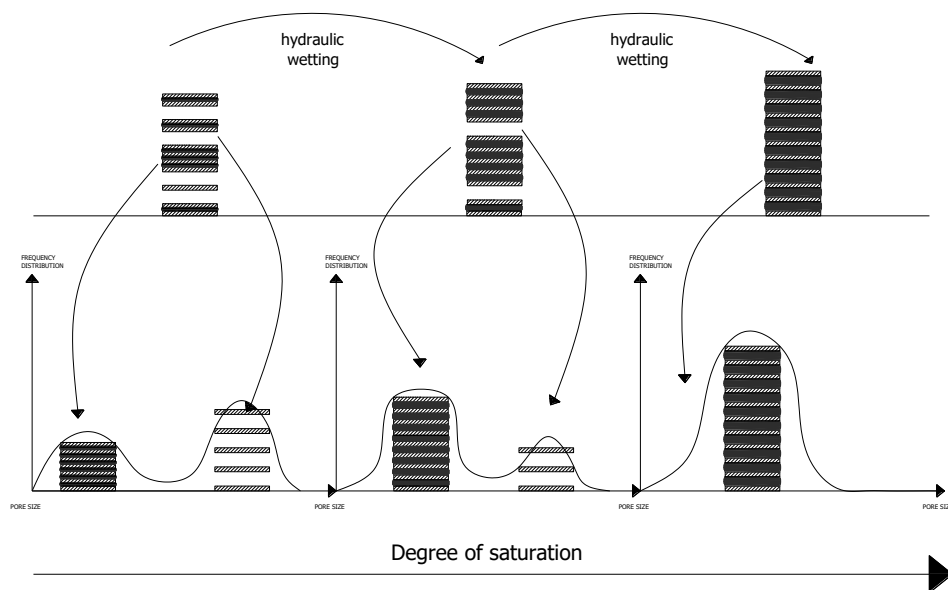
Figure 100. Evolution of the pore size distribution of a compacted sample upon wetting

Monroy (2006) investigated the evolution of the pore size distribution of London clay compacted on the dry side of optimum and then progressively wetted until saturation was achieved in a suction controlled osmotic oedometer.

As shown in Figure 101, the pore size distributions show a decrease in the volume associated with the macro-pores upon wetting. However no change in the modal size of the macro-pores was observed (as long as the macro-pores

exist). On the other hand, the micro-pores, which are filled with water, increase their frequency. Besides, the decrease in suction causes the micro-pores to swell. This is consistent with the evolution of pore-size distribution anticipated in Figure 100.
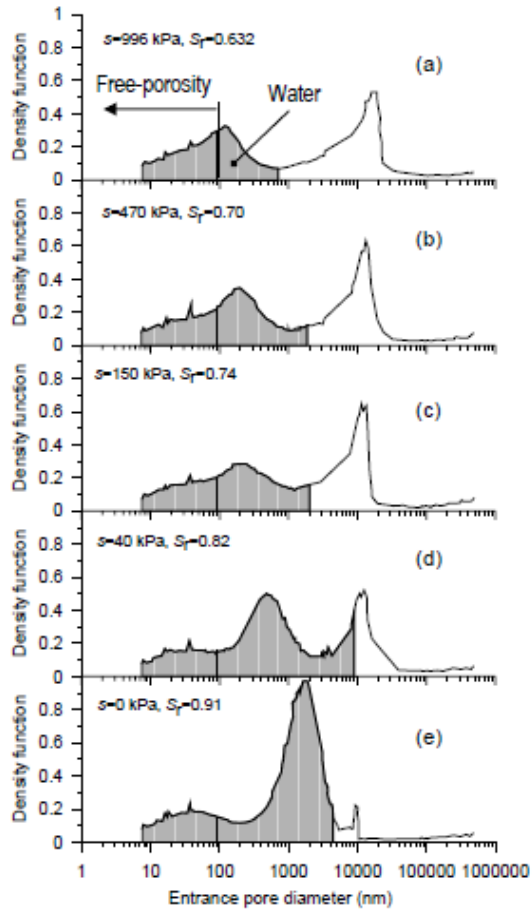
Figure 101. Evolution of pore size distributions of compacted London clay upon wetting (Monroy (2006) after Tarantino (2010))

4.5 Probing the particle-based conceptual microstructural model

4.5.1 Wetting of compacted kaolin

Rationale

When a sample is compacted and then saturated two types of mechanisms are expected (Figure 102):

i)   Water-saturated pores swell because of the decreasing suction

ii)   Air-saturated pores become water-saturated and they collapse.
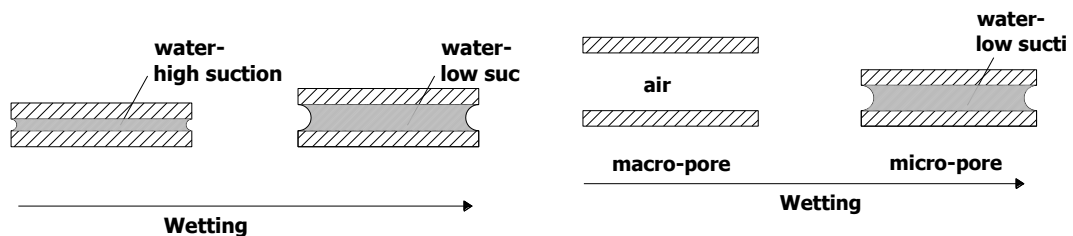
A) Micro-pore swelling   B) Macro-pore collapse

Figure 102. Conceptual model for interparticle space evolution upon wetting of compacted kaolin

Accordingly, one part of the sample (the water-saturated one) swells whereas the part that is initially air-saturated and then wetted collapses. The macro-behaviour is the sum of these two mechanisms, and therefore, depending on the amount of swelling and collapse the overall volume of the sample may reduce or increase.

It is worth underlining that the aggregate-based conceptual model will predict similar response. The macroscopic swelling is associated with the swelling of the aggregates due to the suction decrease and the macroscopic volumetric collapse is associated with the aggregate slippage due to the removal of the stabilising effect of the menisci at the inter-aggregate contact.

The particle-based model can be further exploited. Two samples compacted at the same water content but at different vertical stresses are reported in Figure 103.
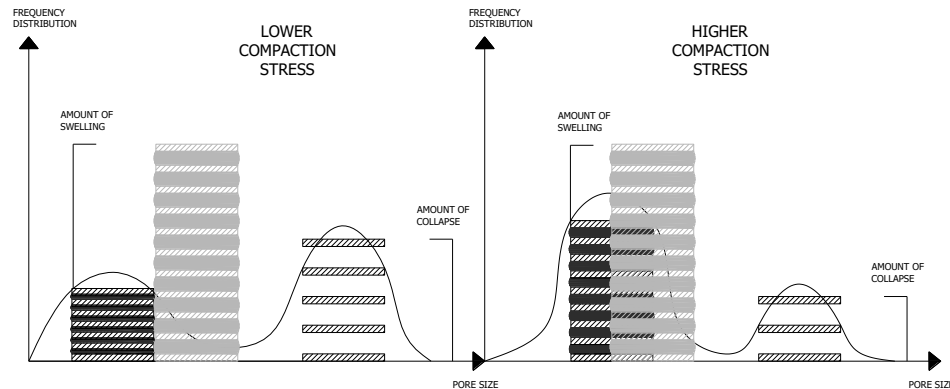
Figure 103. Swelling of two samples compacted at the same water content and different vertical stresses and then saturated unloaded.

The samples in the as-compacted state are reported in black and the samples after being unloaded and saturated is reported in grey. The sample compacted at lower vertical stress has higher suction and therefore the micro-pores are smaller in size than the ones of the sample compacted at higher vertical stress. Moreover, the sample compacted at lower vertical stress has a lower degree of saturation and is therefore characterised by more macro-pores and less micro-pores. When saturated, the two samples will only have micro-pores.

The sketch in Figure 103 shows that the two samples should attain the same void ratio (same height of the column of particles) upon saturation. Nonetheless, the two samples will experience a different degree of yielding (irreversible deformation) associated with the collapse of the initially dry particles in contact and non-contact configuration (for sake of simplicity edge-to-face particles are not shown in Figure 103).

Experimental procedure

Two samples of kaolin clay were compacted at 300 and 1200 kPa vertical stress with a water content of 0.12 in an oedometer cell. After compaction the samples were unloaded and saturated. Afterwards, once saturated, they were consolidated to 2220 kPa vertical stress (Figure 104). Another sample was compacted to 1200 kPa vertical stress at the same water content (w=0.12), saturated under the vertical stress of 1200 kPa, unloaded and consolidated to 2220 kPa vertical stress. The two samples compacted at 1200 and saturated under loaded and unloaded conditions are compared in Figure 105.

A similar set of tests was carried out on kaolin sample compacted to 1200 kPa vertical stress and a water content of 0.24. Again, one sample was saturated before unloading and one sample was saturated after unloading. After saturation consolidation was carried out up to 2220 kPa vertical stress (Figure 106).

The specimens compacted to 1200 kPa vertical stress at water contents equal to 0.12 and 0.24 respectively were prepared for MIP test. In both cases, samples were taken before and after the saturation stage (Figure 107 and Figure 108). Again, dehydration was carried out by means of freeze-drying technique.
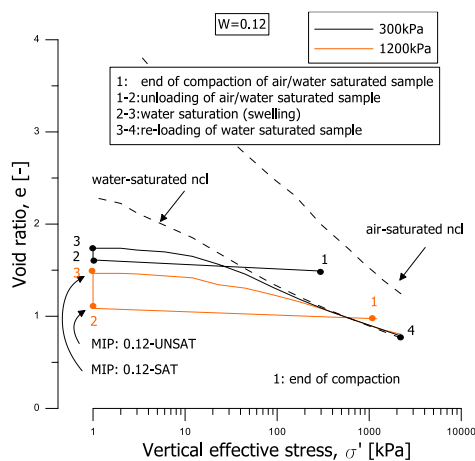
Figure 104. Saturation of kaolin compacted at 300 and 1200 kPa, having moisture content of 0.12.
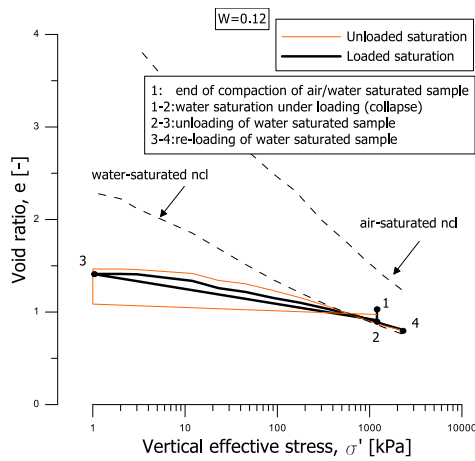
Figure 105. Saturation under loaded and unloaded conditions of kaolin compacted at 1200 kPa, having moisture content of 0.12.
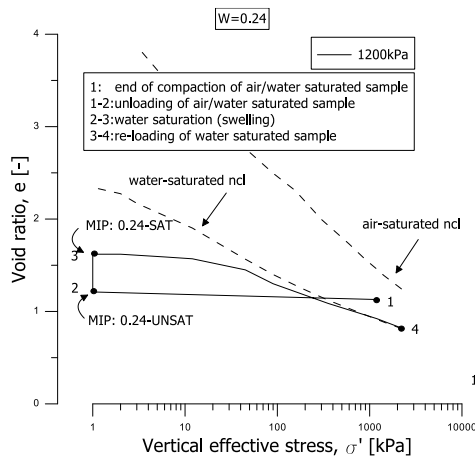
Figure 106 Saturation of kaolin compacted at 1200 kPa, having moisture content of 0.24.

Results

When an air-water saturated sample is water-saturated a swell of the micro-pores and a collapse of macro-pores are expected. As highlighted in Figure 107 and Figure 108, an initial bi-modal pore size distribution becomes mono-modal when the sample is saturated. The macro-pores disappear, becoming micro-pores, and the water-saturated micro-pores, which were subjected to suction, swell, because of the suction reduction. The two initial classes of pores become a unique class, the one corresponding to water-saturated pores at zero suction. The collapse of the macro-pores may or may not prevail on the swelling of the micro-pores depending on the external loading.

If the external (total) stress is high, more slippage of particles in contact configuration and, hence, larger amount of macro-pores collapse upon saturation are expected (Figure 105). On the other hand, at very low total stresses, reduced slippage of particles in face-to-edge configuration would be anticipated and the swelling of the initially water-saturated pores therefore dominates (Figure 104 and Figure 106).

It is worth noting that in both the sample saturated under loading and the sample saturated under unloaded conditions (Figure 105) show the same mechanical behaviour once saturated (path 3-4 in the figure). This result is less trivial than it seems. The fact that the two samples converge to the same normal consolidation line upon loading is not a new concept and this is embedded in the loading-collapse (LC) curve in the Barcelona Basic model. What is worth highlighting here is that the normal consolidation line reached by the compacted sample upon either collapse (path 1-2) or loading (path 3-4) coincides with the normal consolidation line of the clay reconstituted-from-slurry.

This finding leads us to the conclusion that soil samples born under different compaction conditions (water content and compactive effort) and with different apparent microstructure, should be treated as the same soil i.e. unique set of parameter would be required to model constitutive behaviour.

As a further evidence of the commonality between compacted and reconstituted samples, it is worth observing that the pore-size distribution of samples that have been water-saturated corresponds to the pore-size distribution of reconstituted samples (Figure 107 and Figure 108).
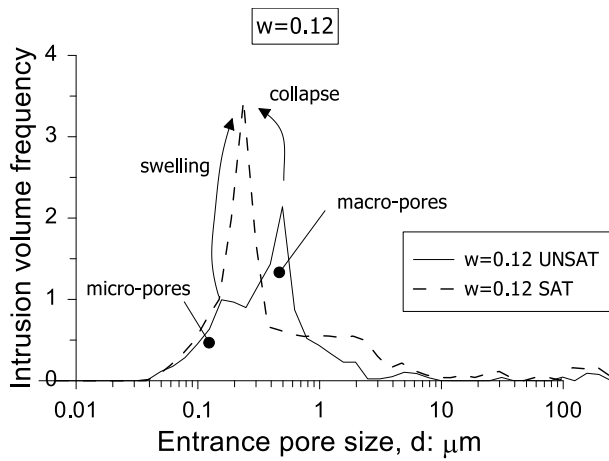
Figure 107. Pore size distribution of compacted kaolin at water content of 0.12 and vertical stress of 1200 kPa. Tests performed before and after the unloaded saturation.
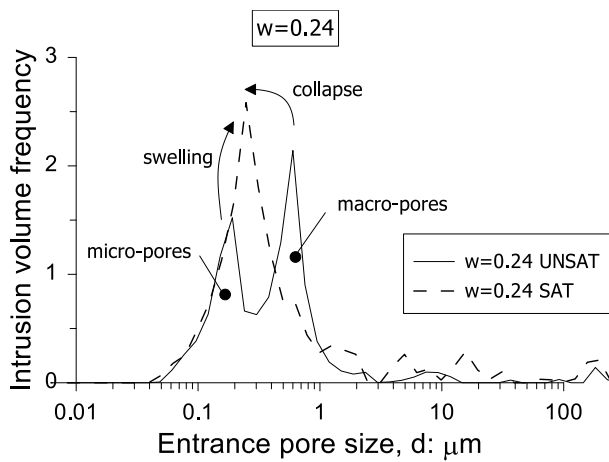
Figure 108. Pore size distribution of compacted kaolin at water content of 0.24 and vertical stress of 1200 kPa. Tests performed before and after unloaded saturation.

4.5.2 Wetting of air-saturated kaolin

Rationale

A sample born air-saturated has a mono-modal pore size distribution (only macro-pores). When such sample is saturated the water will invade all the pores and macro-pores collapse into micro-pores. The evolution of the pore size distribution would be expected to evolve from a mono-modal distribution of macro-pores to a mono-modal distribution of macro-pores (Figure 109).

Accordingly, the void ratio would be expected to move from the compaction curve of the dry powder to the consolidation curve of a reconstituted sample.
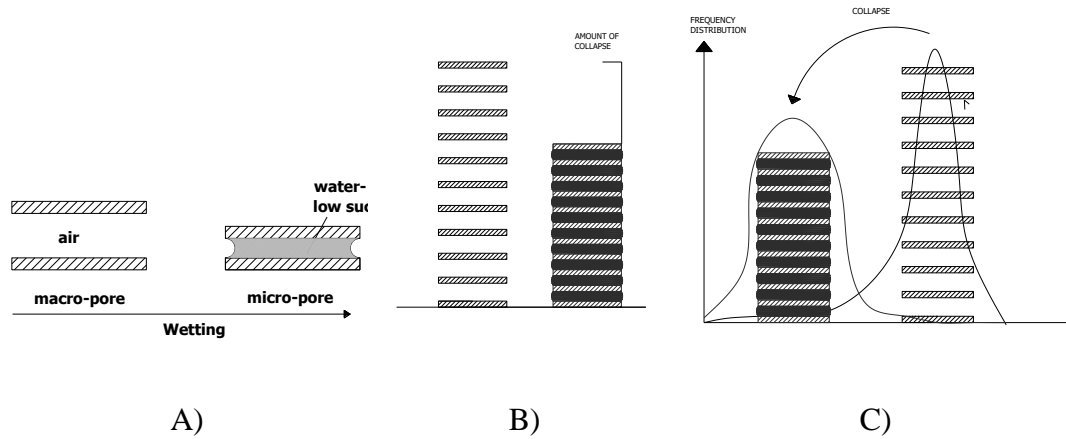
Figure 109. Collapse of a sample born air-saturated and then saturated with water.

A test where the initially dry powder is subjected to saturation and subsequent loading was then planned to verify whether the particle-based conceptual model allows satisfactory prediction of macroscopic behaviour from a qualitative standpoint.

Although saturation of an initially dry powder has little geotechnical significance, this test was aimed at proving the capability of the conceptual microstructural model to encompass from dry to fully saturated states.

It is worth highlighting that the collapse of the initially dry macro-pores could not be anticipated by the traditional 'aggregate' microstructural model. Volumetric collapse upon wetting has been associated with the disappearance of menisci and slippage at the inter-aggregate contacts. However, there are neither aggregates nor menisci in the dry powder and volumetric collapse of dry powder upon wetting cannot therefore be predicted by 'aggregate' microstructural model.

Experimental procedure

Oven-dried kaolin (air-saturated) was compacted in an oedometer cell to different vertical stresses (1, 70, 300 and 1200 kPa). No water was added during the compaction and the sample was kept dry.

Once that the compaction load was reached the sample was unloaded to 1 kPa and water-saturated. After water-saturation the sample was consolidated to 2220 kPa. For the sample compacted to 300 kPa, an additional test was carried out. The sample was water-saturated under loading (300 kPa) and then unloaded and re-loaded up to 2220 kPa.

Samples compacted to 300 and 1200 kPa were MIP tested before and after the water-saturation (Figure 110 and Figure 112). The wet samples were dehydrated by means of freeze-drying technique.

Results

Oven-dried kaolin (air-saturated) exhibits a mono-modal pore size distribution (Figure 80). The modal value corresponds to the macro-pores of the bi-modal pore size distribution of compacted kaolin. Since only macro-pores are present, the water-saturation causes only the collapse of such pores and no pores should swell.
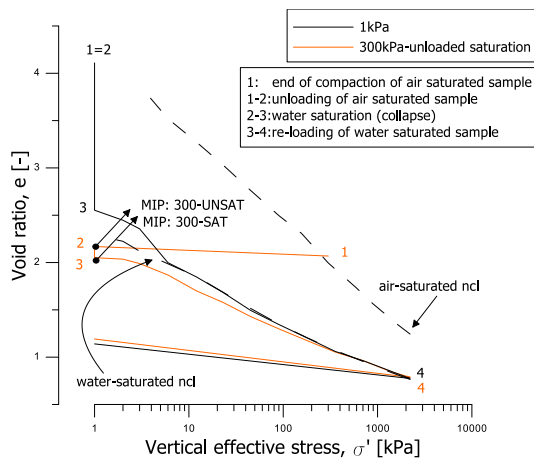
Figure 110. Collapse of air-saturated kaolin compacted at different vertical stress and then water saturated.

Figure 110 shows a sample saturated under 1 kPa vertical stress (1-2-3, black path) and one sample compacted to 300 kPa vertical stress, unloaded and then saturated (1-2-3, orange path).

The sample compacted at 1 kPa had a void ratio higher than 4 and collapsed to a void ratio of 2.6 upon water-saturation. The subsequent compression curve converged to the ncl of the reconstituted samples (3-4, black path).

Similar behaviour was observed for the sample compacted to 300 kPa, unloaded and then water-saturated. Saturation caused a volumetric collapse. The subsequent loading started with an initial compression along an unloading-reloading line (url) until the ncl of the reconstituted sample was reached. Once the ncl was reached, the behaviour was the same as the one of the reconstituted samples.
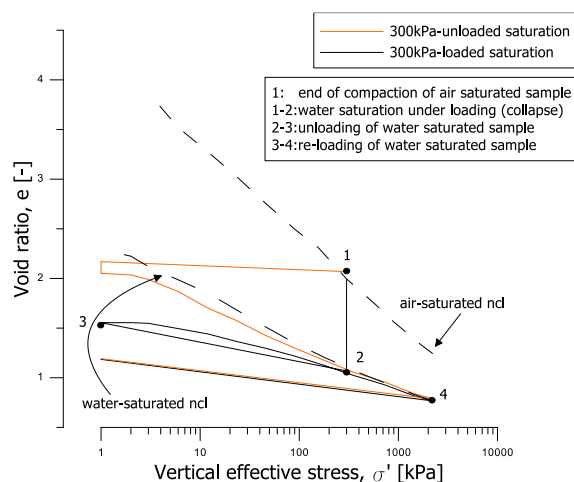
Figure 111. Collapse of air-saturated kaolin under loaded and unloaded conditions compacted at 300kPa vertical stress and then water saturated.

On the other hand, Figure 111 shows an air-saturated sample compacted to 300 kPa and then saturated under loading. Again, volumetric collapse is observed. When an air-borne dry sample is saturated under loading, it collapses onto the ncl, and behaves as a reconstituted sample that has been normally consolidated.

Figure 112 shows the saturation of samples compacted to 1, 70 and 1200 kPa respectively and their subsequent loading. As in the previous plot, all the samples collapse upon wetting and the following compression curves converge the ncl of the reconstituted samples.
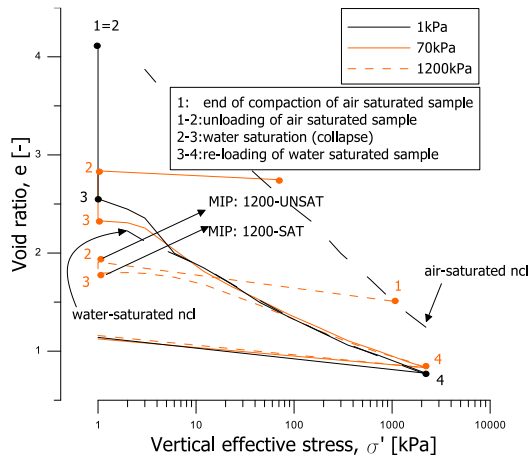
Figure 112. Collapse of air-saturated kaolin compacted to different vertical stresses and then water saturated.

Figure 113 shows the pore size distributions of samples before (full line) and after (dashed line) water-saturation (samples compacted at 300 kPa in grey and at 1200 in black). As expected, the evolution of the pore distribution shows that macro-pores collapse to micro-pores upon water-saturation. On the other side, no pores swell since no pores were water-filled at the onset of saturation. The pore size distribution is mono-modal both before and after the saturation, but the modal value switches from macro pores to micro-pores, as the sample switches from an air-saturated to a water-saturated one.
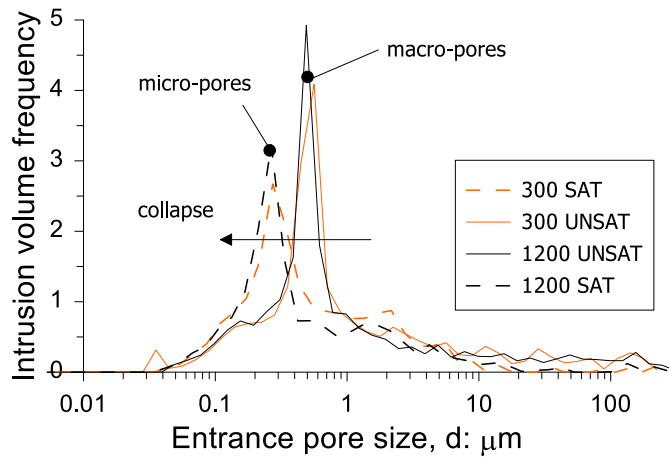
Figure 113 Pore size distribution of air-saturated compacted kaolin before and after unloaded saturation

4.6 An alternate microstructure-based approach to constitutive modelling

The microstructural model put forward in the previous sections was the starting point for the development of a different approach to constitutive modelling of unsaturated soils. A compacted sample is composed by pores that are water-saturated and pores that are air-saturated. For a given state, the void ratio of an air-water saturated sample, e*, can therefore be seen as the weighted average of the void ratio of air-saturated fraction, e_{AIR}, and the void ratio of water-saturated fraction, e_{WATER} (Figure 114). The void ratios of the air-saturated and water-saturated fractions are assumed to lie on the compression curves of the air-saturated (dry) and water-saturated (reconstituted) kaolin respectively as shown Figure 114.
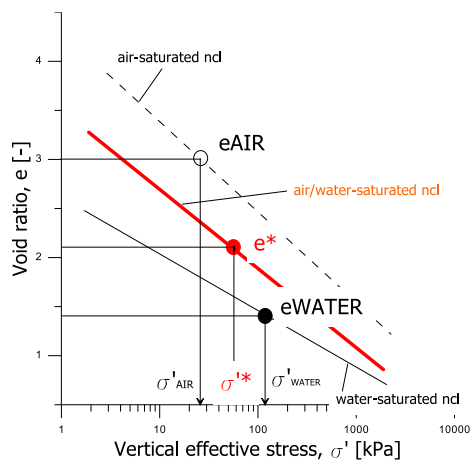
Figure 114. Propose methodology for constitutive modelling

In order to compute e_{AIR} and e_{WATER}, the relevant effective stresses, σ'_{AIR} and σ'_{WATER}, have to be determined. The approach pursed here is to extend to partially saturated soils the theoretical justification provided by Bishop (1960) for the effective stress in saturated soils.

4.6.1 **Void ratio**

According to the proposed approach, the void volume, V_V^C, of a compacted sample is equal to the sum of the volume of voids air-saturated, V_V^A, and the volume of voids water-saturated, V_V^W:

$$V_V = V_V^W + V_V^A \tag{41}$$

The void ratio of a compacted sample, e is defined as the ratio between V_V and the volume of solids, V_s . Therefore by dividing both members of Equation 41 by V_s the following Equation 42 is obtained:

$$\frac{V_V}{V_S} = e \quad = \frac{V_V^W}{V_S} + \frac{V_V^A}{V_S} \tag{42}$$

By dividing and multiplying V_V^W by the volume of solids of the wet particles, V_S^W, and V_V^A by the volume of solids of the dry particles, V_S^A, the void ratio of the compacted soil, e may be expressed as follows:

$$e \quad = \frac{V_V^W}{V_S^w} \cdot \frac{V_S^W}{V_S} + \frac{V_V^A}{V_S^A} \cdot \frac{V_S^A}{V_S} \tag{43}$$

The void ratio of the saturated part, e^W, is defined as the $\frac{V_V^W}{V_S^w}$ and the void ratio of the dry part, e^A, is defined as $\frac{V_V^A}{V_S^A}$. Moreover, the volume of solids of the dry particles, V_S^A, may be expressed as the difference between the volume of solids of the whole compacted sample, V_s and the volume of solids of the wet particles, V_S^W. Equation 43 can then be re-written as:

$$e = e^W \cdot \frac{V_S^W}{V_S} + e^A \cdot \left(1 - \frac{V_S^W}{V_S}\right) \tag{44}$$

The degree of saturation, S_R, is defined as the ratio $\frac{V_V^W}{V_V}$. By multiplying and dividing such ratio by the volume of solids of the compacted sample, V_s and by re-arranging the equation, the following expression for the degree of saturation is obtained:

$$S_R = \frac{V_V^W}{V_V} = \frac{V_V^W}{V_S} \cdot \frac{V_S}{V_V} = \frac{V_V^W}{V_S} \cdot \frac{1}{e} \qquad [45]$$

In the same way, if the second member of equation 45 is multiplied and divided by the volume of solids of the wet particles, V_S^W, Equation 45 becomes:

$$S_R = \frac{V_V^W}{V_S} \cdot \frac{1}{e} = \frac{V_V^W}{V_S^W} \cdot \frac{V_S^W}{V_S} \cdot \frac{1}{e} = \frac{V_S^W}{V_S} \cdot \frac{e^W}{e} \qquad [46]$$

If the term $\frac{V_S^W}{V_S^C}$ is isolated from Equation 46 as follows:

$$\frac{V_S^W}{V_S} = S_R \cdot \frac{e}{e^W} \qquad [47]$$

and substituted in Equation 44, the relationship of the void ratio of the compacted samples, e, as a function of the void ratio of the wet particles, e^W, the void ratio of the dry particles, e^A, and the degree of saturation, S_R, is obtained:

$$e = \frac{e^W \cdot e^A}{e^W \cdot (1 - S_R) + e^A \cdot S_R} \qquad [48]$$

Equation 48 shows that the void ratio e can be expressed as a function of e^W, e^A and the degree of saturation, S_R.

4.6.2 Effective stresses
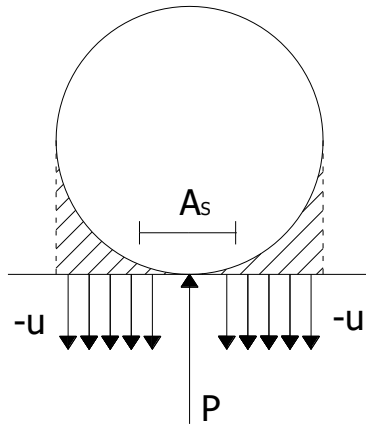
Figure 115. Intergranular stress

For the case of a saturated sample, Bishop (1960) assumed that the effective stress σ'_c, is given by the 'deviatoric' force acting on a single particle per unit total area A:

$$\sigma'_C = \frac{P^C}{A} - u\frac{A_s}{A} \qquad [49]$$

where P^C is defined as the sum of the integranular forces P and A_S is the sum of all the areas of contact A_{Si}.

On the other hand, the average inter-granular stress, σ_i (Figure 115) can be written as follows:

$$\sigma_i = \frac{P^C}{A} = \sigma - \frac{(A^C - A_s)}{A}u \qquad [50]$$

where σ is the external applied stress. By substituting Equation 50 into Equation 49 the effective stress validated experimentally is recovered:

$$\sigma'_C = \sigma - u \qquad [51]$$
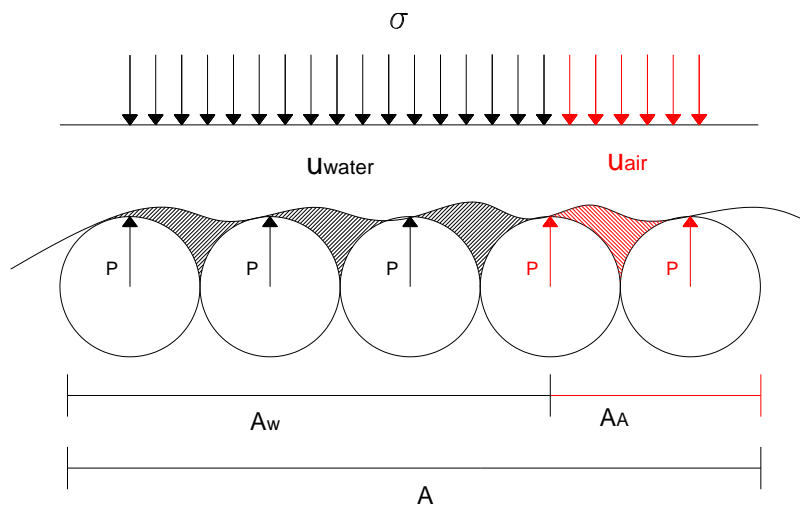
Figure 116. Forces at inter granular contacts in partially saturated soils.

Following the approach pursed by Bishop (1960), it is possible to schematize the forces acting on a partially saturated sample as shown in Figure 116 (particles are presented as spherical for sake of simplicity but they are not meant to be considered of such a shape).

"Now if a soil particle is subjected to a pressure u over the whole of its surface, it undergoes no distortion but a small decrease in volume. Hence it is only that part of the local contact stress which is in excess of u that causes deformation of the soil structure (Bishop, 1960)". Such stress corresponds to that part of the normal stress which controls volume change due to deformation of the soil structure.

Let us denote:

1) P^W and P^A the sum of the forces acting at the contacts of wet particles and dry particles respectively ($P^C = P^W + P^A$);
2) A the total area of the section of the whole sample and A^W and A^A the part of A that is wet and the part that is dry respectively;
3) u_w the pressure of the pore-water, and u_a the pressure of the pore-air;

4) A_S and A_V the area of the solids and the area of the voids, that will be expressed with the superscript C, W or A when they refer to the whole sample, the wet part or the dry part respectively.

Similarly to the case of a saturated sample, let us assume that the effective stress for partially saturated soils σ_C'' is still derived from the 'deviatoric' forces acting on the particles

$$\sigma_C'' A = P^W - u_w A_S^w + P^A - u_A A_S^A \qquad [52]$$

$$\sigma_C'' = \frac{P^W + P^A}{A} - u_w \frac{A_S^w}{A} + -u_A A_S^A$$

$$\sigma_C'' = \sigma_i - u_w \frac{A_S^w}{A} + -u_A \frac{A_S^A}{A}$$

By making the equilibrium of the forces across the whole section A, the intergranular stress σ_i can be written as follows:

$$\sigma_i = \sigma - u_w \frac{A_V^w}{A} - u_A \frac{A_V^A}{A} \qquad [53]$$

By replacing this equation into equation 52, one obtains:

$$\sigma_C'' = \sigma - u_w \left(\frac{A_V^W + A_S^w}{A} \right) - u_A \left(\frac{A_V^A + A_S^A}{A} \right) \qquad [54]$$

$$\sigma_C'' = \sigma - u_w \left(\frac{A^W}{A} \right) - u_A \left(\frac{A^A}{A} \right)$$

By rearranging equation 54 and by splitting the external stress σ between the wet area and the dry area, it is possible to express σ_C'' as a sum of the stresses acting on the wet area and the stresses acting on the dry area:

$$\sigma_C'' = \sigma \left(\frac{A^W}{A} + \frac{A^A}{A} \right) - u_w \left(\frac{A^W}{A} \right) - u_A \left(\frac{A^A}{A} \right) \qquad [55]$$

$$\sigma_C'' = (\sigma - u_w) \left(\frac{A^W}{A} \right) + (\sigma - u_A) \left(1 - \frac{A^W}{A} \right)$$

By assuming that $\frac{A^W}{A}$ equals to the degree of saturation, S_R, Equation 55 can be re-written as follows: ,

$$\sigma_C'' = (\sigma - u_w)S_R + (\sigma - u_A)(1 - S_R) = \sigma_C^W S_R + \sigma_C^A (1 - S_R) \qquad [56]$$

The assumption made in this work is that the first term on the right-hand side of Equation 56 controls the response of the saturated part whereas the second term on the right-hand side of Equation 56 controls the response of the dry part.

4.6.3 Shear stress

The equilibrium of the shear forces across a shear plane can be written as follows:

$$T = \tau A = T^W + T^A \qquad [57]$$

where, T is the shear force acting on the shear plane, T^W and T^A are the components of T acting respectively on the wet and dry part, and τ is average shear stress. The shear stress associated to the wet part, τ^W and the one associate to the dry part, τ^A, can be defined as follows:

$$wet:\ T^W = \tau^W A^W\ \to\ \tau^W = \frac{T^W}{A^W} \qquad [58]$$

$$dry:\ T^A = \tau^A A^A\ \to\ \tau^A = \frac{T^A}{A^A}$$

Therefore the total shear stress τ^c can be written as:

$$\tau = \frac{T^w}{A} + \frac{T^A}{A} = \frac{T^w}{A^W} \cdot \frac{A^W}{A} + \frac{T^A}{A^A} \cdot \frac{A^A}{A} = \tau^W \cdot \frac{A^W}{A} + \tau^A \cdot \frac{A^A}{A} \qquad [59]$$

By assuming the term $\frac{A^W}{A}$ equal to S_R, we can therefore write:

$$\tau = \tau^W \cdot S_R + \tau^A \cdot (1 - S_R) \qquad [60]$$

Equation 60 shows that the tangential stress τ can be expressed as an average of the tangential stresses τ^W and τ^A acting on the wet and dry part respectively weighted by the degree of saturation, S_R. The assumption made in this work is that τ^W is controlled by the effective stress controlling the wet part, $\sigma_C^W = (\sigma - u_w)S_R$, and that τ^a is controlled by the effective stress controlling the dry part $\sigma_C^A = (\sigma - u_A)$.

4.6.4 **Modelling volume change upon hydro-mechanical paths**

Volume change was modelled incrementally starting from an initial state. Let us consider the current step *i*. As shown in Equation 48, the void ratio of a partially saturated sample at the hydro-mechanical step *i*, e_i, can be expressed as a combination of void ratio of the wet particles, e_i^w, the dry particles, e_i^a, and the degree of saturation, S_r^i.

Generally, any mechanical or hydraulic path results in a change in degree of saturation from step *i-1 to* step *i*, $\Delta S_r^i = S_r^i - S_r^{i-1}$. When ΔS_r^i is greater than zero the sample undergoes a hydro-mechanical wetting whereas it undergoes hydro-mechanical drying when ΔS_r^i is lower than zero.

So far, pores have been considered to be divided into two difference classes: wet and dry. To take into account that pores may change their state, from dry to wet or vice versa, it might be useful to divide such classes in other 2 sub-classes:

1. Wet pores - e_i^w
    a. Pores that were wet at step *i*-1 and remain wet at step *i* - e_i^{ww}
    b. Pores that were dry at step *i*-1 and become wet at step *i* (wetted pores) - $e_i^{wetting}$
2. Dry pores - e_i^a
    a. Pores that were dry at step *i*-1 and remain dry at step *i*-1 - e_i^{aa}
    b. Pores that were wet at step *i*-1 and become dry at step *i* (dried pores) - e_i^{drying}

These sub-classes have been defined so that each main class is the sum of the two relative sub-classes:

$$e_i^w = e_i^{ww} \cdot \left(\frac{V^{ww}}{V^w}\right) + e_i^{wetting} \cdot \left(\frac{V^{wetting}}{V^w}\right) \tag{61}$$

$$e_i^a = e_i^{aa} \cdot \left(\frac{V^{aa}}{V^a}\right) + e_i^{drying} \cdot \left(\frac{V^{drying}}{V^a}\right)$$

For every hydro-mechanical path it is necessary to define the amount of pore volume (V^{ww}, $V^{wetting}$, V^{aa} and V^{drying}) that belongs to each sub-class.

Let us consider first the case of soils that are subjected to either wetting or drying as shown in Figure 117.
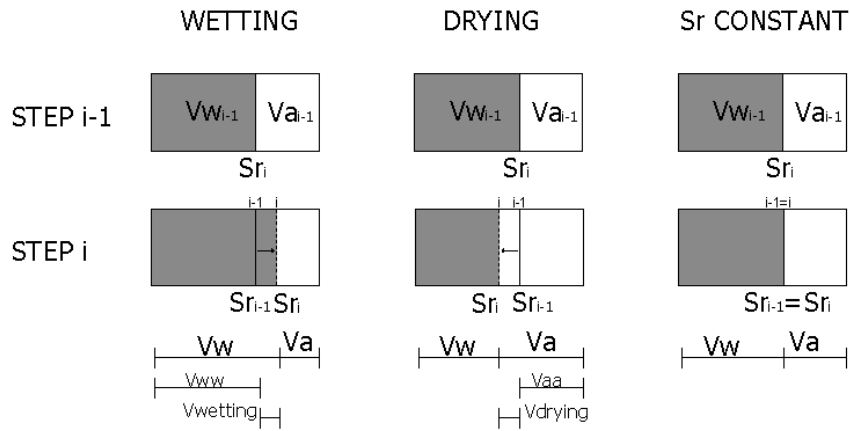
Figure 117. Volume fractions evolution upon wetting and drying paths.

If we consider a wetting path that goes from the step i-1 to the step i, it will be possible to define the following volume fractions at the step i:

$$\frac{V^{ww}}{V^w} = \frac{S_r^{i-1}}{S_r^i}$$

$$\frac{V^{wetting}}{V^w} = \frac{S_r^i - S_r^{i-1}}{S_r^i}$$

$$\frac{V^{aa}}{V^a} = \frac{1 - S_r^i}{1 - S_r^i}$$

$$\frac{V^{drying}}{V^a} = 0$$

[62]

In similar way if we considered a drying a path that goes from the step i-1 to the step i, it will be possible to define the following volume fractions at the step i:

$$\frac{V^{ww}}{V^w} = \frac{S_r^i}{S_r^i}$$

$$\frac{V^{wetting}}{V^w} = 0$$

$$\frac{V^{aa}}{V^a} = \frac{1 - S_r^{i-1}}{1 - S_r^i}$$ [63]

$$\frac{V^{drying}}{V^a} = \frac{S_r^{i-1} - S_r^i}{1 - S_r^i}$$

On the other hand when S_r does not change, the volume fractions at the step i are as follows:

$$\left(\frac{V^{ww}}{V^w}\right)_i = \left(\frac{V^{ww}}{V^w}\right)_{i-1}$$

$$\left(\frac{V^{wetting}}{V^w}\right)_i = \left(\frac{V^{wetting}}{V^w}\right)_{i-1}$$ [64]

$$\left(\frac{V^{aa}}{V^a}\right)_i = \left(\frac{V^{aa}}{V^a}\right)_{i-1}$$

$$\left(\frac{V^{drying}}{V^a}\right)_i = \left(\frac{V^{drying}}{V^a}\right)_{i-1}$$

For the case where the hydraulic path is reversed as shown in Figure 118, the calculations of the volume fractions differs slightly.
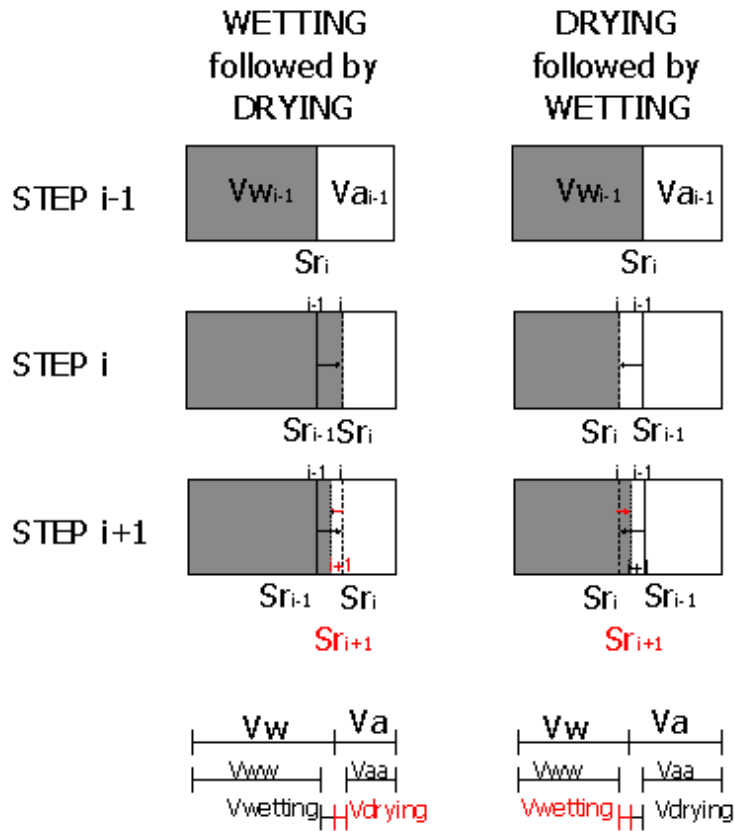
Figure 118. Volume fractions evolutions upon wetting-drying and drying wetting cycles.

For the case where a wetting takes place between steps i-1 and i and a drying takes place between steps i and i+1, the volume fractions can be expressed as follows:

$$\frac{V^{ww}}{V^w} = \frac{S_r^{i-1}}{S_r^{i+1}}$$

$$\frac{V^{wetting}}{V^w} = \frac{S_r^{i+1} - S_r^{i-1}}{S_r^{i+1}}$$

$$\frac{V^{aa}}{V^a} = \frac{1 - S_r^i}{1 - S_r^{i+1}}$$

[65]

$$\frac{V^{drying}}{V^a} = \frac{S_r^i - S_r^{i+1}}{1 - S_r^{i+1}}$$

Similarly, for the case where a drying takes place between steps i-1 and i and a wetting takes place between steps i and i+1, the volume fractions can be expressed as follows:

$$\frac{V^{ww}}{V^w} = \frac{S_r^{i+1}}{S_r^{i+1}}$$

$$\frac{V^{wetting}}{V^w} = \frac{S_r^{i+1} - S_r^i}{S_r^{i+1}}$$

$$\frac{V^{aa}}{V^a} = \frac{1 - S_r^{i-1}}{1 - S_r^{i+1}}$$

$$\frac{V^{drying}}{V^a} = \frac{S_r^{i-1} - S_r^{i+1}}{1 - S_r^{i+1}}$$

[66]

A concise formulation for the volume fractions, where either drying or wetting is considered including hydraulic path reversal can be given as follows:

$$\frac{V^{ww}}{V^w} = \frac{S_r^{MIN}}{S_r^i}$$

$$\frac{V^{wetting}}{V^w} = \frac{S_r^i - S_r^{MIN}}{S_r^i}$$

$$\frac{V^{aa}}{V^a} = \frac{1 - S_r^{MAX}}{1 - S_r^i}$$

$$\frac{V^{drying}}{V^a} = \frac{S_r^{MAX} - S_r^i}{1 - S_r^{i+1}}$$

[67]

where S_r^{MIN} is meant to be the minimum S_r since the beginning of the last wetting path and S_r^{MAX} the maximum over the whole hydraulic history. Equations 67 can be easily implemented into an Excel or Matlab algorithm.

Once the volume fractions in Equation [61 are calculated via Equation[67, $e_i^{ww}, e_i^{aa}, e_i^{wetting}, e_i^{drying}$ remain to be calculated.

The void ratio of the wet pores that were wet at step i-1, e^{ww}, and the void ratio of the dry pores that were dry at step i-1, e^{aa}, are simply computed form the compression curves of samples reconstituted from slurry and made of dry powder respectively.

$$e_i^{ww} = e_{i-1}^{ww} + (\lambda_{recon} \ or \ \kappa_{recon}) \cdot \log(\frac{\sigma_i^w}{\sigma_{i-1}^w}) \qquad [68]$$

$$e_i^{aa} = \left[e_{i-1}^{aa} + (\lambda_{powder} \ or \ \kappa_{powder}) \cdot \log\left(\frac{\sigma_i^a}{\sigma_{i-1}^a}\right) \right] \qquad [69]$$

where λ_{recon} and λ_{powder} are the virgin compression indexes of samples reconstituted from slurry and dry powder respectively and κ_{recon} and κ_{powder} are the elastic compression index of samples reconstituted from slurry and dry powder respectively. As discussed in previous section, the 'effective stresses controlling the response for the dry and wet part respectively are:

$$\sigma_i^w = (\sigma - u) \cdot S_r^i \qquad [70]$$

$$\sigma_i^a = (\sigma - u) \cdot (1 - S_r^i) \qquad [71]$$

When dry pores are wetted, become wet and they behave like a reconstituted soil on the normal consolidation line. Therefore $e_i^{wetting}$ is defined as:

$$e_i^{wetting} = e_{recon_{|\sigma^w=1}} + \lambda_{recon} \cdot \log\left(\frac{\sigma_i^w}{1}\right) \qquad [72]$$

For the case where wet pores are dried, it is assumed that no pore-volume. Therefore, e_i^{drying} is defined as follows:

$$e_i^{drying} = e_{i-1}^w \qquad [73]$$

where e_{i-1}^w is the void ratio at which those pores were before de-saturating.

4.7 Model validation

To demonstrate the capability of the model to simulate volume change behaviour, three experimental hydro-mechanical paths were considered. The void ratios $e_i^{ww}, e_i^{aa}, e_i^{wetting}, e_i^{drying}$ were first calculated according to Equations [68, [69, [72 and [73, then converted into e_i^w and e_i^a using Equations [61 and [67, and finally composed into the global void ratio e via Equation [48. For these three cases, the degree of saturation S_R was taken from the experimental data.

Finally, the capability of the approach to simulate shear strength of unsaturated compacted kaolin is tested.

4.7.1 Case n°1: 1-D compaction

Figure 119a shows the evolution of the void ratio upon compaction. The soil is loaded (path 1-2) and unloaded (path 2-3) at constant water content. Figure 119b shoes the void ratio paths for the sub-classes e_{ww} (pores that remain wet), e_{aa}, (pores that remain dry) and e_{drying} (pores that were wet and are then dried). Figure 119c shows the change in the volume fractions for each sub-class and Figure 119d shows schematically the change in the degree of saturation during the test.

During the compaction (step 1-2) both water-saturated and air-saturated pores are on the respective normal consolidation lines. When the load is decreased (path 2-3) the two sub-classes follow the respective unloading-reloading lines. Moreover, since the degree of saturation is decreasing, a mechanical drying is considered and therefore a third sub-class appear, e_{drying}. Whereas the sub-classes $e_{wetting}$ coincides with e_{ww} since both are on the ncl.
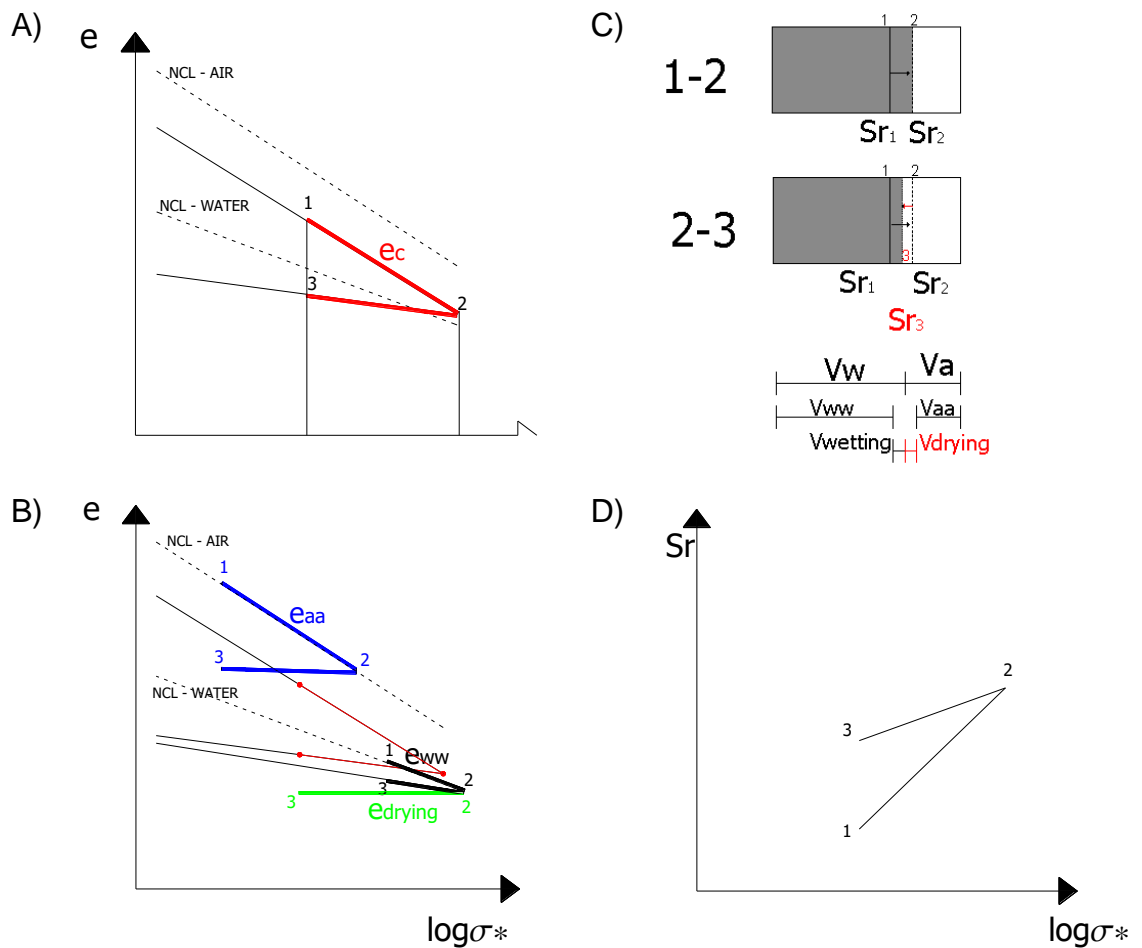
Figure 119. Compaction test simulation

Experimental procedure

1-D compaction tests on kaolin clay were simulated in order to validate the model. The experimental data were taken from Tarantino & De Col (2008). Six samples were loaded and unloaded to 300, 600, 900 and 1200 kPa, with water contents ranging from w=0.236 to w=0.311. Compaction was carried out in a modified oedometer cell where suction was measured during the compaction process by high-capacity tensiometers. As the vertical displacement was monitored during compaction process, the void ratio and hence the degree of saturation could be back calculated at any stage of the test. As no drainage was provided during the test, water content remained constant during compaction and was measured at the end of the test.

Simulation

To simulate the loading and unloading paths:

i) The applied vertical load and the suction and the degree of saturation measured during the test were taken as input stress variables (Tarantino & De Col, 2008)

ii) The compressibility curves of kaolin reconstituted from slurry and kaolin oven-dried were taken as the only 'constitutive' relationships

The two compression curves taken as reference for the compression water-saturated and air-saturated pores are shown in (Figure 71).

Figure 120 shows the experimental data together with the simulated paths. The simulation shows an excellent agreement with the experimental data. This is a remarkable achievement considering that no fittings parameters have been used and only the compression curves for water-saturated reconstituted kaolin and dry kaolin were used to model the data.

w=0.236

w=0.254

w=0.259
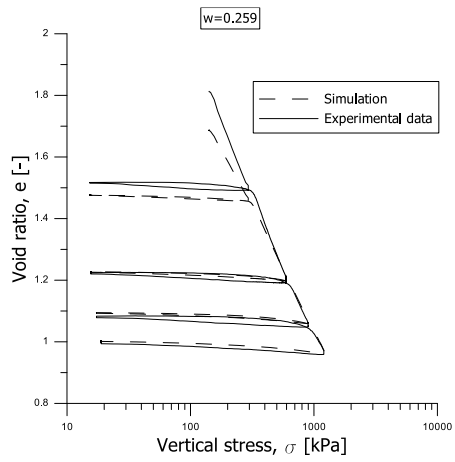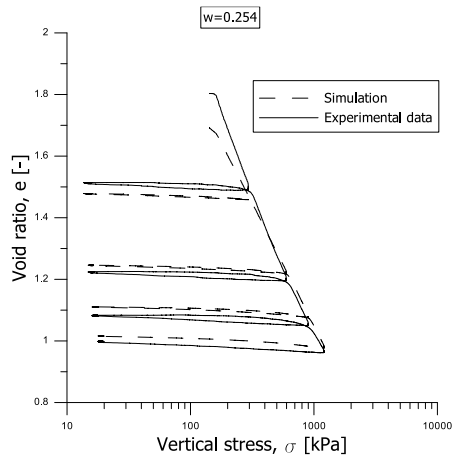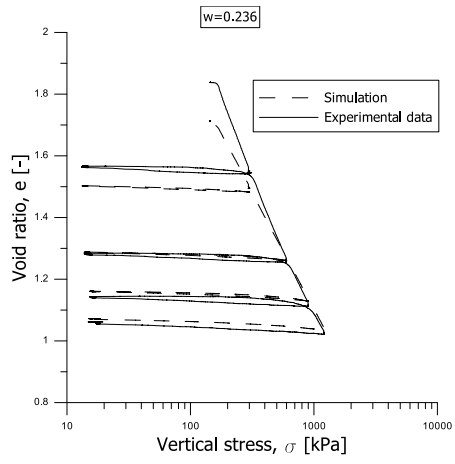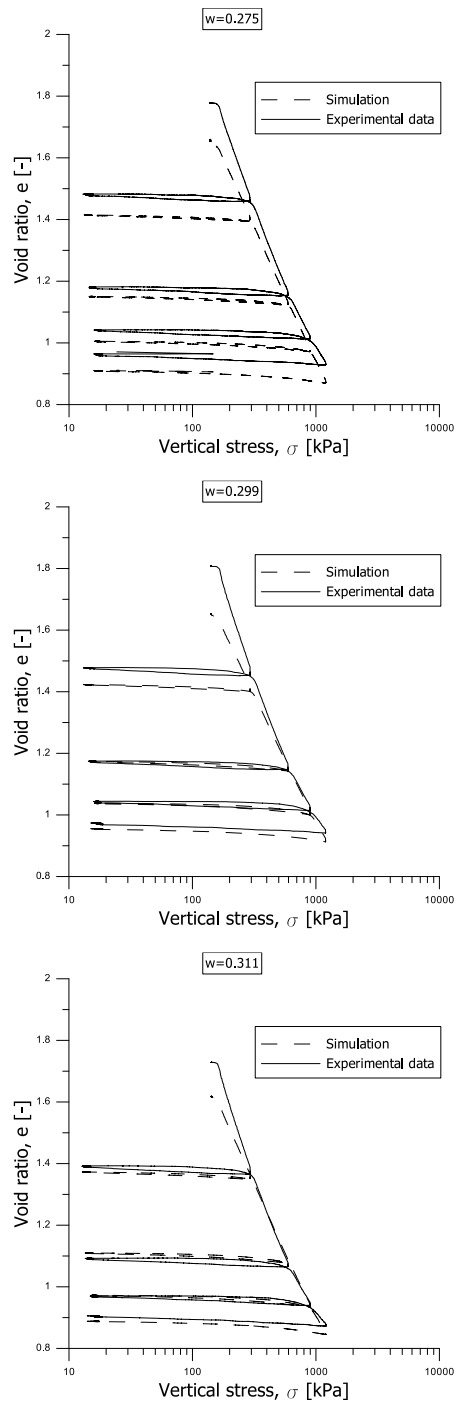
Figure 120. Model simulation of 1D compression of compacted kaolin at different water contents.

To better highlight the separate compression of air-saturated and water-saturated pores, Figure 121 shows the compression paths of the water-saturated part, e_w, and the compression path of the air-saturated part, e_a, for the sample compacted at w=0.236. It is possible to see that the two paths lie on the ncl of sample reconstituted from slurry and oven-dried powder respectively. At any step, the void ratio of the compacted sample is the weighted average of the air-saturated and water-saturated pores.
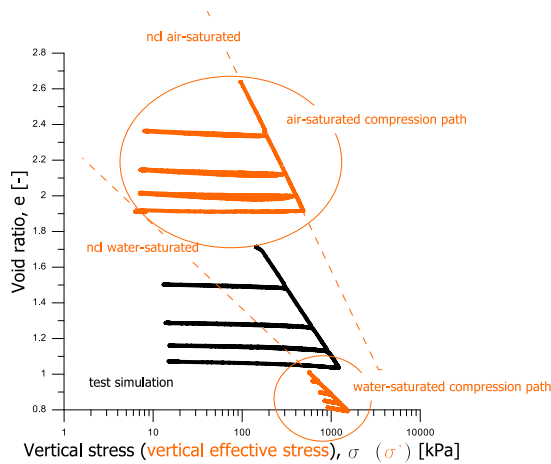
Figure 121. Compression path of the water-saturated part and the compression path of the air-saturated part from simulation of the sample compacted at w=0.236.

4.7.2 Case n°2: wetting of unloaded compacted sample followed by compression under saturated conditions

Figure 122a shows the evolution of the void ratio of a sample that was first compacted (loaded and unloaded under constant water content), saturated at quasi-zero vertical stress, and finally reloaded under saturated conditions.

Figure 122b shows schematically the evolution of the degree of saturation during the test. Figure 122c shows the void ratio of the sub-classes e_{ww} and e_{aa} whereas Figure 122d shows the void ratio of $e_{wetting}$ and e_{drying}..

The test was simulated in 5 steps:

- Step 1-2: compaction;

- Step 2-3: unloading;

- Step 3-4: saturation under quasi-zero stress;

- Step 4-5: reloading under saturate conditions up to the compaction stress (previous maximum vertical stress)

- Step 5-6- further compression by exceeding the compaction stress

Figure 122c and d shows that e_{aa} and e_{drying} both disappear upon saturation (step 3-4) since no dry pores exist anymore ($S_r = 1$). At the same time, e_{ww} keeps swelling upon saturation (step 3-4). At the end of saturation (point 4), the sub-class $e_{wetting}$ appears to lie on the ncl.
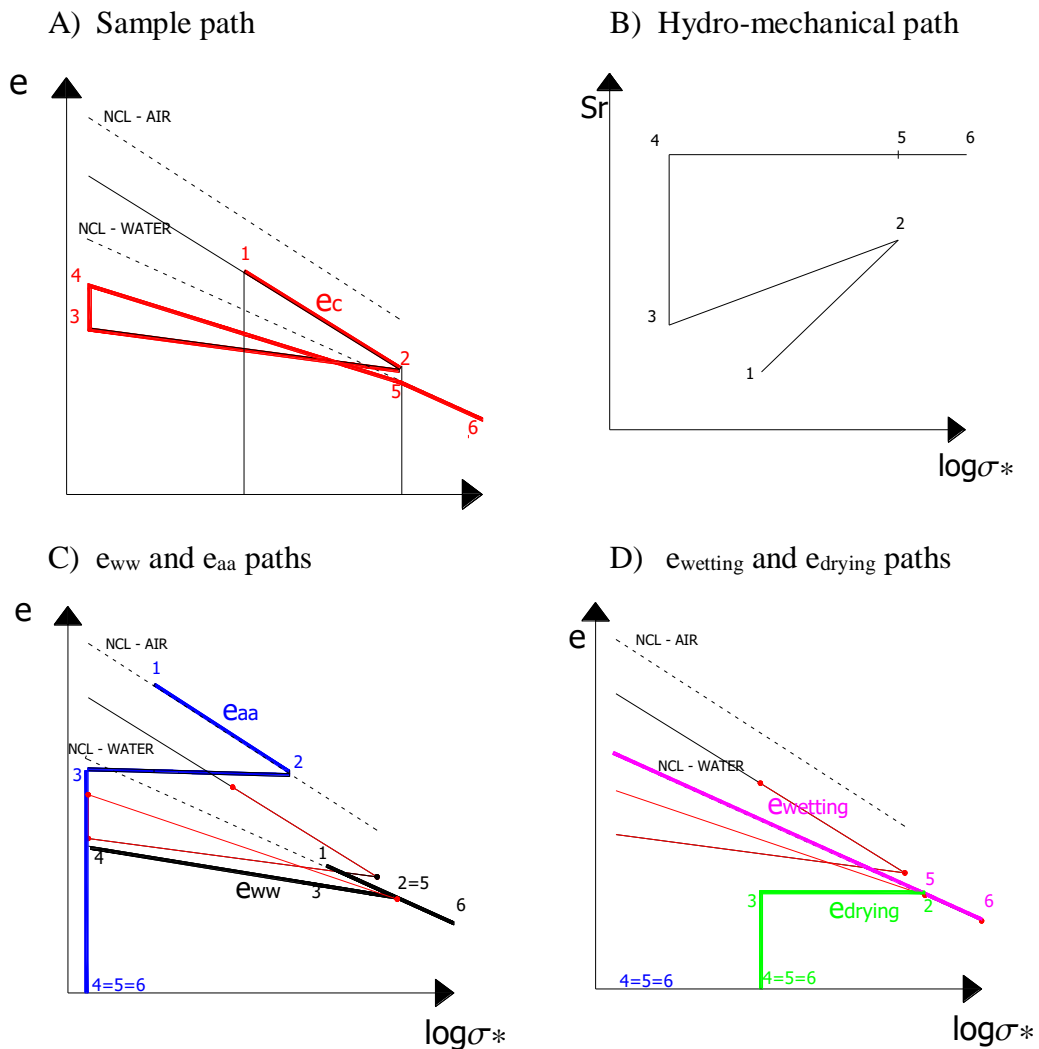
Figure 122. Post compaction unloaded saturation and saturated re-consolidation simulation.

During subsequent re-loading under saturated conditions (steps 4-5 and 5-6), the only sub-classes that contributes to the overall deformation are the saturated ones, e_{ww} and $e_{wetting}$. For the sake of clarity, the re-loading path (step 4-5) is shown in Figure 123, where the overall void ratio of the saturated sample is compared with the ones of the sub-classes e_{ww} and $e_{wetting}$.

In the step 4-5, according to the model laid down in Section 4.6:

- e_{ww} follows the loading and reloading line until the compaction load is not overcome;
- $e_{wetting}$ follows the ncl of the reconstituted samples. Such pores are the pores that were air-saturated and became water-saturated for the first time upon the step 3-4. They therefore behave as 'virgin' (normally consolidated) pores.

As shown in Figure 123, the compressibility of the saturated sample is an average between the compressibility of the two wet sub-classes. Finally, when the vertical load is further increased beyond the compaction vertical stress (step5-6), the whole sample becomes normally-consolidated.
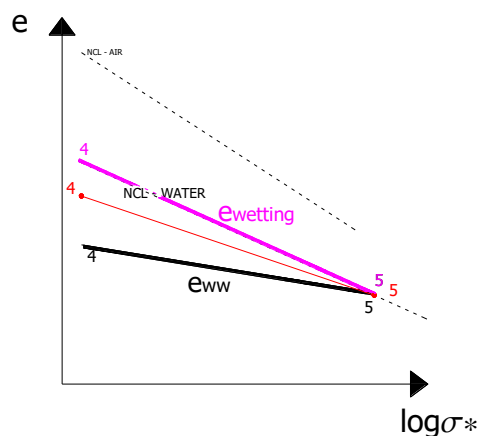
Figure 123. Saturated reconsolidation detail.

Experimental procedure

A sample was prepared at water content equal to 0.24 and compacted to 1200 kPa and then unloaded. Suction was not measured during compaction and

was inferred from a test reported in Tarantino & De Col (2008) carried out at same water content and vertical stress. These data have been used for the stage 1 (end of compaction, path 0-1) and stage 2 (unloading, path 1-2) as reported in Figure 124.

Saturation and subsequent compression were then performed (path 2-3 and path 3-4 respectively in Figure 124) (Tarantino & De Col, 2008) At the end of stage 3 the degree of saturation was assumed to be equal to 1 and suction equal to 0 kPa.

Simulation

The main challenge in this test was to simulate the amount of swelling upon saturation (path 2-3) as the behaviour of unsaturated soils upon saturation is one of the distinctive responses of unsaturated soils.

In order to simulate such test, only the ncl of water-saturated samples and the ncl of air-saturated sample have been used as 'constitutive' relationships. Suction and degree of saturation measurements borrowed from Tarantino & De Col (2008) where used as input variables for path 0-1-2-3.
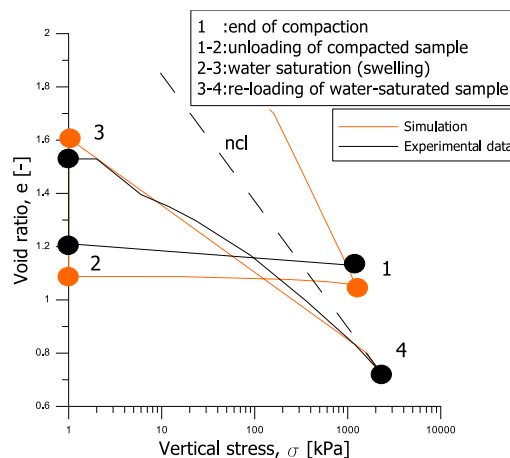
Figure 124. Unloaded wetting simulation of kaolin compacted at water content equal to 0.24 and 1200 vertical stress.

As shown in Figure 124, the simulation captured quite well the swelling upon saturation if one considers that no 'best-fitting' model parameters were used in the simulation.

4.7.3 Volume change of reconstituted kaolin upon drying

Experimental procedure

Kaolin clay was consolidated from slurry at 100 kPa and then let dry to different target water contents. Data have been taken from Tarantino (2010).

Simulation

Figure 125 shows the experimental data from Tarantino (2010) together with the simulation of the void ratio evolution. Suction measurements and degree of saturation were taken from the experimental data were used as input for the modelling simulation. Moreover the ncl of the water saturated kaolin (reconstituted from slurry) was used as reference for the water-saturated part. Since at the initial state (slurry) the pore size distribution was mono-modal, and according to Equation [73, micro-pores cannot become macro-pores, no pores were supposed to be totally de-saturated. Hence only the water-saturated ncl was required for modelling.
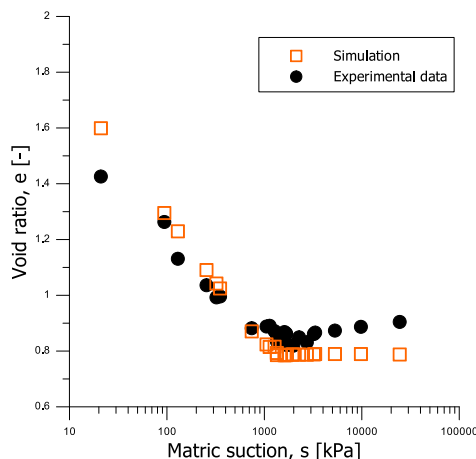
Figure 125. Drying path simulation of kaolin reconstituted from slurry.

It can be observed that the model captures the trend from a qualitative point of view. The model predicts a void ratio following the water-saturated ncl until desaturation and it then predicts a slight swelling when the soil desaturates. From a quantitative point of view the predicted swell is smaller than the actual one. The difference may be due on problem of the model or simply to errors in

measuring the total volume of the sample in the unsaturated range. Indeed sampling very dry sample is a procedure that might have a low repeatability, as it is possible to see by the experimental data trend, which are quite scatter.

4.7.4 Ultimate shear strength

Experimental procedure

Ultimate shearing resistance of kaolin clay compacted at different water contents and vertical stress was investigated in order to validate the model.

Direct shear experimental data were taken from Tarantino & Tombolato (2005). Thirty-three samples compacted at 300, 600 and 900 kPa and having water content ranging from w= 0.24 to w=0.34 were sheared. Shearing was made in a modified direct shear cell where suction was measured by high-capacity tensiometers. The specimens were sheared at horizontal displacement rate of 8mm/day, which is considerably greater (28 times) than the time would have been adopted for direct shear tests on saturated specimen.

To derive the reference states for (reconstituted) water-saturated and the air-saturated (dry) soil, kaolin reconstituted from slurry was consolidated in a direct shear box at 100, 300, 450, 700 and 1200 kPa vertical stress and then sheared. According to Tarantino & Tombolato (2005) the same horizontal displacement rate of 8mm/day was adopted for the set of saturated samples. The shear strength envelope for the reconstituted water-saturated kaolin is shown in Figure 126.

Furthermore, oven dried powder was compressed to 50, 100, 150, 300, 600, 900 and 1200 kPa vertical stress in the direct shear box. After compression, the samples were sheared at an horizontal displacement rate of 0.02mm/h, which is less than the required time would be adopted for direct shear tests on water-saturated specimens.

The shear strength envelope for the air-saturated kaolin (dry powder) is shown in Figure 126.
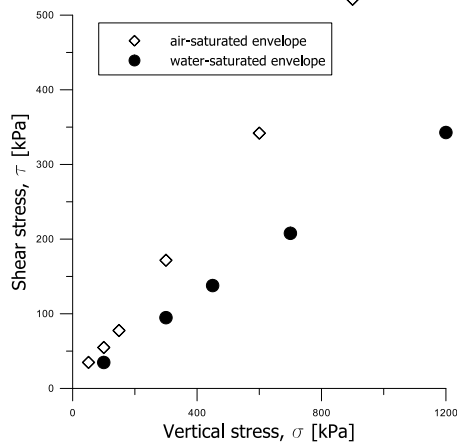
Figure 126. Water-saturated and air-saturated shear envelopes.

Simulation

For each vertical stress the ultimate shear stress of the compacted sample has been calculated by making a weighed sum of the shear strength of the water-saturated and air-saturated parts (Equation [60]). At each step, suction, vertical applied stress and degree of saturation has been used as an input in order to calculate the effective stresses for the dry part and the wet part respectively.

Figure 127 shows the experimental data for the ultimate shear strength of the partially saturated samples together with the simulation in the plane ultimate shear stress, τ, versus applied vertical stress, σ. The quality of the prediction is shown in Figure 128, where the accuracy of the prediction of the suggested approach is compared with the approach proposed by Tarantino & Tombolato (2005). The standard deviation of the 33 samples is less than 25 kPa, which can be considered satisfactory considering the relatively low precision of the direct shear test.
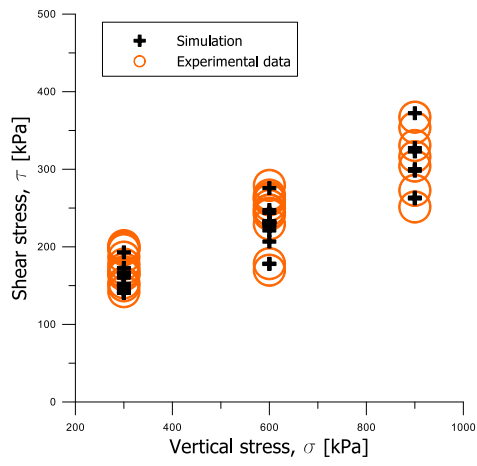
Figure 127. Ultimate shear simulation of kaolin compacted at different water contents and vertical stress.
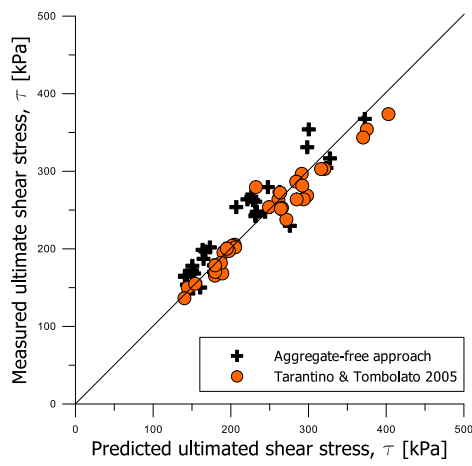
Figure 128 Prediction of the ultimate shear stress against the measured one.

4.8 Conclusions

The chapter showed an alternate microstructural conceptual model for partially saturated soils, which is coherent with the one proposed for the saturated clay. Such a conceptual model was able to interpret from a microstructural point of view several key aspects of macroscopic behaviour for partially saturated clays as well as the evolution of the pore size distribution upon various hydro-mechanical paths. An interesting feature of microstructural conceptual model is its ability to describe coherently the evolution of the pore size distribution over the full range of degrees of saturation from 0 (dry clay) to 1 (saturated clay).

An approach to constitutive modelling based on the microstructural conceptual model has been validated against volume change associated with mechanical and hydraulic paths and shearing resistance. The constitutive approach can be viewed as a further validation of the microstructural conceptual model. Macroscopic volumetric and shear response could be modelled only considering, as a reference, the response in compression and shear of (reconstituted) water-saturated kaolin and (dry) air-saturated kaolin without adding any other constitutive parameter.

Chapter 5.   Effect of pH and electrolyte concentration on kaolin clay from suspension to compacted state

5.1 Introduction

This chapter presents a series of preliminary experiments to investigate the effect of pore water pH and electrolyte concentration on the microstructure and macroscopic behaviour of kaolin clay from suspension to compacted state. These series of tests were carried out at the beginning of the experimental programme to start exploring the effect of pore-water chemistry on clay particle interactions. None of these series of tests were conclusive in the sense that they did not lead to major microstructural findings.

The sedimentation tests were not explored further as the response of suspensions was not the major focus of this dissertation. However, these tests allowed a first insight into the effect of pH and electrolyte concentration on particle interaction and paved the way to the tests presented in Chapter 3. The results obtained may be expanded further in the future and this is the reason why they have been included in this dissertation.

Another series of tests involved the effects of electrolyte concentration on the response of clays in consolidated and compacted states. Although assumptions have been made about particle interaction and configuration of clay prepared with saline pore water, these could not be validated by means of MIP tests because of the effect of the electrolyte on the freeze-drying process. However, experimental data and microstructural conjectures are

worth mentioning as an attempt to include the effects of pore water pH and electrolyte concentration into a single microstructural framework.

The following sections will present results experimental results considering salt concentration ad pH effects on kaolin clay for different ranges of water content:

i) Suspensions (w>2.5)
ii) Slurries (w=1.0)
iii) Compacted (w<0.32)

To allow the chapter to stand alone, basic concepts on the effect of pH and electrolyte concentration are briefly recalled at the beginning of the chapter.

5.2 General considerations on the electrochemistry of kaolin particles interaction

5.2.1 Electrical charges on kaolin surface

Electrical charges on kaolin particle surface change with the pH of the solutions. Surface of particle face is usually assumed to be negatively charged due to the isomorph substitutions. On the other hand, the charge of the particle edges is pH dependant. Kaolin edges are generally positively charged unless the kaolin is mixed with a dispersant solution that gives rise to a negative charge of the edge. As reported in Figure 36, two different electrical configurations can be assumed for kaolin particles, one with 'active' positive edges and one with 'de-activated' negative edges.
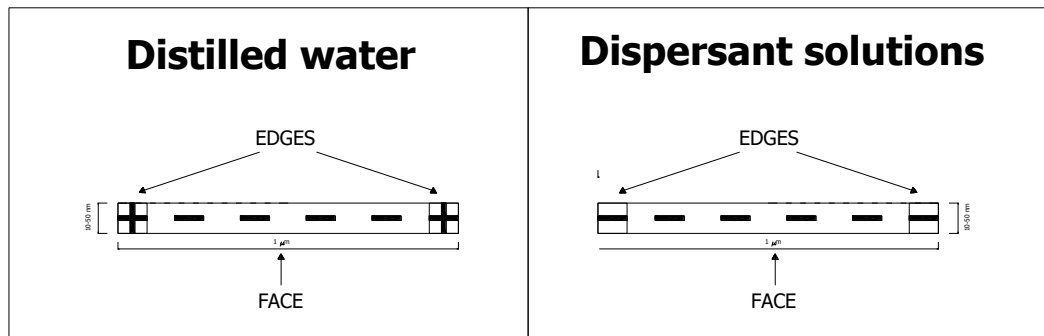
Figure 129. Surface electrical charge on kaolin particles

5.2.2 Interparticle interactions at different pH

Interactions between clay particles immersed in a medium are dominated by the electrical charge of the particle surfaces. According to Van Olphen (1977), the "net potential curve of particle interaction is constructed simply by adding the attractive and the repulsive potential at each particle distance". The forces involved in such particulate suspension are generally assumed to be Van der Waals forces, Coulombian interactions between particle charges, and hydration forces.

In hydrophobic suspension, which include clay suspensions, the hydration effects can be considered to be significant only up to a few molecules of water

from the particle surface if compared with Van der Waals forces (Van Olphen (1977)). As a result, hydration forces are generally considered to be negligible. Interactions between clay particles in suspension are therefore explained by the balance between Coulombian interactions (either attractive or repulsive) and Van der Waals attraction. This theory is often referred to as DLVO theory (Derjaguin & Landau, 1941, Verwey et al., 1948).

Since Van der Waals forces are considered relevant (if compared with the Coulombian forces) only at distances smaller than 10-20 nm (Mitchell & Soga, 2005, Van Olphen, 1977) particle distance is mainly controlled by Coulombian interactions in an electrolyte free suspension. Coulombian interaction forces depend on the dielectric constant of the pore fluid, the electrolyte concentration, and the particle distance.

In this work, kaolin clay particle interaction is considered to be either face-to-face or edge-to-face. For the case of distilled water (or non-alkaline water) and therefore for the case of active positive edges, the two interaction modes can described as follows (Figure 37):

iii)   Face-to-face interaction: The forces involved in this interaction are Coulombian repulsion (clay faces are always negative regardless of the pH of the suspension) and Van der Waals attraction. In an electrolyte-free suspension, Coulombian repulsion is greater than Van der Waals attraction, and therefore the nature of the net interaction is repulsive.

iv)   Edge-to-face interaction. The forces involved in this interaction are Coulombian attraction between the negatively charged clay face and the positively charged edge (edges are positive charged as long as the solution is not alkaline or any dispersant is added) and Van der Waals attraction. Thus the nature of the edge-to-face interaction is attractive when kaolin is suspended in an acidic solution (or distilled water).
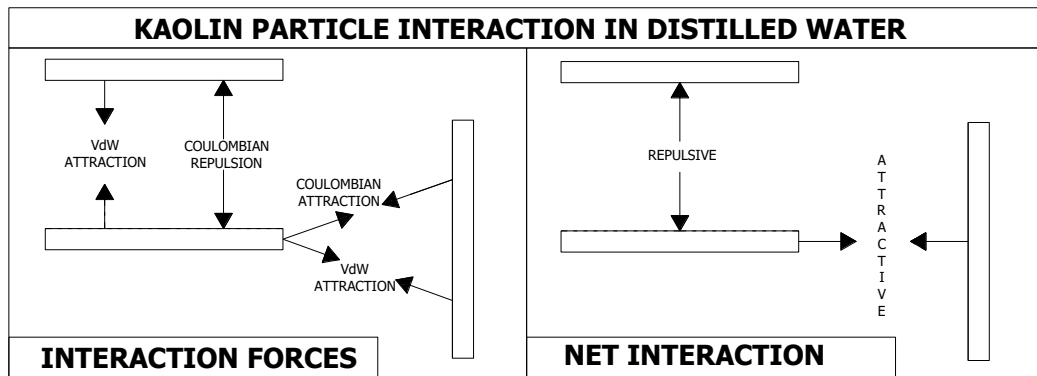
Figure 130. Electrochemical interaction forces of kaolin particles in distilled water

On the other hand, when kaolin clay is mixed with alkaline solution (or dispersant) the particle edges are negatively charged similarly to the particle faces. As shown in Figure 38:

iii)   Face-to-face interaction is repulsive as the net balance between the Coulombian repulsion and the Van der Waals attraction.

iv)   Edge-to-face interaction is also repulsive. Since both the faces and the edges of the particles are negatively charged, Coulombian interaction is always repulsive and therefore particles repel each other. Similarly, to the face-to-face interaction, Coulombian repulsion overwhelms the Van der Waals attraction giving rise to a net repulsive interaction (as long as the electrolyte concentration of the solution is negligible).
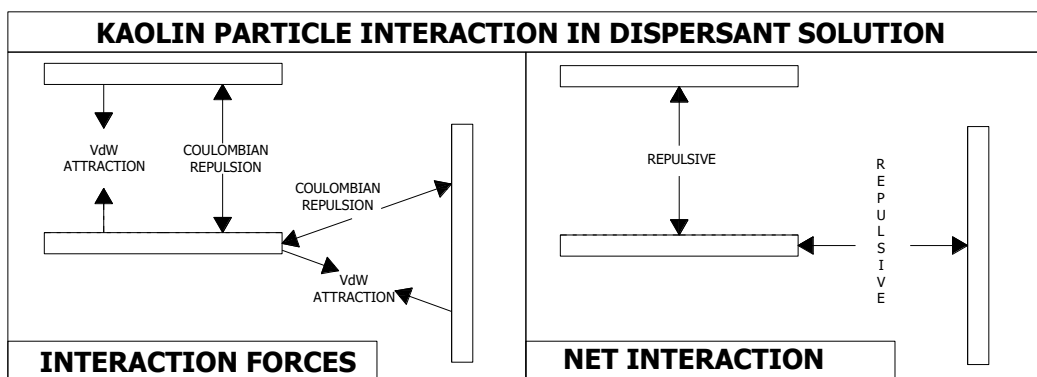
Figure 131. Electrochemical interaction forces of kaolin particles in dispersant solutions

5.2.3 **Interparticle interaction at different electrolyte concentration**

The electrical potential in proximity of the particle surface decreases when an electrolyte is added to clay-water mixture. Figure 132 shows the electrical potential generated by the particle charge for different electrolyte concentrations.
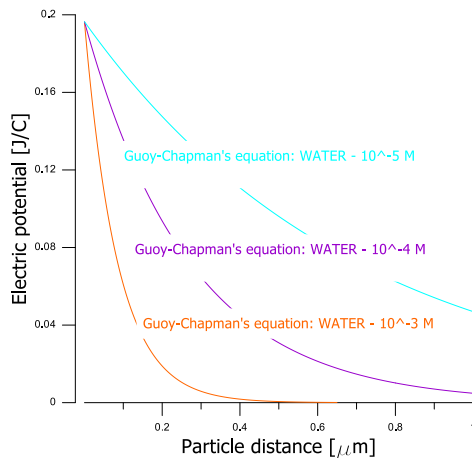
Figure 132. Electrical potential for different electrolyte concentration (Guoy-Chapman's equation).

When the electrolyte concentration is increased in acidic suspensions the electrical field associated with each charged surface decreases. This leads to two major consequences.

i)   If the Coulombian repulsion decreases moderately, electrical repulsion remains higher than the Van der Waals attraction and the interaction still remains repulsive. On the other hand, if the Coulombian repulsion decreases significantly, Van der Waals forces may become dominant and the net interaction may turn into an attractive one.

ii)   If the interaction between edge and face is attractive due to their opposite charge, the interaction remains attractive. However, the higher the electrolyte concentration, the lower is the Coulomb attraction and therefore the lower is the net attractive interaction.
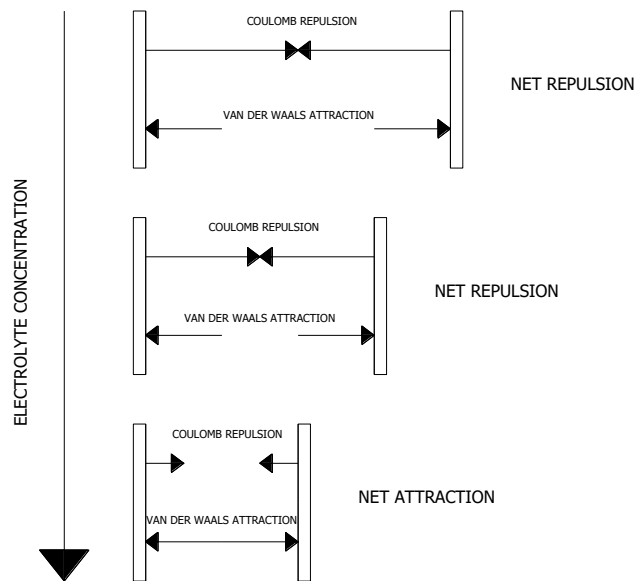
Figure 133. Effect of electrolyte concentration on face to face interaction
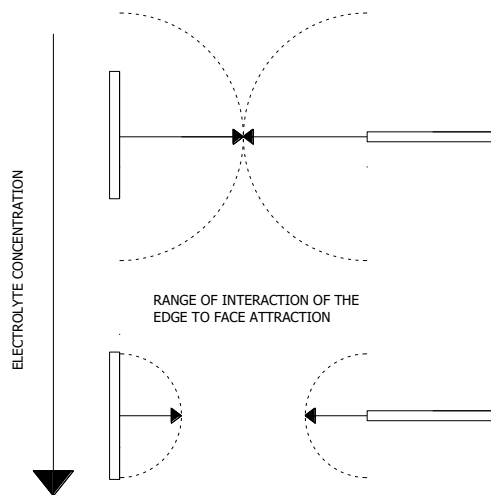
Figure 134. Effect of electrolyte concentration on edge to face interaction

In alkaline suspensions all particle surfaces are negatively charged. An increase in electrolyte concentration results in a decrease in the Coulomb repulsion. Below a threshold, the net interaction can be become attractive due to the Van der Waals attraction overwhelming the Coulomb repulsion. This applies to both face-to-face and the edge-to-face interaction.

5.3 Sedimentation tests

5.3.1 Rationale

Sedimentation tests are commonly used to investigate the particle size distribution of clay. Such tests are generally performed by mixing the clay with a dispersant which is aimed at preventing any particle association. When sedimentation tests are carried out by mixing clay particles with water of different pH and electrolyte concentrations, a particle association must be expected. As a result, the sedimentation can be used to characterise the aggregate size distribution (rather than the particle size distribution). Under the assumption that the net energy between the particles is only controlled by Van der Waals and Coulomb forces, this kind of tests should allow validating some hypotheses on the particle interactions and consequently on the particle configurations.

An alkaline suspension with negligible electrolyte concentration, which should de-activate the edge positive charge, should prevent any particle association and lead to a disperse configuration. On the other hand, when the clay-mixture is not alkaline, positive edges are activated and a flocculated configuration is expected (Figure 135)

DISPERSED   FLOCCULATED
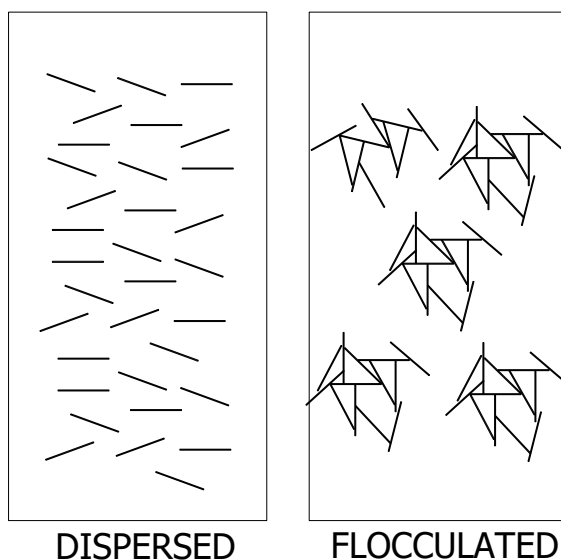
Figure 135. Possible particle configuration in kaolin sedimentation

Starting from these two basic particle configurations, increase in electrolyte concentration in alkaline suspensions may have different effects. Two possible associations may be figured out (Figure 136):

i)   Face-to-face association caused by the decrease in the repulsion between faces. Aggregates are formed by parallel particles that are stacked together.

ii) Face-to-edge association caused by the decrease in the repulsion between edges and faces. As in the acidic suspension particles form flocs of particles associated in an edge-to-face configuration.

DISPERSED PARTICLES

EDGE TO FACE FLOCCULATION

FACE TO FACE AGGRAGATION
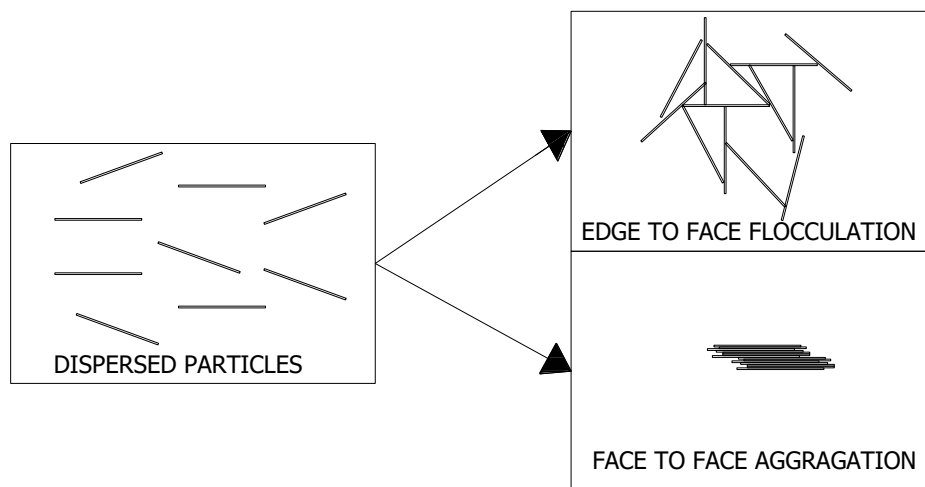
Figure 136. Possible particle associations in alkaline suspensions following an increase in electrolyte concentration.

5.3.2 Experimental procedure

1-L cylinder

Sedimentation tests were performed by adopting similar procedures as the BS 1377-2 standard. Because of the high density of the suspensions at high salt concentration non-standard hydrometers were used. Calibration of the hydrometers was carried out as suggested by the BS.

In order to measure the aggregate size distribution, sedimentation tests were performed on 50 g of kaolin powder mixed with 1 litre of solution. For sedimentation tests acidic and alkaline solutions at different NaCl concentration were prepared. Acidic solutions were prepared at pH 4 by adding HCl (molarity always less than 0.0001 M) to water solutions having different NaCl concentration (0 M, 0.01 M, 0.1 M, 1 M and 5 M).

The amount of Cl^- anions introduced in the system upon the HCl adjunction is equivalent to the amount of Cl^- anions introduces by adding 0.0001 M of NaCl, which can be considered negligible if compared with the NaCl concentration of the suspensions (even in the case of 0 M of NaCl).

Two more samples were prepared with acidic solution but they were mixed with another compound, i.e. $CaCl_2$ at two different concentrations (0.1 M and 1 M).

Alkaline solutions were prepared at pH 9 by adding KOH to water solutions having different NaCl concentration (0 M, 0.01 M, 0.1 M, 1 M and 5 M). Once that kaolin was mixed with the alkaline water, in order to keep the pH equal to 9, 0.3-0.4 g of KOH were added.

The amount of K^+ cations introduced in the system upon KOH adjunction is equivalent to the amount of Na^+ cations introduced by adding 0.01M of NaCl. Under the hypothesis that K^+ and Na^+ cations affect the features of the suspensions in the same way (they are both mono-valent), the introduced amount of K^+ cations can be considered negligible if compared with salt concentration of suspensions.

For each suspension 50 g of kaolin were mixed with 200 ml of the desired solution, and stirred overnight. Afterwards the suspension was transferred to a 1 L measuring cylinder and remaining solution was added up to 1 L graduation mark.

50ml beaker

In order to measure the final volume of the sediment, sedimentation tests using 2.5 g of kaolin powder mixed with 50 ml of desired solution were

performed. For these series of tests, suspensions of kaolin and solution at different pH and salt concentration were mixed directly in a 50ml beaker, without overnight stirring.

The void ratio of the final sediment for each class of suspensions was investigated by letting the suspensions sediment in the 50 ml beakers. All the suspensions were prepared at the same time. Measurements of the final height of the sediment were taken all at the same time when the suspension with the slower sedimentation rate showed the same reading over two consecutive days.

5.3.3 Experimental results

1L cylinder

Figure 137 shows the aggregate size distribution for suspensions at pH 4 and at pH 9 at zero electrolyte concentration. Suspension prepared at pH 9 shows a median Stokes' diameter of 0.98 μm. On the other side, suspension prepared at pH 4 has a median Stokes' diameter of 6.4 μm.
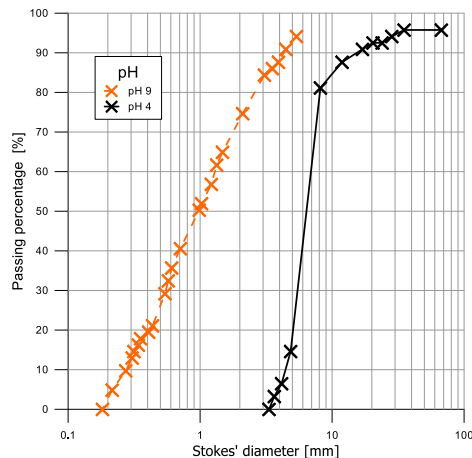
Figure 137: Aggregate size distribution at different pH

The two samples differ only by the electrical charge of the edges, positive for pH 4 and negative for pH 9. Therefore, it is possible to infer that the different aggregate/floc size between the two suspensions is the direct consequence of

the edge-to-face interaction. Generally, particles in dispersed suspensions, such as suspensions prepared at pH 9, are assumed to sediment individually, because of the high electrical repulsion existing between the particle's surfaces, which are all negatively charged. In pH 4 suspensions, edges are positively charged, and therefore there is an attractive interaction between edges and faces due to the opposite charges. Such attraction gives rise to flocs, i.e. particles associated in an edge-to-face configuration.

Figure 139a shows the aggregate size distributions for acidic suspensions at different electrolyte concentration whereas Figure 140 shows the median Stokes' diameters for the acidic suspension at different NaCl concentration.

It can be observed that the higher the salt concentration the smaller the aggregate size. Such behaviour is in agreement with the second mechanisms described above (Figure 134). Since the double-layer reduces in thickness when electrolyte concentration is increased, the probability that two particles in suspensions enter in the mutual attractive range is reduced. This results in smaller flocs (Figure 138).

On the other hand, the face-to-face interaction seems to remain purely repulsive. If particles were associating also in a face-to-face configuration thus forming an aggregate made of face-to-face particles, the equivalent Stokes' diameter of the flocs would have increased. Indeed, the suppression of the double-layer might have caused face-to-face arrangements within the floccule as shown in Figure 138. However, this would have made the floccule denser causing its velocity of sedimentation to increase. This is in contrast with the experimental observation in Figure 139a showing that the velocity of sedimentation decreases with an increase in electrolyte concentration in acidic suspension. It can therefore be inferred that the main effect of salt increase is to reduce the floc size.

For the sake of completeness, Figure 139a shows the effect of two different salts, NaCl and $CaCl_2$ respectively. The two salts differ because the former has a monovalent cation (Na^+) and the latter has a divalent cation (Ca^{++}). The two salts show the same effects on the aggregate size in a qualitative way, but

they differ from a quantitative standpoint. As expected, the divalent cation (Ca^{++}) is more effective than the monovalent one in reducing the attractive forces at the edge-to-fae and, hence, 'breaking' down the flocs.
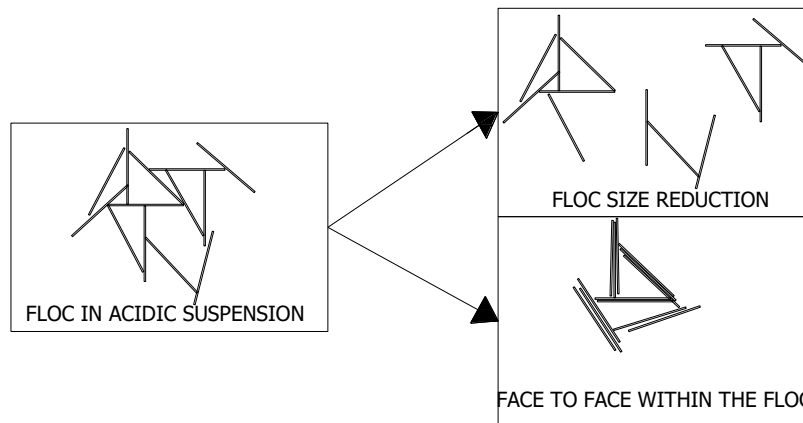
Figure 138. Hypotheses on the effects of electrolyte concentration increase in acidic suspensions

For the case of NaCl, it can be observed that electrolyte concentration does not cause any difference in the equivalent Stokes' diameter as long as the molarity of the solution is less than 0.1 M. This validates the assumption that the addition of HCl in small quantity to increase the pH does not have any 'double layer' effect, i.e. it does not practically alter the electrolyte concentration.

Figure 139b shows the aggregate size distribution of alkaline suspensions at different electrolyte concentrations and Figure 140 shows the median Stokes' diameters for alkaline suspension at different NaCl concentration. The median Stokes' diameter for the alkaline suspension increases with the electrolyte concentration. This may be associated with one of the two mechanisms shown in Figure 136, i.e. either the particles tend to form floccules (edge-to-face interaction) or aggregates (face-to-face interaction). At this stage, none of the two particle arrangements can be excluded.
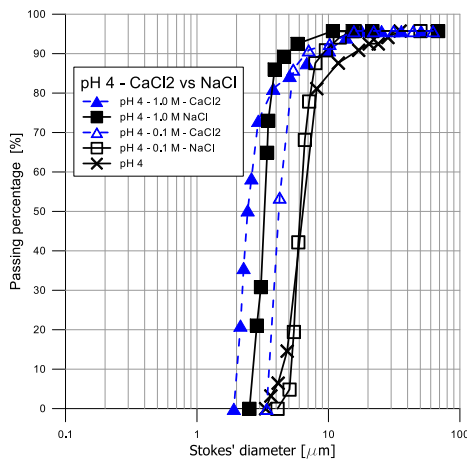
A) *Aggregate size distribution for acidic suspensions at different nacl and cacl₂ concentrations*
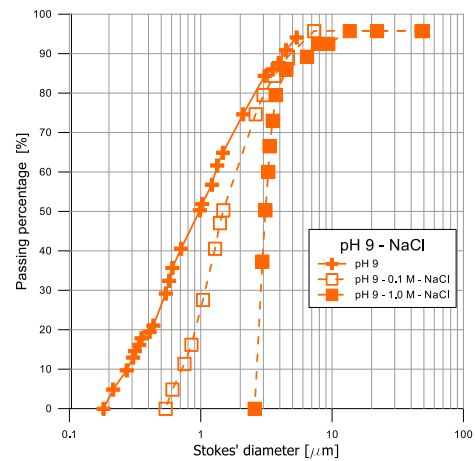
B) *Aggregate size distribution for alkaline suspensions at different nacl concentrations*

Figure 139. Aggregate size distribution for acidic (a) and alkaline (b) suspensions at different electrolyte concentrations.

To address this point, it is worth comparing the evolution of the median Stokes' diameter for the alkaline and acidic suspensions as shown in Figure 140. The median Stokes' diameter change a little when NaCl concentration is increased from 0 M to 0.1 M.

When the electrolyte concentration is increased up to 1M, the median Stokes' diameter reduces from about 6 to 3 μm in acidic suspensions. On the other side, the median Stokes' diameter increases from about 1 to 3 μm when the electrolyte concentration is increased in alkaline suspensions. At 1M, the Stokes' diameters are very similar, despite the different pH of the suspensions.

To understand whether the two curves in Figure 140 tend to join or cross, kaolin suspensions were prepared at the higher NaCl concentration, 5M. Figure 141 shows the aggregate size distribution resulting from sedimentation tests of kaolin suspensions prepared with acidic suspension at 0, 0.1, 1 and 5 M of NaCl concentration. Figure 142 shows the change in median Stokes' diameter for the acidic suspension (pH=4) and the alkaline suspension (pH=9) up to 5M NaCl concentration.
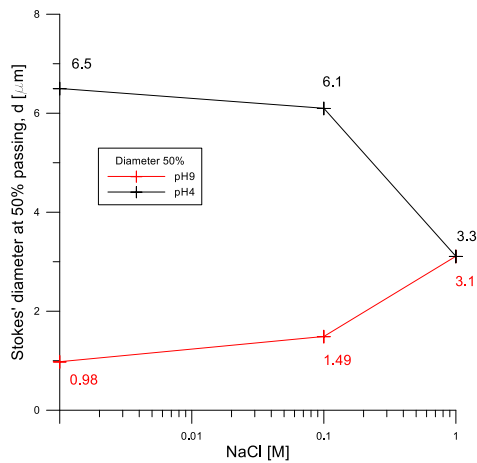
Figure 140: Stokes' diameter at 50% passing for alkaline and acidic suspensions at different NaCl concentrations

It can be observed that the trend for acidic suspension does not change when the NaCl concentration is increased up to 5M. In other words, the sedimentation velocity keeps decreasing when the salt concentration is increased. Accordingly, it can be assumed that the flocs keep reducing in size in the acidic suspension with increasing electrolyte concentrations.
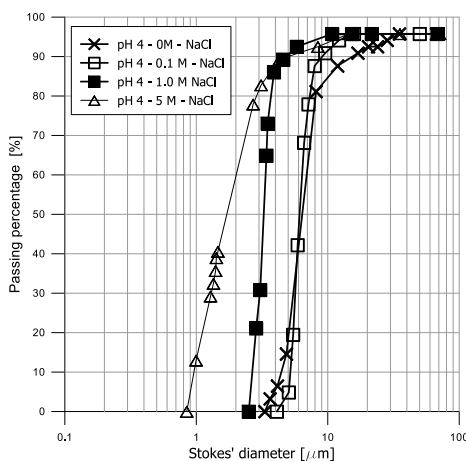
Figure 141. Equivalent Stokes' diameter for kaolin suspensions prepared with acidic solutions at different NaCl concentrations

When inspecting the median Stokes' diameter for the alkaline suspensions at 1M and 5M NaCl concentration, it can be observed that it coincides with the

values recorded for the acidic suspension. Since the acidic suspension is characterised by particles in edge-to-face configuration (flocs), it can be inferred that particles in the alkaline suspension at 1M and 5M NaCl concentration are also in edge-to-face configuration, i.e. they form flocs.

This may suggest that edge-to-face flocculation also occurs in the alkaline suspension at lower NaCl concentration and that the face-to-face aggregation hypothesised in Figure 136 is less probable.

It is also worth noticing that the charge of the edge does not play a role any longer at 1M and 5M NaCl concentration. In fact, the median Stokes' diameter is the same in both the acidic and alkaline solution despite the charge of the edge is positive in the acidic suspension and negative in the alkaline suspension. The edge-to-face attraction at 1M and 5M NaCl concentration should therefore be associated with the van der Waals attraction in both acidic and alkaline solutions.
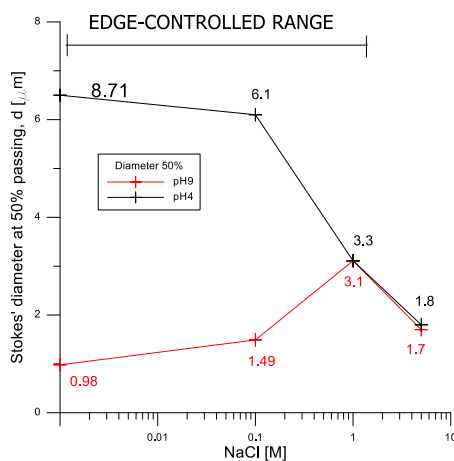
Figure 142. Stokes' diameter at 50% passing for alkaline and acidic suspensions at different NaCl concentrations.

50 ml beaker

A series of sedimentation tests were performed in order to study the final volume of the sediment, by letting the kaolin particles sediment in a 5% kaolin suspension at different pH and NaCl concentrations. The final volume and the

final void ratio of the sediment are shown in Figure 143 and Figure 144 respectively.

It can be observed that the trend of final void ratio versus the NaCl concentration for both the acidic and alkaline suspensions is very consistent with the trend of the aggregate size (compare Figure 144 with Figure 140). The bigger the aggregate size, the higher is the final volume. At 0 M concentration the void ratio of the acidic suspension is almost 3 times higher than the one of the alkaline suspension, whereas the two suspensions show similar void ratio at 1M NaCl concentration (very similar median Stokes' diameters were also observed at 1M NaCl concentration as shown in Figure 140).

| pH 9-0M | pH9-0.01M | pH9-0.1M | pH9-1M | pH4-1M | pH4-0.1M | pH4-0.01M | pH4-0M |
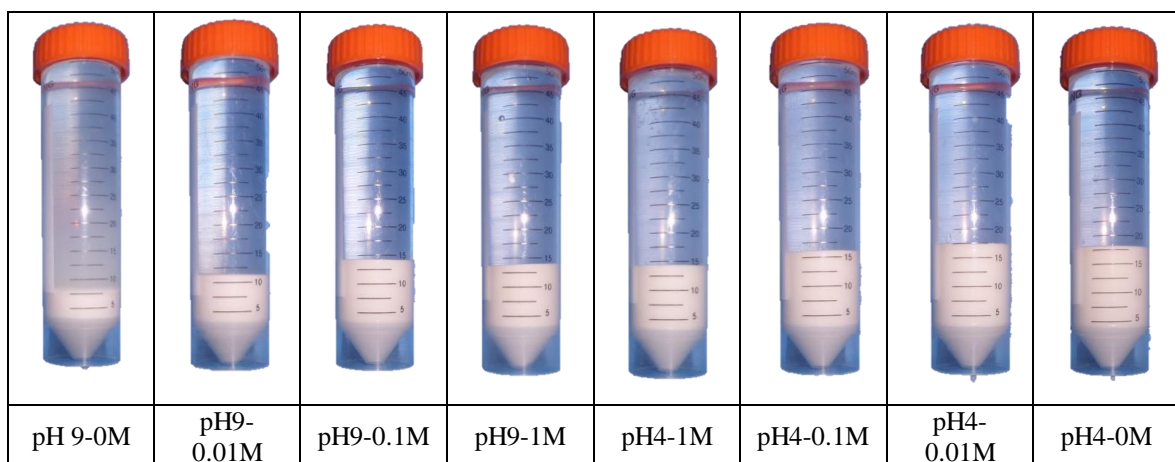
Figure 143: Final volume of the sediment for alkaline and acidic suspensions at different NaCl concentrations

Figure 144 shows the trend of the final void ratio in alkaline and basic suspensions with the NaCl concentration extended to 5M. Similarly, to the median Stokes' diameter, no difference is notable between alkaline and acidic solution when the electrolyte concentration is equal or higher than 1M.
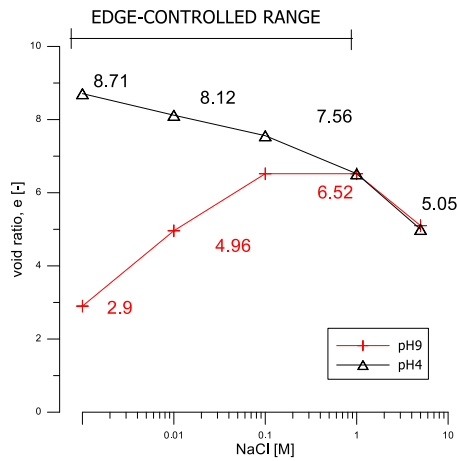
Figure 144. Final volume of the sediment for alkaline and acidic suspensions at different NaCl concentrations

5.3.4 Two alternate hypotheses for alkaline suspensions: parallel stacking or flocculated configuration

Considerations on the sedimentation behaviour

Particle association in alkaline suspension has been hypothesised to occur in either by face-to-face or edge-to-face configuration (Figure 136). In the previous section, it has been suggested that the face-to-face configuration is less probable. To better investigate face-to-face configuration, an attempt was made to estimate the number n of the particles forming one aggregate at different NaCl concentrations. To this end, the mass M of a single clay particle needs to be initially estimated.
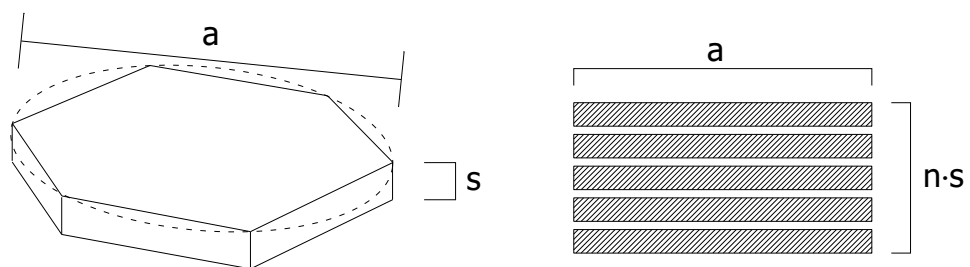
Figure 145. Particle geometry

By assuming that kaolin particles in alkaline solution at zero salt concentration settle as individual particles, it is possible to calculate the mass M of one single particle. As shown in equation 74, it is possible to calculate the mass, M, of one particle, having particle density ρ_s, by assuming that kaolin particle are hexagonal prism, with diameter of the circumcircle a and height of the prism s:

$$M = \frac{3\sqrt{3}}{8} a^2 \cdot s \cdot \rho_s \qquad [74]$$

According to Mitchell & Soga (2005) the thickness, s, of kaolin particle can be assumed between 10-30% in length of the diameter of the circumcircle, a. Therefore, the thickness s was assumed to be a/10. Accordingly, Equation 74 becomes:

$$M = \frac{3\sqrt{3}}{8} \frac{a^3}{10} \cdot \rho_s \qquad [75]$$

The size a can be derived from the Stokes' sphere-equivalent diameter, D_{eq} by assuming that the velocity of sedimentation is only controlled by the mass of the particle. This is a very first approximation as the velocity of sedimentation is also controlled by the shape and orientation of the particle during sedimentation. By comparing the mass of the equivalent Stokes' sphere and the actual particle (Equation76) it is possible to obtain the relation between the diameter, a, of the circumcircle of the base of the hexagonal prism and the calculated Stokes' diameter, $D_{eq,dispersant}$ (Equation77)

$$\frac{3\sqrt{3}}{8} a^2 \cdot \frac{a}{10} \cdot \varrho_s = \frac{\pi}{6} D_{eq,dispersant}^3 \, \varrho_s \qquad [76]$$

$$a = \sqrt[3]{\frac{40}{9\sqrt{3}} \pi \cdot D_{eq}} \qquad [77]$$

According to the test reported in Figure 140, the median Stokes' diameter is $D_{eq,dispersant}$=0.98 μm for the clay in alkaline suspension with no salt (dispersant solution). This results in a diameter of the particles $a = 2.0$ μm and

a thickness of 0.2 μm. By substituting a = 2.0 μm into Equation 75, the mass M of a single particle can be derived.

The number n of particles forming one aggregate at different NaCl concentrations can be estimated by assuming that:

- aggregates are made by a number n of parallel particles,
- the distance between particles within the same aggregate is negligible if compared with particle thickness
  - all the particles have the same size and equal to the median particle computed from the sedimentation test in alkaline solution and zero NaCl concentration.

The mass M_{agg} of the aggregate can be written as

$$M_{agg} = M \cdot n = \frac{\pi}{6} D^3_{eq,aggregate}\, \varrho_S \tag{78}$$

where $D_{eq,aggregate}$ is the median Stokes' diameter from the sedimentation tests in alkaline solutions at different electrolyte concentrations. By combining Equations 75 and 78, the relation between the number of particles, n, and the Stokes' diameter $D_{eq,aggregate}$ is obtained:

$$n = \frac{40}{9\sqrt{3}}\pi \frac{D^3_{eq}}{a^3} \tag{79}$$

Table 2 shows the geometry and the calculated number of particles per aggregate for different NaCl concentrations in alkaline suspension.

Table 2: Aggregate geometry at different NaCl concentration in alkaline solutions

NaCl concentration [M]	$D_{eq,aggregate}$ [μm]	a [μm]	n [-]	Height of the prism [μm]
0	0.98	1.96	1	0.2
0.1	1.49	1.96	4	0.8
1	3.1	1.96	32	6.3

According to Table 2, under the assumption that particles associate in a face-to-face configuration and that the particle-to-particle distance is negligible, when alkaline suspensions have electrolyte concentration of 1M, the aggregates are made of about 32 particles stacked together in a parallel

configuration. This should give rise to aggregates having a prismatic shape with a base diameter of about 1.96 μm and a height of 6.3 μm. Such conclusion seems quite unrealistic. Such kind of particles aggregations has never been seen in any Scanning Electron Imagine if not in very aged kaolinite. This seems to support the assumption that particle association occurs with an edge-to-face mode also in alkaline solutions, i.e. flocs instead of aggregates are forming when an electrolyte is added to the suspension.

5.3.5 On the use of the double layer theory to model mechanical response of suspensions

The effect of electrolyte in alkaline suspensions can be further investigated in terms of double layer repulsions. When kaolin particles are suspended in alkaline solutions all particle surfaces are negatively charged. Therefore, the particle distance is controlled by the difference between double layer repulsion and Van der Waals attraction. As long as the double layer is large enough, the net interaction will be repulsive and particles can be considered as settling down individually. On the other side, when electrolyte concentration is high enough double layer repulsion reduces to the extent that Van der Waals overwhelms the repulsive interaction, giving rise to an interaction attractive in nature. If such combination occurs, particles do not sediment individually anymore, but they associate in aggregates or flocs.

According to Bolt (1956) a simplified equation (discussed by Schofield 1946) can be used in order to take in account the double layer repulsion. By considering the double layer theory (which relates the particle distance with the ions distribution in the fluid) and the swelling pressure (pressure difference between the osmotic pressure in the central plane and osmotic pressure in the bulk solution) a relationship for the void ratio can be inferred. If particles are considered as parallel plates, the void ratio can be expressed as:

$$e = \varrho_S S \cdot d \qquad\qquad [80]$$

where ϱ_S is the particle density, S is the specific surface (14000 m^2/kg) and 2d is the inter-particle distance. By considering the pressure P as the pressure

counterbalancing the double layer repulsion, the void ratio, e, can be expressed by Equation 81 (Bolt, 1956)

$$e = (\log 64 - \log \frac{P}{RT} - 0.4343 \cdot 2 \cdot v\sqrt{\beta c_0}x_0) \cdot \frac{\varrho_S S}{0.4343 \cdot 2 \cdot v\sqrt{\beta c_0}} \qquad [81]$$

where R is the gas constant (J/mol/°K), T is the temperature (°K), v is the ion's valence, β is a constant, it depends upon the temperature ~ 10^{15} cm/mmol, c_0 is the concentration in the bulk liquid, x_0 is a constant dependent upon the surface density of charge of the clay (2/v $\dot{A}$ for kaolin).

Such a theory is based on a number of simplifying assumptions (validity of Gouy's theory, parallel alignment of particles, ideal behaviour of ions and the validity of equation 80) which are considered satisfactory for the purpose of the above calculation. By considering P equal to the final average effective stress of the sediment (average height of the sediment), the expected final void ratio, according to equation 81, can be calculated.

The computed final void ratio for different electrolyte concentrations is reported Figure 146. It is possible to see, that at very low NaCl concentration, the computed void ratio via Equation 81 and the experimental void ratio for the alkaline solutions is similar. This suggests that particles settle individually and in an almost parallel configuration at very electrolyte concentration. Nevertheless, when the electrolyte concentration is increased the experimental trend and the one obtained by Equation 81 are just opposite. According to the double-layer theory, the particle distance (and thus the final void ratio) should decrease when the salt concentration increases if particles settle individually. However, the experimental data show that the void ratio increases when salt is added. Such evidence, which contrasts with the double-layer theory, suggests again that some sort of aggregation/flocculation occurs in the alkaline suspension when salt is added. This would result from the double layer repulsion being overcome by the Van der Waals attraction.
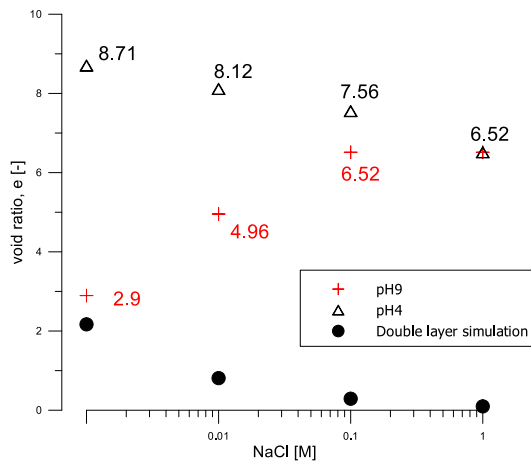
Figure 146: Final void ratio of the sediment for alkaline and acidic suspensions at different NaCl concentration

5.3.6 **Conceptual model**

Particle association occurs only in an edge-to-face mode. The effect of the electrolyte is to enhance the attraction between edges and faces in alkaline solutions and to reduce the attraction between edges and faces in acidic solutions respectively.

A microstructural conceptual model can tentatively be designed as follows:

1) In acidic suspension, particles are flocculated in an edge to face configuration. Therefore, the sedimentation occurs in floccules. The higher the electrolyte concentration the smaller are the floccules, because the attraction between edges and faces reduces due to the suppression of the double-layer (Figure 147a).

2) In alkaline suspension, particles are dispersed. When the electrolyte concentration is increased the repulsion at the edge-to-face is reduced, until the van der Waals attractive forces start to prevail on double-layer repulsion and floccules start forming in an edge-to-face configuration. The higher the electrolyte concentration the bigger the floccules (Figure 147b).
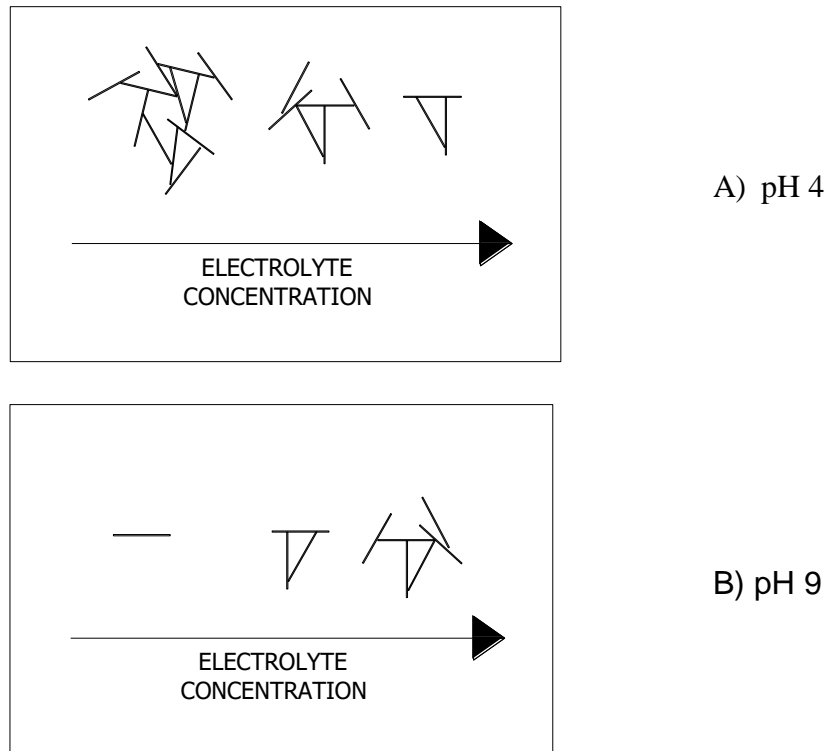
A) pH 4

B) pH 9

Figure 147. Particle configuration at different electrolyte concentration during sedimentation. a) pH4 and b) pH 9.

3) In a sedimentation test, the volume of the final sediment depends on the size of the floccules. The bigger the dimension of the floccules, the bigger is the final volume of the sediment (Figure 148). In acidic suspension, since the size of the floccules reduces with the electrolyte concentration, it follows that the final void ratio also reduces with electrolyte concentration. On the other hand, since the size of the floccules increases with the electrolyte concentration in alkaline suspension, the final void ratio also increases.
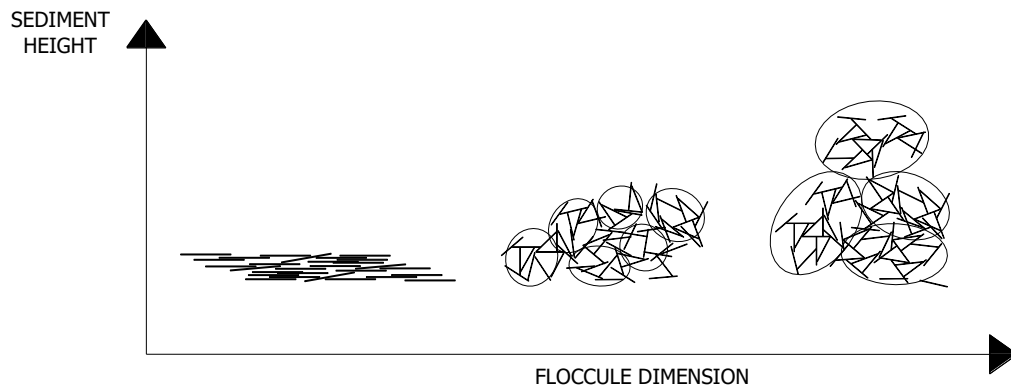
Figure 148. Particle configuration at increasing floccule dimensions in the final sediment.

4) When the electrolyte concentration of 1M is exceeded (indeed only 5M has been tested), no difference was observed between alkaline and acidic solutions. Therefore, the edge charge does no longer control the flocculation. A conceptual model is difficult to figure, although some consideration can be drawn.

At 5M, the solution is close to the limit of salt saturation. Double layer repulsion can be assumed to be nearly zero between faces and between faces and edges as well. Thus, particle interactions may result attractive both at the edge-to-face (as assumed for solution at 1M concentration) and at face-to-face. Face-to-face attraction therefore causes denser flocs to form.

According to Stokes' law, the velocity of sedimentation, v_{SED}, is proportional to the square of the diameter of the equivalent sphere, D_{eq}^2, and to the density of the aggregate, ρ_{agg}:

$$v_{SED} \propto D_{eq}^2 \cdot \rho_{agg} \qquad [82]$$

The density of the aggregate is generally considered to be constant and a change in the velocity of sedimentation is attributed to a change in the equivalent diameter. However, if the density of the aggregate varies (with a mechanism similar to the one reported in Figure 138), a decrease of

sedimentation velocity can also be caused by a decrease of the aggregate density.

The velocity of sedimentation in the alkaline suspension decreases when the salt concentration is increased from 1M to 5M (in contrast to the increase observed when electrolyte concentration was increasing from 0 to 1M). In order to justify the different sedimentation response for the 5M sample, a simple reduction in the floc size is not enough. An increase in density can also be invoked. This point is going to be discussed in more detail in the section on the 1-D compression of consolidated clays prepared with solutions at different NaCl concentrations.

5.4 Effect of pH and electrolyte concentration on slurry state

5.4.1 Rationale

A major assumption made in Chapter 3 is that micro-mechanical behaviour is controlled by particle-to-particle interactions rather than interactions between groups of particles, i.e. aggregates. In the sedimentation tests, two different particle-to-particle configurations have been figured out, dispersed and flocculated.

In order to investigate whether the size of the floccules has an influence on the mechanical behaviour, liquid limit tests have been performed on kaolin clay at different pH and electrolyte concentration.

5.4.2 Liquid limit results

Liquid limit tests of kaolin samples at different pH (4 and 9) and salt concentrations (0M and 1M) were performed following the BS 1377-2 by means of a cone penetrometer.

As shown in Table 3, acidic solutions at 0 and 1 M of NaCl concentration and alkaline solutions at 1M of NaCl concentration, give rise to similar liquid limits. On the other side, for the case of the dispersed samples (alkaline solution with no electrolyte), the liquid limit appears to be very low. For the sake of completeness, a similar test has been performed for a sample of kaolin mixed with distilled water, which results to be very similar to the sample prepared with acidic solutions.

Table 3. Liquid limit at different pH and electrolyte concentrations

pH	NaCl concentration [M]	Liquid limit	Particle configuration
Distilled water (5.8)	0	0.64	Flocculated
4	0	0.65	Flocculated
4	1	0.61	Flocculated
9	0	0.51	Dispersed
9	1	0.62	Flocculated

It therefore appears that the liquid limit depends on the particle arrangement. When particles are dispersed, it can be assumed that the particles are in a non-contact configuration. On the other hand, when particle flocculate, regardless of the floccule dimension, they are in a contact configuration.

5.5 Effect of pH and electrolyte concentration on consolidated state

5.5.1 Rationale

The interaction of clay particles in suspension is controlled by the competition between the kinetic energy of particles or groups of particles (due to Brownian motion) and the net energy. When the water content of the clay-solution mixture is decreased, as is the case in geotechnical problems, particles are driven to contact (or to a closer mutual distance) by external forces (gravity, external load, suction). Particle association is not just controlled by the probability that particle electrical fields overlap but also by the competition between external forces and internal forces (e.g. face-to-face repulsion).

Flocs having different size but same configuration (edge-to-face contact) would have occurred in suspensions at different electrolyte concentration. The different size of flocs gave rise to different rheological properties in the sedimentation tests.

However, when the water content is decreased and flocs are brought into contact, it may be expected that differences among various electrolyte concentrations tend to vanish. Since the flocs likely have an isotropic fabric, no differences would be observed once the flocs are brought into in contact regardless of the initial floc size. The discrete nature (at floc scale) of the sediment would disappear and form a matrix-like structure with no distinction between one floc and another. However, the particle-to-particle nature of interaction may be preserved (edge-to-face in acidic solution and face-to-face repulsion in alkaline solution).
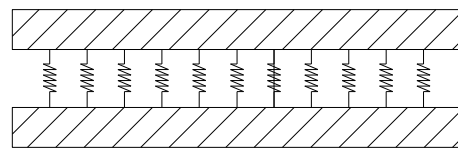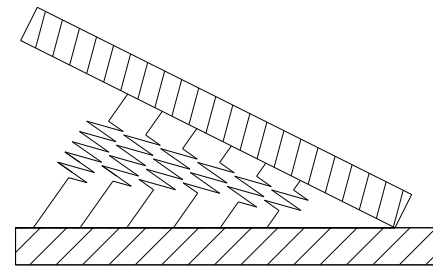
A) Non-contact configuration   B)Contact configuration

Figure 149. Particle configuration

5.5.2 Experimental procedure

Oedometer tests were performed on kaolin reconstituted from slurry at different pH and NaCl concentration. Samples were loaded in steps to 2220 kPa vertical stress and then unloaded. For any loading step, the samples were allowed to fully consolidate. The water content of the sample was measured at the end of the test and the vertical displacement was monitored during the consolidation process, the void ratio could be back-calculated at any stage of the test.

Slurries at pH 4 and different NaCl concentrations (0 M, 0.1 M, 1 M and 5 M) were prepared at the water content w=1.00 (by mixing 100 g of kaolin powder with 100 g of the desired solution). This water content, which is equal to 1.5 the plastic limit, ensured the slurry to be sufficiently fluid to be scooped into the oedometer and sufficiently dense to not extrude when the first loading steps were applied. The pH was controlled as for the sedimentation tests.

Slurries at pH 9 were prepared at different water contents depending on the salt concentration. For NaCl concentration of 0.1 M, 1 M and 5 M, samples were prepared at a water content w=1.00. Again this ensured that the slurry was sufficiently fluid to be scooped into the oedometer and sufficiently dense to not extrude when the first loading steps were applied. The pH of the slurry was controlled by adding 0.3-0.4 g of KOH until pH 9 was reached.

On the other hand, the slurry at pH9 and 0 M NaCl concentration (dispersed solution) was prepared at a reduced water content, w=0.55. In fact, the slurry

prepared at pH=9 and 0 M NaCl concentration was too liquid at w=1.00 to be consolidated without severe extrusion. It was required to reduce the water content w=0.55 to obtain a slurry sufficiently dense. To reach pH 9, 0.3-0.4 g of KOH were added to the slurry.

To investigate the effect of the dispersant, three different dispersant solutions were tested including the ones suggested by the American Standard and the British Standard and a KOH solution (pH 9). Figure 150 shows that the loading and unloading behaviour of the three samples is very similar. As a result, a KOH solution was used to prepare alkaline solutions for the slurry.
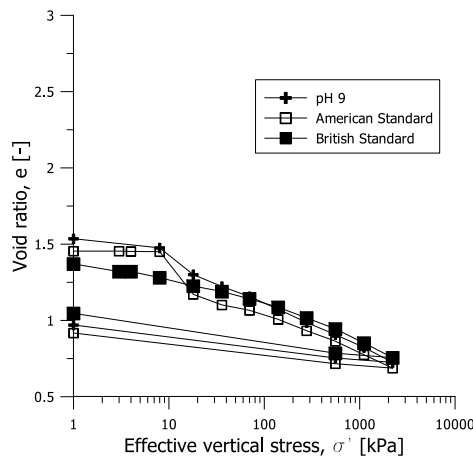
Figure 150: Compression tests. Dispersant comparison

5.5.3 Results and discussion

Figure 151 shows the oedometer tests of kaolin samples in dispersed and flocculated conditions (0 M NaCl concentration). An alkaline solution (pH 9) was used for the dispersed condition and an acidic solution (pH 4) was used for the flocculated condition. Kaolin in acidic solution shows a much more open structure than the dispersed one. Such behaviour suggests that the positive charge of edges plays a role even when the water content is relatively low compared with the suspension. The differences in the mechanical behaviour can be considered as a direct consequence of a different microstructure, where the positively charged edges have a fundamental role. Microstructure

of kaolin in acidic solution is expected to have a higher number of edge-to-face associations when compared with the dispersed one.
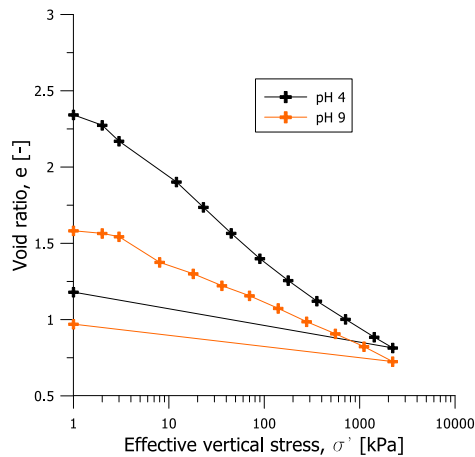
Figure 151: Compression tests with slurries at different pH

Figure 152 shows the kaolin mixed with acidic solution having different NaCl concentrations (0M, 0.1M and 1M). It is possible to see that the mechanical behaviour does not change. Therefore, if two samples have the same initial void ratio and the same compressibility upon loading, it seems straightforward to infer that their microstructure be the same.
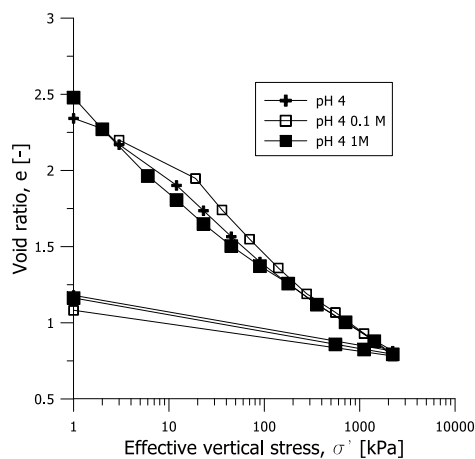
Figure 152: Compression tests. Slurry at pH 4 and different NaCl concentrations

When the same solutions were used in the suspensions, different floc diameters were observed. These differences seem to disappear when

samples are reconstituted from slurry. This behaviour can be explained by assuming that a uniform matrix of particles forms in the slurry, having the same particle configuration than within the flocs (i.e. edge-to-face). When particles are close enough to interact with each other, the range of electrical interaction does not have an influence any longer.

Similarly, oedometer tests of kaolin mixed with alkaline solutions (pH 9) at different NaCl concentrations (0M, 0.1M and 1M) were performed as shown in Figure 153.
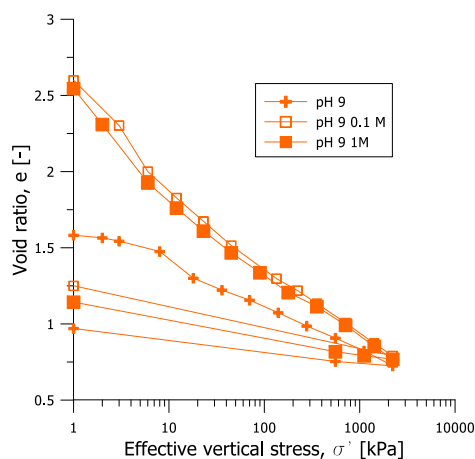
Figure 153: Compression tests. Slurry at pH 9 and different NaCl concentrations

As soon as the electrolyte concentration was high enough (0.1 M) the mechanical behaviour became comparable to the one of the acidic solutions. It might therefore reasonable to infer that, if kaolin with acidic solution and kaolin with alkaline solution at high salt concentration have the same mechanical behaviour, their microstructure must also be similar.

When such samples were considered in the sedimentation tests, it has been concluded that the alkaline samples having high salt concentration have particle associating in an edge-to-face configuration. Consequently, oedometer samples of kaolin prepared with acidic solutions or alkaline solutions with high salt concentration are likely to have the same microstructure and therefore the same mechanical response.

In conclusion, kaolin mixed with alkaline solutions at high salt concentration appears to have same microstructure than the kaolin mixed with acidic solution

(at any salt concentration). The only different microstructure, chemically induced, was obtained when kaolin was mixed with dispersant solution at very low salt concentration.

The compressibility of samples of kaolin mixed with alkaline and acidic solutions at 5 M of NaCl concentration was also investigated. As shown in Figure 154, it appears that no differences exist between acidic and alkaline solutions at very high salt concentration. Such a response seems to be in agreement with the response of the suspensions in alkaline and acidic solutions at 1M and 5M salt concentration (Figure 142 and Figure 144), where the same conclusion was attained.

When samples having a NaCl concentration of 5 M are compared with samples prepared with acidic solutions at low electrolyte concentration, it is possible to see that although the initial void ratio is very similar, the "salty" samples are much more compressible. Different compressibility must be the results of different particle interaction or arrangement. At 5M, the solution is closed to the limit of salt saturation. Face-to-face double layer repulsion can be assumed nearly zero between faces and between faces and edges as well. Thus, particle interactions may result attractive both at the edge-to-face (as assumed for solution at 1M concentration) and at face-to-face, which might affect the strength of the particle contact or the particle mutual distance.
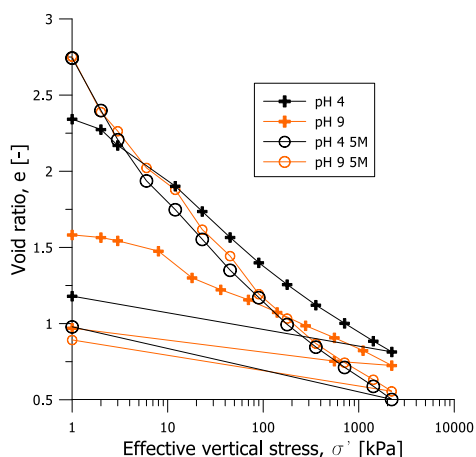
Figure 154. Compression tests. Slurry at pH 9 and pH 4 at 0 and 5 M of electrolyte concentrations

5.6 Effect of deactivation of edge positive charge on compaction tests

5.6.1 Rationale

This set of experiments was an attempt to achieve higher density of compacted samples by acting on the chemical composition of the pore water. Since the only significant mechanical difference in the consolidated clays was observed when dispersant solutions were used, the compaction behaviour of clay prepared with a dispersant solution as compaction fluid was investigated and compared with samples prepared using distilled water.

5.6.2 Experimental procedure

Compaction tests were performed in an oedometer cell as described by Tarantino & De Col (2008). Samples were prepared at 0.10, 0.20 and 0.30 water content. Samples were compacted at 300, 600, 900 and 1200 kPa. The final height of the sample was measured by a calliper at the end of the test. As the vertical displacement was monitored during the compaction process, the void ratio could be back-calculated at any stage of the test. As no drainage was provided during the test, water content remained constant during compaction and was measured at the end of the test.

Dispersant solution was prepared using sodium hexametaphosphate (NaHMP) instead of alkaline solution in order to keep the free-cations concentration at the minimum. To this end, 0.05 g of sodium hexametaphosphate were added for 100 g of kaolin. Such amount resulted to be the minimum required in order to create a disperse sample. Such amount was determined by adding controlled amount of NaHMP to 100 g of kaolin at 0.55 of water content. The dispersion of the sample was evaluated by visual inspection. When the sample appeared in a fluid state (as in Figure 163b) was considered dispersed, and the relative amount of NaHMP was considered the minimum required for 100g of kaolin. Nevertheless, the amount of free cations introduced in the soil could not be considered negligible as in the previous

sedimentations and 1-D consolidation tests. Because of the small amount of water used in compaction, concentration of free cations becomes relatively high.

5.6.3 Results and discussions

As shown in Figure 155, no noticeable differences are observed for the samples compacted with acidic or alkaline solutions. Differences seem perhaps to be relevant only for the lowest compaction stress (300 kPa)

These tests were not very conclusive in the sense that the effect of alkaline solution could not be separated from the effect of salt concentration. In order to guarantee enough presence of OH$^-$ anions in the system, the amount of dispersant (KOH or NaHMP) was chosen according to the mass of the clay used (and not to the mass of water). Such a procedure could not guarantee that the concentration of the Na or K anions added to the system was negligible (since the amount of water was small). Such a procedure therefore did not therefore produce truly dispersed samples (alkaline solution and low salt concentration) but produced a sample having alkaline pore water with a high electrolyte concentration.

As shown in Figure 153, when the salt concentration is high, no differences between alkaline and acidic solution can be observed. Accordingly, the compaction test was essential made on two samples having a very similar microstructure and mechanical behaviour.
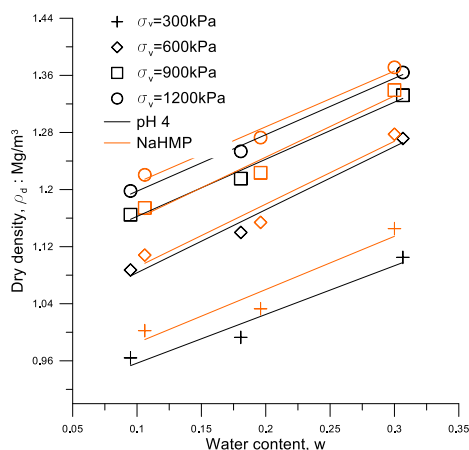
Figure 155. Compaction at different pH.

5.7 Effect on pH and electrolyte concentration on the microstructure

5.7.1 Rationale

In order to validate the microstructural assumptions made when interpreting mechanical behaviour of kaolin samples prepared at different pH and NaCl concentration, the pore size distribution of consolidated samples was studied by means of the mercury intrusion porosimeter. Samples were all dehydrated by freeze-drying technique as described in the previous chapters.

Figure 156 shows the pore size distribution of samples consolidated to 70 and 2220 kPa vertical stress and prepared with either acidic and alkaline solutions at 1M of NaCl concentration. According to the oedometer tests, acidic samples and alkaline samples are expected to have the same microstructure when the NaCl is 1 M, since the compressibility and the void ratio upon compression are the same. Moreover, according to Chapter 3, the PSD of samples consolidated at 70 and 2220 kPa and laying on the url are expected to differ only in terms of macro-pores (right hand-side of the modal value), where the yielding occurs. Indeed, the modal value (micro-porosity) was assumed to refer to the class of pores that have only reversible mechanisms (non-contact configuration) whereas the macro-porosity to the contact configuration, and thus to the pores subjected to yielding.

As expected, in Figure 156 no difference can be noticed between samples having NaCl concentration of 1 M and prepared either with acidic and alkaline solution.

On the contrary, Figure 156 shows a shift between PSD of samples consolidated at 2220 kPa and samples consolidated at 70 kPa. Moreover, the shape of the PSD does not change with the degree of yielding (macro-pores) but seems to be constant. Such behaviour was the same that in Chapter 3 was shown to characterized sample prepared on the ncl and url at the same compression stress. Such shift, it has been usually considered reversible upon

load removal. Both samples (the ones consolidated at 70 kPa and the one consolidated at 2220 kPa) have been unloaded and have the same electrolyte concentration (same osmotic pressure). Such difference seems to be due on different conditions during the freeze-drying process, since the water content of the two samples was different.
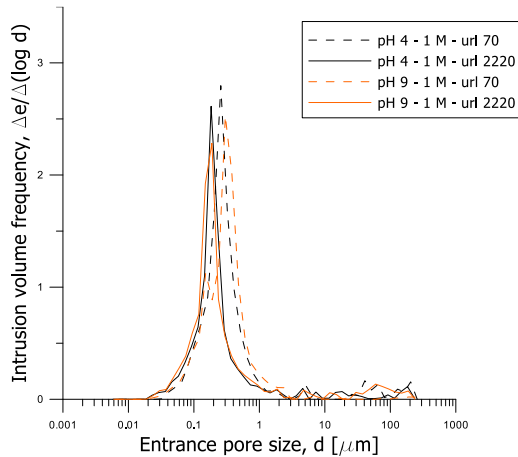
Figure 156. Pore size distribution of consolidated sample prepared with alkaline and acidic solution at 1M of NaCl concentration

Samples prepared with acidic solutions at different NaCl concentrations all show the same mechanical behaviour. These can therefore be assumed to have the same microstructure. Figure 157 shows the pore size distribution of sample consolidated at 70 kPa (Figure 157a) and 2220 (Figure 157b) prepared with acidic solutions at 0M and 1M of NaCl concentration. It can be seen that despite the total void ratio should be the same the pore size distribution is significantly different on the right-side of the modal value. Such area of the pore size distribution has been classified as the class of pores where yielding occurs (see Chapter 3). It can therefore be inferred that yielding occurred in the samples at high salt concentration, during the dehydration process. Dehydration process is made of two stages:

i)   Freezing
ii)   Drying

A) *Samples consolidated a 70 kPa*   B) *Samples consolidated at 2220 kPa*
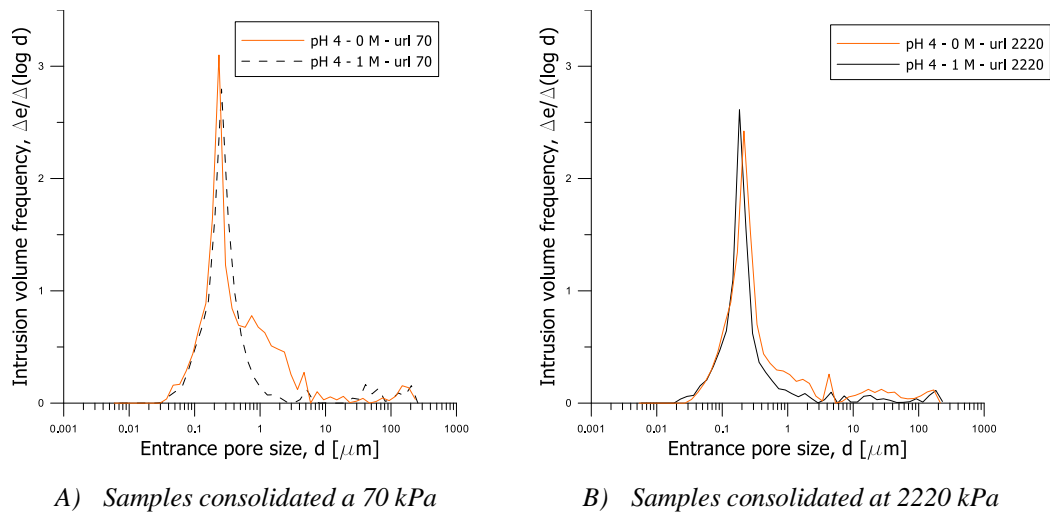
Figure 157. Pore size distribution of consolidated samples prepared with acidic solutions at 0 and 1M of NaCl concentration

5.7.2 On the freeze-drying of samples at elevated electrolyte concentration

The fusion (or freezing point) temperature decreases when salt is dissolved in water. In salty water ice is formed by the following mechanism. Depending on the electrolyte concentration, crystals of ice (where ice is formed by pure water) start forming at temperature between 0 and -21.1 °C. The more crystals are forming, the higher becomes the electrolyte concentration in the liquid (mass of liquid water decreases while mass of dissolved salt stays constant). Once that the liquid solution becomes salt saturated (23.3 % at -21.1°C for the case of NaCl) the temperature of fusion does not decrease anymore, since the electrolyte concentration cannot increase and salt precipitates. At this point the temperature will not decrease until all water becomes ice (Figure 158).

Freezing is made at very low temperature (-159 °C) in the freeze-dryer in order to guarantee a fast freezing which should prevent ice dilatation. If the thermal shock were not high enough, ice dilatation would occur, and therefore salty samples would swell. This does not seem to be the case reported in Figure 157, although a successive shrinkage could have covered this stage.
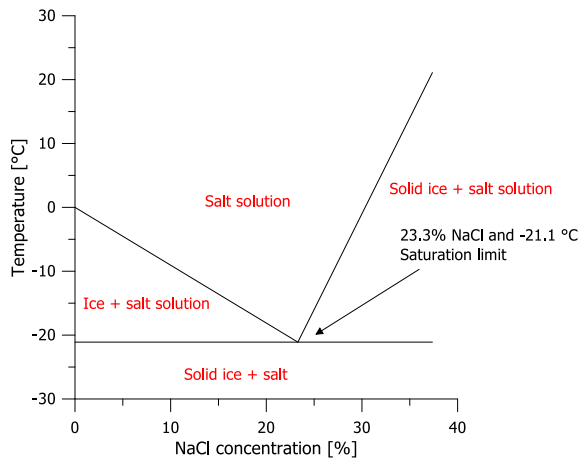
Figure 158. NaCl solution state diagram

On the other hand, once that freezing occurs, ice is removed through sublimation, by applying vacuum. When vacuum is applied, ice is below the water triple point. By keeping the environmental pressure low enough and by supplying energy to the system (heat), ice is forced to transform into the vapour phase rather than the liquid one. If ice sublimation does not occur, ice melts and liquid water evaporates. If evaporation occurs, suction is applied to the sample and therefore shrinks and yielding may occur. Indeed, salty samples in Figure 157 seem to have been exposed to a significant yielding when compared to non-salty samples at the same vertical stress.

Figure 159 shows the cumulative pore size distributions of the samples reported in Figure 157. It can be observed that salty samples show a lower void ratio at the same consolidation stress, even though, according to the oedometer tests, no differences in void ratio should be detected between the two different samples. It seems therefore reasonable to assume that during the dehydration stage ice melts before sublimating (probably because of the presence of ice) and that samples were therefore exposed to high values of suction, which caused yielding.

Similar conclusions can be drawn by inspecting the pore size distribution of samples prepared with acidic solutions at 5 M of NaCl concentration and consolidated to 70 and 2220 kPa vertical stress (Figure 160). Since the salt concentration is higher, a more marked effect has to be expected. The pore size distributions reported in Figure 160 do not show differences despite the

different consolidation stress and the different macro-void ratio. Again, such behaviour seems to support the assumption that freeze-drying of salty samples does not preserve the microstructure, because yielding occurs during the sublimation stage.
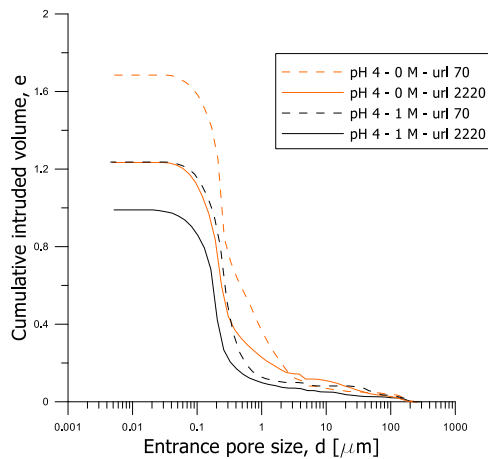
Figure 159. Cumulative pore size distribution of samples consolidated at 70 and 2220 kPa prepared with acidic solutions at 0 and 1 M of NaCl concentration.
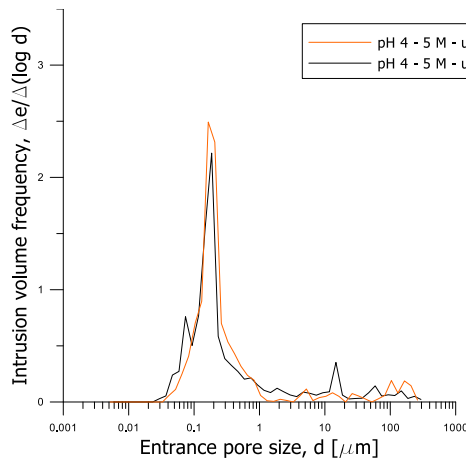
Figure 160. Pore size distribution of sample prepared with acidic solutions at 5M of NaCl concentration and consolidated at 70 and 2220 kPa.

Finally, when samples consolidated to the same vertical stress but prepared with different NaCl concentrations (0M, 1M and 5M) are compared (Figure

161), the effect of electrolyte can be detected on the values on the right-side of the modal pore (yielding area).
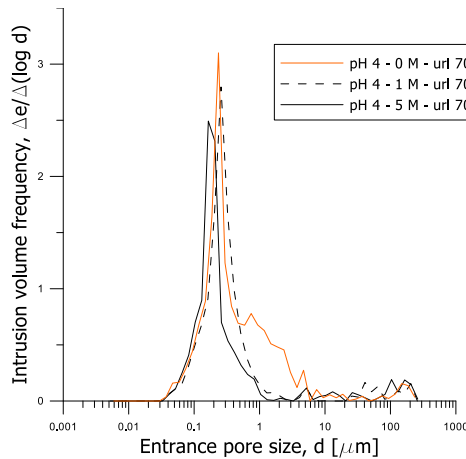
Figure 161. Pore size distribution of samples consolidated at 70 kPa prepared with acidic solutions at different NaCl concentrations.

As a final point, it is worth highlighting another aspect. When samples are prepared with salty solution and then dehydrated, salt precipitates. For the case of 1M NaCl concentration, a sample of kaolin prepared from slurry has an amount of salt that is equal to the 6% of the weight of the dry clay. This amount rises to almost the 30% for the case of samples of 5M. The question arises about where does this salt go and in which porosity it precipitates.

Figure 162 shows two samples of kaolin consolidated to 2220 kPa and then oven dried, one prepared with distilled water and the other one with an electrolyte concentration of 5 M. It can be observed that the sample prepared with an high electrolyte concentration showed parallel cracks as the salt precipitating applies tension forces to the clay (Figure 162).
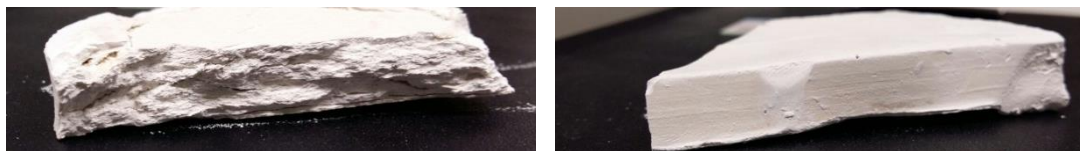
A) Consolidated kaolin prepared with 5M electrolyte concentration

B) Consolidated kaolin prepared with no electrolyte concentration

Figure 162. Visual inspection on oven-dried kaolin

5.8 Conclusions

Assumptions were made on the micromechanical configuration of kaolin particles when exposed to pore water at different pH and electrolyte concentration. Unfortunately, these could not be corroborated by MIP measurements due to the problems in the freeze-drying samples containing salts.

The investigation mainly focused on the rheological behaviour of kaolin suspension and the 1-D compressibility of kaolin reconstituted from slurry.

For both states, two main particle configurations have been assumed to characterise the microstructure:

i)   Particle in contact configuration
ii)   Particles in non-contact configuration

When kaolin is in suspension, non-contact configuration corresponds to dispersed solution. On the other hand, the contact configuration gives rise to flocs of different size. It has then been shown how flocculation may occur both in acidic or alkaline solutions (active or de-activated positive charge of the edges respectively). The addition of an electrolyte reduces the flocs size when the solution is acidic and increases the floc size when it is alkaline. In both cases, it has been assumed that flocculation occurs by means of an edge-to-face contact configuration. When the electrolyte concentration becomes higher than 1 M (for the case of NaCl), the charge of the edges appear to stop governing particle interactions.

When kaolin is reconstituted from slurry, no differences have been noticed at different electrolyte concentrations both when the solution is acidic or alkaline. However, kaolin showed lower compressibility if reconstituted with a dispersant solution. In such case, as already assumed in the chapter 3, the particle configuration is believed to be mainly non-contact. The mechanical response showed to be controlled exclusively by the activation or de-activation of the positive charges of the edges, which control the yielding and not by the

concentration of the electrolyte, which should control the entity of the repulsion between particles.

Although a general framework has been depicted, some important questions (both theoretical and experimental) still remain unsolved. Hypotheses on particle configuration and evolution of the pore size distribution could not have been validated by means of the MIP tests because of the effect of the electrolyte concentration during the freeze-drying process. Nevertheless, as already suggested in chapter 3, it appears that the charge of the particle edge has a major control of the mechanical behaviour from suspension to compacted states.

Appendix

A 1. Considerations on acidic and alkaline solutions

Acidic solutions

Kaolin was mixed with an HCl solution (Figure 163a) in order to generate kaolin particles with edges with positive charge. HCl in water dissociates in H^+ cations and Cl^- anions. The presence of free H^+ cations causes protonation of the potential hydroxides groups present on the edge surface. Under ideal conditions, when protonation occurs, the pH of the solution will slightly increase because of the decreasing number of free cations, which are trapped on the edge's surface. In practice, kaolin dry powder comes already with the edges positively charged. Proof of that is the decreasing of pH when distilled water is mixed with kaolin powder, which is a consequence of a partial deprotonation of the particle edges. To ensure that kaolin particle edges are all positive charged, the pH of solution was checked, and, in case, adjusted down to pH 4 by adding more HCl.

A) Acidic solution   B) Alkaline solution

Figure 163. Kaolin samples prepared at the same water content but at different pH.

Alkaline solutions (dispersed solutions)

Solutions of dispersed kaolin clay (Figure 163b) are obtained by neutralizing the positive charges on particle edges by means of deprotonation of hydroxyl groups. To have a dispersed solution both British and American standards (BS

1377-2 and ASTM D422 respectively) suggest to mix kaolin clay with a sodium hexametaphosphate (NaHMP) solution.

NaHMP is known to be a very efficient dispersant for clay suspensions because of the high negative charge of polyphosphate anions (valence -6). British standard suggests adding also a certain amount of NaOH in order to adjust the pH of the kaolin solution up to values higher than 9.

When hydroxyls anions (OH⁻) are added to a solution, the pH value increases. In kaolin solutions, OH⁻ anions are used for the deprotonation. When OH- are added to clay suspensions, these do not remain free in solution but deprotonate the edges. Therefore, until the most of the edges are not deprotonate, the pH does not rise upon OH- adjunction. Therefore, the measurement of solution pH is used as a mean to check whether all the positive charges of the edges have been neutralized.

A similar mechanism is generally assumed when sodium hexametaphosphate is added. When NaHMP is added to the clay solution, the neutralization of the positive broken edges is due to the polyphosphate anions instead of OH⁻ anions. Moreover, the addition of NaHMP and its dissociation does not cause any change in the water pH (no hydroxyls groups are formed). Though it is necessary to add KOH or similar compounds to rise the pH of the solution in order to check whether all the positive edges have been neutralized.

For dispersant solutions, KOH was preferred to SHMP in order to have only one predominant type of dispersed anions (OH⁻) which can act as positive charge neutralizer and pH riser at the same time. Moreover, for double layer considerations, it seems easier to deal with strong salts that dissociate in monomolecular anions and cations. Besides, the phosphate anions, resulting from the dissociation of the sodium hexametaphosphate, is bigger in dimension than general mono-molecular anions, which again may interfere with the double layer.

When kaolin clay is mixed with water having pH 9, the pH of the solution decreases to values below 7 because of the occurring deprotonation reaction

(proton H^+ are released by the kaolin surfaces). The pH was therefore adjusted up to 9 by adding more KOH, in order to guarantee the deprotonation of all the edges.

Conclusions

This thesis has focused on outlining the mechanisms at the particle level that control the hydro-mechanical behaviour of clay under saturated, partially saturated, and dry conditions. The main motivation behind this work was to propose a microstructural conceptual model which could serve towards the development of DEM models.

Microstructural conceptual models proposed for clays have been following two different approaches depending on whether the clay is in saturated or partially saturated state. For saturated clays, the single particle has been considered to be the 'elementary unit' whereas elementary unit has been considered to be the aggregate in partially saturated compacted clays. This view hampers the development of DEM models because it would be difficult to create continuity between saturated and partially saturated states.

This work has proposed a microstructural conceptual model that has proven capable to interpret key features of the macroscopic behaviour of clays from dry to saturated states, i.e. over the whole range of degree of saturation. The nature of clay particle interaction has been assumed to remain the same when moving from saturated to partially saturated states. The conceptual microstructural model has therefore the potential to be implemented into a DEM model and was presented in a 'ready to go' form, i.e. mechanical and electro-chemical interactions were schematised in a form suitable for DEM implementation. Indeed, an embryonic DEM model was presented to prove the potential of the approach proposed.

The review of existing conceptual models for clay particle interaction and particle configuration allowed the development of a model built around a few key concepts, i.e. clay particles interact mainly by means of Coulombian forces (either repulsive or attractive) and mechanical forces (friction) and clay particles can be either in contact or non-contact configuration. The microstructural 'particle-based' conceptual model was then progressively built

by examining data from mercury intrusion porosimetry, which allowed analysing changes in microstructural features in a quantitative fashion.

The microstructural 'particle-based' conceptual model was initially developed for clays in saturated states and then extended to partially saturated states. Coulombian forces were assumed to control the particle mutual distance and were visualised as springs. Mechanical forces were assumed to control slippage at the interparticle contacts and were visualised as sliders. The balance between Columbian and mechanical forces control particle configuration, which can be characterised by either contact or no-contact. Reversible and non-reversible mechanisms have been associated with these two configurations. Slippage at the particle contact was inferred to be the mechanisms controlling the non-reversible volume change. On the other hand, reversible mechanisms have been associated with both contact and non-contact configuration. However, reversible volume change of contact configuration has been found to be the more relevant from a quantitative point of view.

This conceptual model was the extended to partially saturated clays and was shown to be capable of interpreting key aspects of macroscopic behaviour of partially saturated clays as well as the evolution of the pore size distribution upon various hydro-mechanical paths. A distinctive feature of the microstructural conceptual model is its ability to describe coherently the evolution of the pore size distribution over the full range of degrees of saturation, from 0 (dry clay) to 1 (saturated clay).

An approach to constitutive modelling based on the microstructural conceptual model has been validated against volume change associated with both mechanical and hydraulic paths and shearing resistance. The constitutive approach can be viewed as a further validation of the microstructural conceptual model. A major achievement was that macroscopic volumetric and shear response could be modelled only considering, as 'constitutive' relationships, the response in compression and shear of (reconstituted) water-

saturated kaolin and (dry) air-saturated kaolin. No other constitutive parameters were added.

Future works

This thesis work started as a study on the microstructure of clay particles. Presumptuously, the initial aim was to investigate a theoretical model which could motivate particle association into aggregates and extend such microstructural conceptual model, which is generally adopted only for compacted clays, to clays in saturated conditions. The ultimate purpose was therefore to unify two states of clay, saturated and unsaturated, that generally are considered behaving almost as two different materials under a single conceptual model.

The research presented in this thesis has led to a totally different result. In order to coherently interpret the experimental data a microstructural conceptual model based on single particle interactions (instead of aggregate interactions) was postulated. Such a conceptual model resigned us to the discrete nature of clays, where single particles play the main role in the hydro-mechanical interpretation of clay behaviour. Since such a concept is considered by the author as a starting point for new research rather than a conclusive piece of work, many different topics have been investigated in this thesis. Often not definitive conclusions have been made (e.g. chapter 5) but new approaches or ideas have been tested and have been proven to be promising. The whole thesis is based on a particle-based conceptual model. As this is a brand new conceptual model a significant amount of work has still to be carried out to test and validate this approach. So far, there are two main limitations of the work presented in this thesis:

1. A set of images proving the proposed particle configuration is still missing. The SEM technique is generally the technique employed to image clay. However, this technique is dependent (as already highlighted) on sample dehydration, which can be a relevant source of error. Moreover, SEM imaging is possible only on surfaces which are failure surfaces. As already discussed such a technique is not

considered by the author entirely reliable, although it is the best existing option right now.

A study of other techniques for imaging clay are planned. Techniques including nanotomography might result in a more reliable imaging technique.

2. Although a wide range of clays has been considered in the literature review, experimental pore side distributions have been carried out only on samples of kaolin clay. Analysis of literature data was not possible since dry powder data are missing. In order to consider if the proposed conceptual model can be extended to all the non-active clays, future research work should also investigate different kinds of non-active clays (although these are mainly represented by kaolin clays).

On the other hand, if one accepts the particle-based conceptual model, natural extensions of the work presented in this thesis are listed below:

3. The creation of a Discrete Element Model has been addressed as one of the main driving forces of this research work. As highlighted in the conclusions chapter, the conceptual model proposed in chapter 3 is ready to be implemented in a DEM. Once created, such a model could be easily converted to work also for partially saturated conditions (since the conceptual model is the same for saturated and partially saturate states). The exploitation of such a model in simulating laboratory tests carried out on clay under different hydro-mechanical conditions is therefore a natural follow on study of this thesis.

4. In chapter 4 a particle-based approach is proposed for partially saturated clays. The obvious continuation is the formulation of a constitutive model for partially saturated clays. Such a constitutive, model formulation should, of course, be followed by experimental test validation. Controlled suction tests, might be of relevance, due to their historical importance in the support of the aggregate-based models. Ultimate state has been only partially investigated. The approach has

been proven to work also for ultimate shear, but this was still a preliminary analysis, although it appears to be very promising.

The accomplishing of point 3 and 4 will provide two important tools to revise some fundamental geotechnical aspects (as already highlighted in the thesis). Extending the particle-based conceptual model to active clays would be interesting and a turning point in the impact of such work. Illite which has a mineralogy of the same nature of swelling clays but whose swell is limited, is probably the best clay to start with. Severely swelling clays, as montmorillonite clays, might also been interesting, especially to check whether the concept of an air-saturated macro-porosity can be exploited.

Another future application, especially in order to bring such conceptual model to "non-laboratory environments", will be to test it for soils which are a mixture of clay and coarser material (i.e. clay/silt or clay/sand).

During this research project, in order to investigate the clay microstructure, many different topics have been scrutinised. The thesis provided a certain amount of preliminary data or interesting tools which are open to further investigation and exploitation as stand-alone research projects of various impact.

The main topics are briefly summarised below:

5. Clay imaging under hydro-mechanical loading paths (chapter 2-3-4)
6. Study of the possible ways of interpreting a PSD provided by mercury intrusion porosimeter analysis. Exploitation of the intrusion/extrusion model proposed in chapter 2, by comparing synthetic PSD with measured PSD.
7. Reliability of PSD from mercury intrusion porosimetry analysis when compared with PSD from Nuclear Magnetic Resonance technique (chapter 2 and 5)

8. Coupling of the extrusion/intrusion model proposed in chapter 2 and the particle based approach to solve clay problems that are discrete in nature (e.g. gas extraction in claystone).

9. Coupling of the model extrusion/intrusion model proposed in chapter 2 and imaging technique to investigate bi-phase intrusion/extrusion problems in micro-porous media (e.g. cavitation in high capacity tensiometer)

10. Investigation of the mechanical behaviour of contaminated clays (chapter 3)

11. Microstructure of natural clays versus microstructure of reconstituted clays adopting a particle based approach (chapter 3 and 5)

12. Enhancing clay stability via chemicals (chapter 3 and 5)

13. Investigation of marine clays and the effect of electrolytes in natural clays (chapter 5)

14. Enhancing clay compaction by using high salt concentration samples (chapter 5)

15. In chapter 5 the liquid limit was shown to not be a clay index, but to vary with the chemistry of the pore fluid.

16. Extension of the particle-based approach to clays exposed to different electrolyte solutions (chapter 5)

17. Microstructural analysis of clay exposed to different electrolyte solutions by means of NMR (Nuclear Magnetic Resonance) technique in order to avoid problems related to the presence of salt during dehydration (chapter 5)

18. Hydraulic micro-mechanism of drying clays (chapter 4)

19. Degree of saturation evolution adopting a particle based approach (chapter 4)

References

Alleman, J. E., Russell, E. K., Jr, W. L. L. & Wukasch, R. F. 1985. Biofilm cryopreparation for scanning electron microscopy. *Water Research,* 19**,** 1073-1078.

Alonso, E., Gens, A. & Hight, D. Special problem soils. General report. Proceedings of the 9th European conference on soil mechanics and foundation engineering, Dublin, 1987. 1087-1146.

Alonso, E., Pinyol, N. & Gens, A. 2012. Compacted soil behaviour: initial state, structure and constitutive modelling. *Geotechnique,* 63**,** 463-478.

Alonso, E. E., Pereira, J.-M., Vaunat, J. & Olivella, S. 2010. A microstructurally based effective stress for unsaturated soils. *Geotechnique,* 60**,** 913-925.

Anandarajah, A. 1997. Structure of sediments of kaolinite. *Engineering Geology,* 47**,** 313-323.

Anandarajah, A. 2000. Numerical simulation of one-dimensional behaviour of a kaolinite. *Geotechnique,* 50**,** 509-519.

Anandarajah, A. & Amarasinghe, P. 2012. Discrete-element study of the swelling behaviour of Na-montmorillonite. *Geotechnique,* 63**,** 674-681.

Anandarajah, A. & Amarasinghe, P. M. 2011. Microstructural investigation of soil suction and hysteresis of fine-grained soils. *Journal of geotechnical and geoenvironmental engineering,* 138**,** 38-46.

Anandarajah, A. & Chen, J. 1997. Van der Waals attractive force between clay particles in water and contaminants. *Soils and foundations,* 37**,** 27-37.

Anderson, M. T. & Lu, N. 2001. Role of microscopic physicochemical forces in large volumetric strains for clay sediments. *Journal of engineering mechanics,* 127**,** 710-719.

Andreola, F., Castellini, E., Manfredini, T. & Romagnoli, M. 2004. The role of sodium hexametaphosphate in the dissolution process of kaolinite and kaolin. *Journal of the European Ceramic society,* 24**,** 2113-2124.

ASTM 1984. Standard Test Method for Determination of Pore Volume and Volume Distribution of Soil and Rock by Mercury Intrusion Porosimetry. *ASTM D 4404-84.*

AsTM, D. 2487-00 Standard classification of soils for engineering purposes (Unified Soil Classification System). *Annual Book of ASTM Standards, Section,* 4.

Bishop, A. W. 1960. *The principles of effective stress*, Norges Geotekniske Institutt.

Bolt, G. 1956. Physico-chemical analysis of the compressibility of pure clays. *Geotechnique,* 6**,** 86-93.

Brady, N. C. & Weil, R. R. 1996. *The nature and properties of soils*, Prentice-Hall Inc.

Braggs, B., Fornasiero, D., Ralston, J. & Smart, R. S. 1994. The effect of surface modification by an organosilane on the electrochemical properties of kaolinite. *Clays and Clay Minerals,* 42**,** 123-136.

Butlanska, J., Arroyo, M., Gens, A. & O'Sullivan, C. 2013. Multi-scale analysis of cone penetration test (CPT) in a virtual calibration chamber. *Canadian Geotechnical Journal,* 51**,** 51-66.

Butt, H. J., Graf, K., Kappl, M. & Wiley, J. 2003. *Physics and chemistry of interfaces*, Wiley Online Library.

Carty, W. 1999. The colloidal nature of kaolinite. *American ceramic society bulletin,* 78**,** 72-76.

Casimir, H. & Polder, D. 1948. The influence of retardation on the London-van der Waals forces. *Physical Review,* 73**,** 360.

Casini, F., Vaunat, J., Romero, E. & Desideri, A. 2012. Consequences on water retention properties of double-porosity features in a compacted silt. *Acta Geotechnica,* 7**,** 139-150.

Cetin, H., Fener, M., Söylemez, M. & Günaydin, O. 2007. Soil structure changes during compaction of a cohesive soil. *Engineering Geology,* 92**,** 38-48.

Chang, C. S., Chang, Y. & Kabir, M. G. 1992. Micromechanics modeling for stress-strain behavior of granular soils. I: Theory. *Journal of Geotechnical Engineering,* 118**,** 1959-1974.

Chapman, D. L. 1913. LI. A contribution to the theory of electrocapillarity. *The London, Edinburgh, and Dublin Philosophical Magazine and Journal of Science,* 25**,** 475-481.

Chen, J. & Anandarajah, A. 1998. Influence of pore fluid composition on volume of sediments in kaolinite suspensions. *Clays and Clay Minerals,* 46**,** 145-152.

Chen, J., Anandarajah, A. & Inyang, H. 2000. Pore fluid properties and compressibility of kaolinite. *Journal of geotechnical and geoenvironmental engineering,* 126**,** 798.

Choi, I.-K., Wen, W.-W. & Smith, R. 1993. The effect of a long chain phosphate on the adsorption of collectors on kaolinite. *Minerals engineering,* 6**,** 1191-1197.

Cui, L. & O'sullivan, C. 2006. Exploring the macro-and micro-scale response of an idealised granular material in the direct shear apparatus. *Geotechnique,* 56**,** 455-468.

Cui, Y. & Delage, P. 1996. Yielding and plastic behaviour of an unsaturated compacted silt. *Geotechnique,* 46**,** 291-311.

Cundall, P. 2001. A discontinuous future for numerical modelling in geomechanics? *Proceedings of the ICE-Geotechnical Engineering,* 149**,** 41-47.

Cundall, P. & Strack, O. 2013. Modeling of microscopic mechanisms in granular material. *Mechanics of granular materials: new models and constitutive relations,* 63.

Cundall, P. A. & Strack, O. D. 1979. A discrete numerical model for granular assemblies. *Geotechnique,* 29**,** 47-65.

D. L. Chapman 1913. A contribution to the theory of the electrocapillarity. *Philos. Mag. ,* 25,**,** 475 ().

Delage, P. 2010. A microstructure approach to the sensitivity and compressibility of some Eastern Canada sensitive clays. *Geotechnique,* 60**,** 353-368.

Delage, P., Audiguier, M., Cui, Y.-J. & Howat, M. D. 1996. Microstructure of a compacted silt. *Canadian Geotechnical Journal,* 33**,** 150-158.

Delage, P. & Lefebvre, G. 1984. Study of the structure of a sensitive Champlain clay and of its evolution during consolidation. *Canadian Geotechnical Journal,* 21**,** 21-35.

Delage, P., Lefebvre, G., Sridharan, A., Jayadeva, M., Murty, B. & Nagaraj, T. 1983. Double-layer theory and compressibility of calys-discussion. Thomas Telford Services LTD. Thomas Teldford House, 1 Heron Quay, London England E14 4JD.

Delage, P., Marcial, D., Cui, Y. & Ruiz, X. 2006. Ageing effects in a compacted bentonite: a microstructure approach. *Geotechnique,* 56**,** 291-304.

Delage, P. & Pellerin, F. M. 1984. Influence de la lyophilisation sur la structure d'une argile sensible du Quebec. *Clay Minerals,* 19**,** 151-160.

Delage, P., Tessier, D. & Marcel-Audiguier, M. 1982. Use of the Cryoscan apparatus for observation of freeze-fractured planes of a sensitive Quebec clay in scanning electron microscopy. *Canadian Geotechnical Journal,* 19**,** 111-114.

Derjaguin, B. & Landau, L. 1941. Theory of the stability of strongly charged lyophobic sols and of the adhesion of strongly charged particles in solutions of electrolytes. *Acta Physicochim URSS,* 14**,** 633-662.

Di Maio, C. 1996. Exposure of bentonite to salt solution: osmotic and mechanical effects. *Geotechnique,* 46**,** 695-707.

Diamond, S. 1970. Microstructure and pore structure of impacted-compacted clays. *Clays Clay Miner,* 19**,** 239-249

Fisher, R. 1926. On the capillary forces in an ideal soil; correction of formulae given by WB Haines. *The Journal of Agricultural Science,* 16**,** 492-505.

Gallipoli, D., Gens, A., Sharma, R. & Vaunat, J. 2003. An elasto-plastic model for unsaturated soil incorporating the effects of suction and degree of saturation on mechanical behaviour. *Géotechnique.,* 53**,** 123-136.

Ganor, J., Mogollón, J. L. & Lasaga, A. C. 1995. The effect of pH on kaolinite dissolution rates and on activation energy. *Geochimica et Cosmochimica Acta,* 59**,** 1037-1052.

Giesche, H. 1997. Within the hysteresis: Insight into the bi-modal pore size distribution of close-packed spheres. *Special Publications of the Royal Society of Chemistry,* 213**,** 171-179.

Giesche, H. 2006. Mercury porosimetry: a general (practical) overview. *Particle & particle systems characterization,* 23**,** 9-19.

Gouy, G. 1910. Constitution of the electric charge at the surface of an electrolyte. *J. phys,* 9**,** 457-467.

Grim, R. E. 1968. Clay Mineralogy McGraw-Hill. *New York***,** 596.

Gupta, V., Hampton, M. A., Stokes, J. R., Nguyen, A. V. & Miller, J. D. 2011. Particle interactions in kaolinite suspensions and corresponding aggregate structures. *Journal of Colloid and Interface Science.*

Hamaker, H. 1937. The London—van der Waals attraction between spherical particles. *physica,* 4**,** 1058-1072.

Huertas, F. J., Chou, L. & Wollast, R. 1998. Mechanism of kaolinite dissolution at room temperature and pressure: Part 1. Surface speciation. *Geochimica et Cosmochimica Acta,* 62**,** 417-431.

Institution, B. S. 1377 (1990) Methods of Test for soils for civil Engineering Purposes. *BS 1377-2.*

Ioannidis, M. A. & Chatzis, I. 1993. A mixed-percolation model of capillary hysteresis and entrapment in mercury porosimetry. *Journal of Colloid and Interface Science,* 161**,** 278-291.

Katti, D. R., Matar, M. I., Katti, K. S. & Amarasinghe, P. M. 2009. Multiscale modeling of swelling clays: A computational and experimental approach. *KSCE Journal of Civil Engineering,* 13**,** 243-255.

Kemball, C. 1946. On the surface tension of mercury. *Trans. Faraday Soc.,* 42**,** 526-537.

Keren, R. & Sparks, D. 1995. The role of edge surfaces in flocculation of 2: 1 clay minerals. *Soil Science Society of America Journal,* 59**,** 430-435.

Kretzschmar, R., Holthoff, H. & Sticher, H. 1998. Influence of pH and humic acid on coagulation kinetics of kaolinite: A dynamic light scattering study. *Journal of Colloid and Interface Science,* 202**,** 95-103.

Lambe, T. W. 1958. The structure of compacted clay. *Journal of the Soil Mechanics and Foundations Division, ASCE,* 84**,** 1-34.

Lambe, T. W. A mechanistic picture of shear strength in clay. Research Conference on shear strength of cohesive soils, 1960. ASCE, 555-580.

Lifshitz, E. 1956. The theory of molecular attractive forces between solids. *Sov. Phys. JETP,* 2**,** 73-83.

Liu, S. & Sun, D. 2002. Simulating the collapse of unsaturated soil by DEM. *International journal for numerical and analytical methods in Geomechanics,* 26**,** 633-646.

Lowell, S. & Shields, J. E. 1981. Hysteresis, entrapment, and wetting angle in mercury porosimetry. *Journal of Colloid and Interface Science,* 83**,** 273-278.

Lu, N., Anderson, M. T., Likos, W. J. & Mustoe, G. W. 2008. A discrete element model for kaolinite aggregate formation during sedimentation. *International journal for numerical and analytical methods in Geomechanics,* 32**,** 965-980.

Matthews, G. P., Ridgway, C. J. & Spearing, M. C. 1995. Void space modeling of mercury intrusion hysteresis in sandstone, paper coating, and other porous media. *Journal of Colloid and Interface Science,* 171**,** 8-27.

Milonni, P. & Lerner, P. 1992. Extinction theorem, dispersion forces, and latent heat. *Physical Review A,* 46**,** 1185.

Milonni, P. W. & Shih, M. L. 1992. Casimir forces. *Contemporary Physics,* 33**,** 313-322.

Mitchell, J. & Soga, K. 2005. Fundamentals of Soil Behavior, Jon Wiley and Sons Inc. *Hoboken, NJ.*

Mitchell, J. K. The fabric of natural clays and its relation to engineering properties. 1956.

Mitchell, J. K. & Soga, K. 1976. *Fundamentals of soil behavior*, Wiley New York.

Monroy, R. 2006. *The influence of load and suction changes on the volumetric behaviour of compacted London Clay.* Imperial College London (University of London).

Monroy, R., Zdravkovic, L. & Ridley, A. 2010. Evolution of microstructure in compacted London Clay during wetting and loading. *Geotechnique,* 60**,** 105-119.

Moore, C. & Mitchell, J. 1974. ELECTRO MAGNETIC FORCES AND SOIL STRENGTH. *Geotechnique,* 24.

Ng, T.-T. 1994. Numerical simulations of granular soil using elliptical particles. *Computers and geotechnics,* 16**,** 153-169.

Ng, T.-T. & Dobry, R. 1994. Numerical simulations of monotonic and cyclic loading of granular soil. *Journal of Geotechnical Engineering,* 120**,** 388-403.

Nicholas, M., Joyner, P., Tessem, B. & Olson, M. 1961. The effect of various gases and vapors on the surface tension of mercury. *The Journal of Physical Chemistry,* 65**,** 1373-1375.

O'Brien, N. R. 1971. Fabric of kaolinite and illite floccules. *Clays and Clay Minerals,* 19**,** 353-359.

O'Sullivan, C. 2011. *Particulate discrete element modelling*, Taylor & Francis.

Oda, M. & Konishi, J. 1974. Microscopic deformation mechanism of granular material in simple shear. *Soils and foundations,* 14**,** 25-38.

Olgun, M. & Yildiz, M. 2012. Influence of acetic acid on structural change and shear strength of clays. *Iranian Journal of Science and Technology Transaction B-engineering,* 36**,** 25-38.

Padday, J. 1957. A new method for measuring the spreading coefficient of a liquid on a solid surface. *Proc. 2nd Intern. Congr. Surface Activity***,** 136-142.

Penumadu, D. & Dean, J. 2000. Compressibility effect in evaluating the pore-size distribution of kaolin clay using mercury intrusion porosimetry. *Canadian Geotechnical Journal,* 37**,** 393-405.

Péron, H., Delenne, J.-Y., Laloui, L. & El Youssoufi, M. S. 2009. Discrete element modelling of drying shrinkage and cracking of soils. *Computers and geotechnics,* 36**,** 61-69.

Rand, B. & Melton, I. E. 1977. Particle interactions in aqueous kaolinite suspensions:: I. Effect of pH and electrolyte upon the mode of particle interaction in homoionic sodium kaolinite suspensions. *Journal of Colloid and Interface Science,* 60**,** 308-320.

Romero, E., Della Vecchia, G. & Jommi, C. 2011. An insight into the water retention properties of compacted clayey soils. *Geotechnique,* 61**,** 313.

Romero, E., Gens, A. & Lloret, A. 1999. Water permeability, water retention and microstructure of unsaturated compacted Boom clay. *Engineering Geology,* 54**,** 117-127.

Romero, E. & Simms, P. H. 2008. Microstructure investigation in unsaturated soils: a review with special attention to contribution of mercury intrusion porosimetry and environmental scanning electron microscopy. *Geotechnical and Geological Engineering,* 26**,** 705-727.

Sachan, A. & Penumadu, D. 2007. Effect of microfabric on shear behavior of kaolin clay. *Journal of geotechnical and geoenvironmental engineering,* 133**,** 306.

Schofield, R. 1946. Ionic forces in thick films of liquid between charged surfaces. *Transactions of the Faraday Society,* 42**,** B219-B225.

Schofield, R. & Samson, H. 1954. Flocculation of kaolinite due to the attraction of oppositely charged crystal faces. *Discuss. Faraday Soc.,* 18**,** 135-145.

Seed, H. B. & Chan, C. K. 1959. Thixotropic characteristics of compacted clays. *Transactions of the American Society of Civil Engineers,* 124**,** 894-916.

Sides, G. & Barden, L. 1971. The microstructure of dispersed and flocculated samples of kaolinite, illite, and montmorillonite. *Canadian Geotechnical Journal,* 8**,** 391-399.

Simpson, B. & Tatsuoka, F. 2008. Geotechnics: the next 60 years. *Geotechnique,* 58**,** 357-368.

Sloane, R. L. & Kell, T. 1966. The fabric of mechanically compacted kaolin. *Clays and Clay Minerals,* 14**,** 289-295.

Sposito, G. 1984. *The surface chemistry of soils*, Oxford University Press.

Sridharan, A. & Venkatappa Rao, G. 1973. Mechanisms controlling volume change of saturated clays and the role of the effective stress concept. *Geotechnique,* 23**,** 359-382.

Stawinski, J., Wierzchos, J. & García González, M. T. 1990. Influence of calcium and sodium concentration on the microstructure of bentonite and kaolin.

Steitz, R., Gutberlet, T., Hauss, T., Klösgen, B., Krastev, R., Schemmel, S., Simonsen, A. C. & Findenegg, G. H. 2003. Nanobubbles and their precursor layer at the interface of water against a hydrophobic substrate. *Langmuir,* 19**,** 2409-2418.

Stern, O. 1924. The theory of the electrolytic double-layer. *Zeit. Elektrochem,* 30**,** 508-516.

Tarantino, A. 2007. A possible critical state framework for unsaturated compacted soils. *Geotechnique,* 57**,** 385-389.

Tarantino, A. 2009. A water retention model for deformable soils. *Geotechnique,* 59**,** 751-762.

Tarantino, A. Unsaturated soils: compacted versus reconstituted states. 5th International Conference on Unsaturated Soil, 2010. 113-136.

Tarantino, A. & De Col, E. 2008. Compaction behaviour of clay. *Geotechnique,* 58**,** 199-213.

Tarantino, A. & Tombolato, S. 2005. Coupling of hydraulic and mechanical behaviour in unsaturated compacted clay. *Geotechnique,* 55**,** 307-317.

Thornton, C. 2007. A numerical examination of the direct shear test. *Geotechnique,* 57**,** 343-354.

Thornton, C. & Liu, L. 2000. DEM simulations of uni-axial compression and decompression. *Compaction of soils, granulates and powders,* 2**,** 251-261.

Tsakiroglou, C., Kolonis, G., Roumeliotis, T. & Payatakes, A. 1997. Mercury penetration and snap-off in lenticular pores. *Journal of Colloid and Interface Science,* 193**,** 259-272.

Tsakiroglou, C. D. & Payatakes, A. C. 1998. Mercury intrusion and retraction in model porous media. *Advances in colloid and interface science,* 75**,** 215-253.

Van Olphen, H. 1977. *Clay Colloid Chemistry: For Clay Technologists, Geologists and Soil Scientists*, John Wiley.

Verwey, E. J. W., Overbeek, J. T. G. & Van Nes, K. 1948. *Theory of the stability of lyophobic colloids: the interaction of sol particles having an electric double layer*, Elsevier New York.

Wahid, A. S., Gajo, A. & Di Maggio, R. 2011a. Chemo-mechanical effects in kaolinite. Part 1: prepared samples. *Geotechnique,* 61**,** 439-447.

Wahid, A. S., Gajo, A. & Di Maggio, R. 2011b. Chemo-mechanical effects in kaolinite. Part 2: exposed samples and chemical and phase analyses. *Geotechnique,* 61**,** 449-457.

Wang, Y. H. & Siu, W. K. 2006. Structure characteristics and mechanical properties of kaolinite soils. I. Surface charges and structural characterizations. *Canadian Geotechnical Journal,* 43**,** 587-600.

Wardlaw, N. & McKellar, M. 1981. Mercury porosimetry and the interpretation of pore geometry in sedimentary rocks and artificial models. *Powder Technology,* 29**,** 127-143.

Washburn, E. W. 1921. Note on a Method of Determining the Distribution of Pore Sizes in a Porous Material. *Proc Natl Acad Sci U S A,* 7**,** 115-6.

Webb, P. A. 2001. An introduction to the physical characterization of materials by mercury intrusion porosimetry with emphasis on reduction and presentation of experimental data. Micromeriticis Instrument Corporation.

Yao, M. & Anandarajah, A. 2003. Three-dimensional discrete element method of analysis of clays. *Journal of engineering mechanics,* 129**,** 585-596.

Yoshinaka, R. & Kazama, H. 1973. Microstructure of compacted kaolin clay. *Soils and foundations,* 13**,** 19-34.

Zhu, H., Zhou, Z., Yang, R. & Yu, A. 2007. Discrete particle simulation of particulate systems: theoretical developments. *Chemical Engineering Science,* 62**,** 3378-3396.